# A PARAMETRIC INVESTIGATION OF THE ANNULAR JET CONCEPT FOR OBTAINING AFTERBODY DRAG DATA AT TRANSONIC MACH NUMBERS

Earl A. Price, Jr.
ARO, Inc., a Sverdrup Corporation Company

PROPULSION WIND TUNNEL FACILITY
ARNOLD ENGINEERING DEVELOPMENT CENTER
AIR FORCE SYSTEMS COMMAND
ARNOLD AIR FORCE STATION, TENNESSEE 37389

February 1978

Final Report for Period 4 — 12 November 1976

Property of U. S. Air Force
AEDC LIBRARY
F40600 77 C 0003

Prepared for

ARNOLD ENGINEERING DEVELOPMENT CENTER/DOTR
ARNOLD AIR FORCE STATION, TENNESSEE 37389

This report has been reviewed by the Information Office (OI) and is releasable to the National Technical Information Service (NTIS). At NTIS, it will be available to the general public, including foreign nations.

APPROVAL STATEMENT

This report has been reviewed and approved.

ELTON R. THOMPSON
Project Manager, Research Division
Directorate of Test Engineering

Approved for publication:

FOR THE COMMANDER

MARION L. LASTER
Director of Test Engineering
Deputy for Operations

REPORT DOCUMENTATION PAGE		READ INSTRUCTIONS BEFORE COMPLETING FORM
1 REPORT NUMBER AEDC-TR-77-104	2 GOVT ACCESSION NO.	3 - RECIPIENT'S CATALOG NUMBER
4. TITLE (and Subtitle) A PARAMETRIC INVESTIGATION OF THE ANNULAR JET CONCEPT FOR OBTAINING AFTERBODY DRAG DATA AT TRANSONIC MACH NUMBERS		5 TYPE OF REPORT & PERIOD COVERED Final Report, 4-12 November 1976
		6 PERFORMING ORG. REPORT NUMBER
7. AUTHOR(s) Earl A. Price, Jr., ARO, Inc.		8 CONTRACT OR GRANT NUMBER(s)
9 PERFORMING ORGANIZATION NAME AND ADDRESS Arnold Engineering Development Center Air Force Systems Command Arnold Air Force Station, TN 37389		10. PROGRAM ELEMENT, PROJECT, TASK AREA & WORK UNIT NUMBERS Program Element PE65807F
11 CONTROLLING OFFICE NAME AND ADDRESS Arnold Engineering Development Center/DOS Air Force Systems Command Arnold Air Force Station, TN 37389		12. REPORT DATE February 1978
		13 NUMBER OF PAGES 176
14 MONITORING AGENCY NAME & ADDRESS(If different from Controlling Office)		15. SECURITY CLASS. (of this report) UNCLASSIFIED
		15a DECLASSIFICATION DOWNGRADING SCHEDULE N/A

16 DISTRIBUTION STATEMENT (of this Report)

Approved for public release; distribution unlimited.

17 DISTRIBUTION STATEMENT (of the abstract entered in Block 20, if different from Report)

18 SUPPLEMENTARY NOTES

Available in DDC.

19 KEY WORDS (Continue on reverse side if necessary and identify by block number)

annular nozzles   drag
jet plumes   transonic flow
simulator
plumes

20. ABSTRACT (Continue on reverse side if necessary and identify by block number)

    A parametric experimental program was conducted at free-stream Mach numbers of 0.6, 0.9, and 1.2 to investigate the plume simulation characteristics of annular jets. Plume simulation evaluation was based upon comparisons of afterbody pressure drag from integration of afterbody pressure measurements. Data were obtained on a 15-deg boattail afterbody attached to a strut-supported cylindrical centerbody. Geometric variables covered a range of sting-to-nozzle exit diameter ratios from 0 to 0.95 and nozzle area ratios from 1.0 to 1.5. High pressure air

DD $_{1 \text{ JAN } 73}^{\text{FORM}}$ 1473   EDITION OF 1 NOV 65 IS OBSOLETE

20. ABSTRACT (Concluded)

at ambient temperature was utilized for the exhaust gas. The results indicate that matching of the exhaust plume maximum diameter provides a reasonable afterbody drag correlation, accounting for effects of annular jet, nozzle exit-to-throat area ratio, and nozzle pressure ratio for conditions where drag follows the classical trend indicative of a plume shape dependence. Plume diameter correlation was not successful, for the pressure ratios of this investigation, for annular jet configurations having sting-to-nozzle exit diameter ratios of 0.95 at all Mach numbers and 0.866 at Mach number 1.2. There were no significant differences in the trends with angle of attack between the annular and conventional jet configurations over the angle-of-attack range from −2 to 6 deg.

AFSC
Arnold AFS Tenn

PREFACE

The work reported herein was conducted by the Arnold Engineering Development Center (AEDC), Air Force Systems Command (AFSC), for the Directorate of Test Engineering Research (AEDC/DOTR), under Program Element 65807F. The test was conducted by ARO, Inc., AEDC Division (a Sverdrup Corporation Company), operating contractor for the AEDC, AFSC, Arnold Air Force Station, Tennessee, under ARO Project Number P41T-J9A in support of Research Project Number P32P-H0A. The manuscript (ARO Control No. ARO-PWT-TR-77-69) was submitted for publication on October 14, 1977.

CONTENTS

ILLUSTRATIONS

Figure

APPENDIXES

1.0 INTRODUCTION

The present generation of high performance variable nozzle aircraft has resulted in the need to more accurately define the drag characteristics of the aircraft aft-fuselage and nozzle regions. Typically, the afterbody region of aircraft models must be modified to accommodate a sting for basic aerodynamic testing in the wind tunnel. Drag increments from such altered aerodynamic models and throttle-dependent increments may be quite significant in terms of the overall drag of the aircraft and are the two basic reasons for conducting what are typically referred to as nozzle-afterbody tests.

One of the problems frequently encountered in the conduct of such tests is the model support system interference. In the past, the most common practice has been to support the aircraft model in the forward fuselage region by a strut and to use compressed air for simulation of the engine exhaust plume. Interference effects from such a support system can introduce significant errors in the measured values of the aircraft afterbody drag, typically similar to the results shown in Refs. 1 and 2. These errors, which vary with Mach number and configuration, could result in misleading conclusions when aircraft afterbody drag is evaluated to determine optimum afterbody configurations. The concept of supporting a model with a sting extending into the engine exhaust nozzle and simulating the exhaust jet with an annular jet becomes particularly attractive for minimizing support system interference. This is particularly true if proper exhaust plume simulation can be obtained. This general concept has been tried, and several reports are available in the literature for both the solid plume simulators (e.g., Refs. 1, 3, and 4) and the annular jet concept. The annular jet data (Refs. 5, 6, and 7) have, in general, been limited in terms of geometric variables and to a certain extent in terms of test conditions investigated.

The experimental results reported herein were obtained during a parametric study of engine exhaust nozzle area ratio and sting-to-nozzle exit diameter ratio, geometric parameters which are frequently encountered when the annular jet problem is considered. The purpose of this investigation was to evaluate correlation parameters which could be used to duplicate the afterbody pressure drag of a model having conventional axisymmetric nozzle exhaust flow using a sting-supported model having annular nozzle exhaust flow.

2.0 APPARATUS

2.1 TEST FACILITY

The investigation was conducted in the 16-foot Transonic Wind Tunnel (16T) of the Propulsion Wind Tunnel Facility (PWT) at the Arnold Engineering Development Center

(AEDC). Tunnel 16T is a closed-circuit, continuous flow wind tunnel capable of being operated at Mach numbers from 0.20 to 1.60 within a stagnation pressure range from approximately 200 to 3,400 psfa, depending upon the Mach number. A more extensive description of the tunnel and its operating characteristics is contained in Ref. 8.

2.2 MODEL AND SUPPORT SYSTEM

A sketch of the test installation is presented in Fig. 1. The model consisted of a strut-supported cylindrical centerbody with a conical nose and a 15-deg boattailed afterbody. The model had an overall length of approximately 147 in., a maximum diameter of 9.86 in., and a 14-deg half-angle conical nose. The support strut was tapered from the model to the floor with the thickness-to-chord ratio varying from 0.053 at the model to 0.088 at the tunnel floor; the strut swept aft from the model at an average angle of 35 deg. A photograph of the installation is shown in Fig. 2, and a sketch of the afterbody contour with tabulated values for the external surface coordinates is presented in Fig. 3.

The general arrangement of the internal portion of the model with a dummy sting installed is illustrated in Fig. 4. High pressure air was ducted through the strut into the flow duct of the model. The dummy stings were threaded on the upstream end and attached to the sting support bracket in the flow duct; additional support for each dummy sting was provided by a slip fit through the center of the choke plate. For obtaining conventional jet data the stings were removed, and a perforated filler plug was installed in the choke plate.

Eleven nozzles (shown in Fig. 5) were used to obtain the various nozzle area ratios with the different dummy stings. To facilitate nozzle changes, the model was designed for changing nozzles through the flow duct exit without removing the afterbody and aft portion of the flow duct. This required the use of segmented nozzle holders, as shown in Fig. 5. Three sets of holders were built to accommodate the various sizes of nozzles required. All nozzles had a divergence half angle of 5 deg, with the exception of the nozzle used for area ratio 1.0 data, nozzle 12, which was designed for parallel flow at the exit. A photograph showing the six segments which comprise each nozzle holder and the nozzles which were used with each holder is presented in Fig. 6. A dimensional sketch of the dummy stings is shown in Fig. 7, and a photograph of the four stings is shown in Fig. 8. A photograph of the aft portion of the model with a sting installed is presented in Fig. 9.

The following matrix illustrates the combination of nominal nozzle area ratios, sting-to-nozzle exit diameter ratios, and Mach numbers for which data were obtained.

D_s/D_N	0			0.543			0.707			0.866			0.95		
M_∞ / A/A*	0.6	0.9	1.2	0.6	0.9	1.2	0.6	0.9	1.2	0.6	0.9	1.2	0.6	0.9	1.2
1.00	x	x								x	x	x			
1.13	x	x	x	x	x	x		x	x	x	x	x	x	x	x
1.22	x	x	x				x	x	x						
1.31	x	x	x				x	x	x		x	x			
1.49	x	x	x	x	x	x	x	x	x	x	x	x	x	x	x

This matrix permits evaluating the effects of sting-to-nozzle exit diameter ratio at a constant area ratio and determining the effects of nozzle area ratio at constant sting-to-nozzle exit diameter ratio.

2.3 INSTRUMENTATION

The afterbody section of the model was instrumented with 65 pressure orifices in rows along the top, side, and lower surfaces of the model. Coordinates of each pressure orifice are presented in Table 1. Model chamber pressure was determined from four static pressure taps in the flow duct at MS 133.45. Mass flow rates of the air exhaust were calculated from pressure and temperature measurements in a critical flow venturi metering section located in the facility piping system. Two of the stings (A and C) were instrumented with 24 pressure taps, as shown in Fig. 7. These were connected for selected configurations with the pressure tubing extending from the end of the sting and supported by a 1/4-in. cable which spanned the tunnel vertically as shown in the photograph in Fig. 10. Model angle of attack was determined from a strain-gage angular position indicator.

3.0 PROCEDURE

3.1 TEST CONDITIONS

Data were obtained at free-stream Mach numbers of 0.6, 0.9, and 1.2. The nominal free-stream Reynolds number was 2.0 x 10^6 per foot. Angle of attack was varied from -2.0 to 6.0 deg for selected configurations with nozzle flow at design pressure ratio. The nozzle pressure ratio was varied for all configurations at zero angle of attack.

3.2 TEST TECHNIQUE

The primary testing technique for a given geometric configuration consisted of obtaining data as a function of nozzle exit static-to-tunnel free-stream static pressure ratio (NSPR). The parameter NSPR was displayed in real time to ensure recording data at the

desired nozzle pressure ratios. In general, data were recorded for the pressure ratio range from jet-off to a value in excess of twice the nozzle design pressure ratio. When time permitted, data were recorded at several nozzle pressure ratios in the region between jet-off and design pressure ratio, where afterbody drag changes are generally large. For selected configurations, data were recorded in 2-deg increments over the angle-of-attack range, -2 to 6 deg, with the nozzle operating at design pressure ratio. Schlieren photographs were taken at five points spanning the NSPR range for each configuration.

3.3 DATA REDUCTION

Pressure coefficients were calculated from the static pressure measured at each orifice on the afterbody in addition to those on the sting. The pressure distributions for each of the three rows (see Table 1) on the boattail were integrated, on the assumption that the pressure along each row was imposed over the entire boattail projected area, independent of the remaining two rows. Therefore, a pressure drag coefficient was calculated based on the measurements on each of the top, side and bottom rows. The reference area for the drag coefficients was the model maximum cross-sectional area (76.062 in.^{2}). Drag coefficients from the top row of pressures, CDPT, are used exclusively in this report. The top row of orifices was selected because it is considered to be the least affected by the strut at subsonic Mach numbers. Also, it was shown in Ref. 9 that data along the top and bottom rows of a configuration similar to the present one were correlated equally well. The nozzle total pressure was calculated from one-dimensional, isentropic relationships using flow duct static pressure and the area ratio between the flow duct and the nozzle throat.

3.4 UNCERTAINTY OF MEASUREMENTS

The uncertainty of the major test parameters is tabulated below. The uncertainty in these parameters includes the uncertainties in the individual pressure transducers and in the tunnel reference systems. Uncertainty is defined as

$$U = \pm(B + t_{0.95} \, S)$$

where B is the bias and S is the precision, and $t_{0.95}$ is a function of the number of samples utilized in the calibration of a given instrument. For these results a value of 2 was used for $t_{0.95}$. For each test parameter, values of bias and precision were determined from propagating errors from each source by the Taylor series method.

Parameter	Mach Number		
	0.6	0.9	1.2
CDPT	±0.0014	±0.0007	±0.0049
C_p (Boattail)	±0.018	±0.013	±0.009
C_p (Sting)	±0.076	±0.021	±0.009
NPR	±0.021	±0.032	±0.047
NSPR	±0.006	±0.008	±0.013

It is evident from the preceding tabulation that there is considerable variation in the calculated uncertainty of CDPT with Mach number, using the propagation of error techniques. The uncertainty for Mach number 1.2 is significantly higher than the uncertainties for the subsonic Mach numbers and is larger than would be expected from the trends in the data. A comparison of repeat points revealed that data repeatability was similar at each Mach number, with an average spread of 0.0012 in CDPT between two data points at the same condition. The maximum spread in drag coefficient of any one repeated condition was 0.0034. In a comparison of data from various configurations for a given test installation using the same instrumentation, data repeatability is believed to be of more practical interest. Therefore, the repeatability given here for CDPT is believed to represent a more realistic uncertainty than do those numbers calculated from conventional propagation of error techniques.

4.0 EXPERIMENTAL RESULTS

In general, the text of this report contains only the afterbody drag coefficients obtained from integrating the measured pressures on the top row of orifices. Presentation of the pressure distributions from each data point included would be too bulky to include in the report; however, selected pressure distributions illustrating the various effects discussed in the report are presented in Appendix A. As stated previously, the afterbody pressure drag coefficients were nondimensionalized by model maximum cross-sectional area. Since aircraft drag data are usually nondimensionalized by wing area, which is generally approximately fifteen times fuselage cross-sectional area for fighter-type aircraft, it requires approximately 15 of these "body" drag counts (0.0015 in CDPT) to equal a typical aircraft drag count (0.0001). Except where specifically noted on the figures, all the results presented were obtained at zero angle of attack.

For each configuration and Mach number investigated, data were obtained over the NPR range from jet-off to over twice the design pressure ratio (NSPR > 2.0). The maximum NSPR obtained depended somewhat upon configuration and Mach number. A

typical variation of afterbody pressure drag with nozzle pressure ratio (NPR) for a conventional jet configuration is presented in Fig. 11. Although the shape of the curve may vary with configuration and Mach number, this figure is presented to illustrate the different regions of the curve since reference will be made to them in the subsequent sections of this report. The jet-off point is typically followed by a significant decrease in drag to what is termed here the low pressure ratio drag "bucket." This decrease in drag is attributed to a reduction of the flow expansion over the boattail as the low pressure model base region is eliminated by the small nozzle flows. This drag "bucket" region is followed by a region dominated by entrainment of the flow over the afterbody by the jet and is characterized by an increase in drag with NPR. Acceleration of the entrained afterbody flow results in lower afterbody pressure and hence higher drag. A peak jet-on drag point typically is reached at or before design pressure ratio is reached (for afterbodies without separated flow) and is followed by a decrease in drag with increasing pressure ratio. This latter region is dominated by plume shape effects. As the plume becomes larger with increasing NPR, interference extends forward, increasing the pressure on the afterbody and thus decreasing drag. Additional discussions of the general nature of the afterbody drag curve may be found in Refs. 4 and 9.

In general, afterbody jet effects data available in the literature have rather sparse documentation of the drag curve in the overexpanded jet region. During this investigation, data were recorded at small NPR intervals in this region in an attempt to obtain complete documentation and a better understanding of the effects of stings on the afterbody drag. In obtaining experimental data for such a curve, one must exercise special care if reliable jet-off and low pressure drag bucket data are to be obtained. For example, experience has shown that high pressure air control valves of the size required to control the maximum air weight flow are inadequate as shutoff valves for obtaining jet-off data. Very small amounts of leakage will invalidate the jet-off points; therefore, two valves in series, with a vent between them, were utilized to obtain the jet-off points for this investigation. A further problem is that the small weight flows required to define the drag bucket are difficult to control with the large control valves. A smaller auxiliary bypass system was utilized during this test to obtain these points.

4.1 EFFECTS OF D_s/D_N

Experimental data are presented in Figs. 12 through 16 for the integrated afterbody pressure drag to illustrate the effect of D_s/D_N on the afterbody drag for each nozzle area ratio. Data are presented for the model at zero angle of attack and, in general, for each of the Mach numbers 0.6, 0.9, and 1.2. For each configuration the drag coefficients are plotted as a function of jet total to free-stream static pressure ratio (NPR). It may be observed from these figures that increasing sting diameter has large effects on drag in certain regions of drag-versus-NPR curves.

First of all it should be noted that drag coefficients for jet-off points decrease with increasing sting diameter. This trend has previously been documented experimentally (e.g., Ref. 3) and is as expected since, as the sting fills the base area, the flow expansion on the boattail is decreased. For these data, as D_s/D_N approaches 1.0 the jet-off drag level falls near the same level as the low pressure drag bucket. These trends indicate that for this configuration use of a cylindrical plume simulator equal to the nozzle exit diameter ($D_s/D_N = 1.0$) to represent the shape of the exhaust plume at design pressure ratio would result in considerable error in the prediction of afterbody drag. The effect of dummy sting diameter on jet-off drag is summarized in Fig. 17 for each of the Mach numbers. Symbols on this figure represent the average of all jet-off points obtained at a given Mach number and sting diameter during this investigation. The brackets on each symbol indicate the total variation in the measured drag coefficients at a particular condition.

A second point to be observed in the data is that the minimum drag coefficient in the "drag bucket" approaches a near-constant value regardless of sting size or area ratio. Conditions where the curve fairing does not go through this minimum drag point are generally felt to be conditions where sufficient data were not taken to accurately define this region.

The effect of sting diameter on the remainder of the overexpanded jet region does not follow consistent trends for all area ratios and Mach numbers. For several combinations of Mach number and area ratio (e.g., Figs. 13a, 13c, 14a, 14c, 16a, and 16c) the trend is for drag to increase in this region as sting diameter is increased. This is a trend which seems most feasible in a region dominated by jet entrainment. However, since there are other data at different Mach numbers and area ratios which exhibit the opposite trend (e.g., Figs. 19b, 21b, and 22b) it must be concluded that the explanation of sting size effects in this region are complex and are related not only to the entrainment and plume size but also to Mach number and nozzle area ratio.

In the underexpanded jet region the basic data trends with sting diameter were consistent for all conditions investigated. For the range of variables investigated, increasing sting diameter generally has the effect of reducing the sensitivity of the afterbody drag to NPR. Therefore, as NPR is increased, the disagreement in drag between a configuration of any given sting diameter and the conventional jet becomes larger. This region of the drag curve for conventional exhaust plumes is typically dominated by plume shape effects, because as plume size increases with NPR the afterbody experiences an increase in pressure from plume blockage, thus decreasing drag. This typical trend was observed for the present data except for the largest sting ($D_s/D_N = 0.95$) at all Mach numbers and for the second largest sting ($D_s/D_N = 0.866$) at $M_\infty = 1.2$. Drag data at these conditions tend to be relatively insensitive to NPR at the larger values but generally exhibit a slight increase with NPR. This indicates that entrainment, not plume shape, is the dominant influence on afterbody drag.

4.2 EFFECTS OF A/A*

The data presented in the previous section constitute a complete set of the basic drag results from this investigation. These results are presented again, however, in Figs. 18 through 22 to more clearly illustrate the effects of A/A* on afterbody drag by also presenting data from various values of A/A* at constant values of D_s/D_N. The data from the conventional jet configuration (Fig. 18) are seen generally to increase with increasing A/A* at a given value of NPR. The exception to this trend is some crossover in the overexpanded jet region, particularly at $M_\infty = 1.2$. For results at pressure ratios beyond the maximum drag point, the data curves tend to diverge. The difference between the slopes of the curves indicates that as A/A* is increased the sensitivity of afterbody drag to NPR decreases.

The trends in the annular jet drag data (Figs. 19 through 22) with A/A* are similar to those of the conventional jet when $D_s/D_N \leqslant 0.707$. For example, the maximum jet-on drag at Mach numbers 0.6 and 0.9 increases with increasing A/A*. At $D_s/D_N = 0.866$ the data for subsonic Mach numbers generally have higher drag at the larger values of A/A*, and in general the drag curves become relatively flat. At $M_\infty = 1.2$ for $D_s/D_N = 0.866$ and at all Mach numbers for $D_s/D_N = 0.95$ the effects of A/A* were very small. In general, after the low pressure minimum drag point, the drag coefficients continue to increase slightly with NPR over the complete NPR range of this investigation. This indicates that entrainment is the dominant influence on afterbody drag for these configurations.

4.3 EFFECTS OF ANGLE OF ATTACK

A potential problem area in utilizing the sting-supported annular jet concept is the effect the stings might have on the afterbody drag with the model at angle of attack. To investigate this effect, selected configurations were tested at the design pressure ratio of the nozzle over the angle-of-attack range from -2 to 6 deg. The results of this study are presented in Figs. 23 and 24 for the nominal area ratio nozzles of 1.13 and 1.49, respectively. Data are presented for each Mach number of this investigation. It should be noted that positive a is nose down; therefore, the pressure orifices utilized for drag integration are on the windward side of the model at positive angles of attack. Adverse angle-of-attack effects from the sting must be deduced from differences in slope of the CDPT versus a curves for the different sting diameters. Constant differences in drag coefficient between conventional and annular jet configurations indicate the basic sting effect and not adverse effects of angle of attack. The data obtained on these configurations generally resulted in parallel curves for the conventional and annular jet configurations. Changes in slope that were obtained do not follow consistent trends and are within the repeatability of the data. It may be concluded, therefore, from these data that there were no significant adverse angle-of-attack effects caused by the annular jet configurations at angles of attack up to 6 deg.

4.4 PLUME CHARACTERISTICS

As was mentioned previously, the stings representing values of D_s/D_N = 0.543 and 0.866 were instrumented with static pressure taps for obtaining plume diagnostic pressure data. Representative data from these sting pressures, along with schlieren photographs, are presented in Figs. 25 through 28 to illustrate various effects on the plume characteristics. The effects of pressure ratio are presented in Fig. 25a (pressure coefficient results) and Fig. 25b (schlieren photographs) for D_s/D_N = 0.543 and A/A* = 1.134 at M_∞ = 0.9. The classical periodic nature of the plumes is evident in the sting pressure distributions, where the expansions and compressions of the plume flow were measured, as well as in the schlieren photographs. As NPR is increased, the increase in plume diameter is evident from the schlieren photos. Also, the length of the periodic segments or wavelength of the plume increases with increasing NPR, as is evident from both the pressure data and schlieren photographs.

The lengths of the plume segments at NSPR $\approx$ 2 are approximately twice those at NSPR $\approx$ 1. This follows closely the trend in the variation of plume segment length with NSPR predicted by the empirical relation of Eq. (1) in Ref. 10 for conventional full plumes. The increase in strength of the expansion and compression regions of the plumes with increasing NSPR is not as evident in the schlieren photographs, but may be seen in the pressure data. The strength of these regions is seen to diminish as one moves down the sting. Since the plume definition is clearer at higher pressure ratios, the remaining effects will be presented primarily for NSPR $\approx$ 2.0.

The effects of sting diameter on the plume characteristics are presented in Fig. 26 for NSPR $\approx$ 2.0. Pressure data are presented for the two instrumented stings, and schlieren photographs are presented for each sting diameter as well as for the conventional jet. Increasing the sting size resulted in shorter length plume segments and large reductions in the magnitude of the peak pressures in the expansion and compression regions. The pressure variations with the large sting configuration become essentially damped out after three periodic segments of the plume. The smaller size and strength of these plume segments are apparently overcome by the mixing of the free-stream flow and viscous effects from the flow along the sting. The effect of nozzle area ratio at NSPR $\approx$ 2.0 on the plume characteristics for D_s/D_N = 0.543 is presented in Fig. 27. These results indicate an increase in plume wavelength with increasing A/A* (or nozzle exit Mach number). A similar trend in wavelength for conventional jets was reported in Ref. 10.

All of the plume characteristics thus far presented have been for a free-stream Mach number of 0.9. A comparison of plume characteristics from each Mach number of this investigation is presented in Fig. 28. In this figure, pressure data are presented at NSPR $\approx$ both 1.0 and 2.0; however, schlieren photographs are presented only for the higher

pressure ratio. In terms of pressure coefficient, these results indicate a decrease in the strength of the expansion and compression peaks with increasing Mach number, as well as by more rapid damping of the plume waves. The photographic results support the conclusions drawn from the pressure data in that the plume appears to diffuse into the free-stream flow more rapidly as Mach number increases. It is concluded from these results that, where comparisons can be made, the annular plume characteristics vary in a fashion similar to conventional plumes. This was noted particularly in regard to the variation of plume primary wavelength with NPR and with A/A* (nozzle exit Mach number).

5.0 CORRELATION OF RESULTS

In many instances the attempts to correlate afterbody drag results have been prompted by the desire to match results from hot and cold jet plume data. These efforts have frequently involved such parameters as specific heat ratio, gas constant, temperature, and related parameters. Since these parameters were fixed for the present test and since the effects of D_s/D_N may be evaluated at constant values of A/A*, the conventional type correlation parameters (incremental change in Prandtl Meyer angle, NSPR · A/A*, etc.), which are functions of these parameters, would provide no better correlation of the effects of sting diameter than does NPR. Plume maximum diameter does, however, vary with sting size, and following the suggestion of Ref. 5 the use of this parameter for correlation purposes was evaluated.

5.1 CORRELATION OF D_s/D_N EFFECTS

An illustration of how the plume shape varies with sting size from an underexpanded jet is shown in Fig. 29. These plume shapes were calculated by the method of characteristics (MOC) (Ref. 11) for a jet issuing into quiescent air. The results shown are for a constant NSPR of 2 and for a nominal nozzle area ratio of 1.13. Results of these calculations indicate that for underexpanded jets at the same nozzle area ratio and pressure ratio, annular nozzles produce plumes of smaller maximum diameter and shorter longitudinal period than do conventional nozzles. These changes vary uniformly with increasing sting size. Physically, this may be visualized by considering the expansion and compression waves associated with the jet plumes. Since these waves propagate along characteristics, the interaction of the waves with the free stream, which determines the shape of the plume boundary, is a function of the distance the interior surface reflecting the waves toward the plume boundary is located from the longitudinal axis of the nozzle. Compression waves tend to reduce the plume diameter by turning the flow toward the longitudinal axis of the nozzle, whereas expansion waves tend to increase the diameter by turning the flow away. In the case of the annular nozzle, the interior surface (i.e., the sting), reflecting the waves toward the plume boundary, is displaced from the nozzle longitudinal

axis, causing the wave-plume boundary interactions to occur over shorter axial distances. Thus both the plume diameter and period are reduced.

Schlieren photographs obtained at $M_\infty = 0.9$ were presented in Fig. 26b for the same area ratio and sting diameters used for the theoretical plume shapes shown in Fig. 29. Measurements of plume diameter from these schlieren photographs are compared with those from the MOC calculations in Fig. 30. The agreement is surprisingly good considering that the MOC calculations are for quiescent ambient conditions. The disagreement at the maximum sting size is in a region where measurements were difficult to make from the schlieren photographs. It should be remembered that the variation in plume diameter with D_s/D_N shown in these figures will vary with NSPR, with annular and conventional nozzle plumes both becoming cylindrical and equivalent to the nozzle exit diameter at design pressure ratio. Therefore, the extent to which plume shape affects the data would be expected to increase as pressure ratio increases above the design value. This was, of course, the trend with sting diameter which the data exhibited in Figs. 12 through 16. These results are presented again in Figs. 31 through 35 for comparison with drag coefficient as a function of a correlation pressure ratio (NPR1). For selected configurations data are also presented as a function of another correlation pressure ratio (NPR3). Each of these correlation pressure ratios follows the methodology of comparing annular jet data with conventional jet data at the same maximum plume diameter. In these figures the annular jet drag coefficient data for nozzle pressure ratios greater than design have been plotted at the pressure ratio of a conventional jet which would be required to produce the same maximum plume diameter. Data at pressure ratios less than design have been plotted at the actual pressure ratios. The difference in NPR1 and NPR3 results from the different methods used for calculating maximum plume diameter. NPR1 is the conventional jet pressure ratio obtained from one-dimensional stream tube area relationships, which corresponds to a plume diameter, D_{max}, determined from the actual annular jet pressure ratio, NPR. The method of characteristics, rather than one-dimensional flow equations, was used to determine NPR3.

An illustration of the procedure for determining each of the correlation pressure ratios for a given annular jet data point is presented in Fig. 36. In this example, it is assumed that a configuration having $A/A^* = 1.133$ and $D_s/D_N = 0.707$ was tested at a measured annular jet pressure ratio of 9.5. As is demonstrated by following the arrows on each figure, this pressure ratio and configuration result in the same plume maximum diameter as a conventional nozzle at a pressure ratio of 6.3 using NPR1 (Fig. 36a) or 6.85 using NPR3 (Fig. 36b). Therefore, a data point obtained at NPR = 9.5 would, for this correlation, be plotted at NPR1 = 6.3 or NPR3 = 6.85, depending on which method was chosen for the correlation.

It should be pointed out that to utilize the method just described for an actual sting-supported annular jet, the opposite procedure would be followed. That is, with a given conventional jet NPR an annular jet NPR would be determined which would produce the same maximum plume diameter. Curves similar to those in Fig. 36b were constructed by the method of characteristics and used for each case where NPR3 correlations are shown. The values of NPR1 were computed for each data value. As sting size is increased, the reduced sensitivity of plume size to NPR, which may be seen in Fig. 36, coincides with the reduced sensitivity of afterbody drag to NPR, which was discussed earlier (Section 4.1). These trends in afterbody drag and plume size with NPR are the basic reasons for attempting the correlations (NPR1 and NPR3) shown in Figs. 31 through 35. As may be seen in these figures, both of these pressure ratios do reasonably well in correlating the data in the underexpanded jet region.

The MOC solution (NPR3) is no doubt a preferred method for predicting actual plume diameter; however, there appears to be no advantage in utilizing it over the one-dimensional solution (NPR1) for purposes of correlating the drag results. This is attributed to the fact that what is in effect used from these plots (Fig. 36) is an increment in NPR required to adjust the annular data to conventional data (or vice versa). This increment appears to be reasonably consistent between the two methods, although the actual plume diameters that the two methods predict are considerably different, as may be seen in the example shown in Fig. 36.

Since the one-dimensional flow solution lends itself more readily to a quick analytical solution than does the MOC technique, it was utilized for each underexpanded jet pressure ratio in this investigation. As may be seen in Figs. 31 through 35, the maximum pressure ratios obtained during this test were not large enough to correlate data from the two large sting configurations over a significant range of underexpanded pressure ratios. The general trends in drag with NPR for these large sting configurations tend to be relatively flat or slightly increasing in the underexpanded jet region for the range of pressure ratios considered. Additional testing would be required on these larger stings at higher underexpanded pressure ratios to properly evaluate this correlation technique. The pressure ratio range of this test was sufficient, however, to document the jet-on drag peak and subsequent drag decrease for the smaller stings ($D_s/D_N = 0.707$ and 0.543), and the correlation appears to be adequate for the underexpanded pressure ratios at all Mach numbers.

In addition to the comparison of the two methods which may be made using the data in Figs. 31 through 35, plots are presented in Fig. 37 which illustrate the degree to which each of the correlation methods was successful in correlating the annular jet data to the conventional jet results at 1.5 times the design pressure ratio. These correlations indicate reasonable results at all Mach numbers. The NPR1 correlation is within 35 body

drag counts for all conditions. There are no apparent trends with A/A*, and no advantage is seen for using NPR3 (MOC technique) correlation over the simpler NPR1 technique. It should be noted that the conclusions drawn here for the correlation parameters are based primarily upon data from sting sizes of D_s/D_N = 0.543 and 0.707, with limited points at small area ratios for D_s/D_N = 0.866.

At design pressure ratio these techniques do not provide any correlation for the data since the plume is theoretically cylindrical and equal to the nozzle exit area for both annular and conventional jets. Since this is generally the most important point for evaluation of afterbody jet effects, a comparison is presented in Fig. 38 of the increments in drag coefficient at NSPR = 1.0 between the conventional and annular jet configurations. At subsonic Mach numbers the largest difference was approximately 55 body drag counts, which would typically represent about 3 aircraft drag counts. At Mach number 1.2, however, the difference was significantly larger, having a maximum of approximately 140 body drag counts difference for the largest sting.

5.2 CORRELATION OF A/A* EFFECTS

Data are presented in Figs. 39 through 43 to show the correlation of the drag results from configurations of different area ratios. The basic data, plotted as a function of NPR, are presented in the top plot in each figure for reference purposes. The second plot in each figure is a correlation of data at underexpanded jet pressure ratios based upon plume maximum diameter as determined by one-dimensional flow relationships as discussed in the preceding section. A third plot is included for the conventional jet results (Fig. 39) which is a similar attempt at correlation using the method of characteristics to predict the maximum plume diameter. In each of the two methods the data have been correlated to the curve obtained for the maximum area ratio configuration. Therefore, an experimental point obtained on a configuration which has an area ratio less than maximum (A/A* $\approx$ 1.49) would be shifted to the right on the plot to the NPR for the maximum A/A* which would give the same maximum plume diameter.

An example of the procedure for determining the correlation pressure ratio NPR2 for a data point on a conventional jet configuration having an area ratio of 1.134 is presented in Fig. 44. In this example it is assumed that a data point was obtained at NPR = 5.5. As may be seen by following the arrows in the figure, this results in the same plume maximum diameter as the A/A* = 1.490 configuration has at NPR = 9.2. Thus, an experimental point obtained at NPR = 5.5 would for the correlation be plotted at NPR2 = 9.2. The decision to correlate the data to the maximum value of A/A* was somewhat arbitrary. The same methodology could be used to correlate the data to any of the other area ratios.

Each of the correlation pressure ratios is seen to collapse the conventional jet data (Fig. 39) in the underexpanded jet region quite well. This region is collapsed to a total drag coefficient band width of approximately 40 body drag counts at each of the Mach numbers from an uncorrelated maximum span of 320 drag counts. The degree of correlation achieved by this method indicates that plume diameter is the dominant influence on the afterbody drag in this region.

The relationship of drag to the conventional plume maximum diameter is illustrated in a different form in Fig. 45. In this figure, crossplots of the drag from the different area ratio nozzles (Fig. 39) at constant values of NPR are presented as a function of plume maximum diameter ratioed to nozzle exit diameter (D_{max}/D_N). These values of D_{max}/D_N were determined from one-dimensional flow area rationships. Nozzle pressure ratios of 3, 4, and 6 are shown here to illustrate the influence of plume diameter on a region of the drag curve which overlaps both overexpanded and underexpanded jet pressure ratios. The dashed line is a least squares straight line fit of these data. Maximum jet-on drag occurred near NPR = 3 for all area ratios, and thus represented the approximate dividing point between the portion of the drag curve dominated by entrainment effects (NPR < 3) and that portion dominated by plume shape effects (NPR > 3). For these pressure ratios the data generally demonstrate a consistent trend of decreasing afterbody drag with increasing maximum plume diameter in both the underexpanded and overexpanded jet regions. These data fall within an overall band of approximately 50 body drag counts. The extent to which the data do not correlate may, in addition to data uncertainty, be attributed to entrainment effects. For example, at M_∞ = 0.9 there is a consistent trend of increasing drag with increasing NPR at constant values of D_{max}/D_N. This is a trend that would be expected from entrainment of the flow over the afterbody because of the increased velocity and density of the exhaust plume as pressure ratio is increased. Extension of this type correlation to pressure ratios below the peak drag point (NPR ≈ 3.0 for this case) is not deemed practical since this is the region where entrainment effects (i.e., increasing drag with increasing NPR) are predominant. It may be concluded from this figure that the increase in maximum jet-on drag with increasing A/A* for the conventional jet results may be correlated by maximum plume diameter. A comparison of additional conventional-type correlation parameters for these data is presented in Appendix B.

Correlation of nozzle area ratio effects for the annular jet configurations (Figs. 40 through 43) are presented only from the one-dimensional flow solution since no advantage has been shown in using the MOC solution. For values of D_s/D_N ≤ 0.707 (Figs. 40 and 41) the data at all Mach numbers are correlated reasonably well by NPR2. At D_s/D_N = 0.866 the drag coefficient remains essentially constant after the peak jet-on drag is reached; therefore, the correlation procedure does very little to bring the data

together. For the largest sting size (D_s/D_N = 0.95, Fig. 43) there was very little effect of A/A^* on the basic data, and the drag results generally continued to increase with NPR. This trend indicates that entrainment has the dominant influence on afterbody drag for these conditions and, therefore, that use of the plume shape parameter NPR2 tends to force the results apart at all Mach numbers.

Plots of drag versus D_{max}/D_N are presented in Figs. 46 through 49 for each value of D_s/D_N tested during this investigation. These plots were generated by cross-plotting the data for the different area ratio nozzles at constant values of NPR. As was done for the conventional nozzle data (Fig. 45), a least squares straight line fit through these data is represented by the dashed line. In each case values of NPR were chosen which would show data for both underexpanded and overexpanded plume shapes. These plots indicate a trend similar to the conventional jet data (decreasing drag coefficient with increasing plume diameter) for the majority of test conditions. The exceptions are for data obtained at M_∞ = 1.2 for D_s/D_N = 0.866 and at all Mach numbers for D_s/D_N = 0.95 where, as discussed previously (Figs. 42 and 43), the data are dominated by entrainment of the afterbody flow rather than by plume shape effects. The least squares fits of the data from each of the stings are compared with the conventional jet results in Fig. 50. With the exception of the results dominated by entrainment, the agreement of the annular jet results with the conventional jet results is excellent, considering the fact that this figure includes results from various pressure ratios, area ratios, and sting diameters. The maximum difference in the least squares curve fits between the conventional jet results and the correlatable annular jet results at D_{max}/D_N = 1.0 is approximately 35 body drag counts. Figure 50 also serves to illustrate that there are limits which vary with Mach number and sting size above which plume diameter does not correlate the data near design pressure ratio. For this afterbody configuration, it may be concluded that the D_s/D_N = 0.95 configuration is too large for proper correlation at all Mach numbers of this investigation and the D_s/D_N = 0.866 configuration is too large at M_∞ = 1.2.

The plots presented in Figs. 45 through 49 may also be used to deduce some facts regarding the future utilization of the annular jet concept in wind tunnel tests. As the results presented thus far have indicated, simulation of a given conventional jet drag level may be achieved within certain limits by duplicating the plume maximum diameter. It is evident from these plots that plume diameter may be changed either by changing NPR for a given area ratio or by changing area ratio at a given NPR. Area ratio itself then need not be matched, as long as the combination of area ratio and NPR is such that the maximum plume diameter is matched. In a test program designed for obtaining data on a given configuration using both the conventional and annular jet techniques a saving on hardware cost could be achieved by using the same nozzles for both techniques. Introducing a sting into the conventional nozzles would increase the area ratio of the

nozzle, and (as may be seen from these plots to simulate a given plume diameter with a higher area ratio nozzle) a corresponding higher NPR would be required. This would be possible, of course, only if the model had adequate pressure capability. The same principle may be applied when a model must be used with limited pressure capability. For this case, although different nozzles would be required, use of an annular nozzle with a lower area ratio than the conventional nozzle would permit simulation of the plume diameter with a lower NPR than if area ratio were matched.

6.0 CONCLUDING REMARKS

A parametric experimental program was conducted to evaluate the effectiveness of annular jets in simulating full plume interference effects on afterbody pressure drag. Results were obtained at Mach numbers 0.6, 0.9, and 1.2 at a free-stream Reynolds number of 2.0×10^6 per foot. A single afterbody model (15-deg boattail) was utilized to evaluate the effects of changes in sting-to-nozzle exit diameter ratio from 0 to 0.95 and nozzle area ratio from 1.0 to 1.5. High pressure air at ambient temperature was used to simulate the nozzle exhaust.

The significant results and conclusions may be summarized as follows:

1. Matching of the exhaust plume maximum diameter was found to provide a reasonable afterbody drag correlation, accounting for effects of annular jet, nozzle exit-to-throat area ratio, and nozzle pressure ratio for conditions where drag follows the classical trend indicative of a plume shape dependence (i.e., decreasing drag with increasing pressure ratio).

2. For the conditions of this investigation, data from configurations having dummy sting-to-nozzle exit diameter ratios equal to 0.95 at all Mach numbers and equal to 0.866 at Mach number 1.2 followed a trend with nozzle pressure ratio indicative primarily of entrainment effects. Therefore, a plume diameter correlation was not successful for the pressure ratios of this investigation.

3. Data were correlated using both the method of characteristics and one-dimensional flow area relationships to calculate plume diameter. There were no advantages found in utilizing the method of characteristics over the simpler one-dimensional solution.

4. There were no adverse effects of angle of attack on the annular jet configurations over the angle range from -2 to 6 deg.

5. At Mach number 0.9 for a nozzle static pressure ratio of 2.0 the significant decrease in exhaust plume diameter with increasing dummy sting diameter as measured from schlieren photographs agreed closely with predictions made by the method of characteristics for plumes in quiescent air.

7.0 COMMENTS ON DESIGN REQUIREMENTS FOR ANNULAR JET TESTING

In designing the test hardware for a sting-supported model utilizing the annular jet concept there are several factors which must be considered. The ultimate choice of support hardware must result from trade-off studies being made in light of the relative importance of various parameters to the test objectives.

Selection of sting size is the most critical design decision. From the standpoint of plume simulation, the smallest sting possible should be selected. Sting stress limits and internal volume requirements for instrumentation leads and high pressure gas requirements, however, all run counter to use of a minimum diameter sting. In general, the first attempt at selecting a sting size should be guided by stress limits, based upon the desired run conditions. It is then appropriate to check whether the selected sting size falls within a range of sting-to-nozzle exit diameter ratios that would be expected to produce reasonable plume simulation. For sting sizes larger than desirable, the relative merits of reducing dynamic pressure or angle of attack, or perhaps reducing wing span if a lifting body is being tested should be evaluated against the error resulting from improper plume simulation. The following diagram illustrates some of the design factors and therefore where possible trade-offs are involved in designing a sting for annular jet tests.
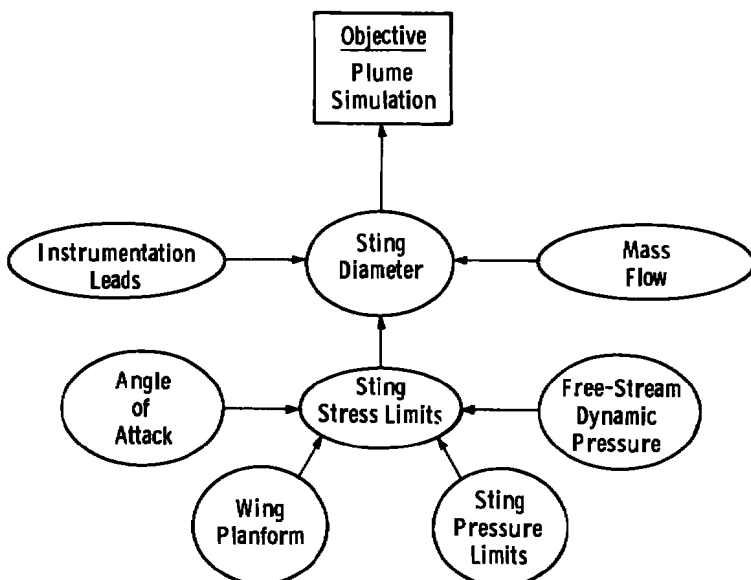
Recent sting designs for tests in the Propulsion Wind Tunnel Facility (PWT) on fighter-type aircraft models indicate the feasibility of testing high closure, cruise-type nozzles with sting-to-nozzle exit diameter ratios on the order of 0.86 at Reynolds numbers of approximately 2.2 x 10^6 per foot and at angles of attack up to approximately 8 deg. The results of this report indicate that adequate simulation should be obtained for such a design at subsonic Mach numbers. For larger nozzle exit diameters the same sting should permit adequate simulation at supersonic Mach numbers.

As mentioned previously, providing sufficient space for instrumentation leads can be a problem. For pressure-instrumented models, Scanivalves® mounted inside the model are recommended to minimize the volume required inside the sting.

On the basis of the correlation obtained in this report it appears that nozzle area ratio of the annular nozzle does not have to match the conventional nozzle which it is to simulate. By use of a smaller area ratio nozzle for the annular test, the chamber pressure requirements in the model may be lowered if model pressure limits are encountered.

There are two additional design parameters that have not been investigated for an annular jet application. These are nozzle divergence angle and location of the sting flair relative to the annular nozzle. In general, annular jet models tested to date have maintained the same divergence angle as the conventional nozzle which they were simulating. Tests are being planned for the PWT in the near future to investigate the influence of sting flair location on the annular plume simulation.

REFERENCES

1. Galigher, Lawrence L. "Integrated Airframe Nozzle Performance Characteristics of a Generalized Twin-Jet, Air Superiority Fighter Aircraft Model at Mach Numbers from 0.6 to 1.6." AEDC-TR-73-125 (AD912073L), July 1973.

2. Galigher, Lawrence L., Yaros, S. F., and Bauer, R. C. "Evaluation of Boattail Geometry and Exhaust Plume Temperature Effects on Nozzle Afterbody Drag at Transonic Mach Numbers." AEDC-TR-76-102 (AD030852), October 1976.

3. Reubush, David E. "Experimental Study of the Effectiveness of Cylindrical Plume Simulators for Predicting Jet-On Boattail Drag at Mach Numbers up to 1.30." NASA TND-7795, November 1974.

4. Bergman, Dave. "Effects of Engine Exhaust Flow on Boattail Drag." Journal of Aircraft, Vol. 8, No. 6, June 1971, pp. 434-439.

5. Watson, T. L. and Anderson, R. D. "Exhaust System Interaction Program: Analysis of Wind Tunnel Data on a 4.7 Percent Scale F-15 Jet Effects Model in the McDonnell Polysonic Wind Tunnel, PSWT 319." MDCA2135, McDonnell Douglas Corporation, St. Louis, Missouri, January 1973.

6. Price, Earl A., Jr. "Afterbody Aerodynamic Characteristics and Support System Interference on a Twin-Jet Fighter-Type Aircraft Model at Mach Numbers from 0.6 to 1.5." AEDC-TR-74-13 (AD918789L), April 1974.

7. Bowers, Douglas L. "Investigation of the Annular Sting Support Concept for Aftbody Nozzle Testing." AIAA Paper No. 77-961, July 1977.

8. Test Facilities Handbook (Tenth Edition). "Propulsion Wind Tunnel Facility, Vol. 4." Arnold Engineering Development Center, May 1974.

9. Peters, W. L. "An Evaluation of Jet Simulation Parameters for Nozzle Afterbody Testing at Transonic Mach Numbers." AEDC-TR-76-109 (ADA031525), October 1976.

10. Love, E. S. and Grigsby, C. E. "Some Studies of Axisymmetric Free Jets Exhausting from Sonic and Supersonic Nozzles into Still Air and into Supersonic Streams." NACA RM L54L31, May 1955.

11. Prozam, R. J. "Development of a Method of Characteristics Solution for Supersonic Flow of an Ideal, Frozen, or Equilibrium Reacting Gas Mixture." LMSC/HREC A782535-A, Lockheed Missiles and Space Company, Huntsville, Alabama, April 1966.
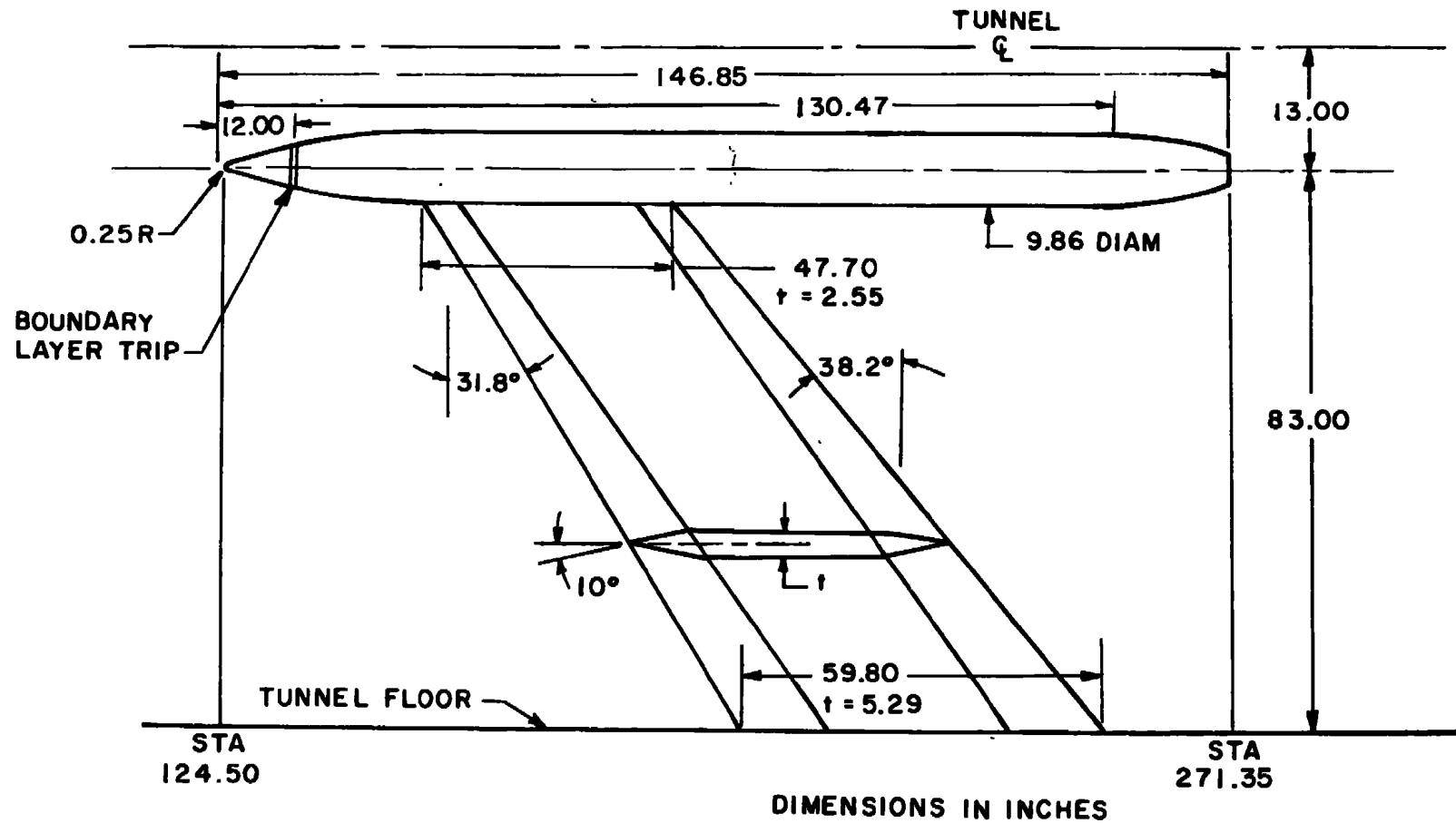
Figure 1. Basic model dimensions and location in test section.

AEDC
7372-76
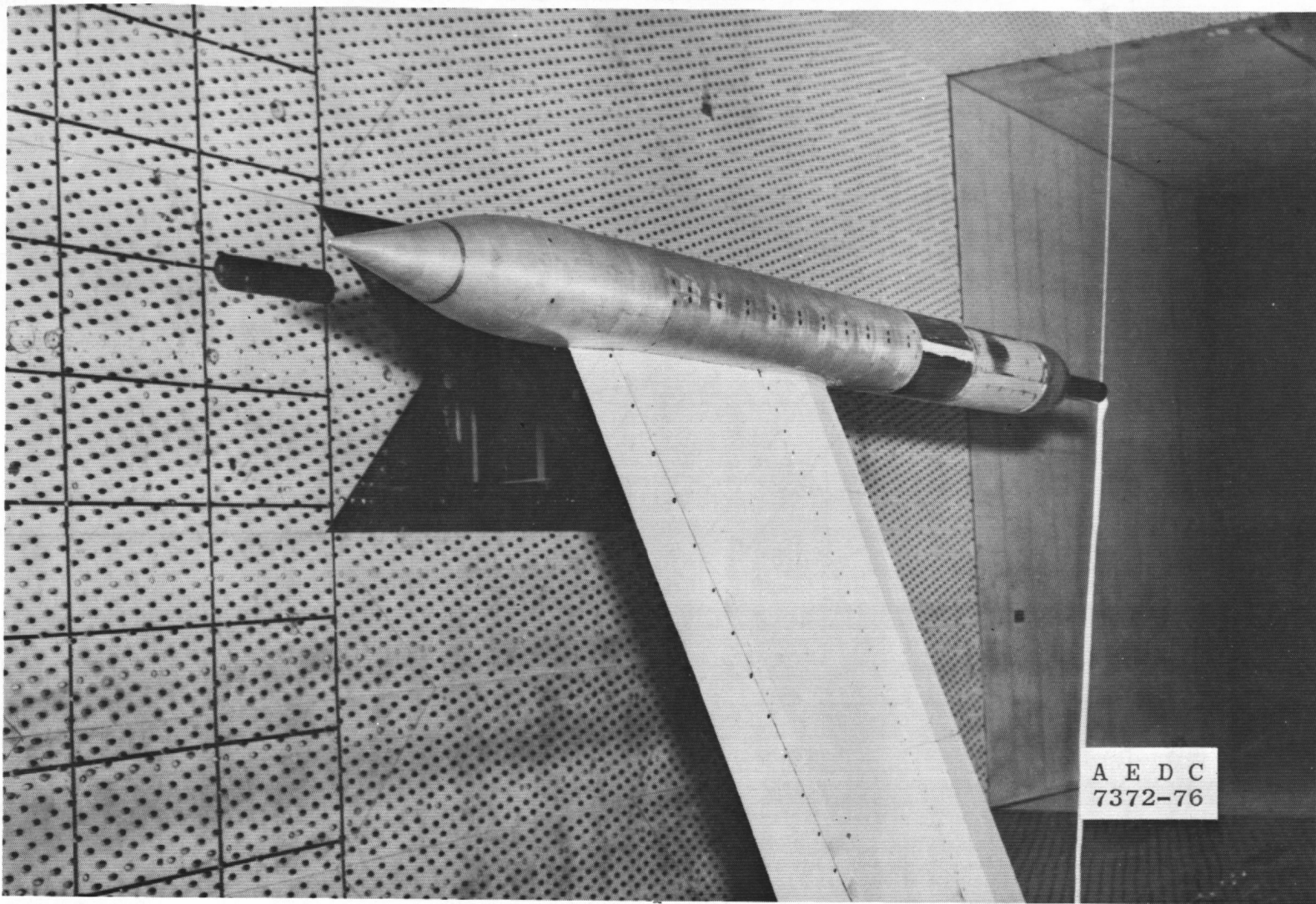
Figure 2. Model installation photograph.
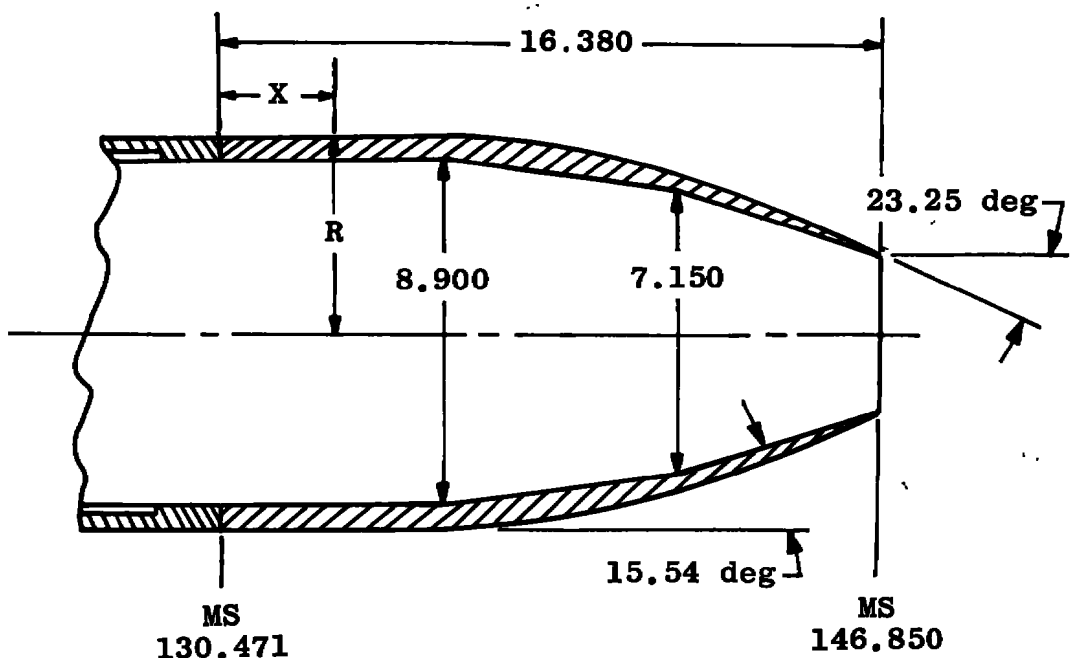
Stations and Dimensions in Inches

X	R	X	R
0	4.930	11.322	3.977
6.146	4.930	11.569	3.903
6.392	4.920	11.815	3.826
6.639	4.908	12.062	3.747
6.895	4.884	12.308	3.666
7.132	4.859	12.555	3.579
7.378	4.829	12.801	3.495
7.625	4.795	13.048	3.410
7.871	4.760	13.294	3.321
8.118	4.721	13.541	3.229
8.364	4.677	13.787	3.135
8.611	4.629	14.034	3.043
8.857	4.580	14.280	2.946
9.103	4.531	14.527	2.848
9.350	4.479	14.773	2.749
9.597	4.427	15.020	2.641
9.843	4.373	15.266	2.532
10.090	4.313	15.513	2.423
10.336	4.252	15.759	2.315
10.583	4.189	16.006	2.214
10.830	4.120	16.252	2.125
11.076	4.050	16.499	2.046

Figure 3. Sketch of afterbody contour with surface coordinates.
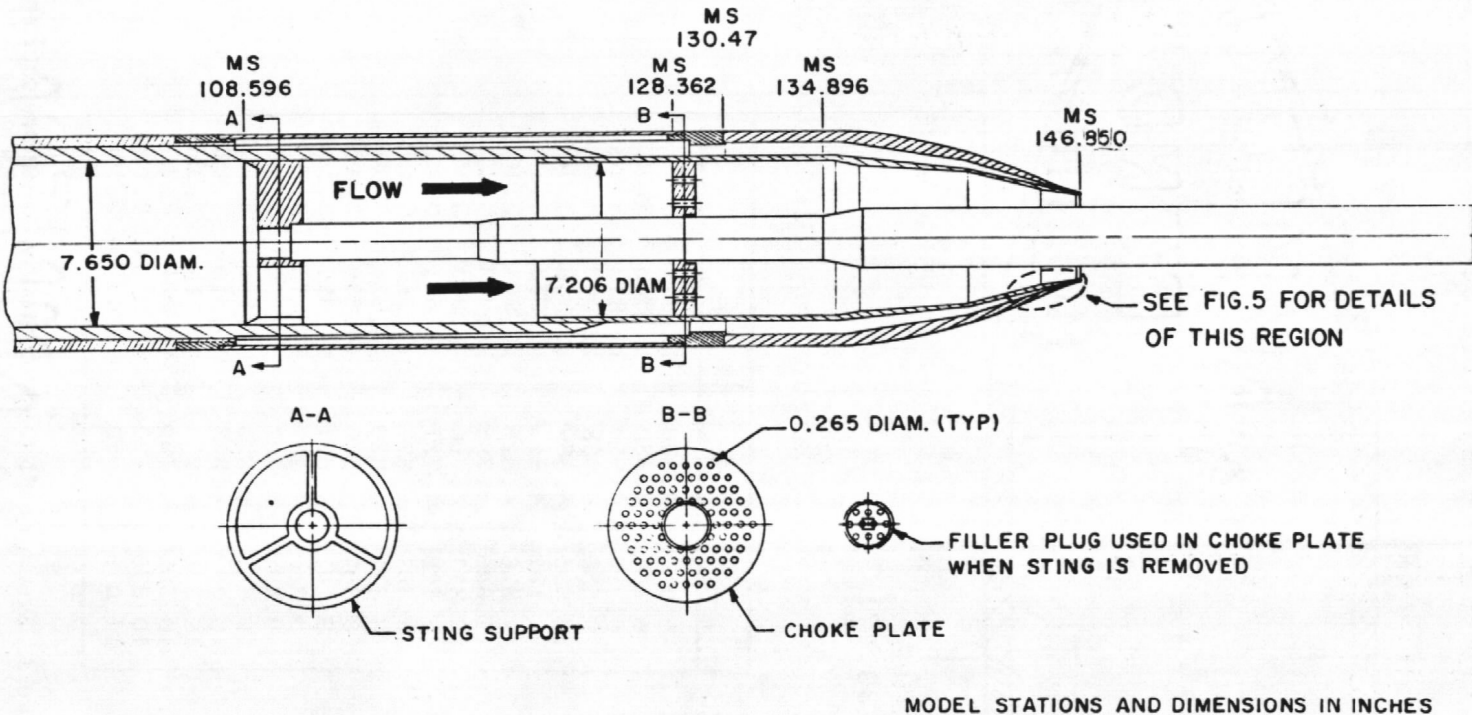
Figure 4. General arrangement of internal model components.

Figure 5. Internal nozzle sketches.
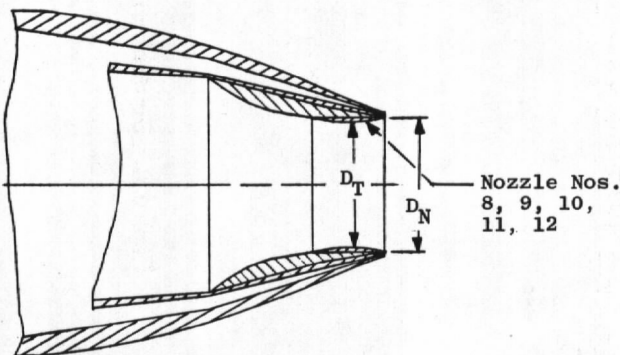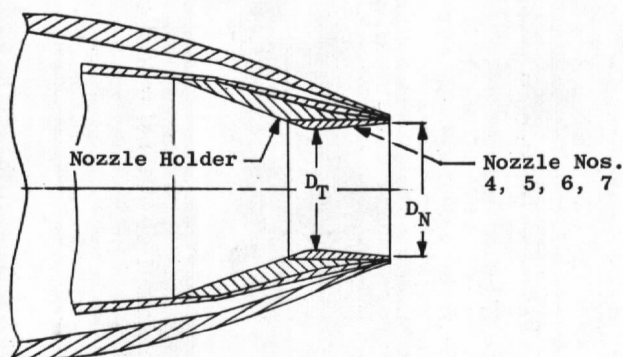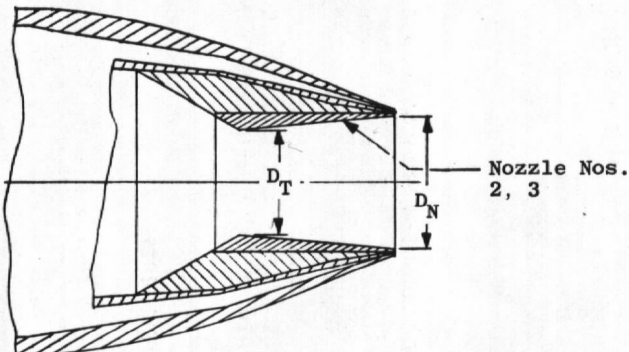
As built

Nozzle No.	D_T	D_N	
2	3.132	3.823	1.487
3	3.354	3.824	1.3
4	3.459	3.822	1.22
5	3.492	3.821	
6	3.587	3.820	1.135
7	3.648	3.825	
8	3.658	3.821	
9	3.706	3.820	
10	3.762	3.822	
11	3.799	3.820	
12	3.822	3.822	1.00

31
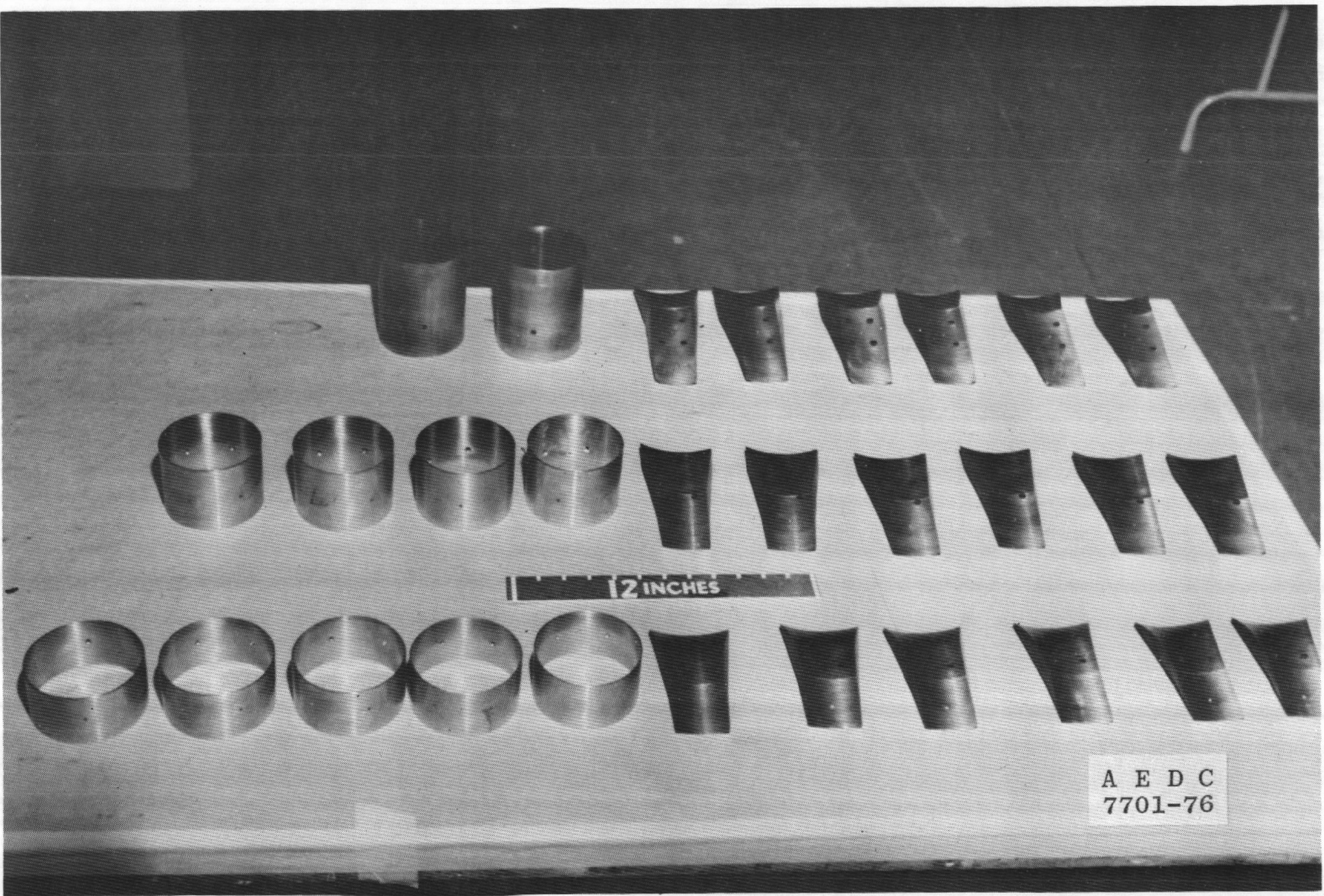
Figure 6. Photograph of nozzles and nozzle holder components.

55.33

L

25.75

19.72

10.00

10°

10°

1.90

2.00

2.07

BASE OF MODEL
IS AT TAP NO.9

TAP NO. 24

DIAM.
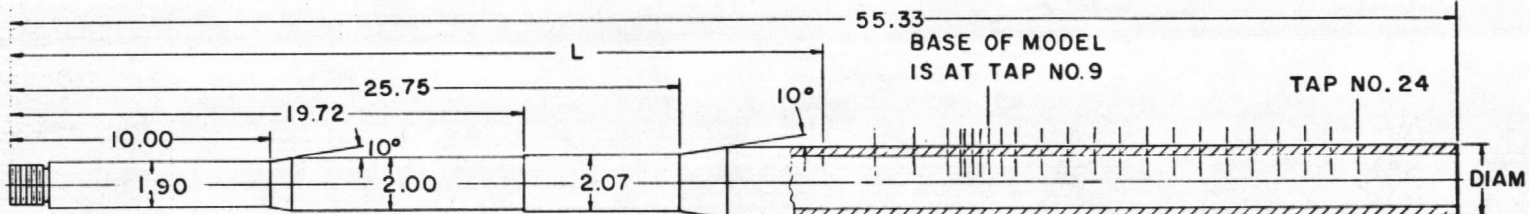
PRESSURE TAP LOCATION
ON STINGS A AND C

PRESSURE TAP NO.	L	PRESSURE TAP NO.	L
1	31.285	13	40.616
2	33.285	14	41.616
3	34.736	15	42.616
4	36.056	16	43.616
5	36.556	17	44.616
6	36.690	18	45.616
7	36.964	19	46.616
8	37.279	20	47.616
9	37.616	21	48.616
10	38.116	22	49.616
11	38.616	23	50.616
12	39.616	24	51.616

STING	DIAM
A	2.074
B	2.701
C	3.308
D	3.629

DIMENSIONS IN INCHES

Figure 7. Dimensioned sketch of dummy stings.
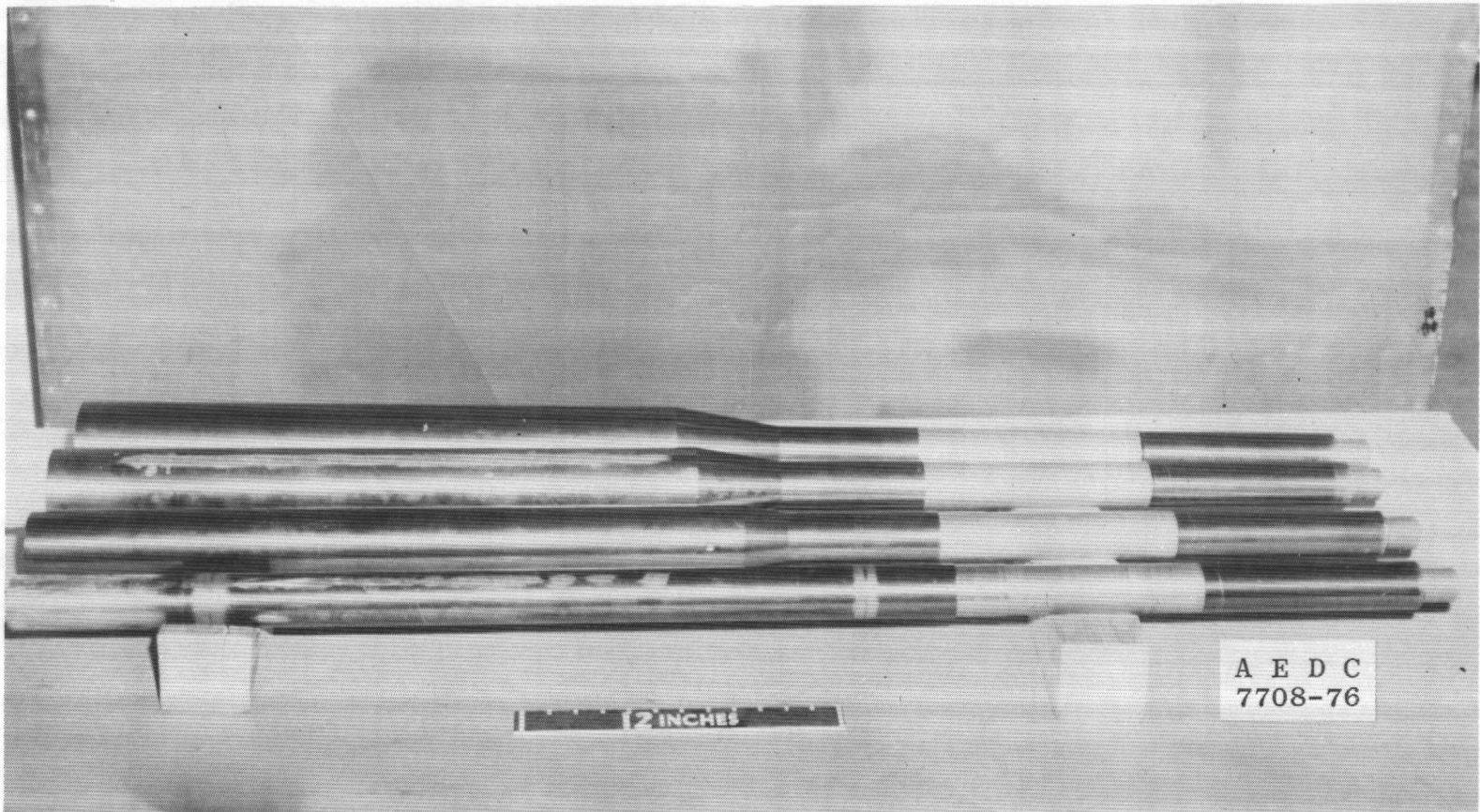
Figure 8. Sting photograph.
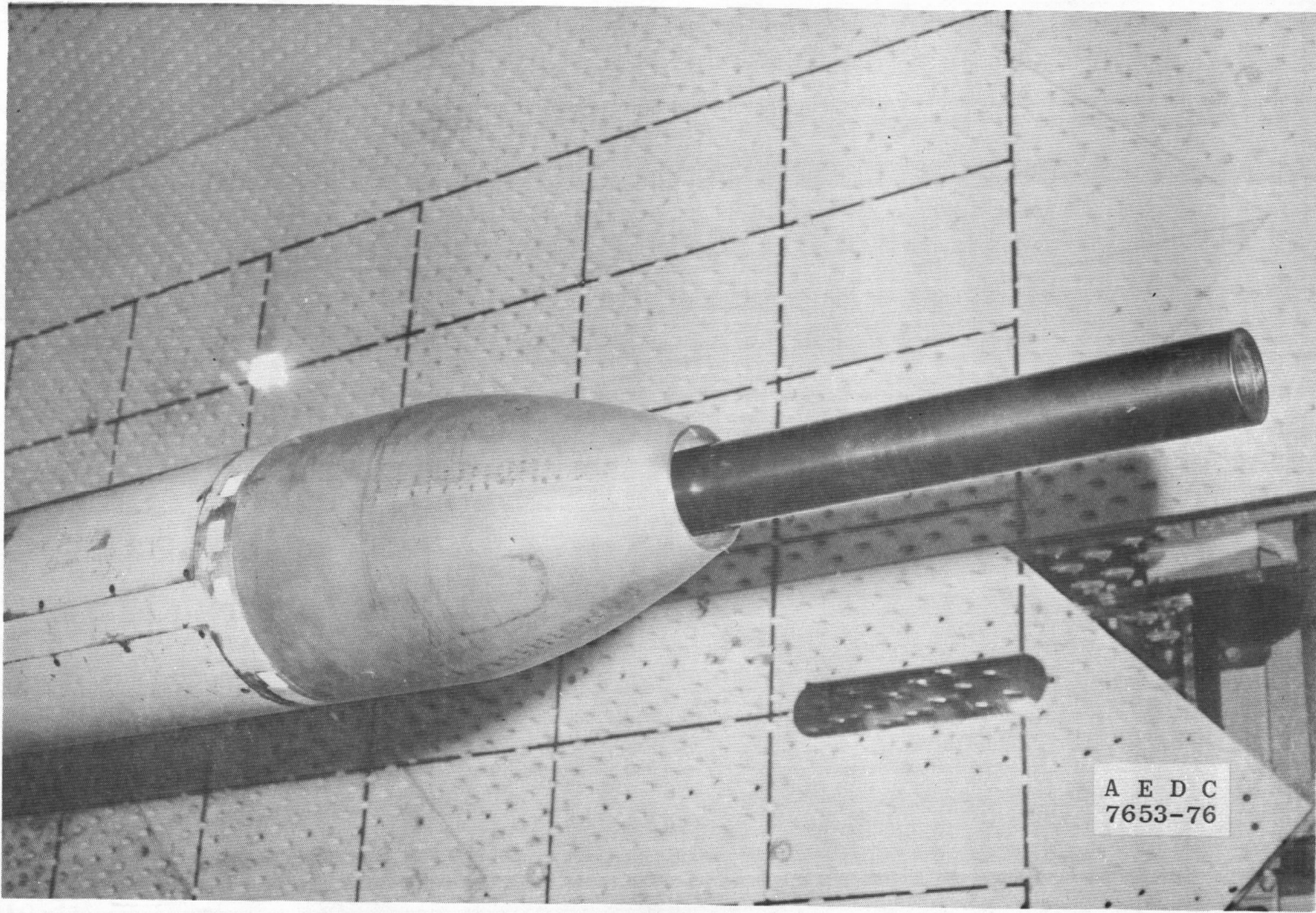
Figure 9. Sting installation photograph.
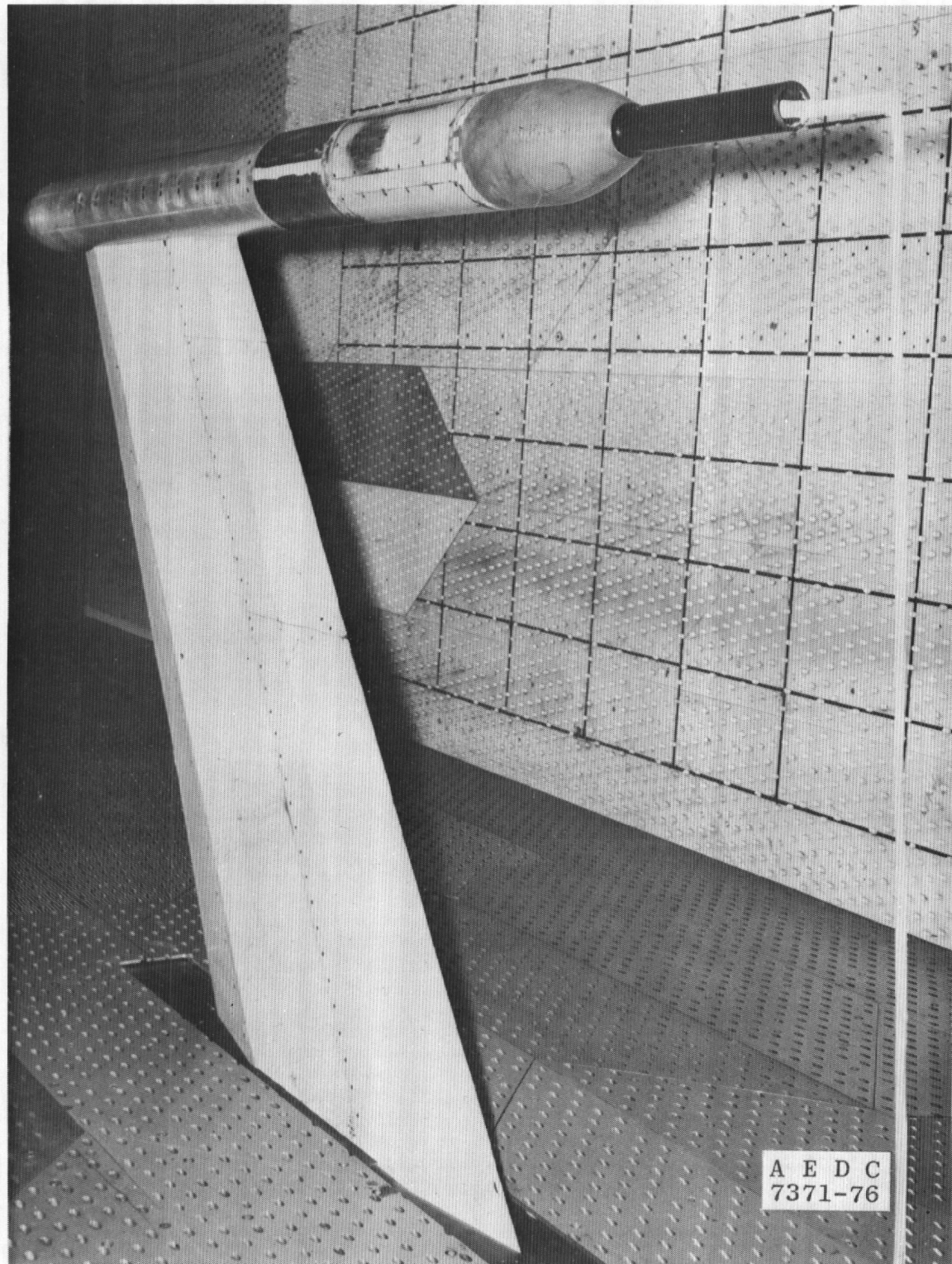
Figure 10. Photograph with instrumentation support
cable installed.
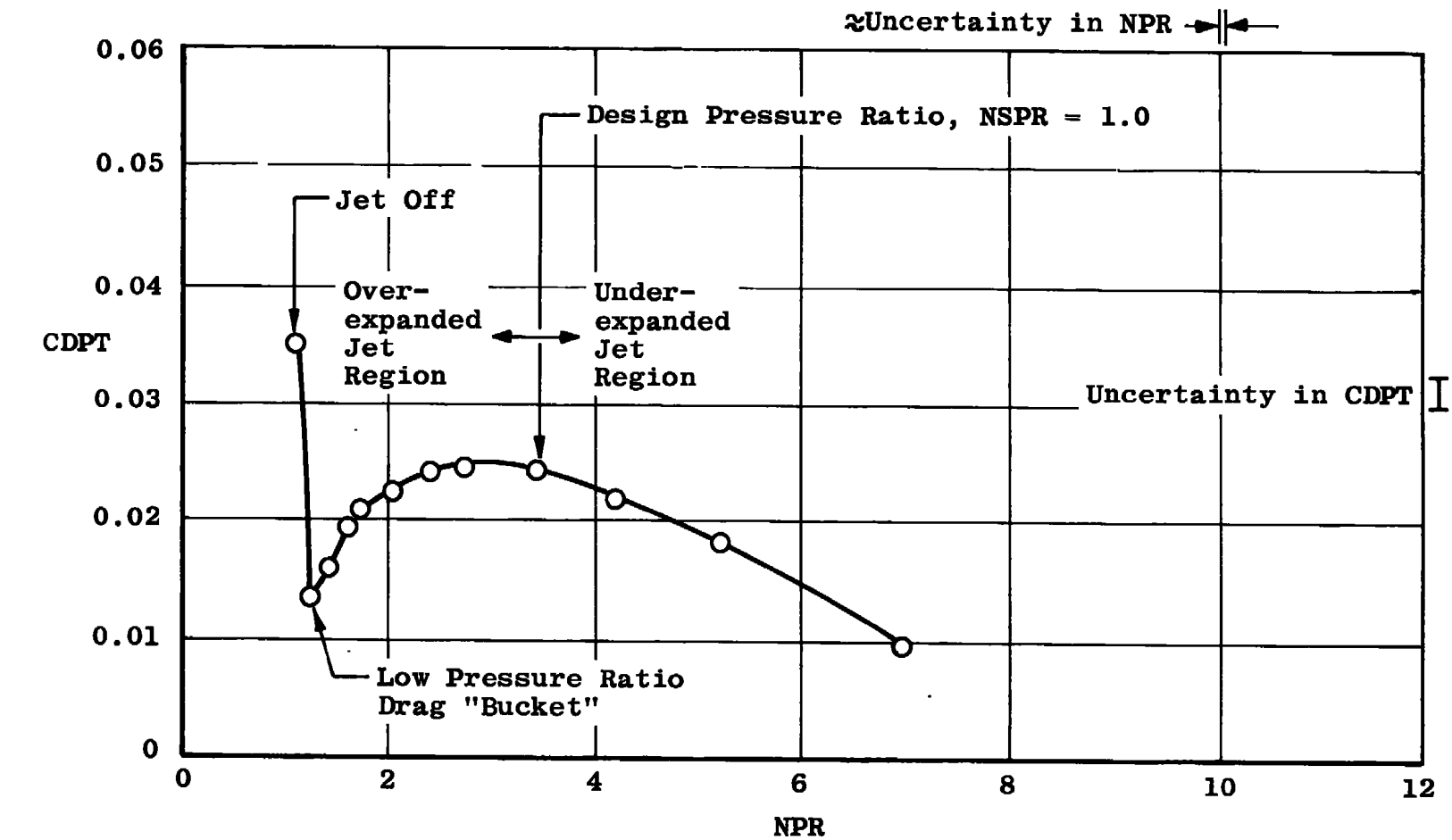
Figure 11. Typical variation of afterbody pressure drag with NPR.

SYM	A/A*	D_S/D_N	
⊙	1.000	0.0	46
◇	1.000	0.866	41
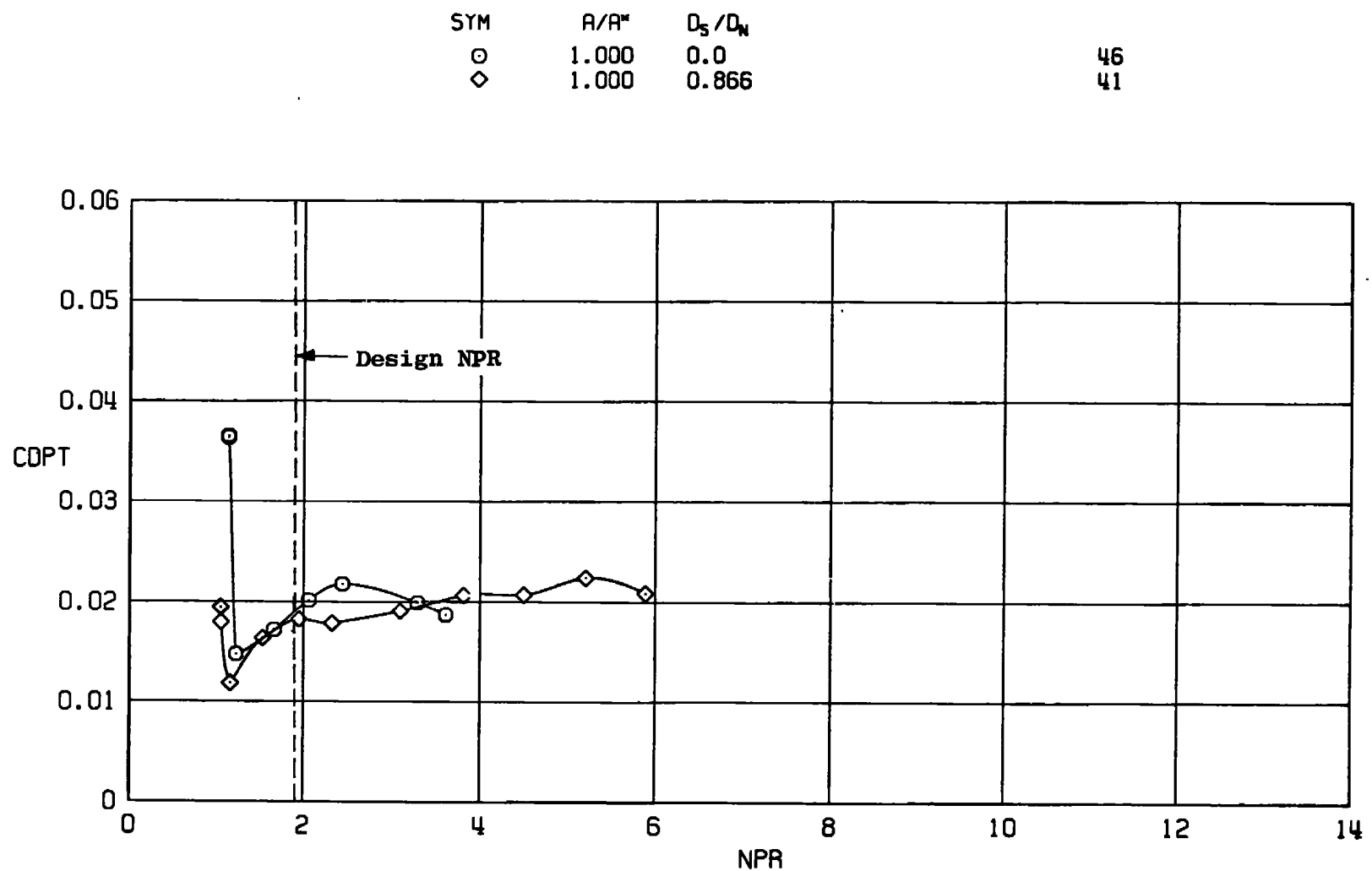
a. $M_\infty = 0.6$

Figure 12. Sting size effects on afterbody drag,
A/A* = 1.0.

SYM	A/A^*	D_S/D_N	
⊙	1.000	0.0	47
◇	1.000	0.866	42
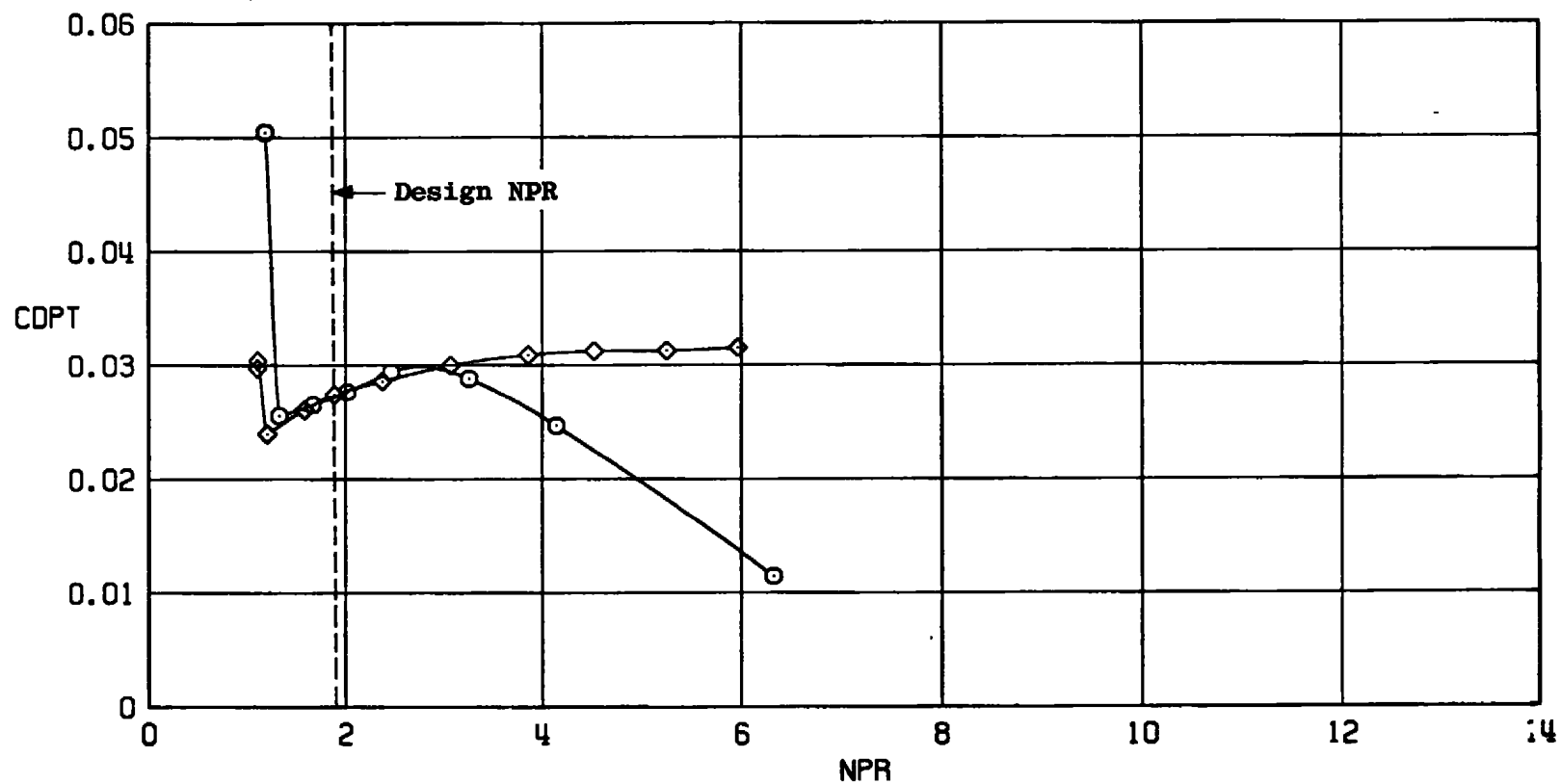
b. $M_\infty = 0.9$

Figure 12. Concluded.

SYM	A/A*	D_S/D_N	
O	1.134	0.0	84
□	1.134	0.543	9
◇	1.142	0.866	35
X	1.127	0.950	52
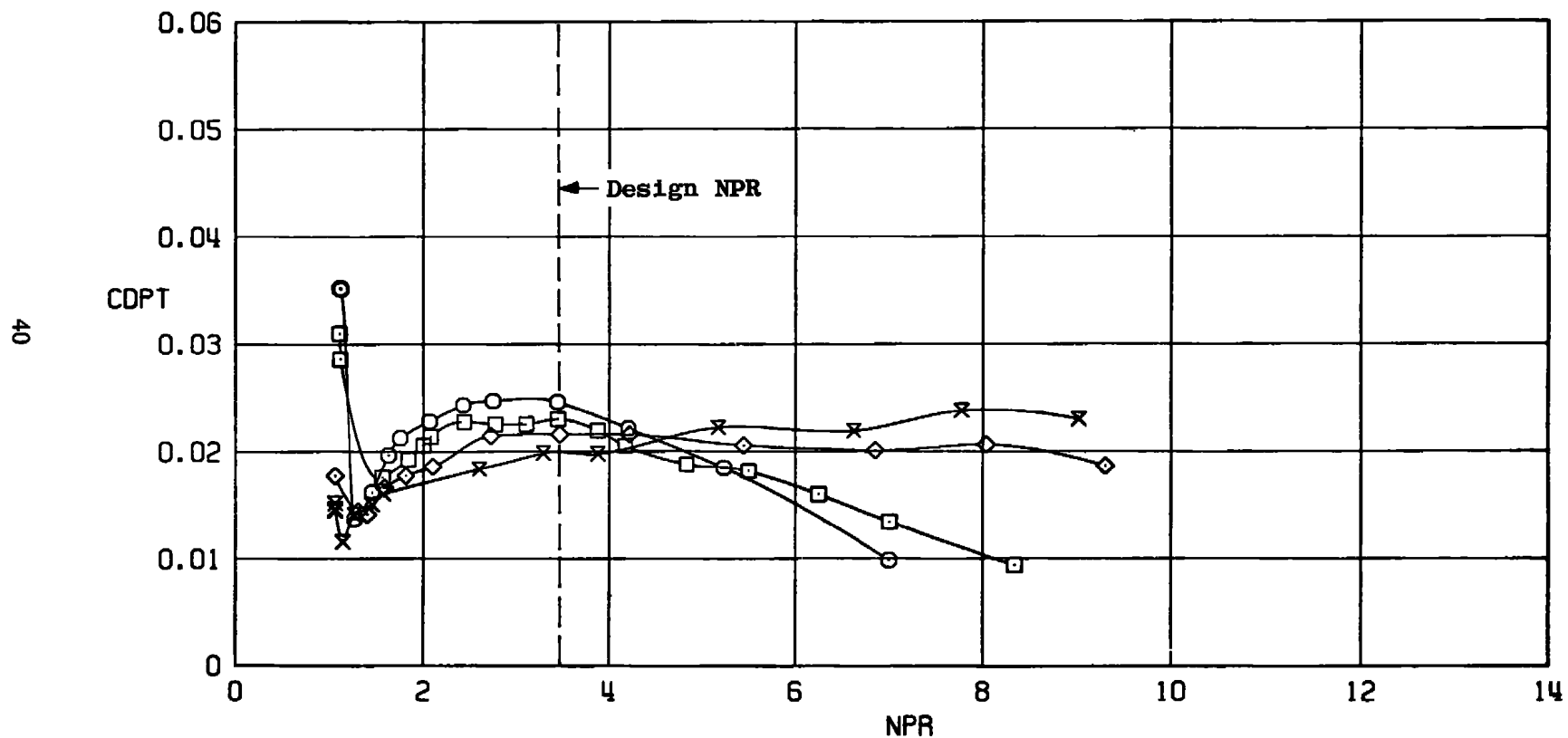
a. $M_\infty = 0.6$

Figure 13. Sting size effects on afterbody drag,
$A/A^* \approx 1.13$.

SYM	A/A^*	D_S/D_N	
○	1.134	0.0	86
▢	1.134	0.543	10
△	1.133	0.707	14
◇	1.142	0.866	36
✕	1.127	0.950	54
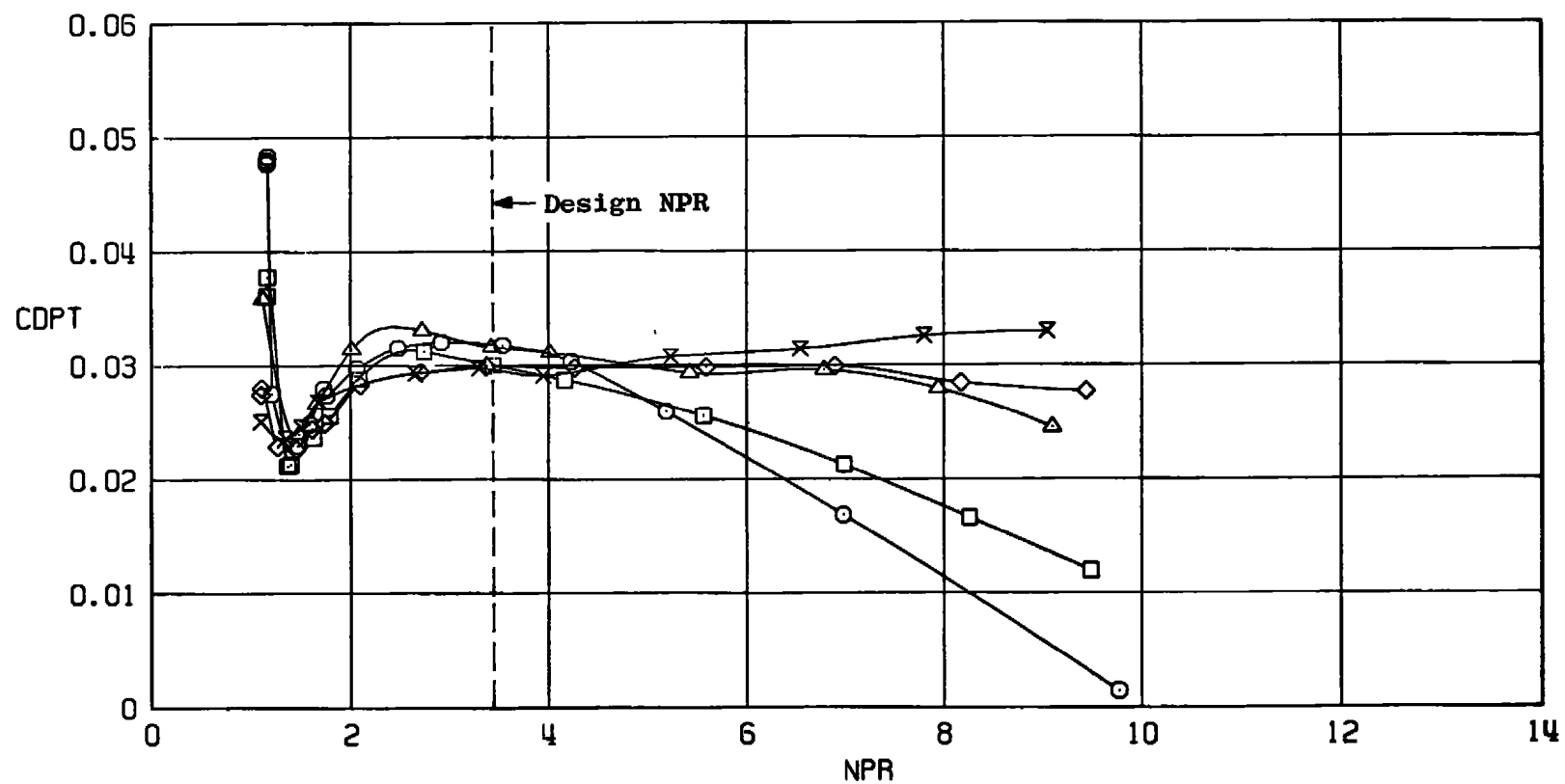
b. $M_\infty = 0.9$
Figure 13. Continued.

SYM	A/A*	D_S/D_N	
○	1.134	0.0	88
□	1.134	0.543	11
△	1.133	0.707	17
◇	1.142	0.866	38
X	1.127	0.950	56
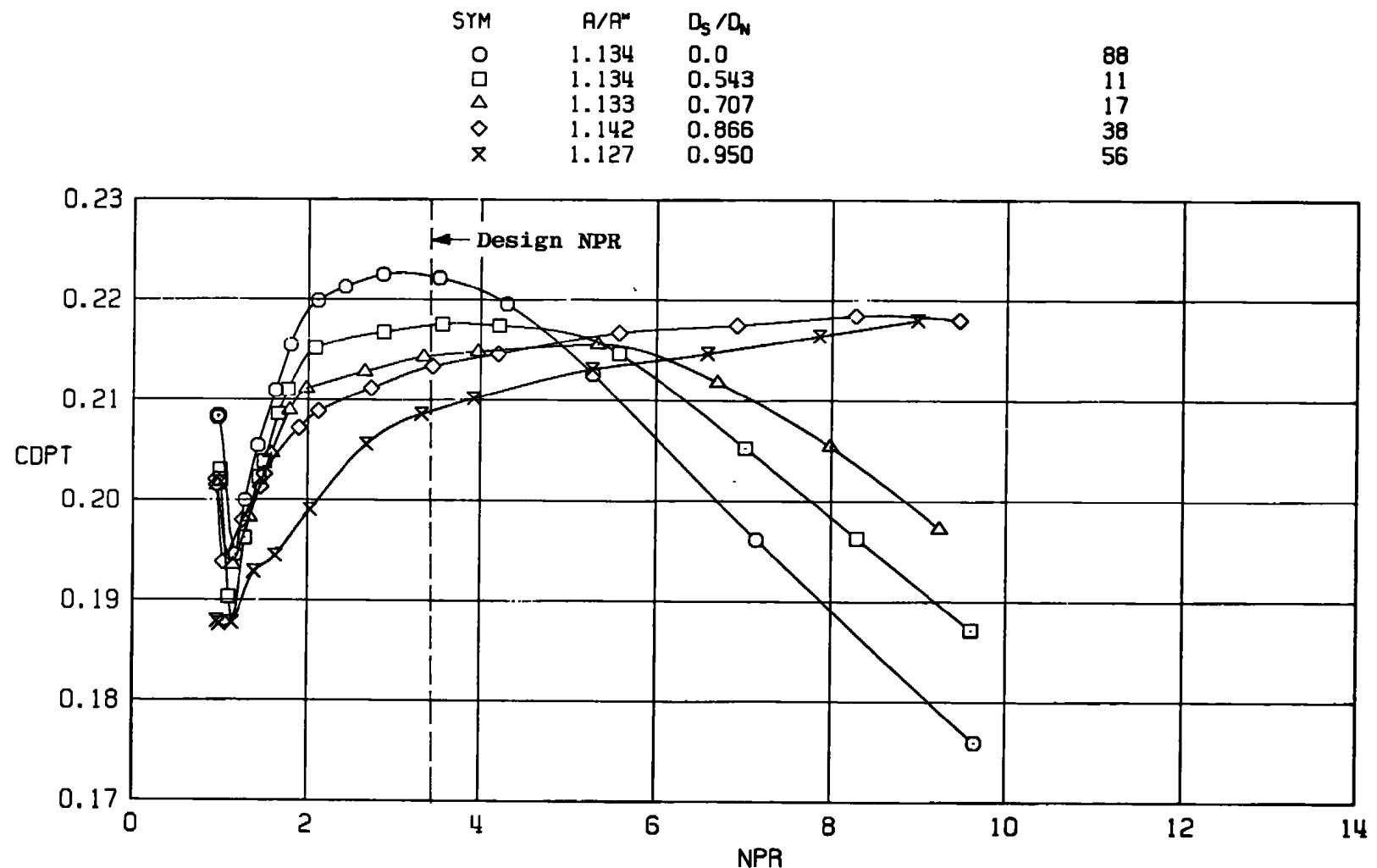
c. M_∞ = 1.2
Figure 13. Concluded.

SYM	A/A*	D_S/D_N	
○	1.221	0.0	92
△	1.220	0.706	69
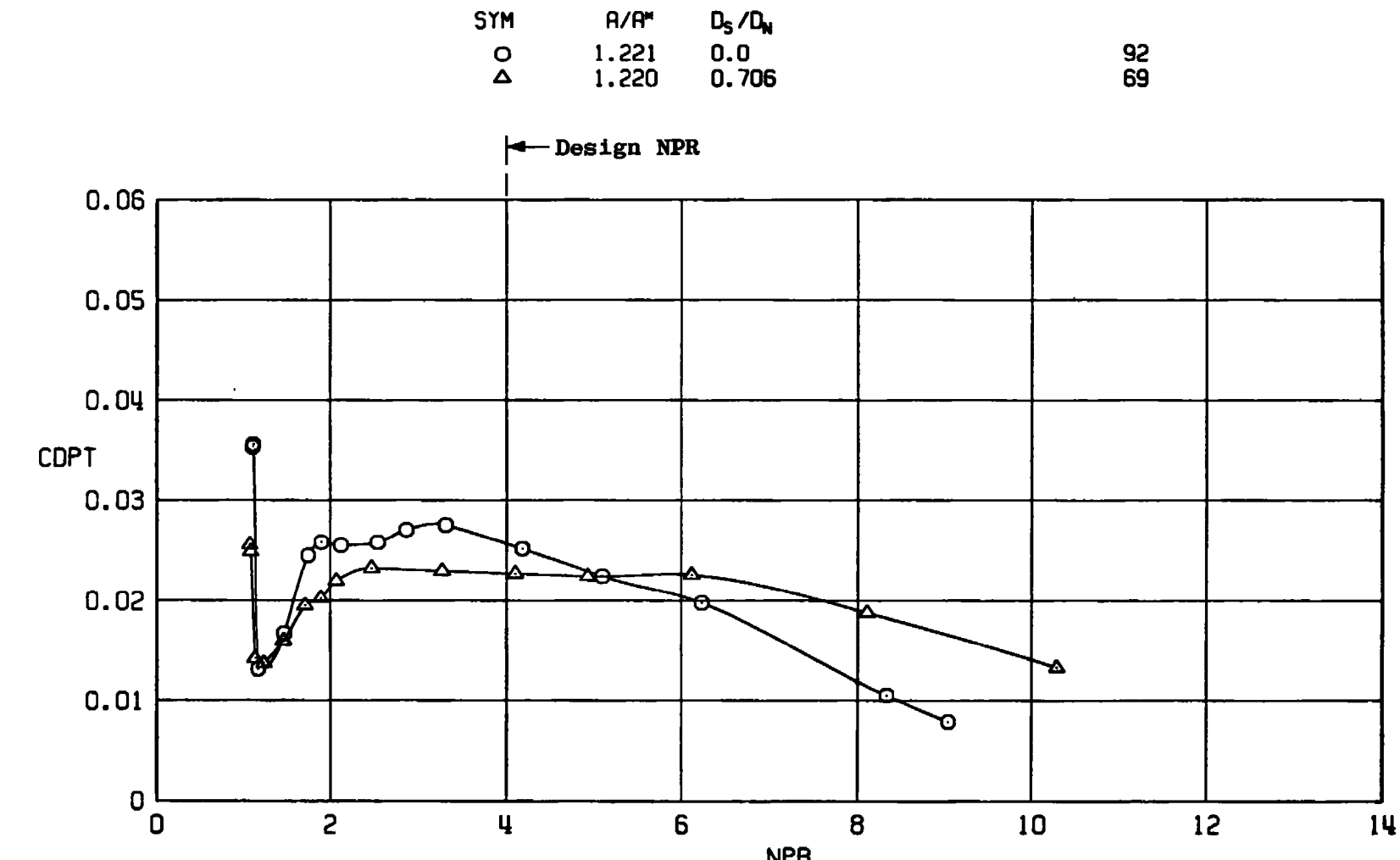
a. $M_\infty = 0.6$

Figure 14. Sting size effects on afterbody drag,
A/A* ≈ 1.22.

SYM	A/A*	D_S/D_N	
○	1.221	0.0	93
△	1.220	0.706	70
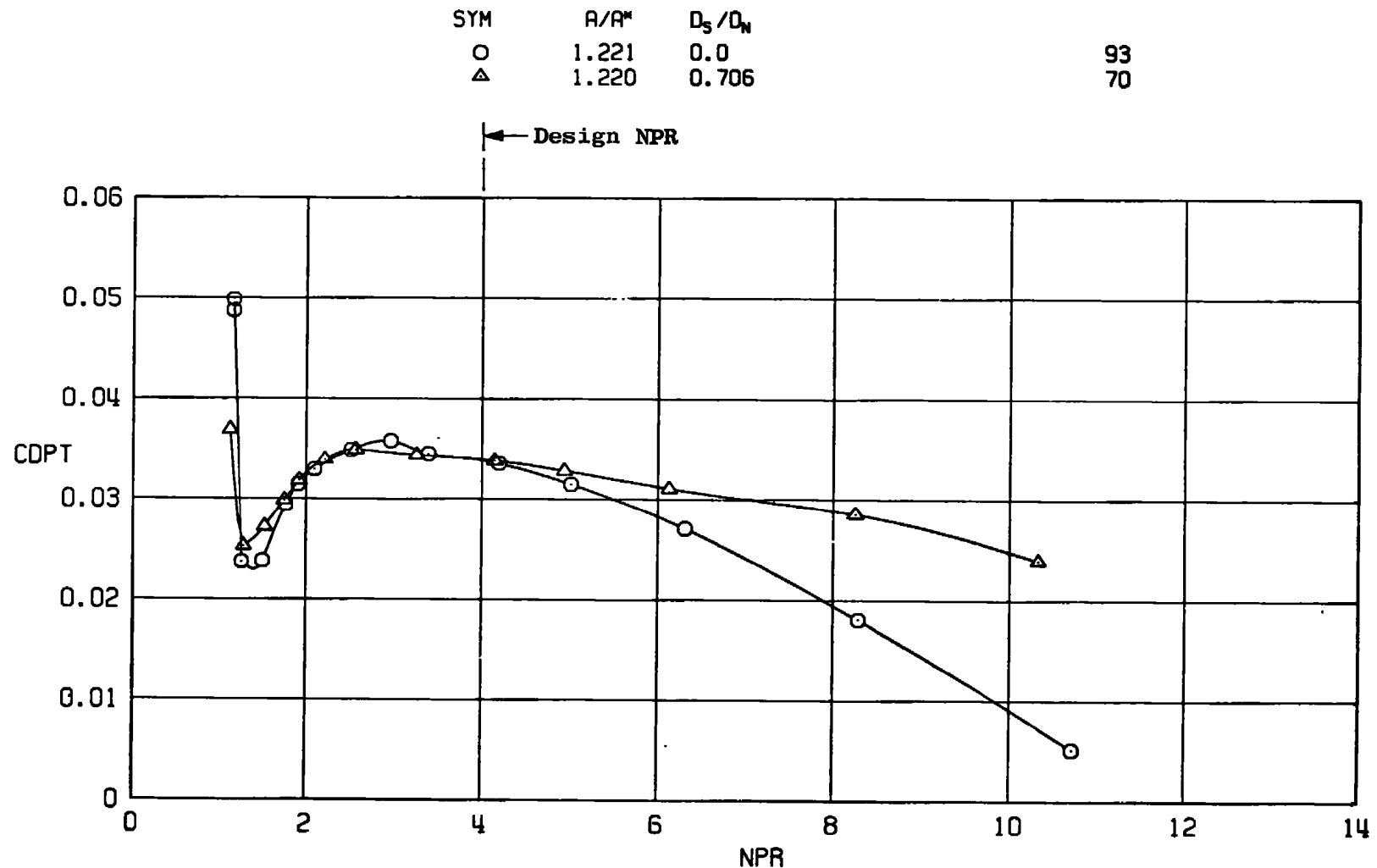
b. $M_\infty = 0.9$
Figure 14. Continued.

SYM	A/A*	D_S/D_N	
○	1.221	0.0	94
△	1.220	0.706	71
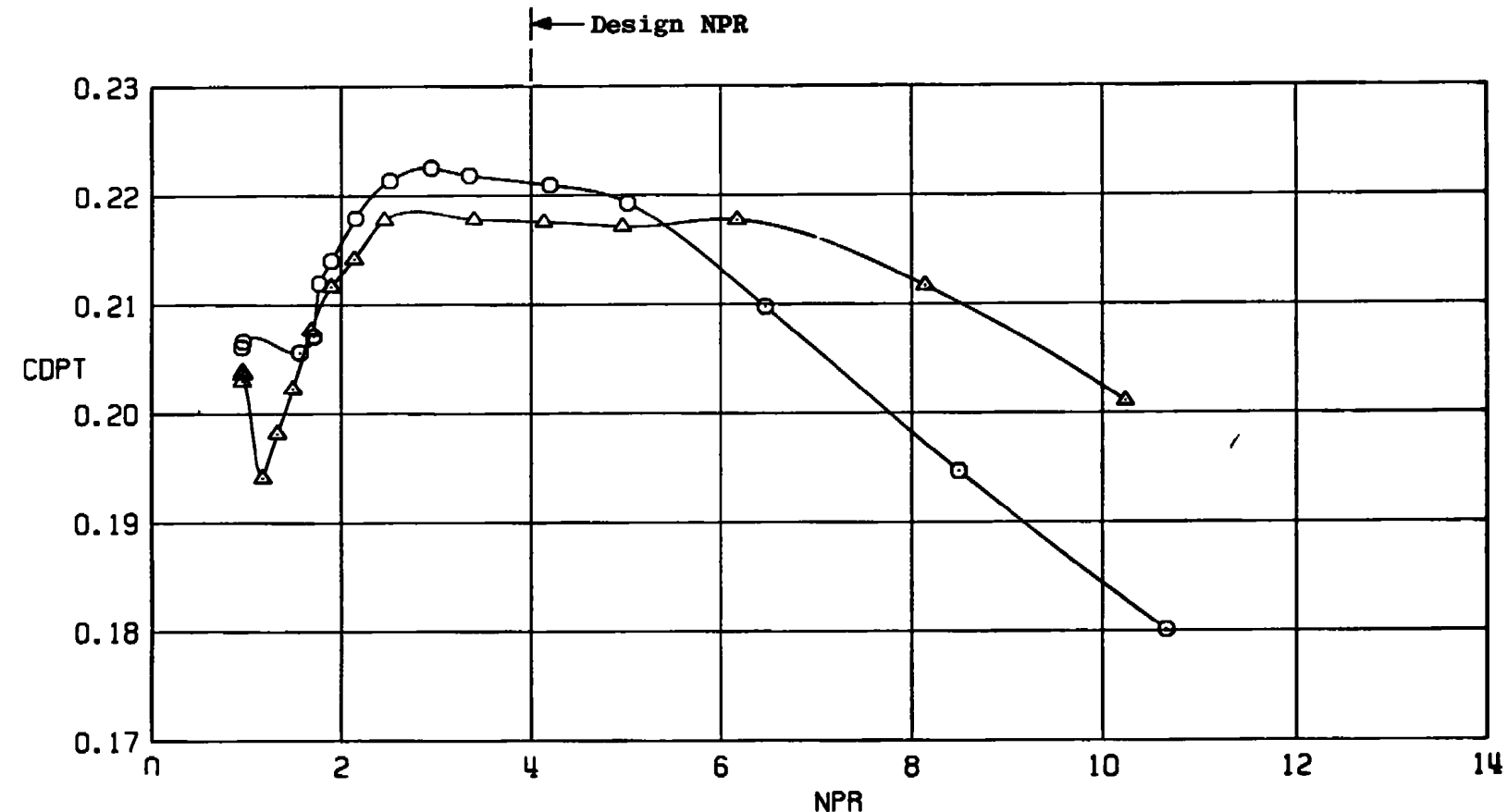
c. $M_\infty = 1.2$
Figure 14. Concluded.

SYM	A/A*	D_S/D_N	
O	1.300	0.0	109
△	1.310	0.707	97
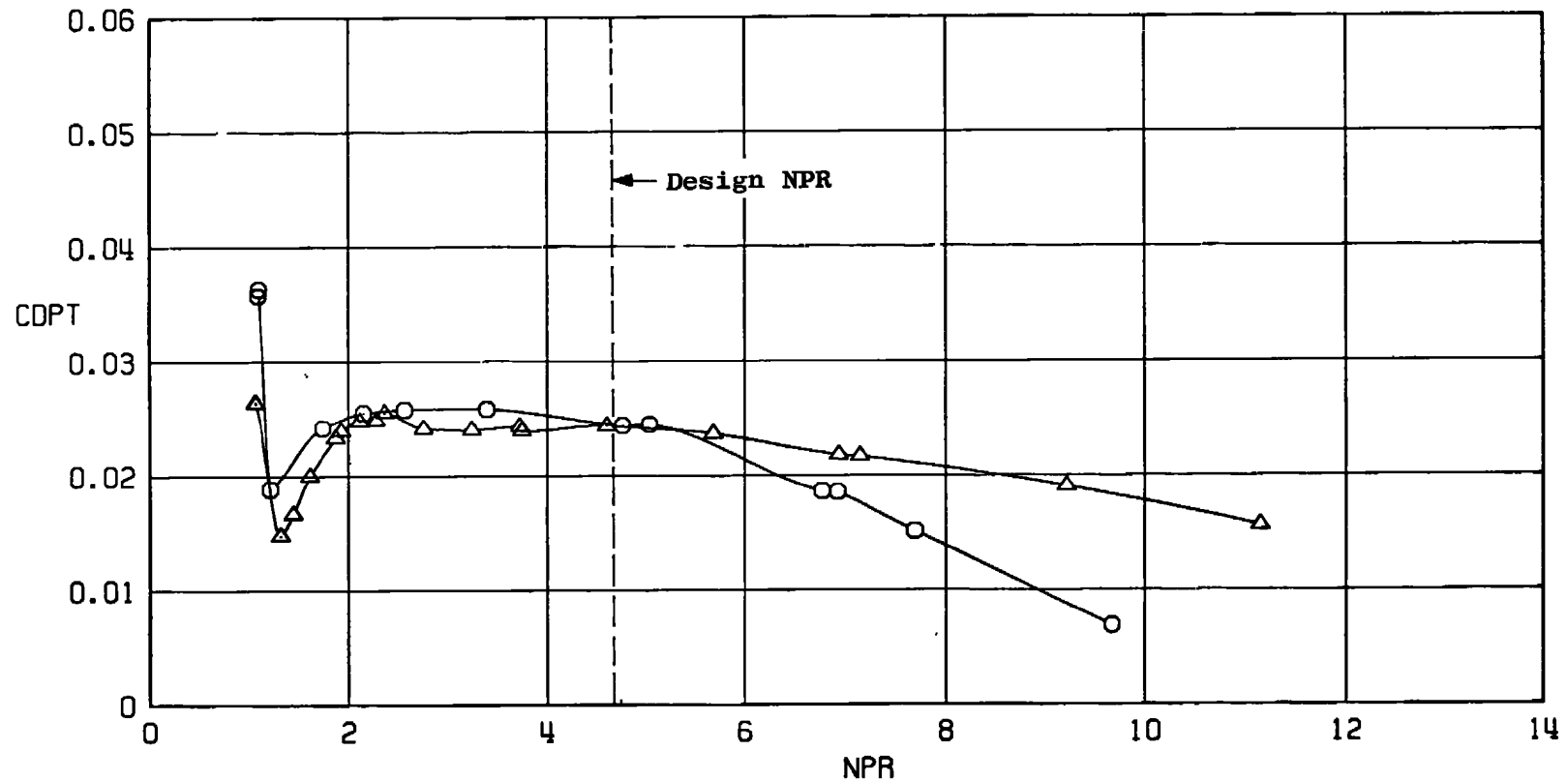
a. $M_\infty = 0.6$
Figure 15. Sting size effects on afterbody drag,
$A/A^* \approx 1.31$.
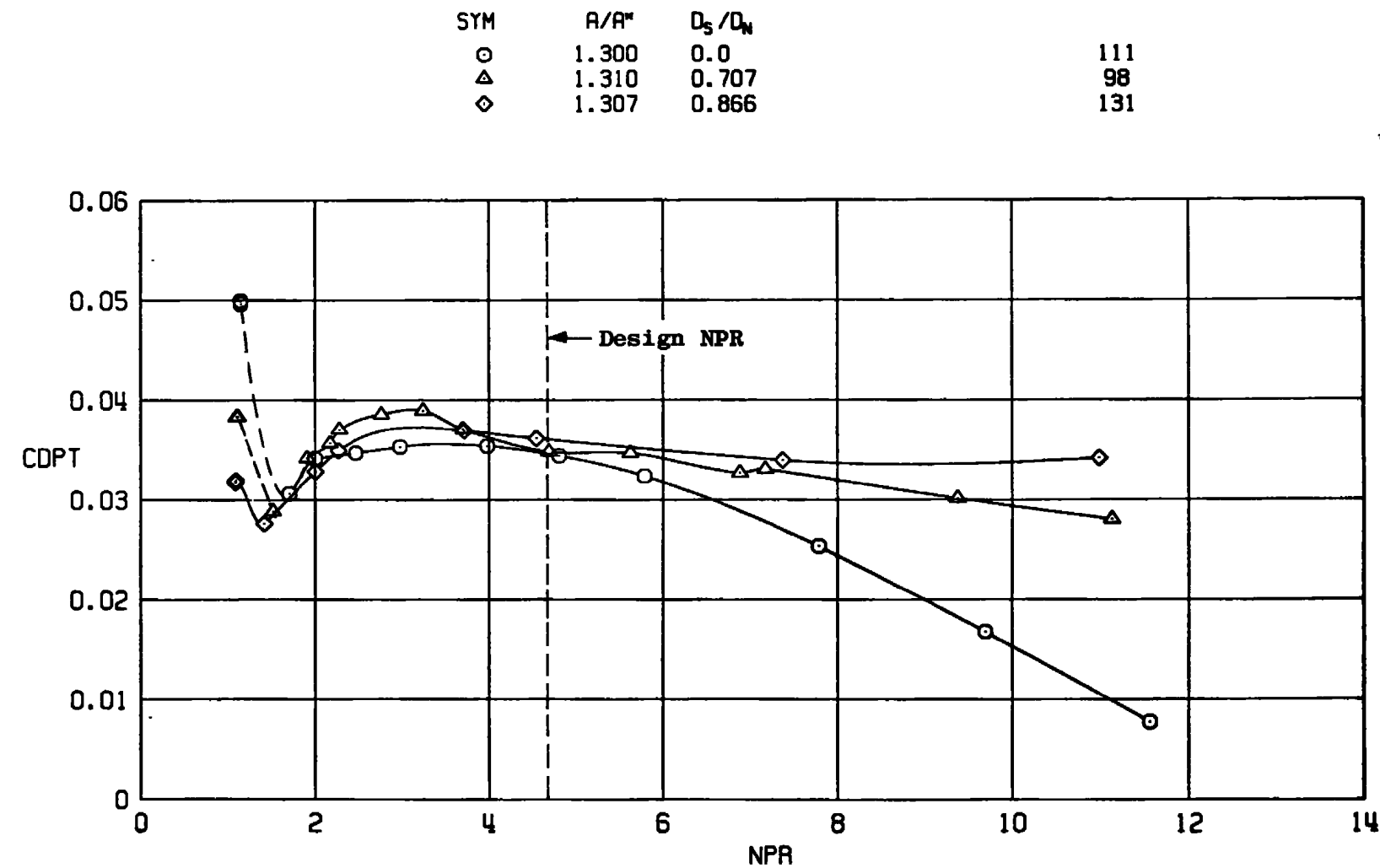
b. $M_\infty = 0.9$
Figure 15. Continued.

SYM	A/A*	D_S/D_N	
○	1.300	0.0	113
△	1.310	0.707	99
◇	1.307	0.866	132

CDPT

Design NPR

NPR
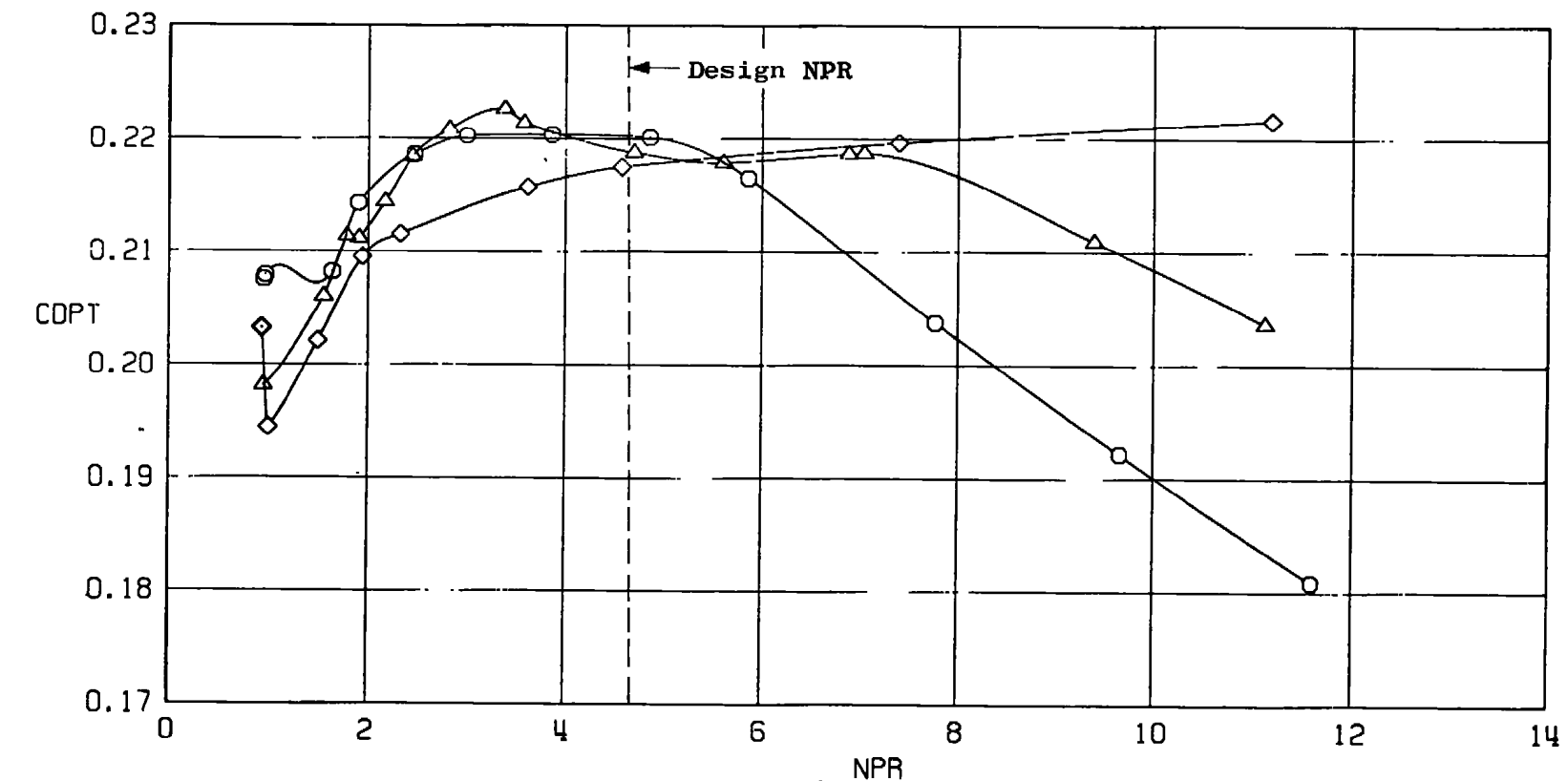
c. $M_\infty = 1.2$

Figure 15. Concluded.

SYM	A/A*	D_S/D_N	
O	1.490	0.0	118
□	1.486	0.542	104
△	1.491	0.707	74
◇	1.500	0.866	128
X	1.463	0.949	60
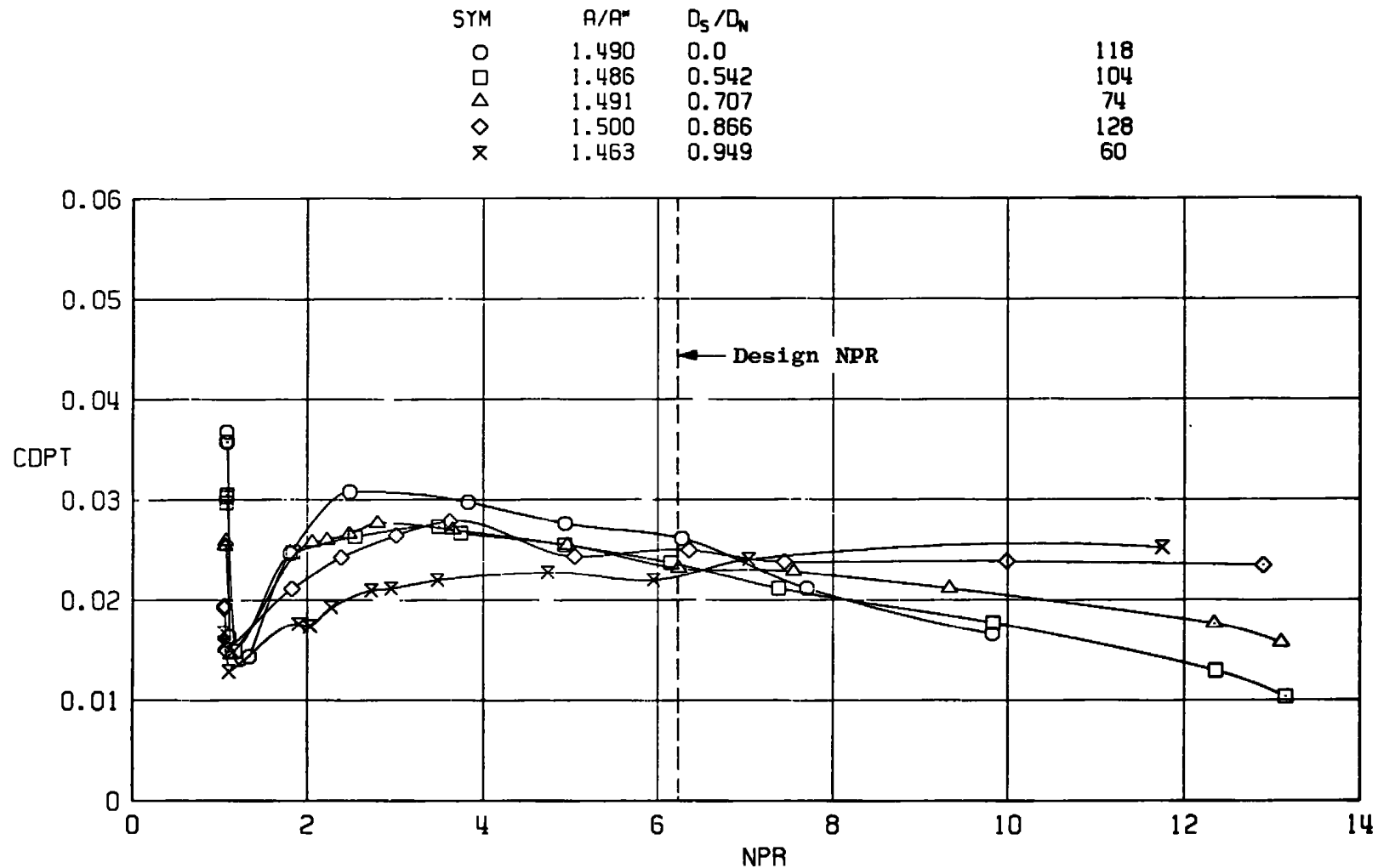
a. $M_\infty = 0.6$

Figure 16.   Sting size effects on afterbody drag,
A/A* ≈ 1.49.

SYM	A/A*	D_S/D_N	
○	1.490	0.0	120
□	1.486	0.542	105
△	1.491	0.707	76
◇	1.500	0.866	126
✕	1.463	0.949	62
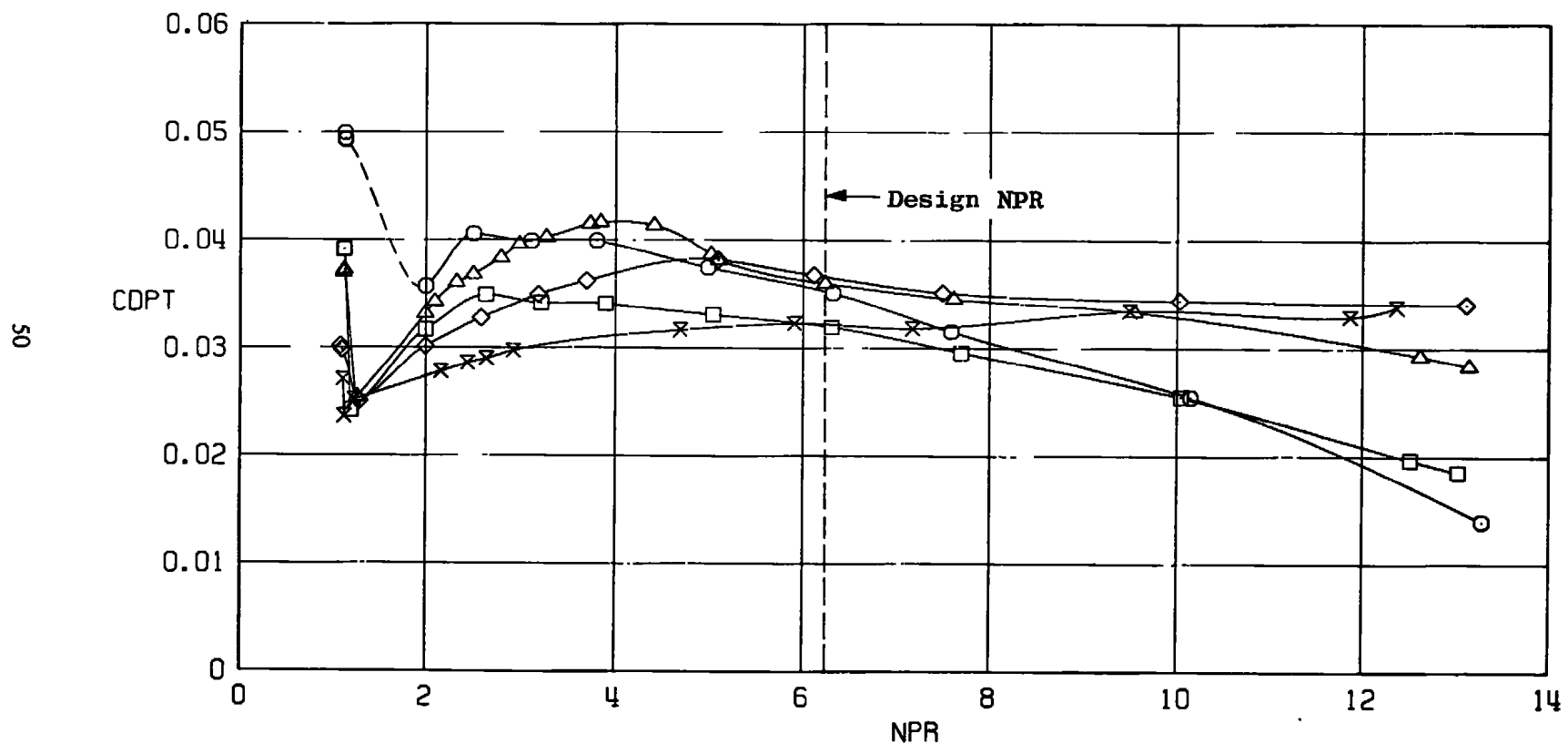
b. $M_\infty = 0.9$

Figure 16. Continued.

SYM	A/A^*	D_S/D_N	
⊙	1.490	0.0	122
□	1.486	0.542	106
△	1.491	0.707	78
◇	1.500	0.866	127
✕	1.463	0.949	64
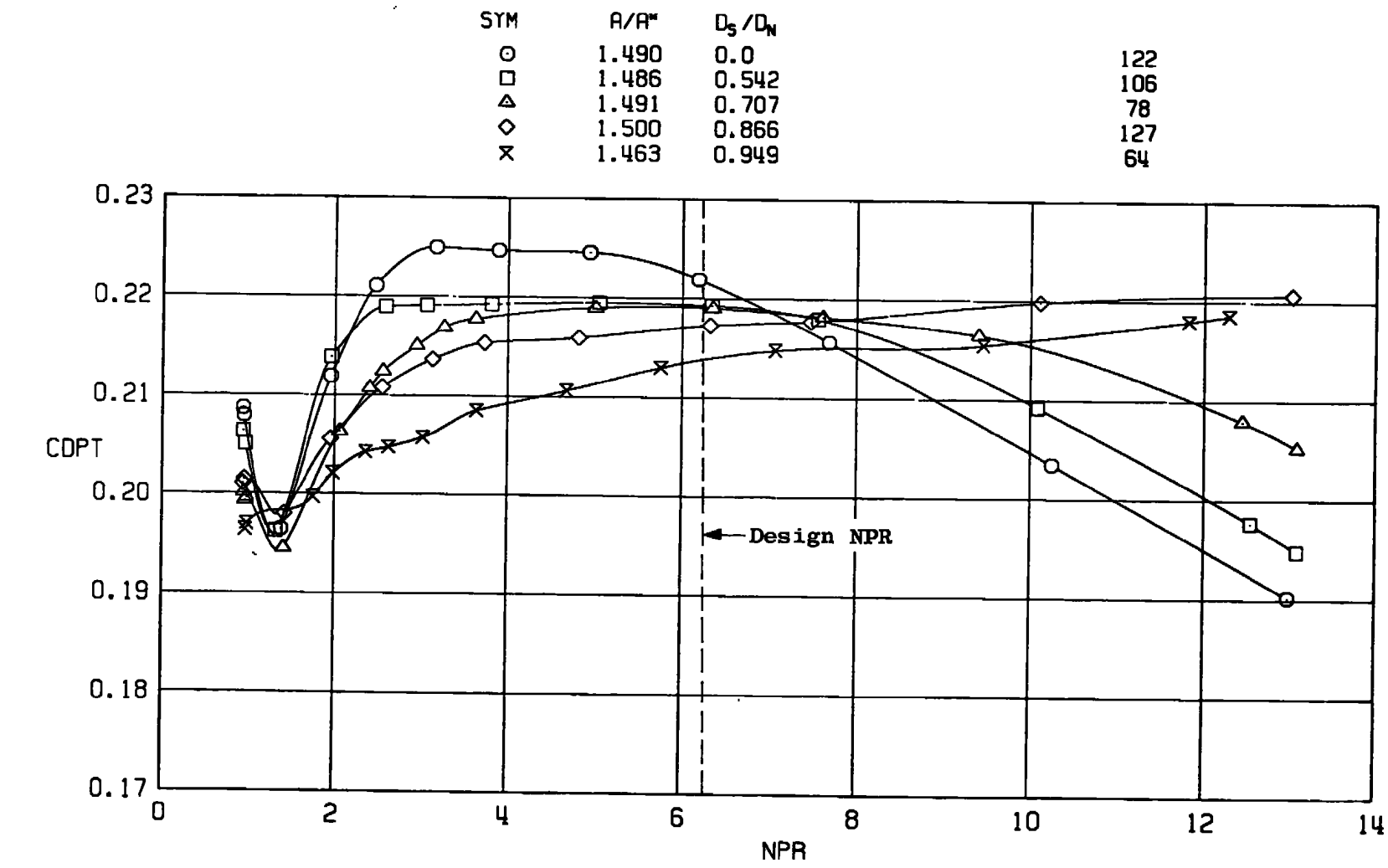
c. $M_\infty = 1.2$

Figure 16. Concluded.
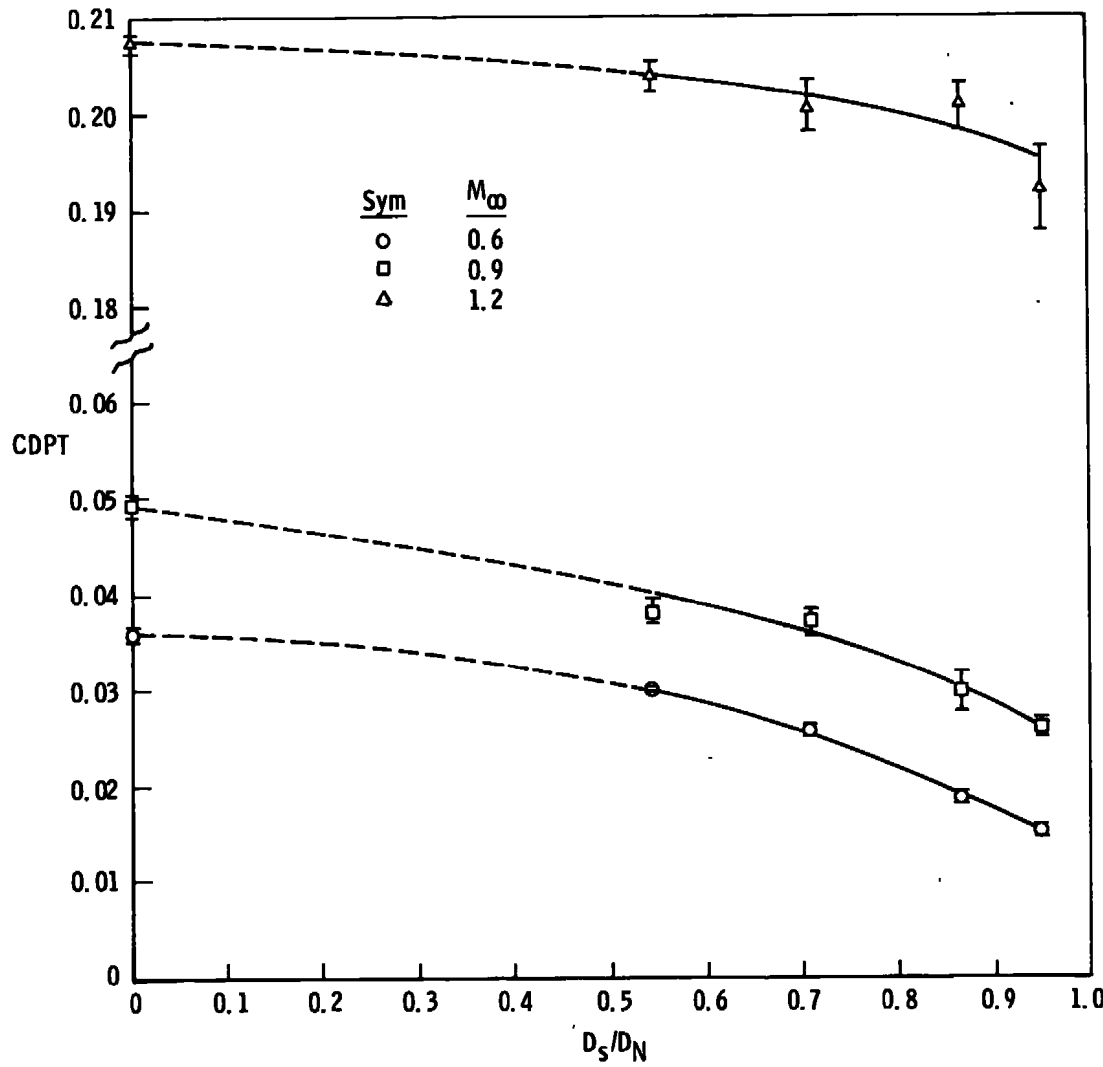
Figure 17. Variation of jet-off afterbody drag with sting size.

SYM	A/A*	D_S/D_N	
○	1.000	0.0	46
□	1.134	0.0	84
△	1.221	0.0	92
◇	1.300	0.0	109
⊠	1.490	0.0	118
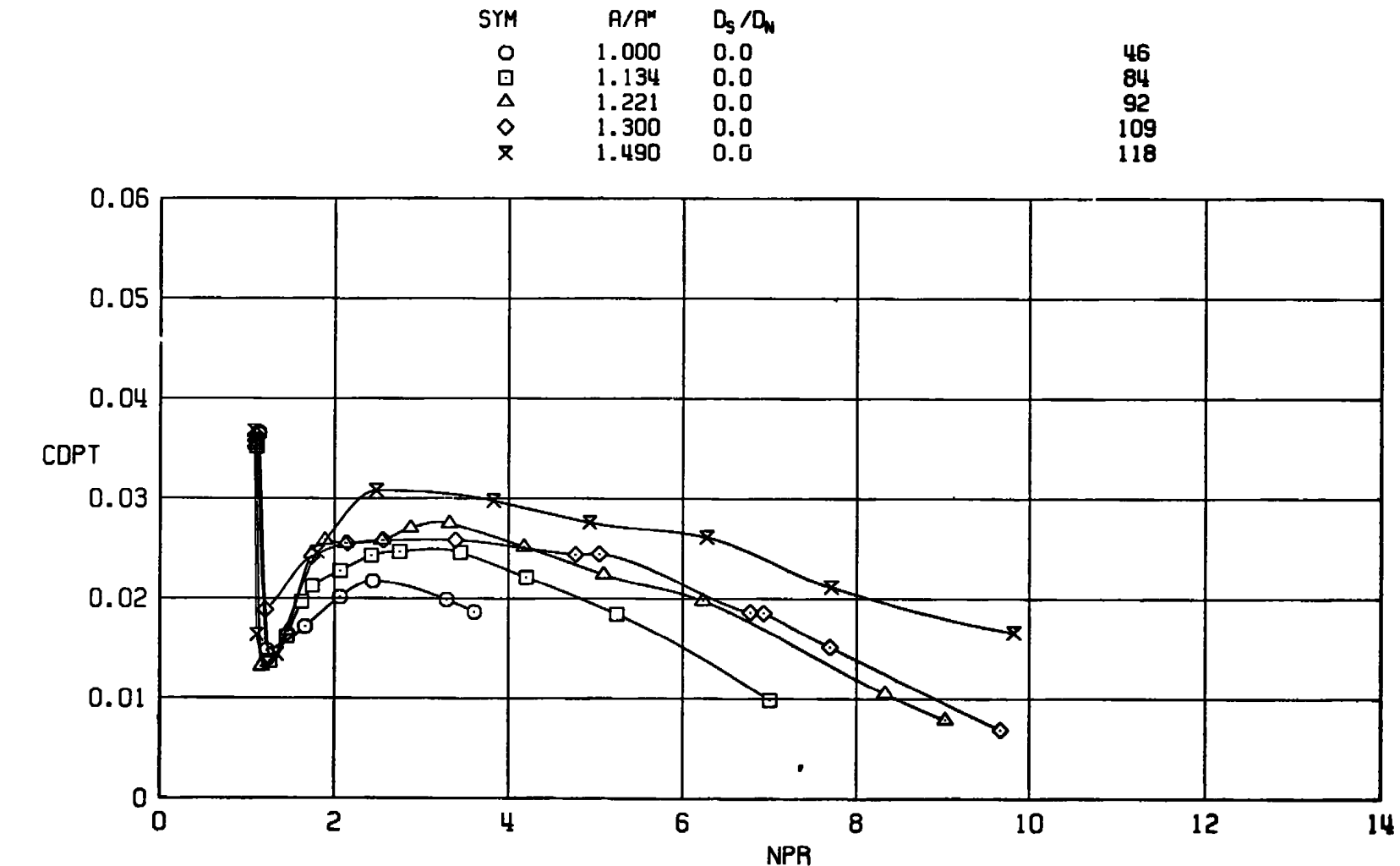
a. $M_\infty = 0.6$

Figure 18. Nozzle area ratio effects on afterbody drag,
$D_s/D_N = 0$.

SYM	A/A^*	D_S/D_N	
⊙	1.000	0.0	47
⊡	1.134	0.0	86
△	1.221	0.0	93
◇	1.300	0.0	111
✕	1.490	0.0	120
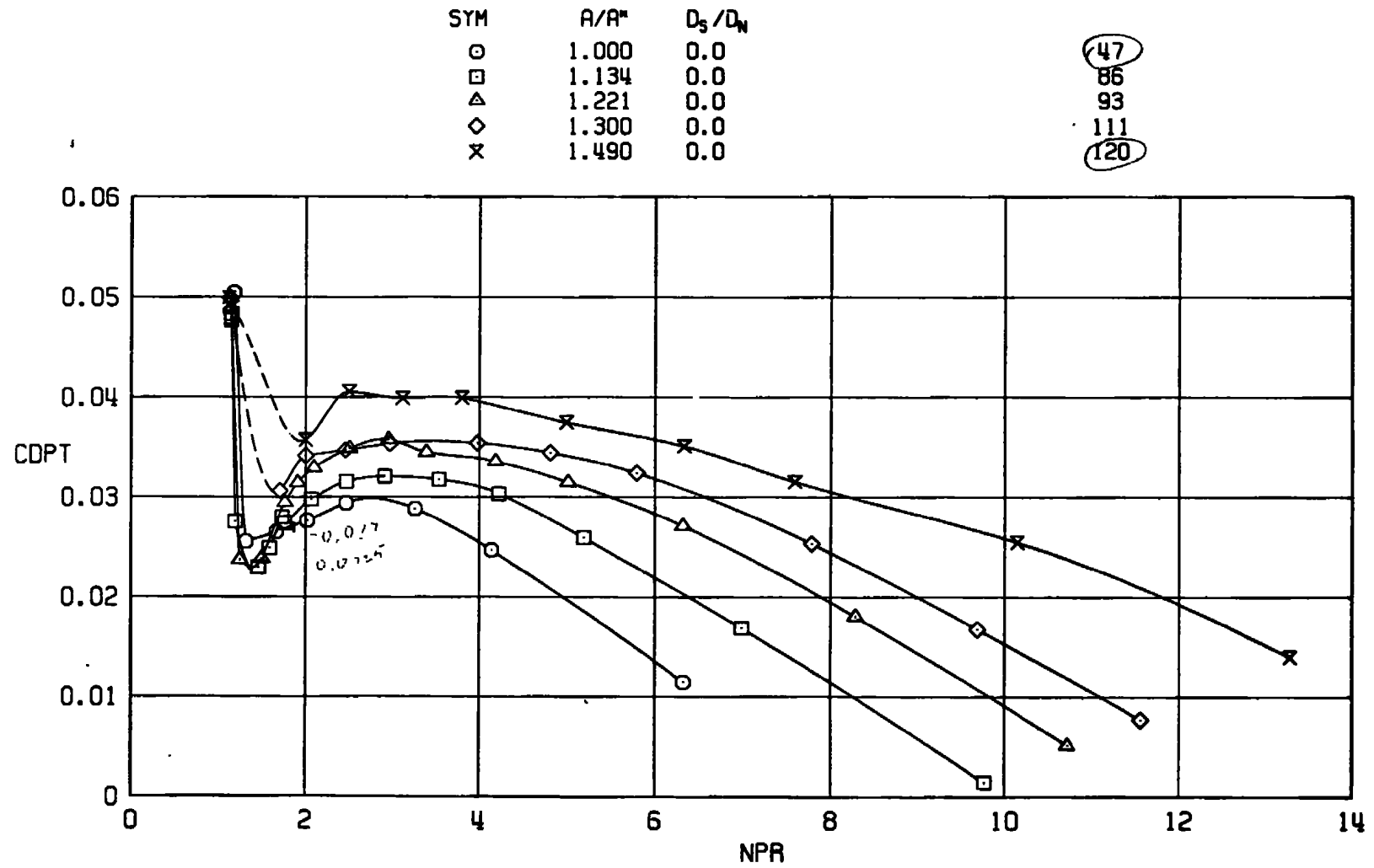
b. $M_\infty = 0.9$

Figure 18. Continued.

SYM	A/A*	D_S/D_N	
□	1.134	0.0	88
△	1.221	0.0	94
◇	1.300	0.0	113
✕	1.490	0.0	122
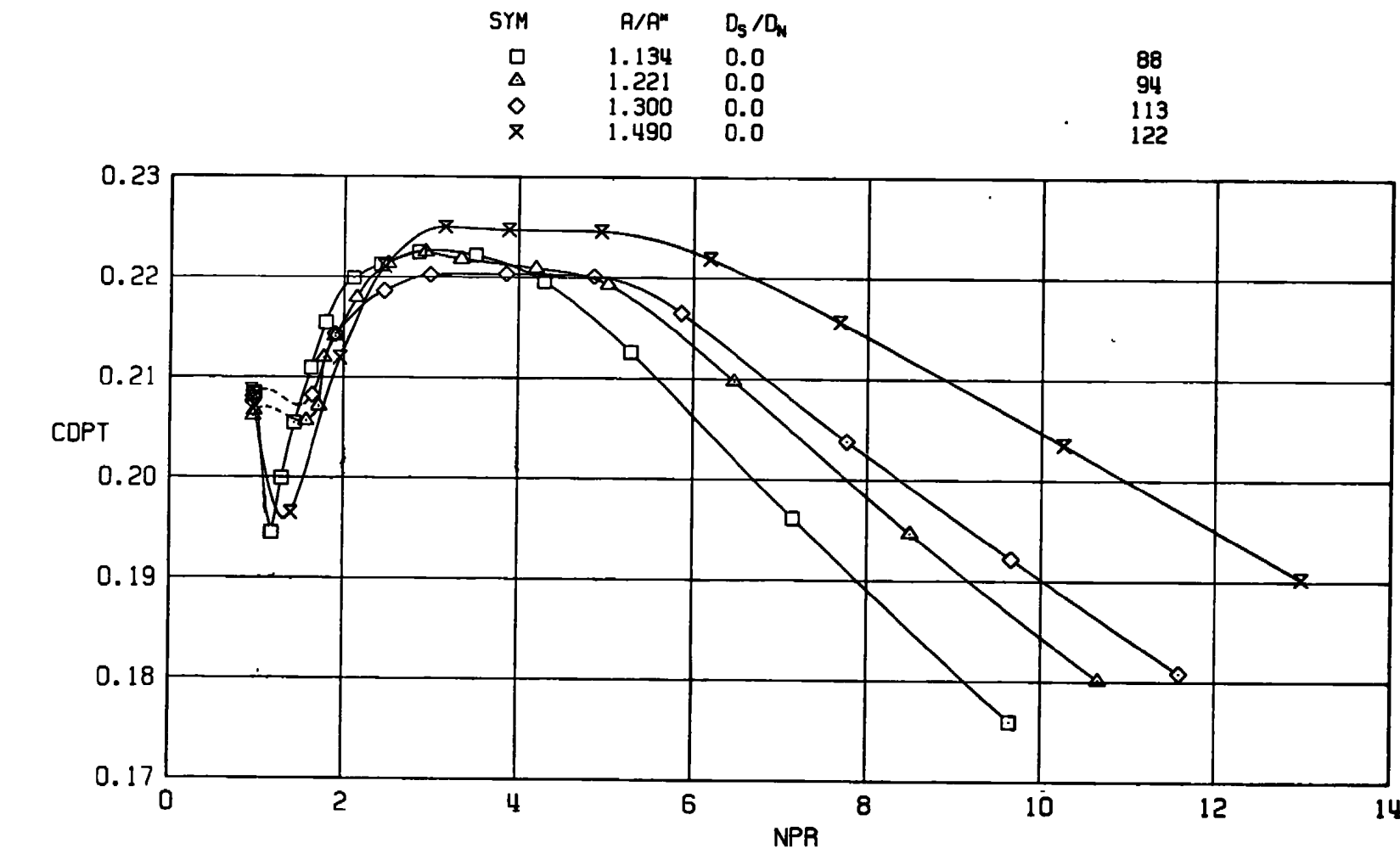
c. $M_\infty = 1.2$

Figure 18. Concluded.
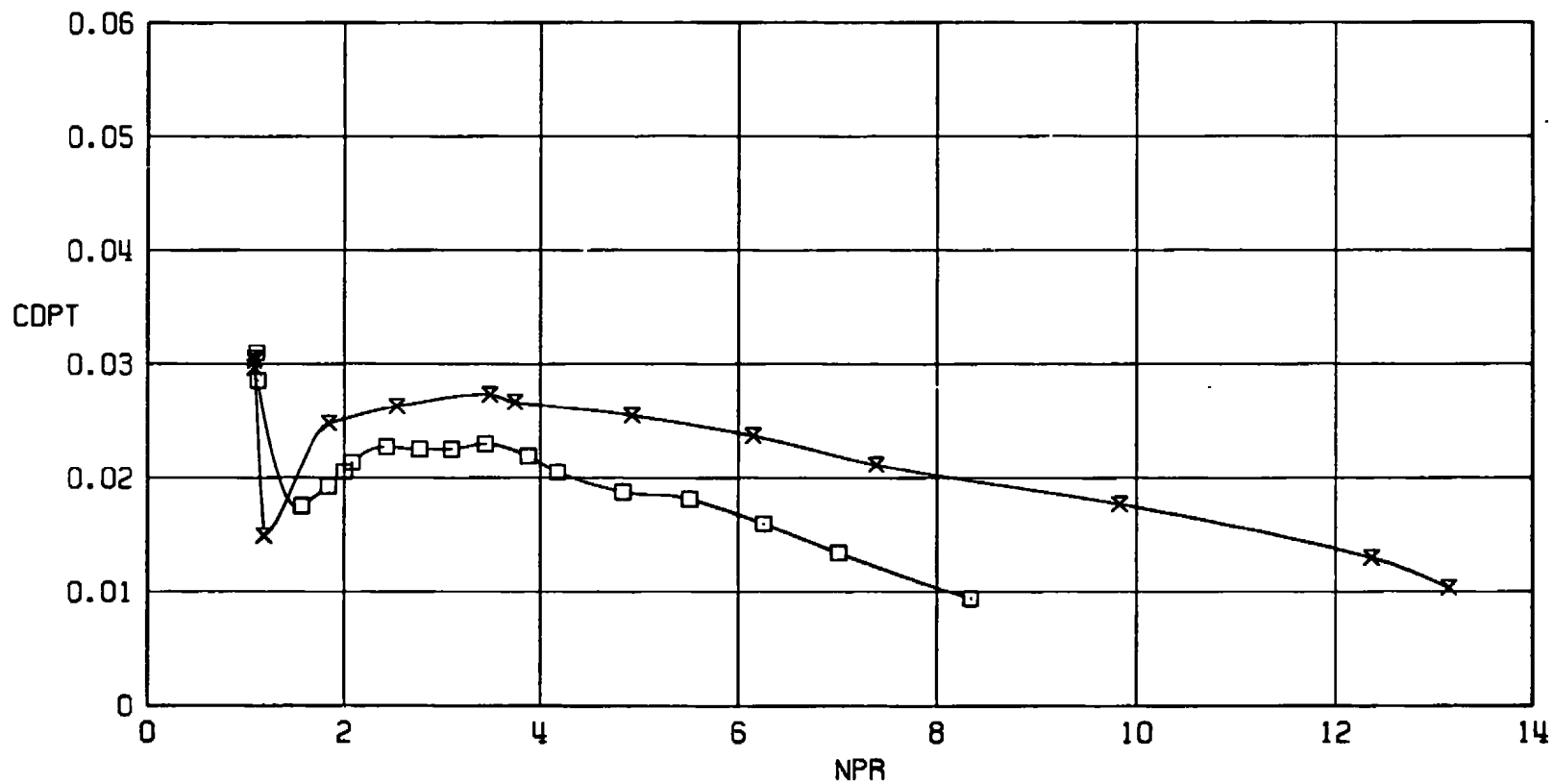
a. $M_\infty = 0.6$

Figure 19. Nozzle area ratio effects on afterbody drag,
$D_s/D_N = 0.543$.

SYM	A/A*	D_S/D_N	
□	1.134	0.543	10
X	1.486	0.542	105
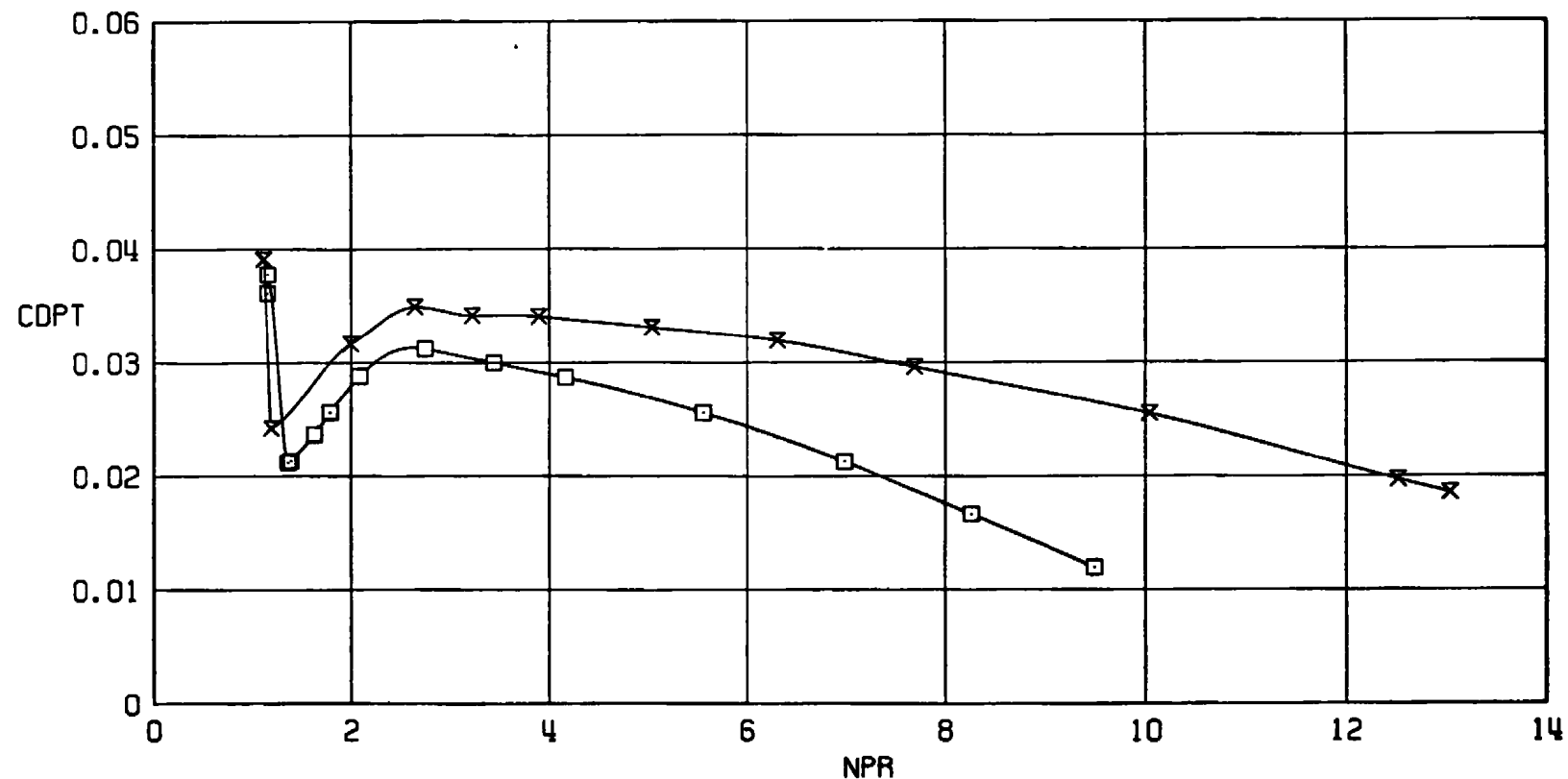
b. $M_\infty = 0.9$

Figure 19. Continued.

SYM	A/A*	D_S/D_N	
□	1.134	0.543	11
✕	1.486	0.542	106
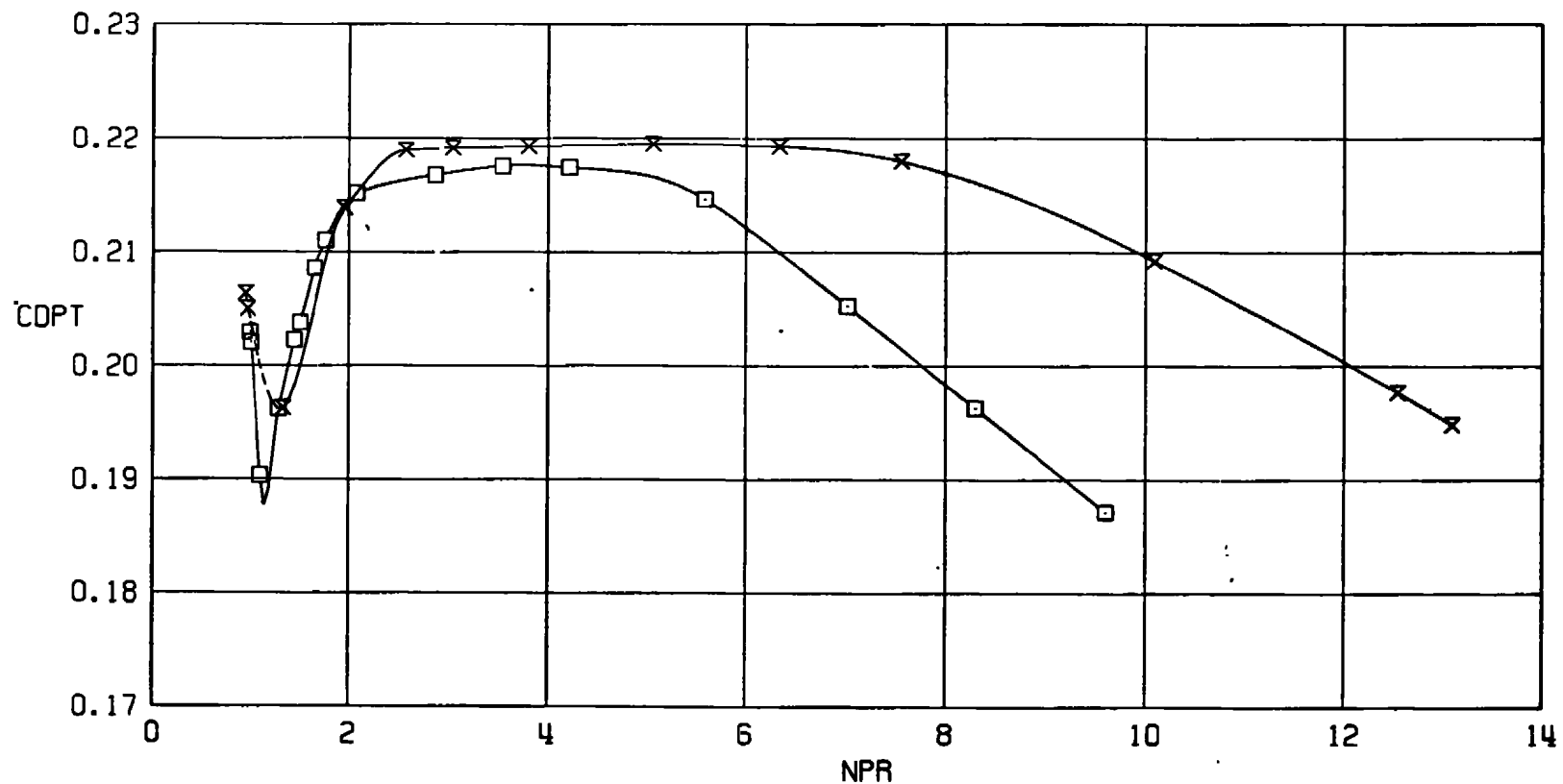
c. $M_\infty = 1.2$

Figure 19. Concluded.

SYM	A/A*	D_S/D_N	
△	1.220	0.706	69
◇	1.310	0.707	97
✕	1.491	0.707	74
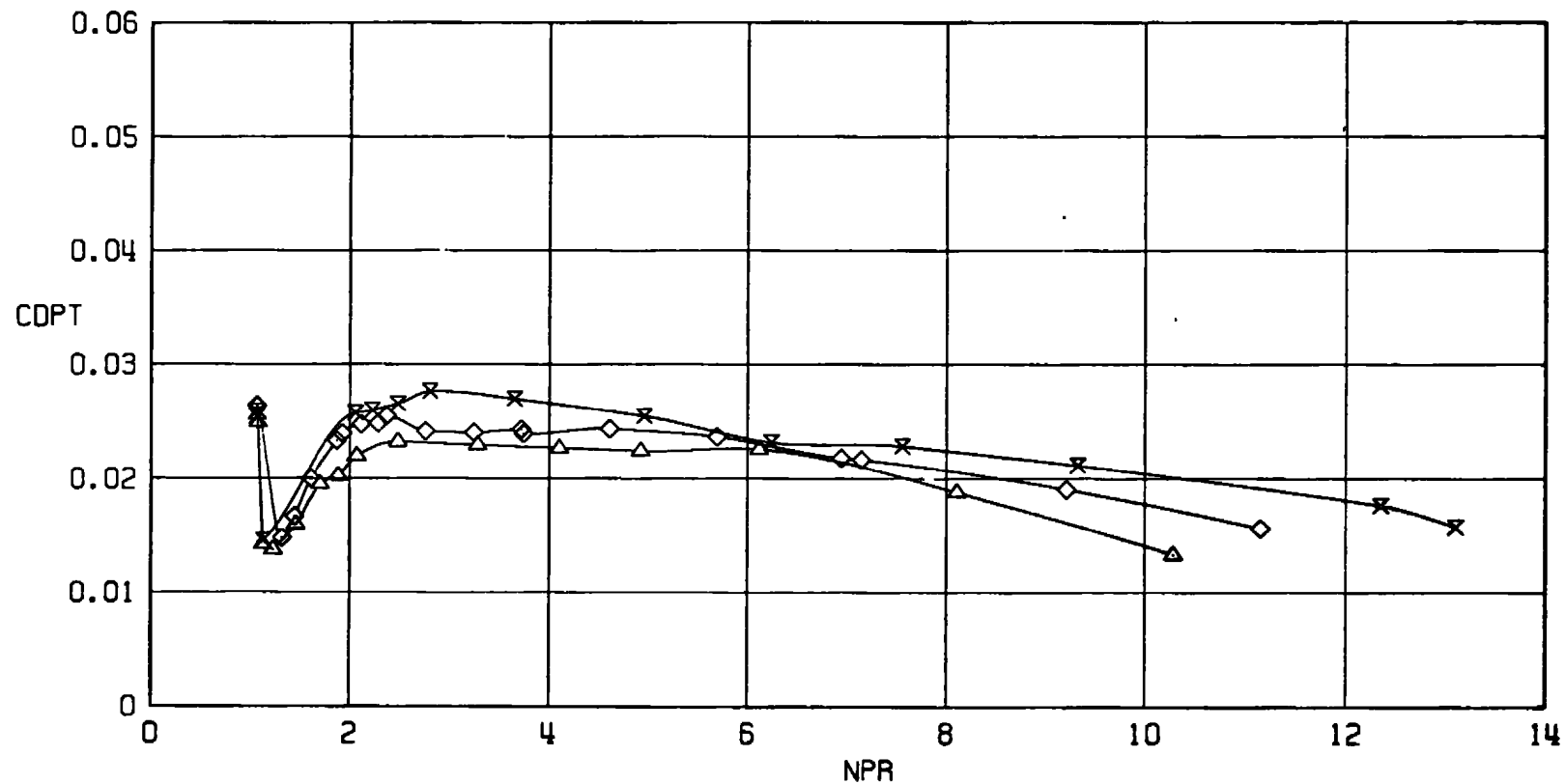
a. $M_\infty = 0.6$

Figure 20. Nozzle area ratio effects on afterbody drag, $D_s/D_N = 0.707$.

SYM	A/A*	D_S/D_N	
□	1.133	0.707	14
△	1.220	0.706	70
◇	1.310	0.707	98
✕	1.491	0.707	76
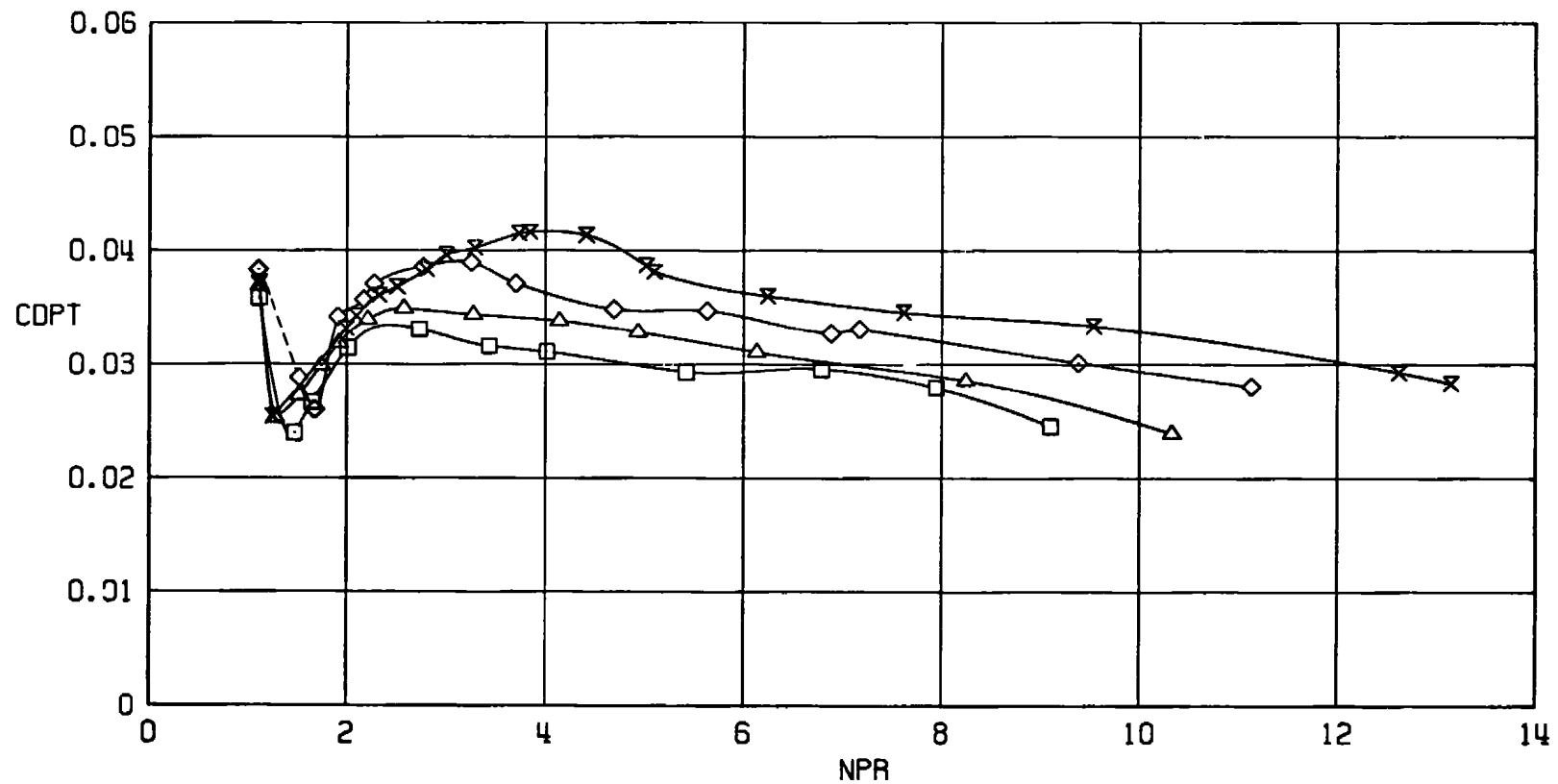
b. $M_\infty = 0.9$

Figure 20. Continued.

SYM	A/A^*	D_S/D_N	
□	1.133	0.707	17
△	1.220	0.706	71
◇	1.310	0.707	99
✕	1.491	0.707	78
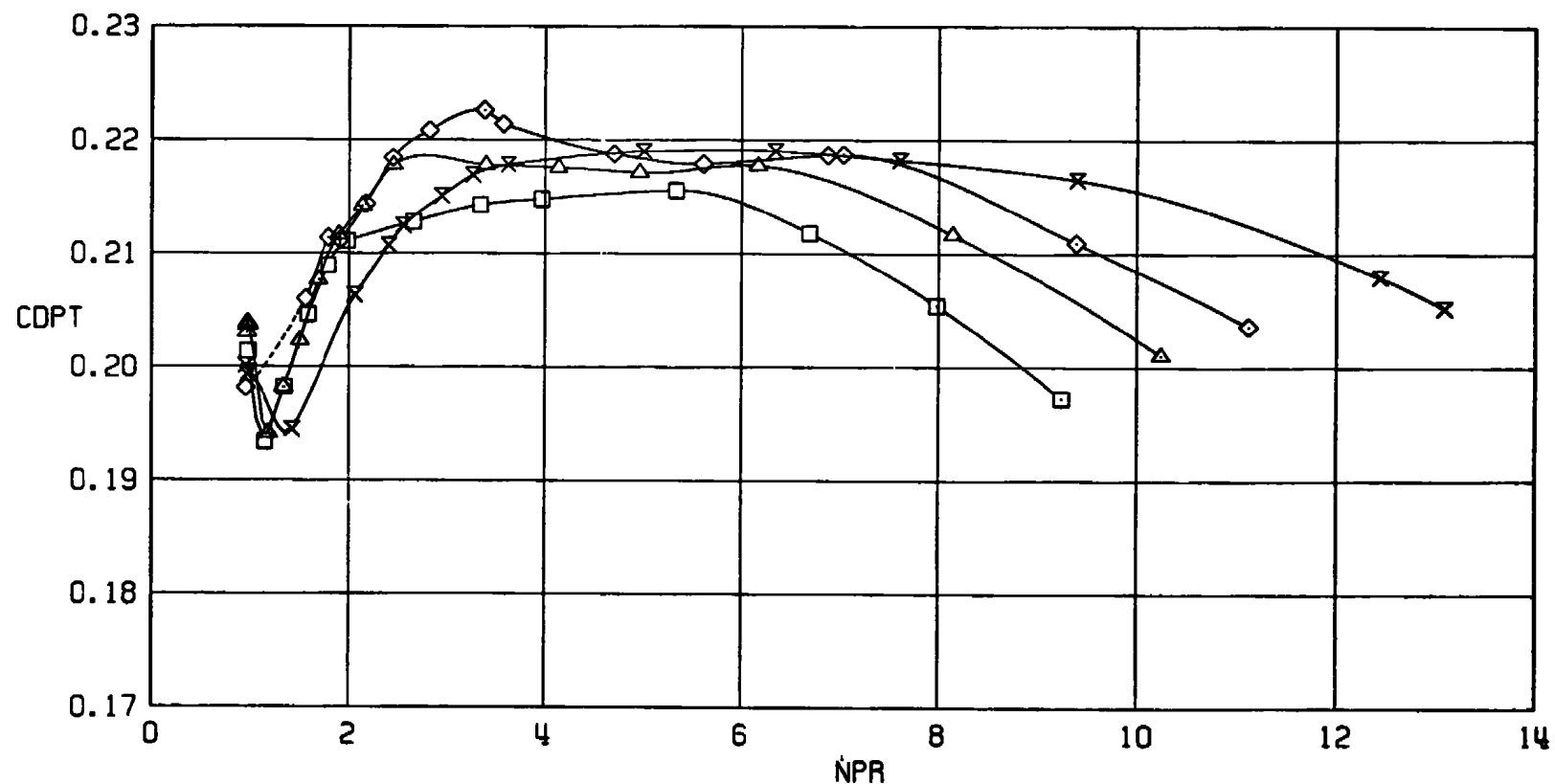
c. $M_\infty = 1.2$

Figure 20. Concluded.

SYM	A/A*	D_S/D_N	
O	1.000	0.866	41
□	1.142	0.866	35
X	1.500	0.866	128
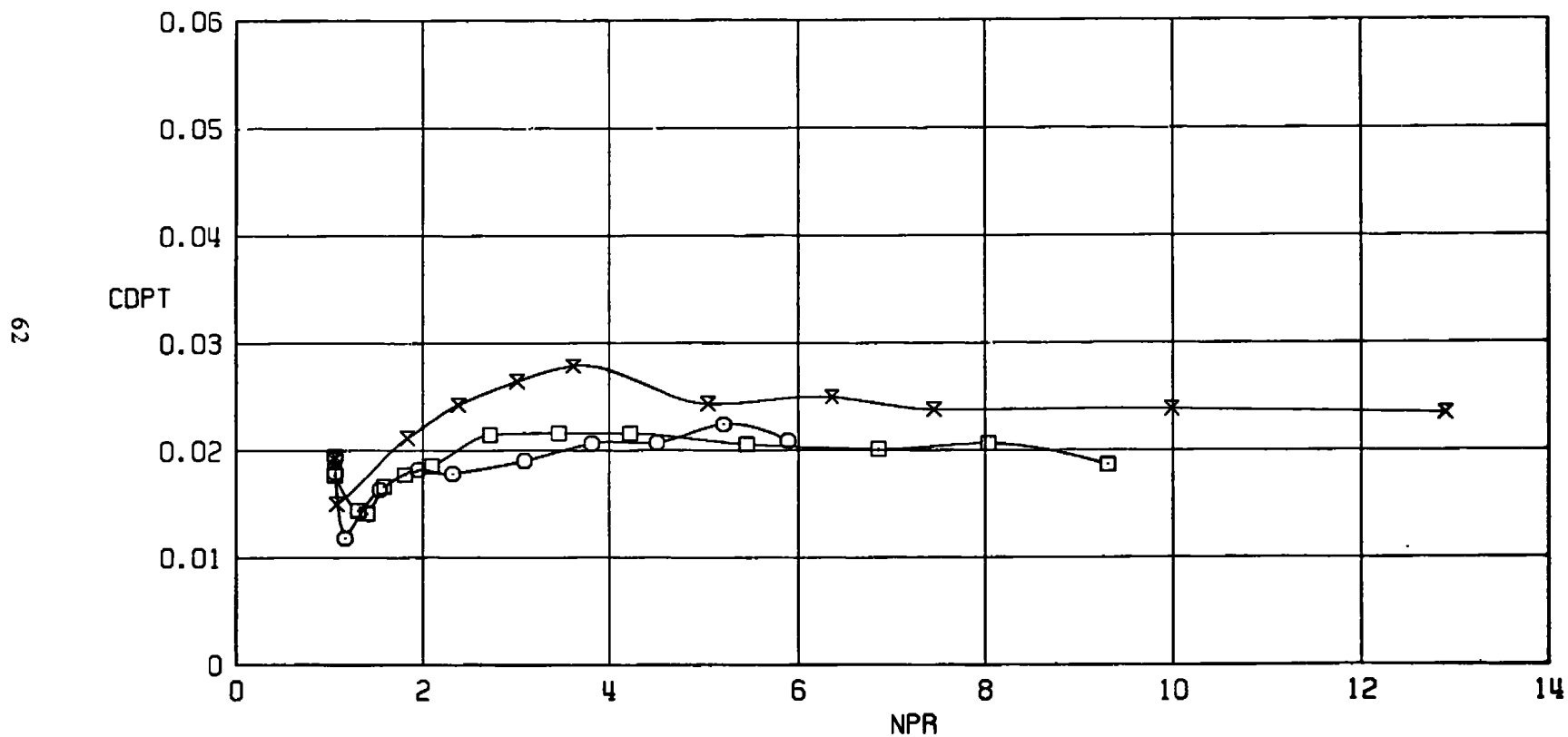
a. $M_\infty = 0.6$

Figure 21. Nozzle area ratio effects on afterbody drag,
$D_s/D_N = 0.866$.

SYM	A/A*	D_S/D_N	
○	1.000	0.866	42
□	1.142	0.866	36
◇	1.307	0.866	131
✗	1.500	0.866	126
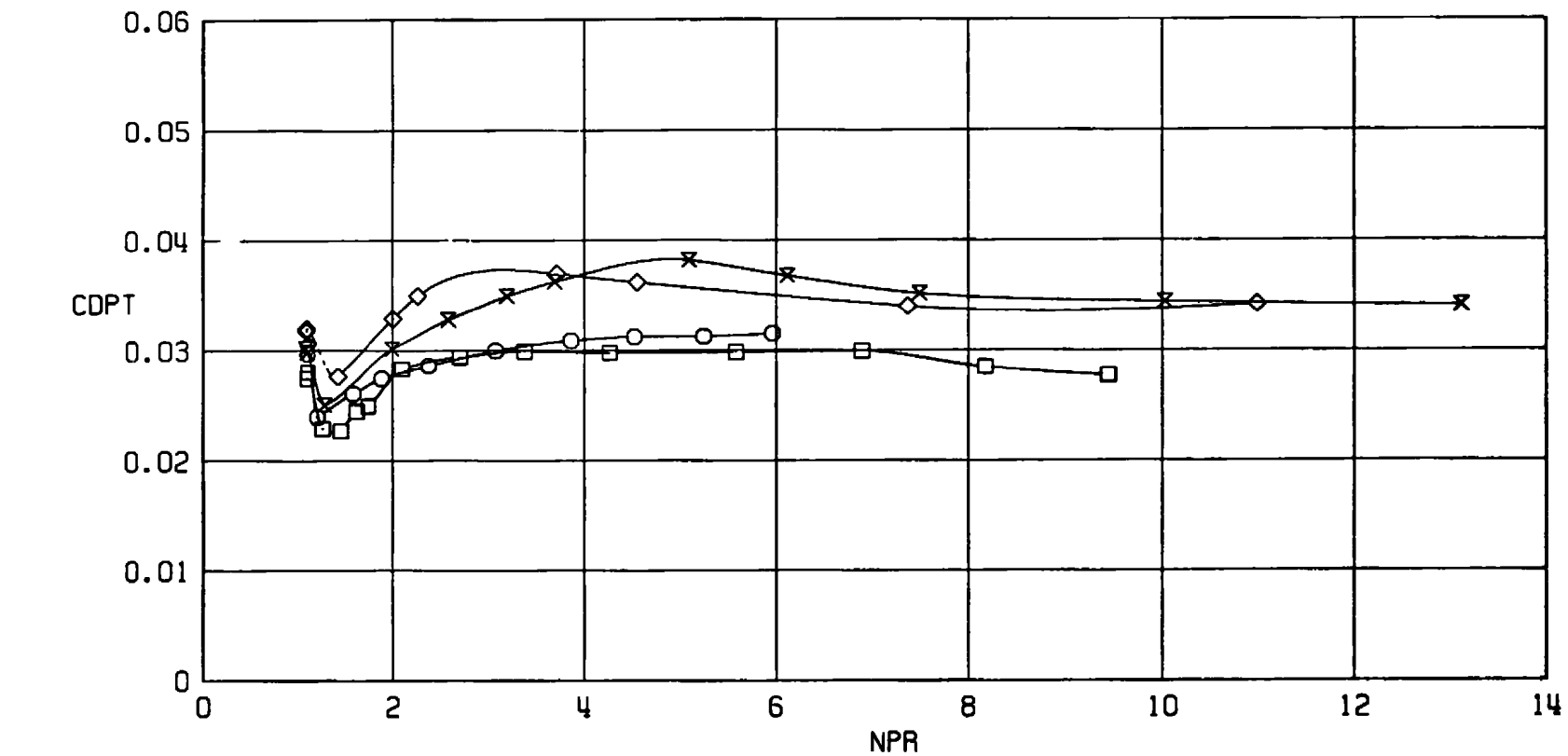
b. $M_\infty = 0.9$

Figure 21. Continued.

SYM	A/A*	D_S/D_N	
⊙	1.000	0.866	43
□	1.142	0.866	38
◇	1.307	0.866	132
X	1.500	0.866	127
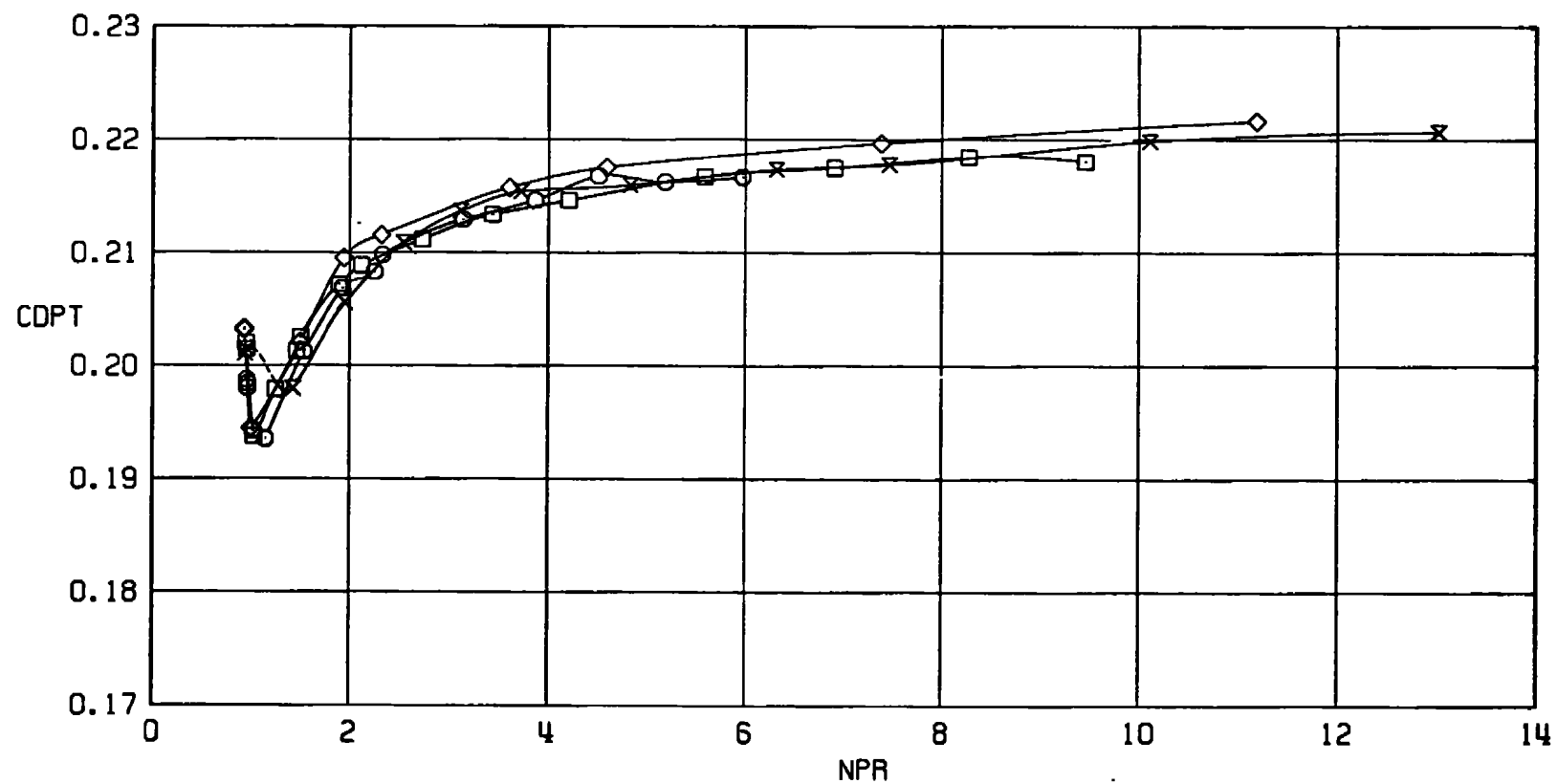
c. $M_\infty = 1.2$
Figure 21. Concluded.

SYM	A/A*	D_s/D_N	
□	1.127	0.950	52
X	1.463	0.949	60

CDPT

NPR
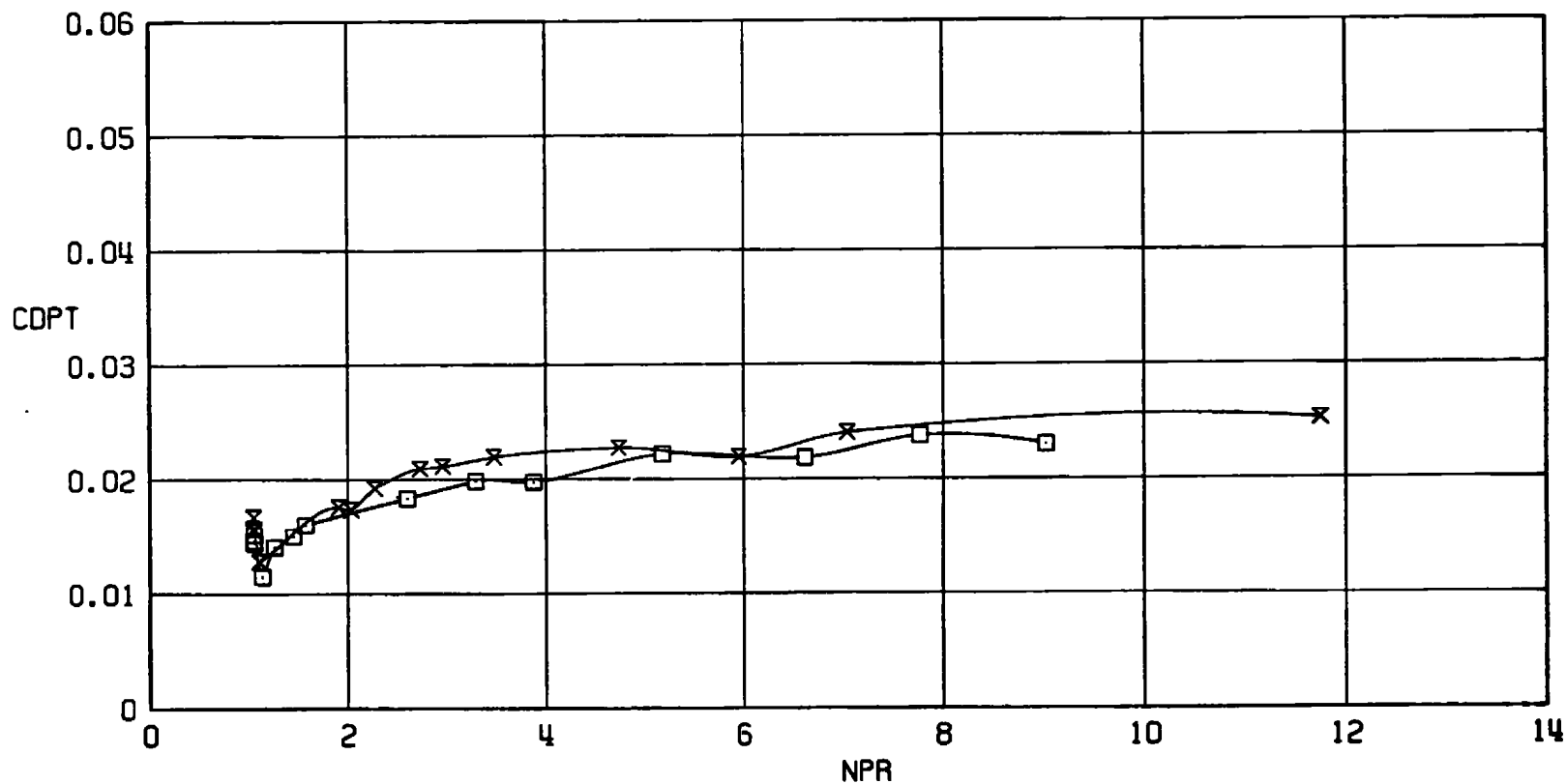
a. $M_\infty = 0.6$

Figure 22. Nozzle area ratio effects on afterbody drag,
$D_s/D_N = 0.95$.

SYM	A/A^*	D_S/D_N	
□	1.127	0.950	54
X	1.463	0.949	62
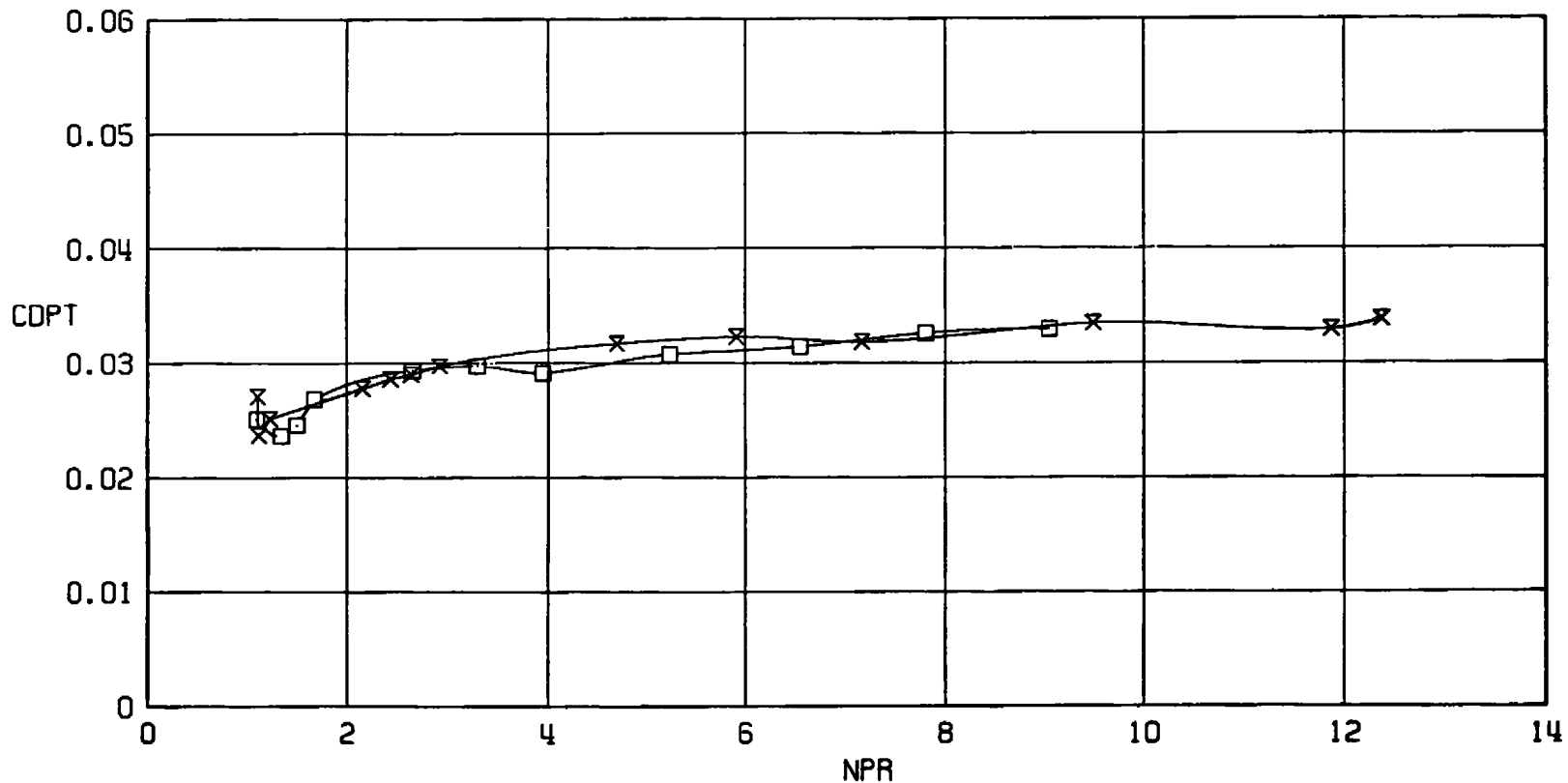
b. $M_\infty = 0.9$

Figure 22. Continued.

SYM	A/A^*	D_S/D_N	
□	1.127	0.950	56
X	1.463	0.949	64
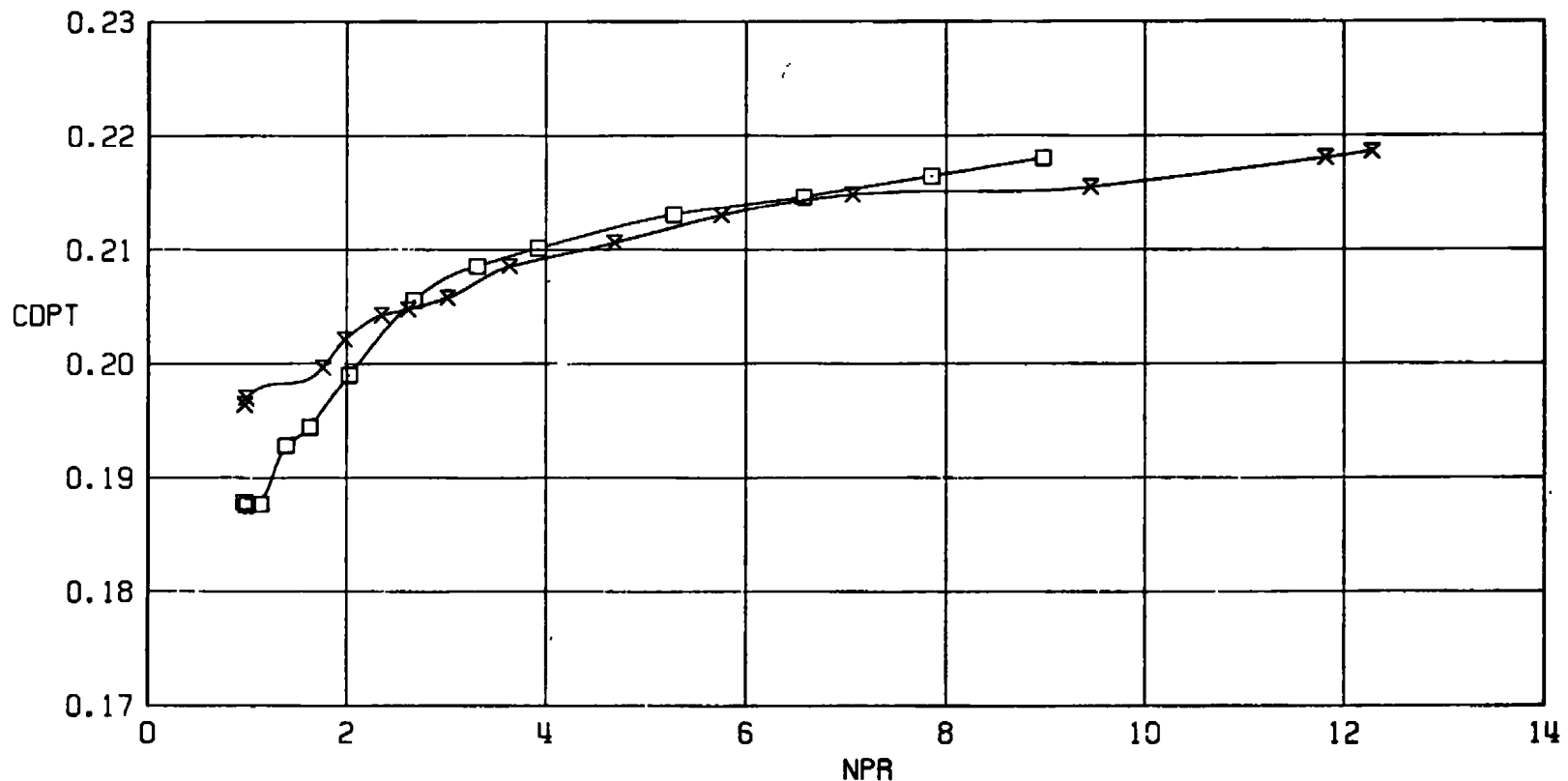
c. $M_\infty = 1.2$

Figure 22. Concluded.

SYM	A/R*	D_3/D_4
O	1.134	.0.0
△	1.133	0.707
X	1.127	0.950
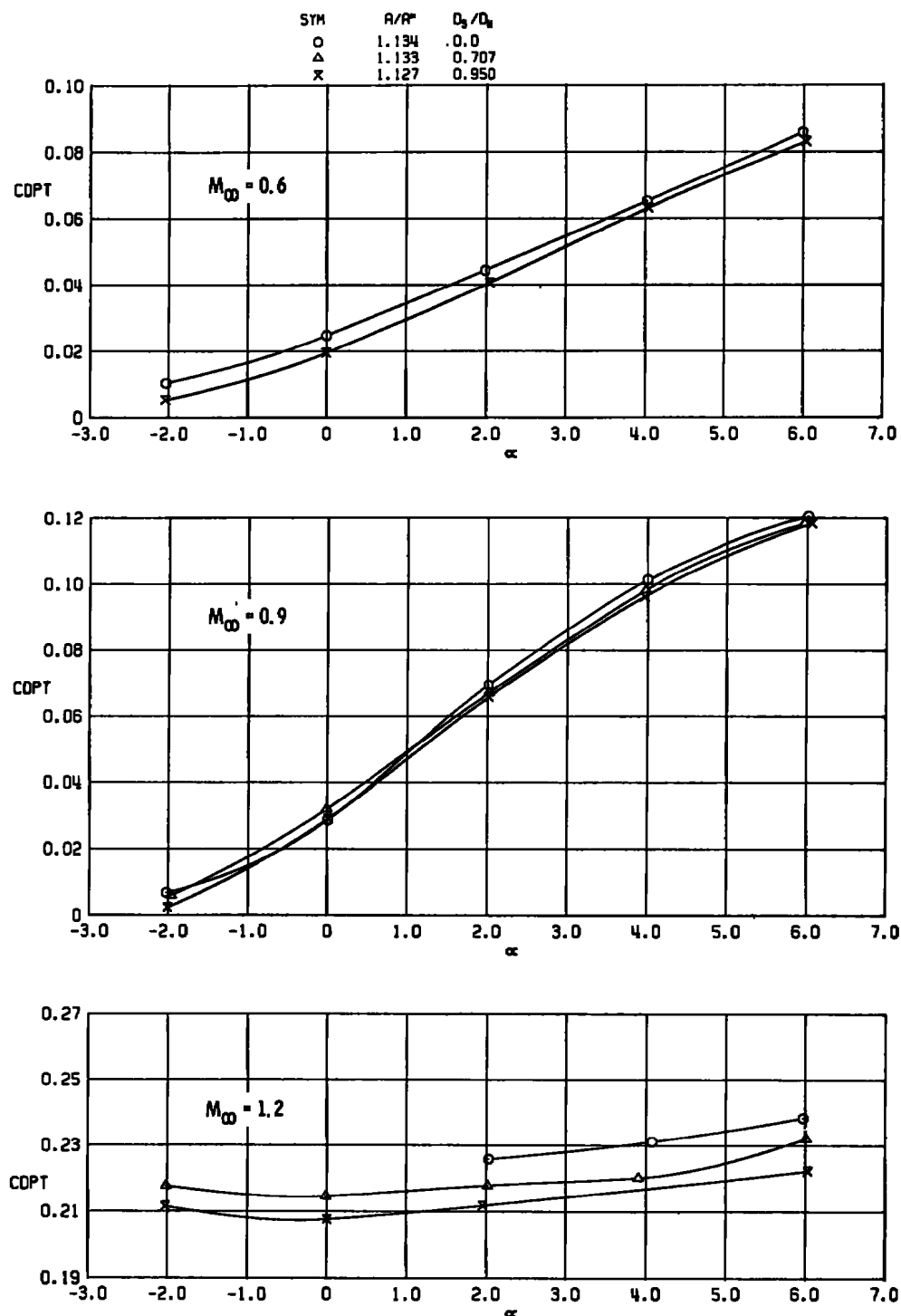
Figure 23. Influence of the annular jet on afterbody drag
sensitivity to angle of attack, A/A* ≈ 1.13.

SYM	P/P°	D_s/D_m
o	1.490	0.0
△	1.491	0.707
x	1.463	0.949
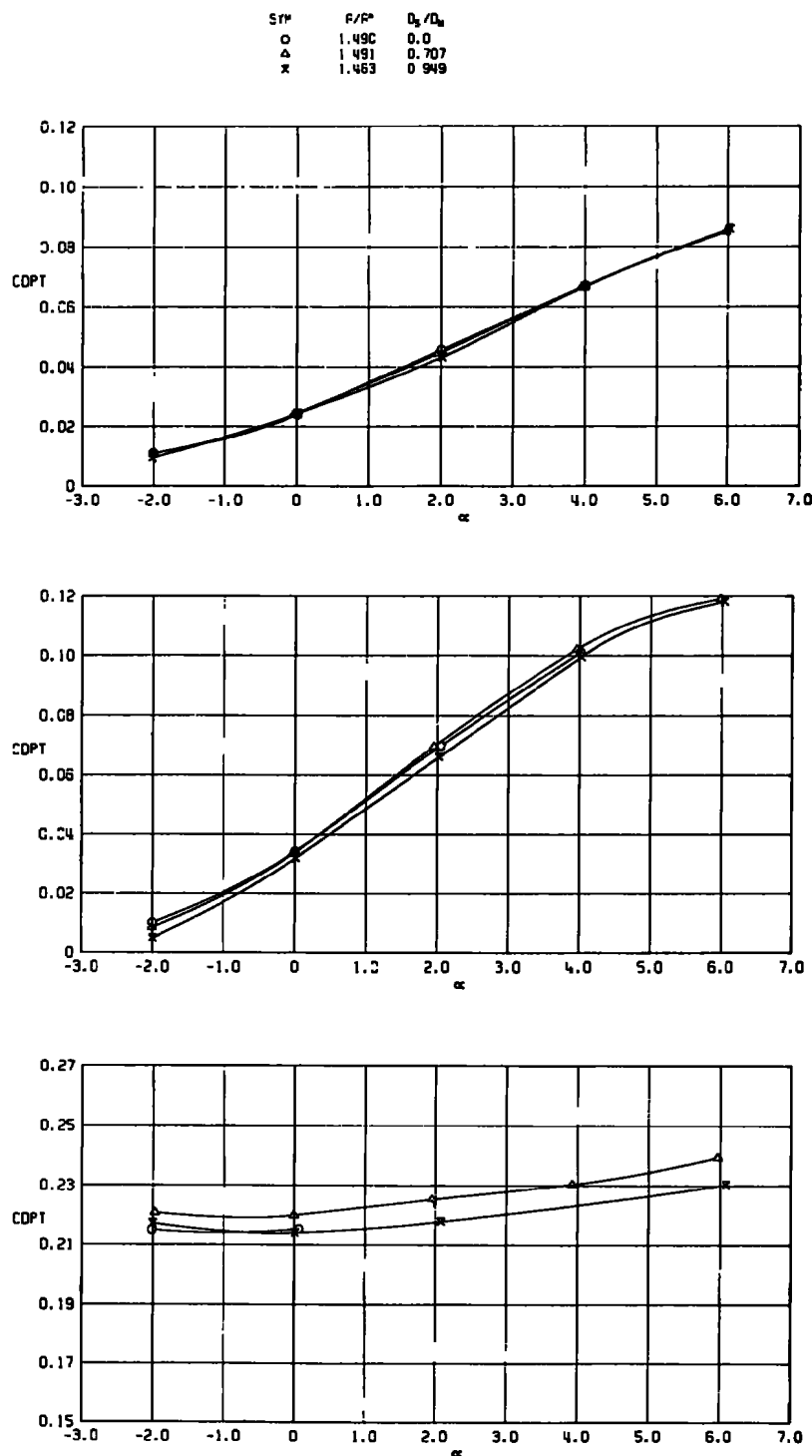
Figure 24. Influence of the annular jet on afterbody drag
sensitivity to angle of attack, A/A* ≈ 1.49.

SYM	A/A*	D_s/D_N	NPR	NSPR	PN/PT
O.	1.134	0.543	2.74	0.820	10.08
▢	1.134	0.543	3.44	1.029	10.09
△	1.134	0.543	5.56	1.665	10.11
◇	1.134	0.543	6.99	2.093	10.12
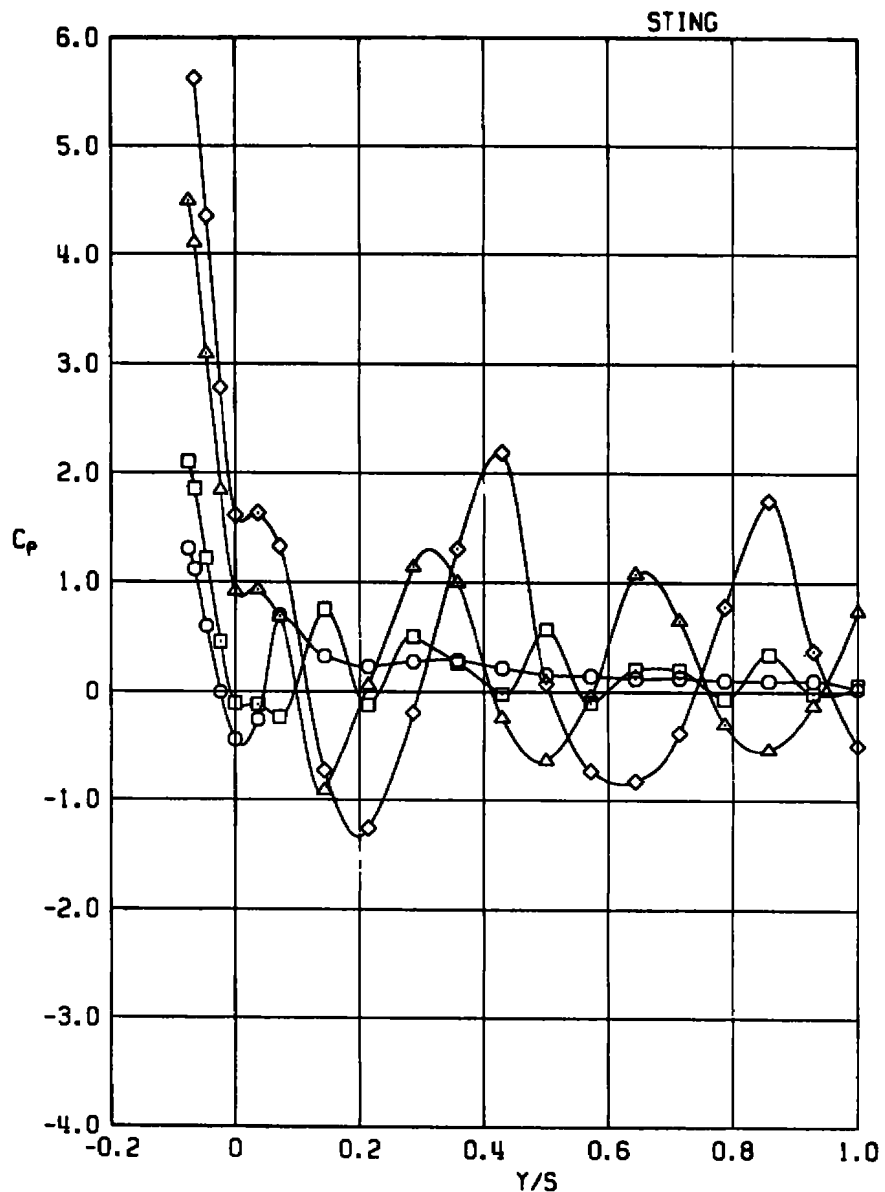
a. Sting pressure distributions

Figure 25. Nozzle pressure ratio effects on exhaust plume characteristics, D_s/D_N = 0.543, A/A* = 1.134 M_∞ = 0.9.
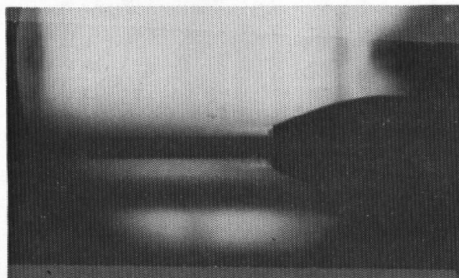
NPR = 2.74
NSPR = 0.820
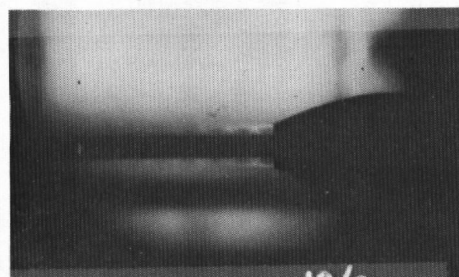
NPR = 3.44
NSPR = 1.029
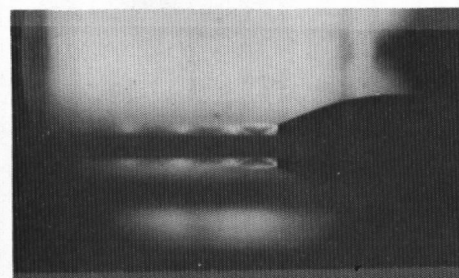
NPR = 5.56
NSPR = 1.665
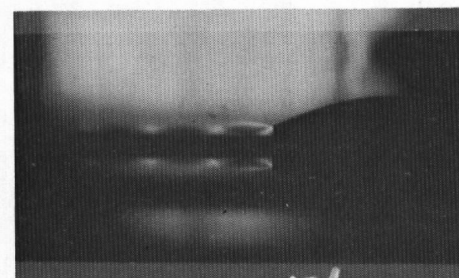
NPR = 6.99
NSPR = 2.093

b. Schlieren photographs
Figure 25. Concluded.

SYM	A/A*	D_S/D_N	NPR	NSPR	PN/PT
□	1.134	0.543	6.99	2.093	10.12
◇	1.142	0.866	6.89	2.028	36.12
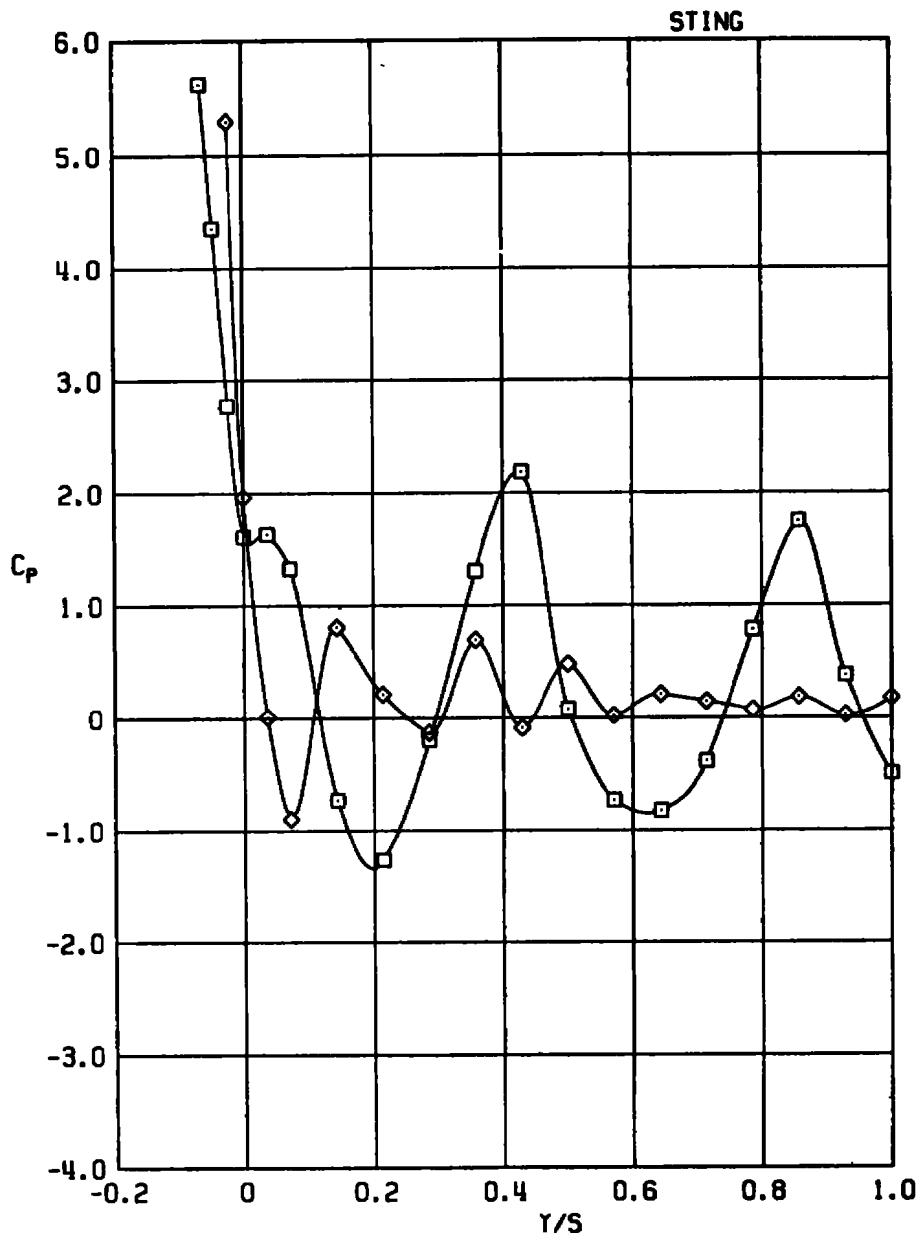
a. Sting pressure distributions

Figure 26. Sting size effects on exhaust plume characteristics,
A/A* ≈ 1.13, NSPR ≈ 2.0, M_∞ = 0.9.
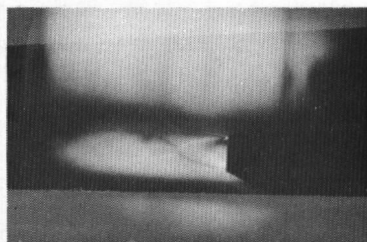
D_S/D_N = 0

A/A^* = 1.134

NPR = 6.981

NSPR = 2.092

D_S/D_N = 0.543

A/A^* = 1.134

NPR = 6.987

NSPR = 2.093
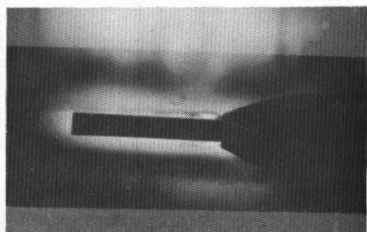
D_S/D_N = 0.707

A/A^* = 1.133

NPR = 6.786

NSPR = 2.038
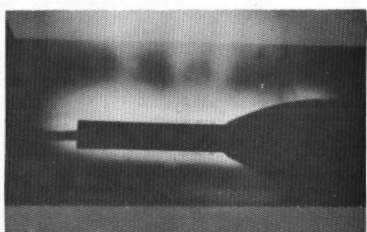
D_S/D_N = 0.866

A/A^* = 1.142

NPR = 6.893

NSPR = 2.028
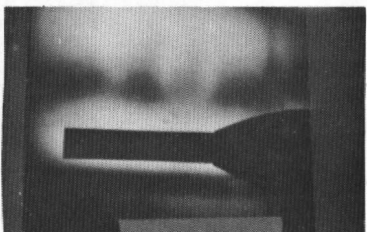
D_S/D_N = 0.95

A/A^* = 1.127

NPR = 6.547

NSPR = 1.997

b. Schlieren photographs
Figure 26. Concluded.

SYM	A/A*	D_S/D_N	NPR	NSPR	PN/PT
□	1.134	0.543	6.99	2.093	10.12
X	1.486	0.542	12.52	2.044	105.15
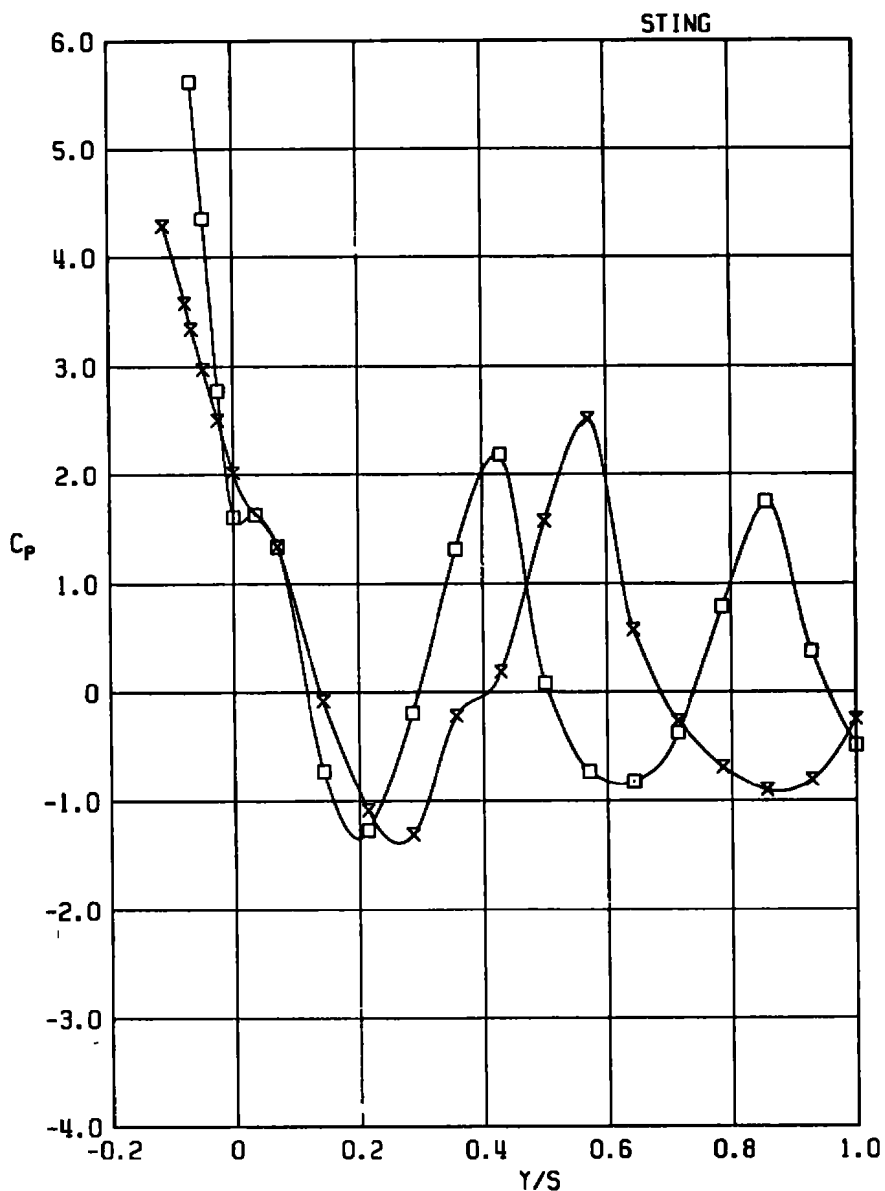
a. Sting pressure distributions

Figure 27. Nozzle area ratio effects on exhaust plume
characteristics, D_s/D_N = 0.543, NSPR ≈ 2.0,
M_∞ = 0.9.
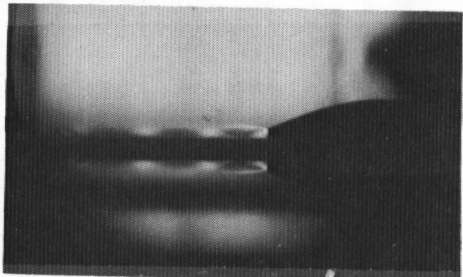
$$A/A^* = 1.134$$
$$NPR = 6.99$$
$$NSPR = 2.093$$
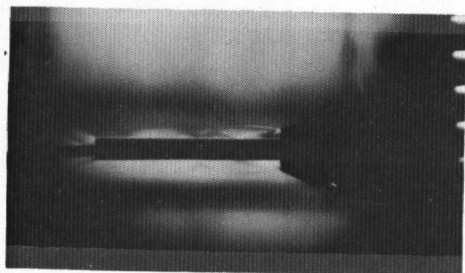
$$A/A^* = 1.486$$
$$NPR = 12.52$$
$$NSPR = 2.044$$

b. Schlieren photographs
Figure 27. Concluded.

SYM	A/A*	D_s/D_N	NPR	NSPR	M_∞	PN/PT
○	1.134	0.543	3.44	1.032	0.6	9.10
□	1.134	0.543	3.44	1.029	0.9	10.09
△	1.134	0.543	3.55	1.062	1.2	11.11
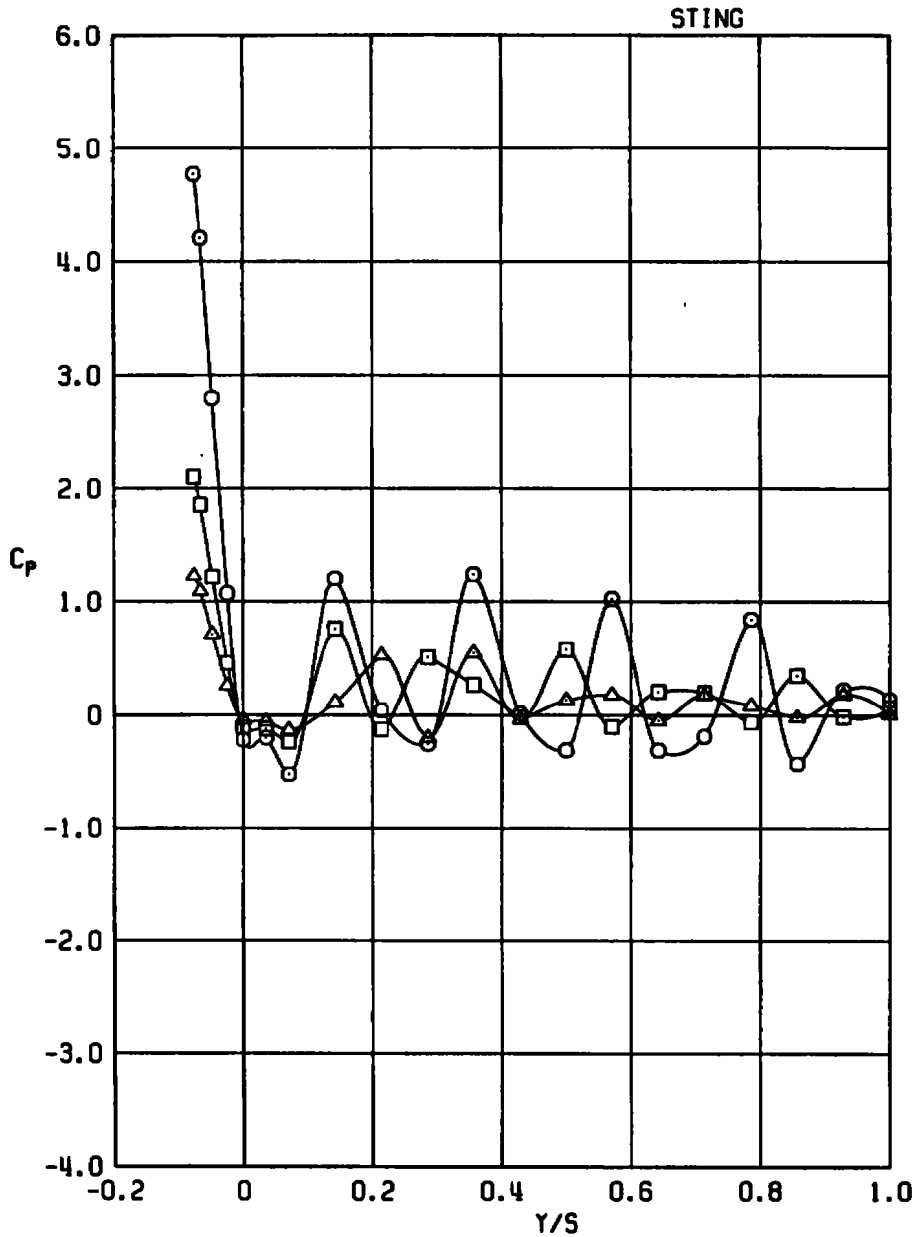
a. Sting pressure distributions, NSPR ≈ 1.0

Figure 28. Free-stream Mach number effects on exhaust plume characteristics, D_s/D_N = 0.543, A/A* = 1.134.

SYM	A/A*	D$_S$/D$_N$	NPR	NSPR	M$_\infty$	PN/PT
⊙	1.134	0.543	7.00	2.098	0.6	9.16
⊡	1.134	0.543	6.99	2.093	0.9	10.12
△	1.134	0.543	7.02	2.101	1.2	11.14
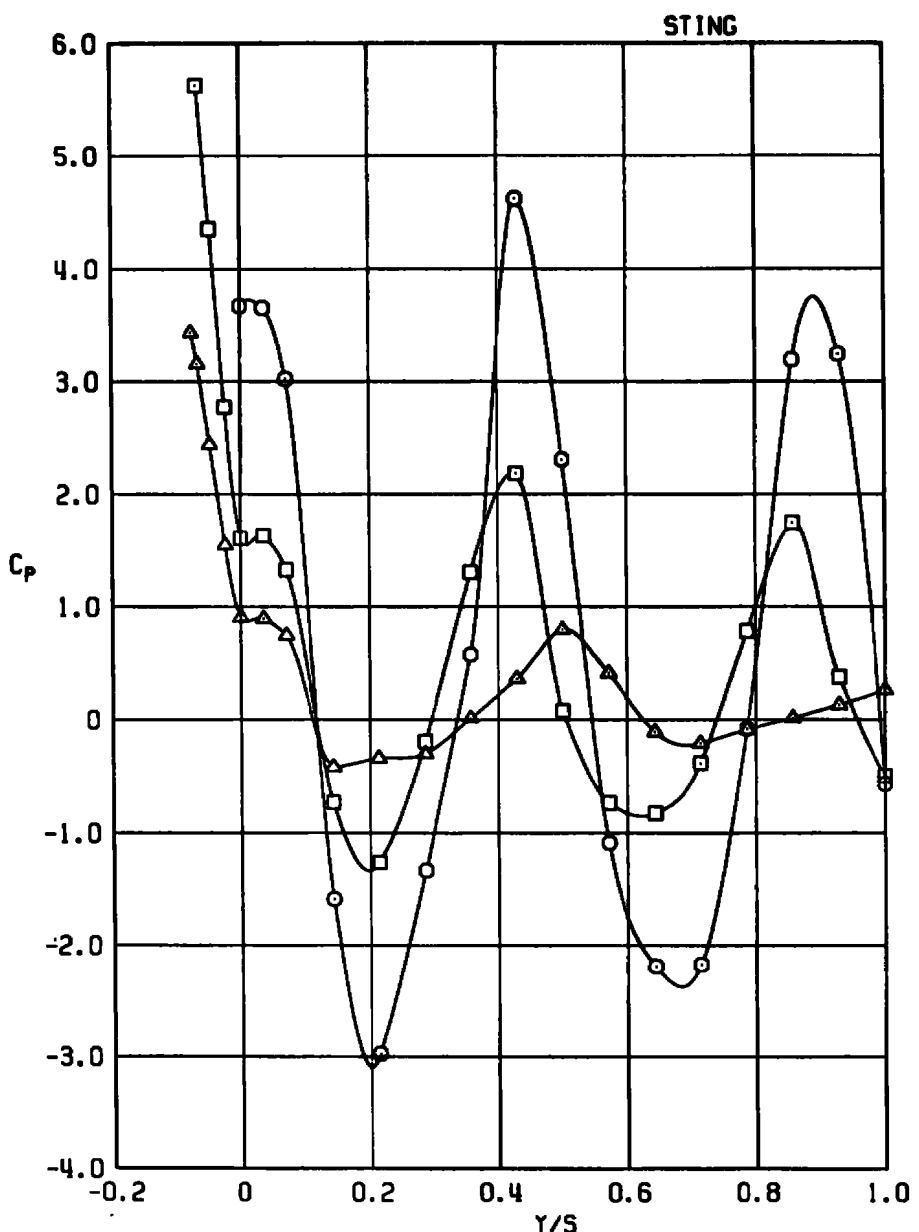
b. Sting pressure distributions, NSPR ≈ 2.0
Figure 28. Continued.
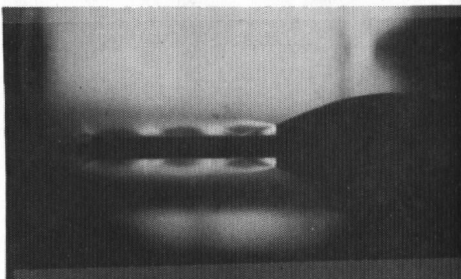
M_∞ = 0.6
NPR = 7.00
NSPR = 2.098
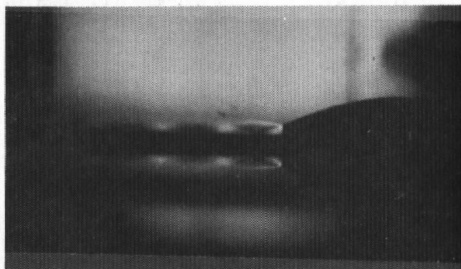
M_∞ = 0.9
NPR = 6.99
NSPR = 2.093
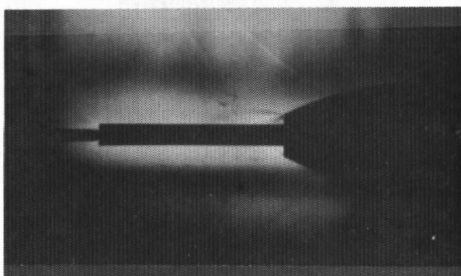
M_∞ = 1.2
NPR = 7.02
NSPR = 2.101

c. Schlieren photographs, NSPR ≈ 2.0
Figure 28. Concluded.

NSPR = 2.0

A/A* = 1.134

$NPR = 6.64$

R_P/R_N

1.6
1.4
1.2

1.0

0.8
0.6
0.4
0.2

D_s/D_N - 0.95   0.866   0.707   0.543   0.0

-1.2   -0.8   -0.4   0   0.4   0.8   1.2   1.6   2.0   2.4   2.8   3.2   3.6   4.0   4.4

Y/R_N
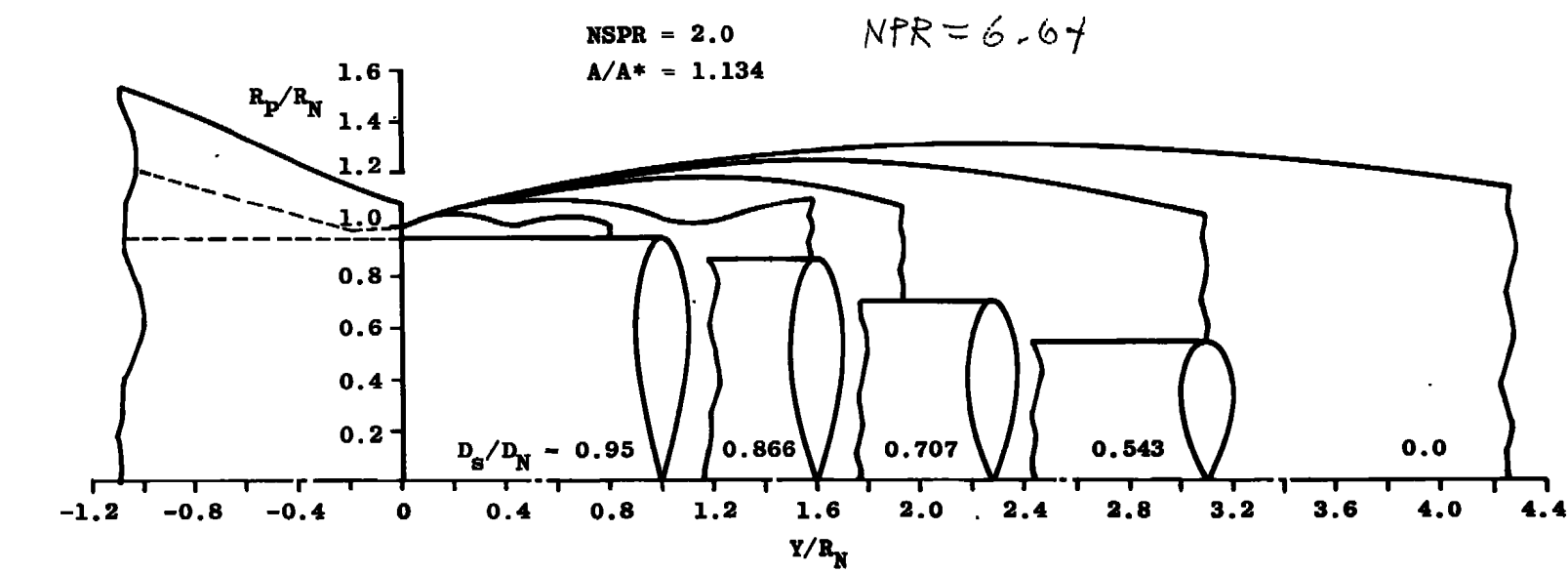
Figure 29. Variation of plume shape with annular jet sting size
as determined by MOC.
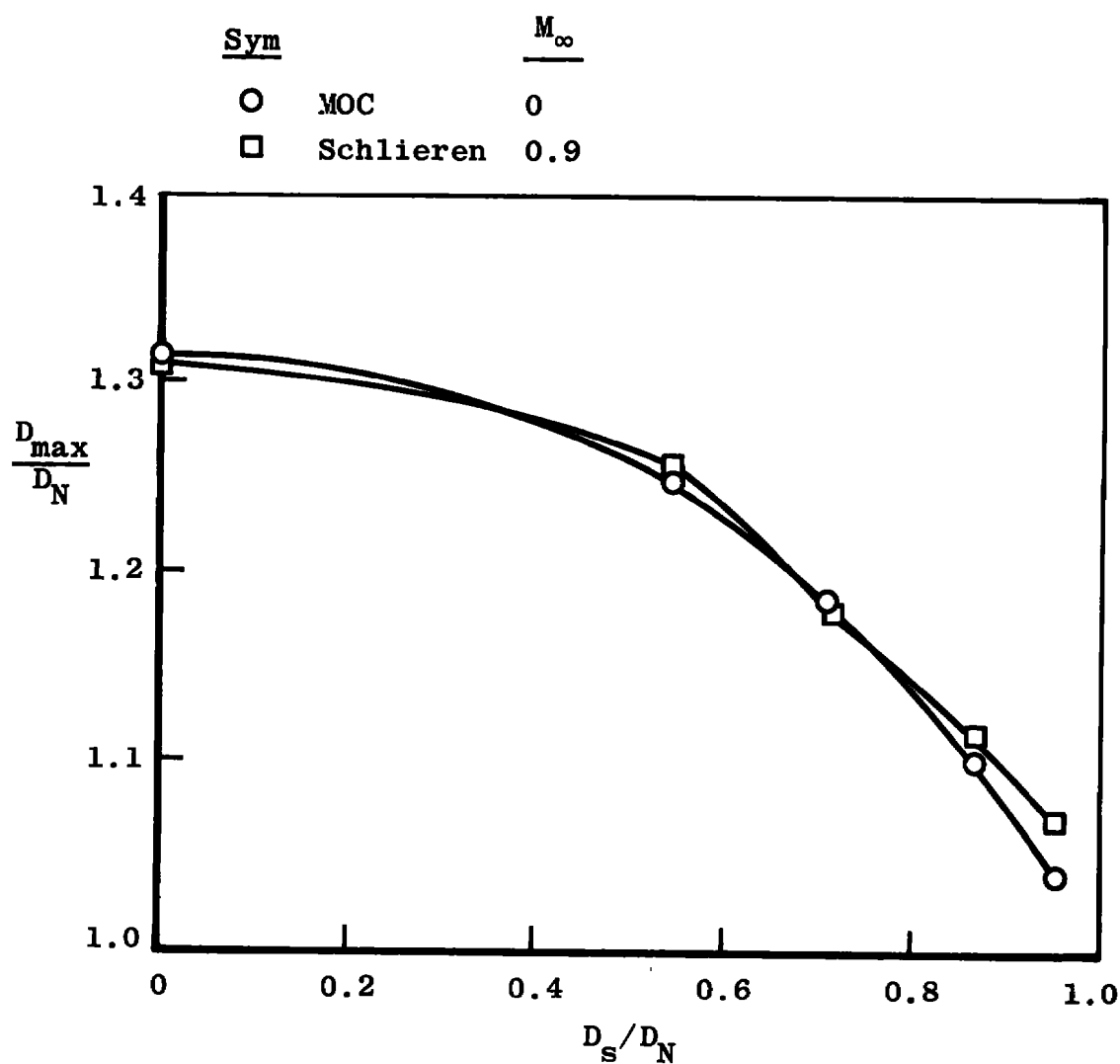
Figure 30. Variation of plume maximum diameter with sting
diameter, NSPR ≈ 2.0, A/A* ≈ 1.13.
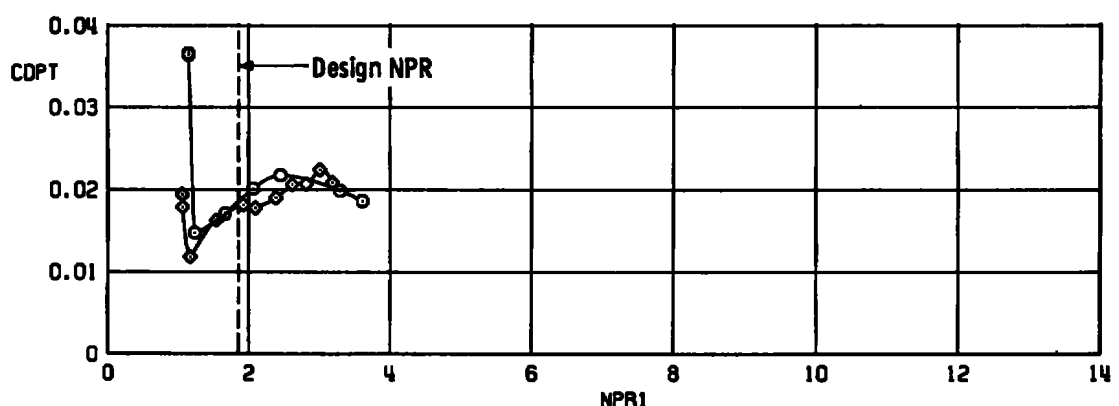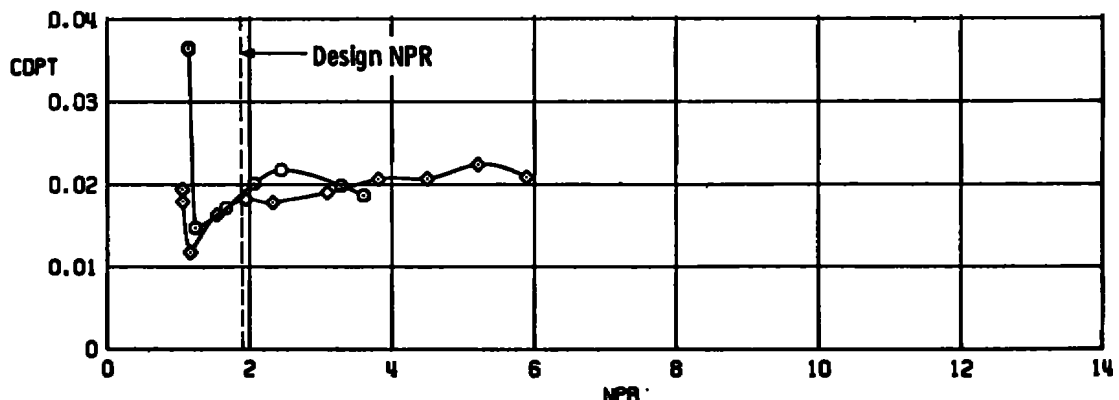
a. $M_\infty = 0.6$

Figure 31. Correlation of sting size effects on afterbody drag,
A/A* = 1.0.
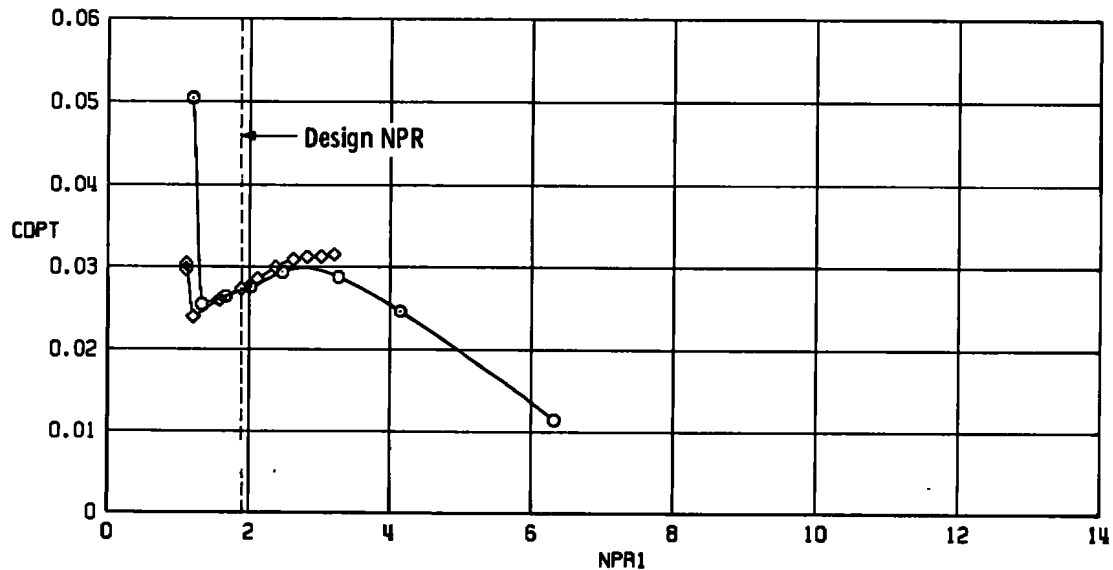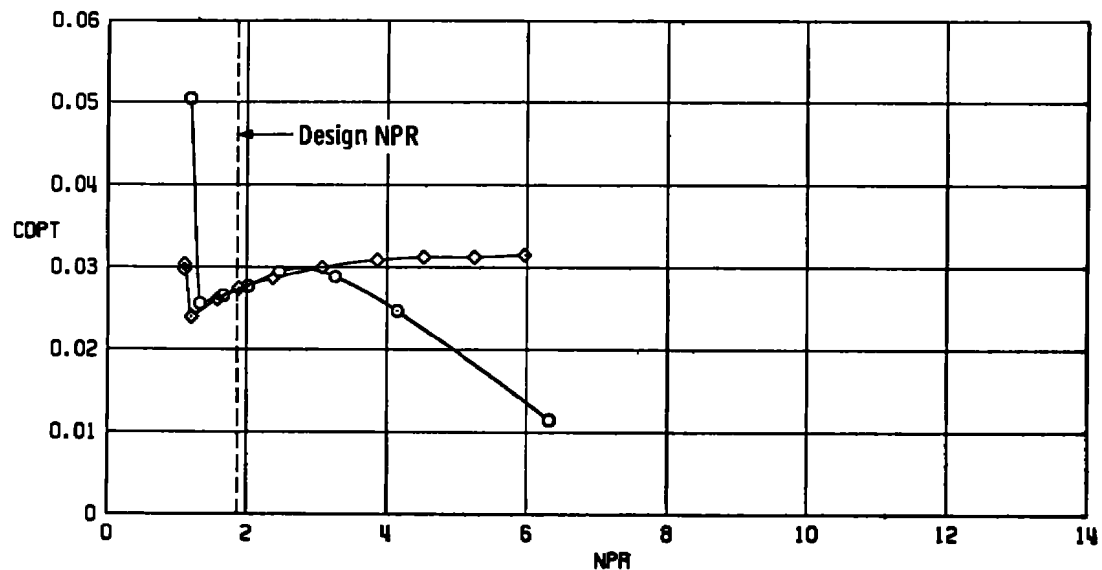
b. $M_\infty = 0.9$
Figure 31. Concluded.
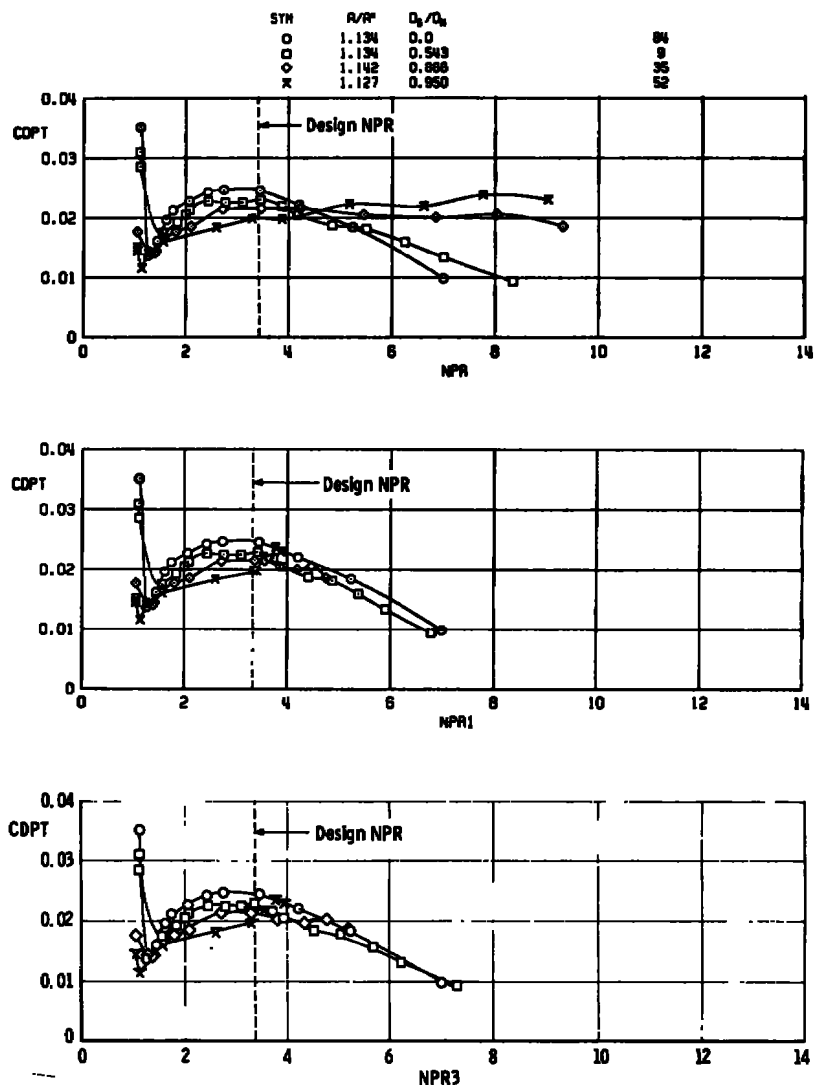
a. $M_\infty = 0.6$

Figure 32. Correlation of sting size effects on afterbody drag, $A/A^* \approx 1.13$.
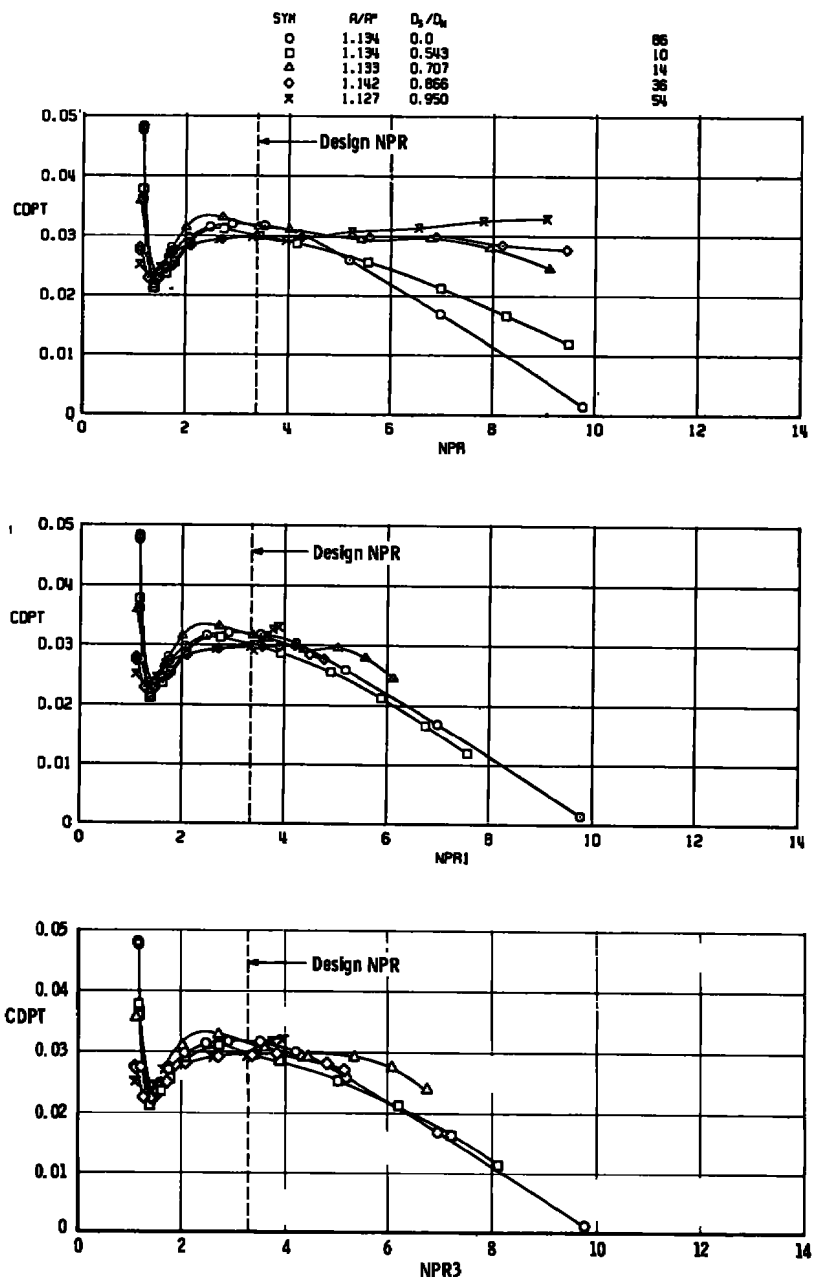
b. $M_\infty = 0.9$
Figure 32. Continued.
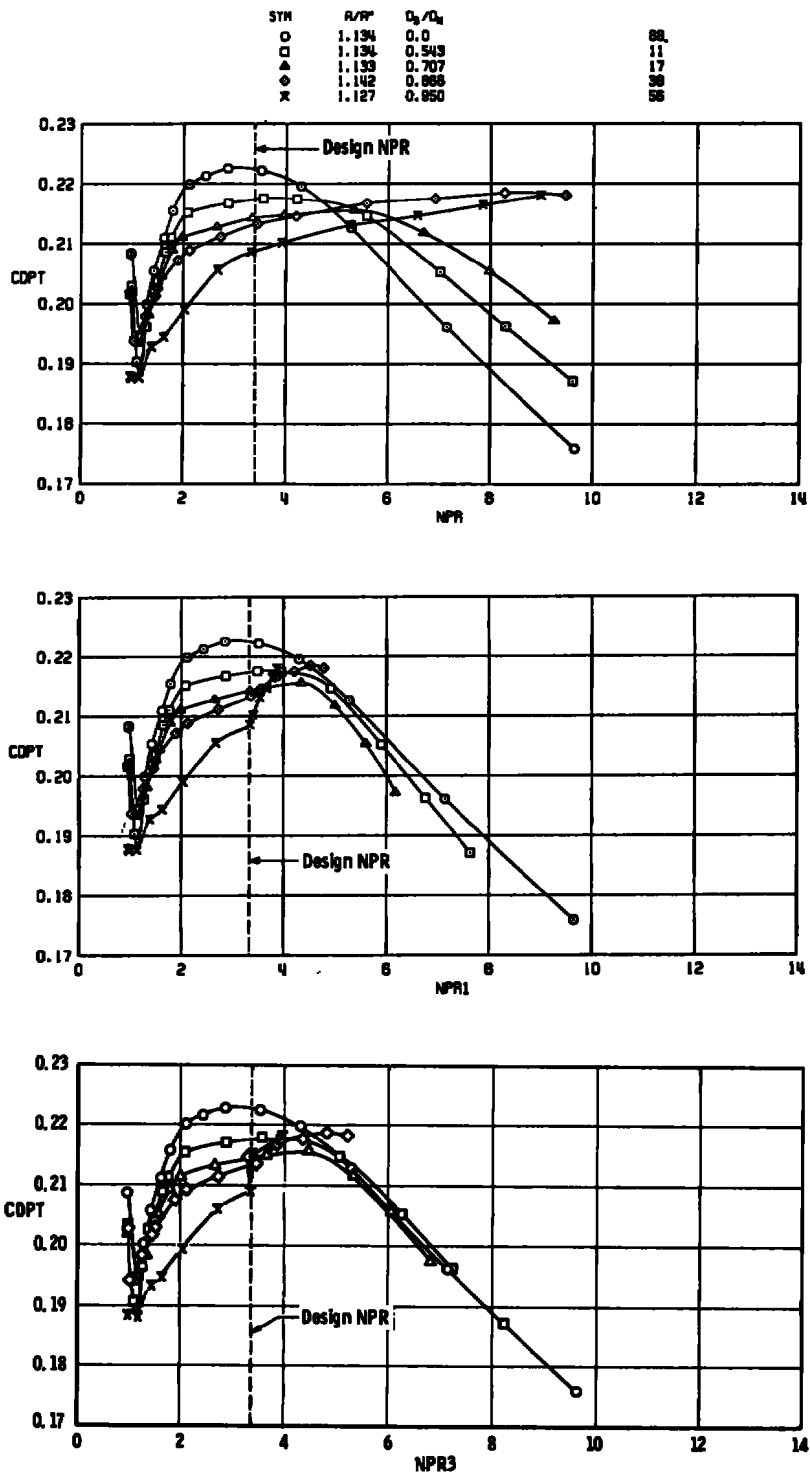
c. $M_\infty = 1.2$

Figure 32. Concluded.

SYM	A/A*	D_s/D_N	
O	1.221	0.0	92
△	1.220	0.706	69

|◄─── Design NPR

|◄─── Design NPR
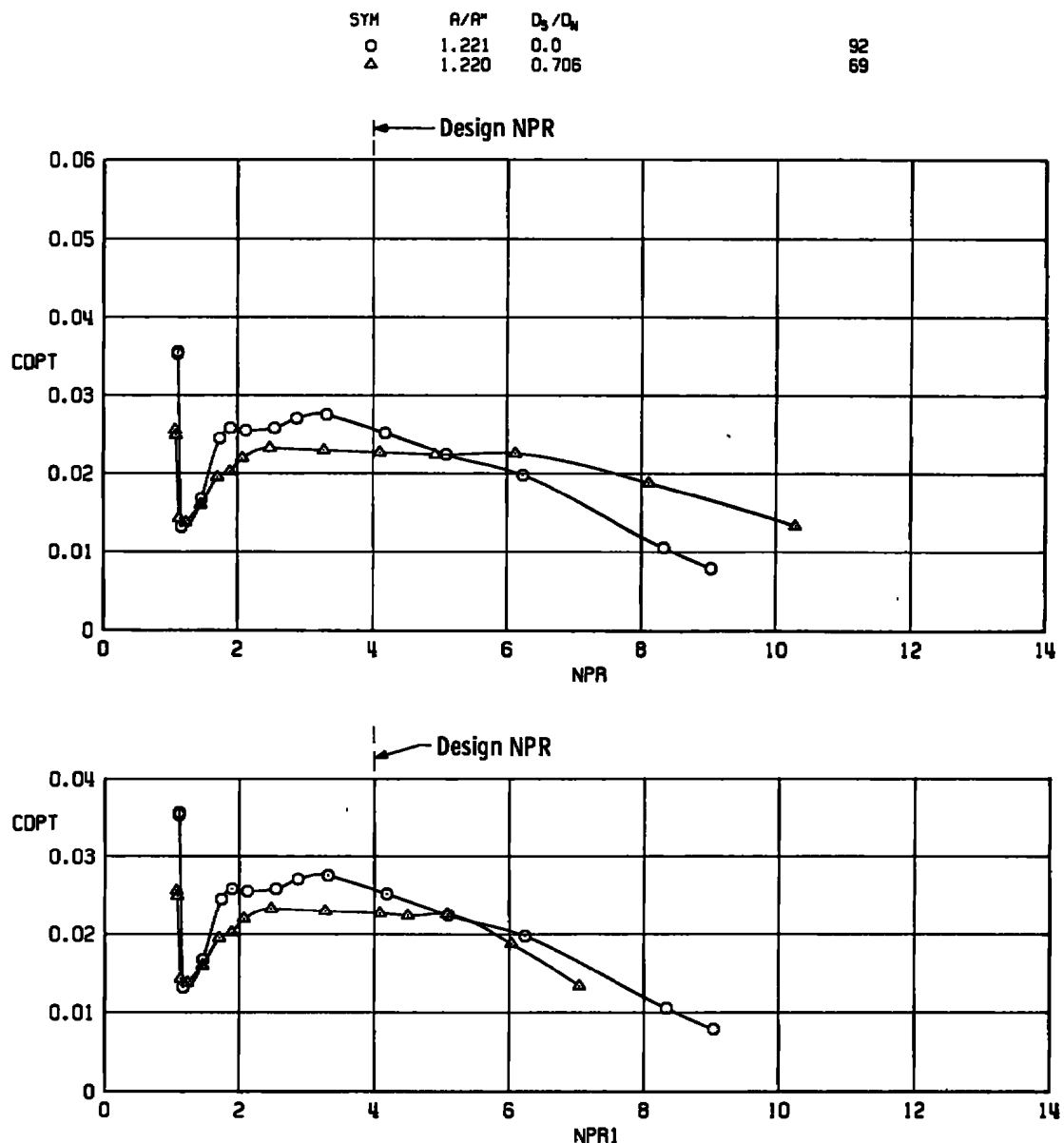
a. $M_\infty = 0.6$

Figure 33. Correlation of Sting Size Effects on Afterbody Drag, A/A* ≈ 1.22.
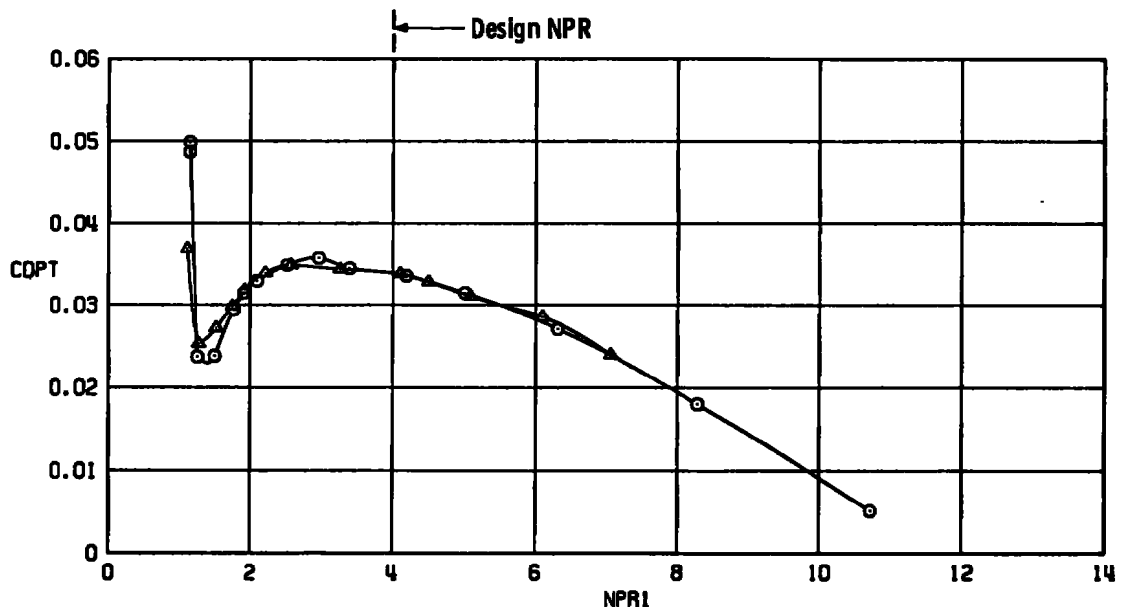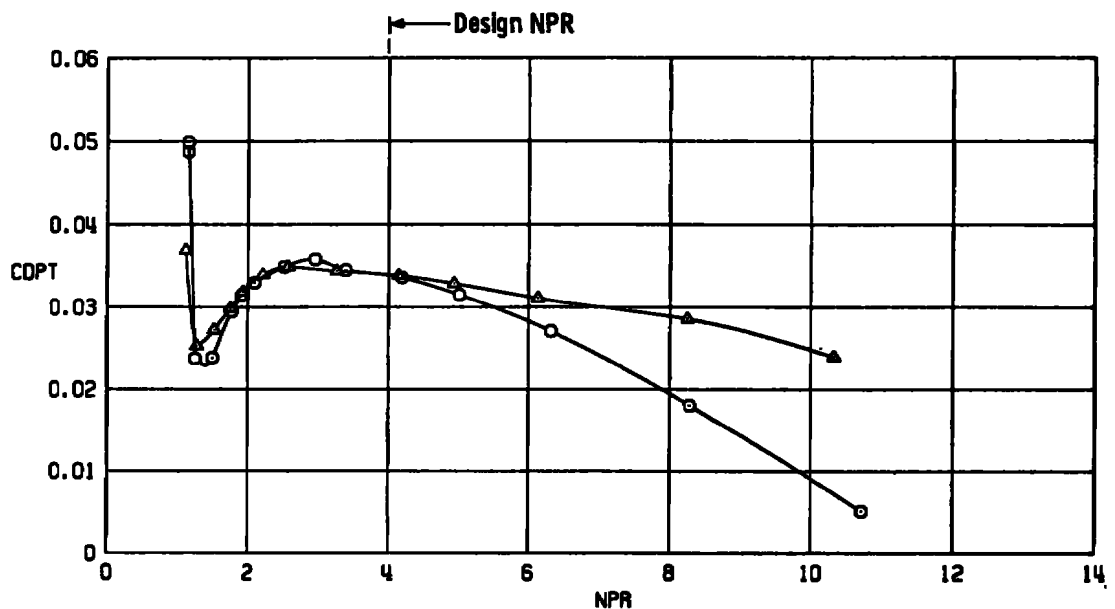
b. $M_\infty = 0.9$
Figure 33. Continued.
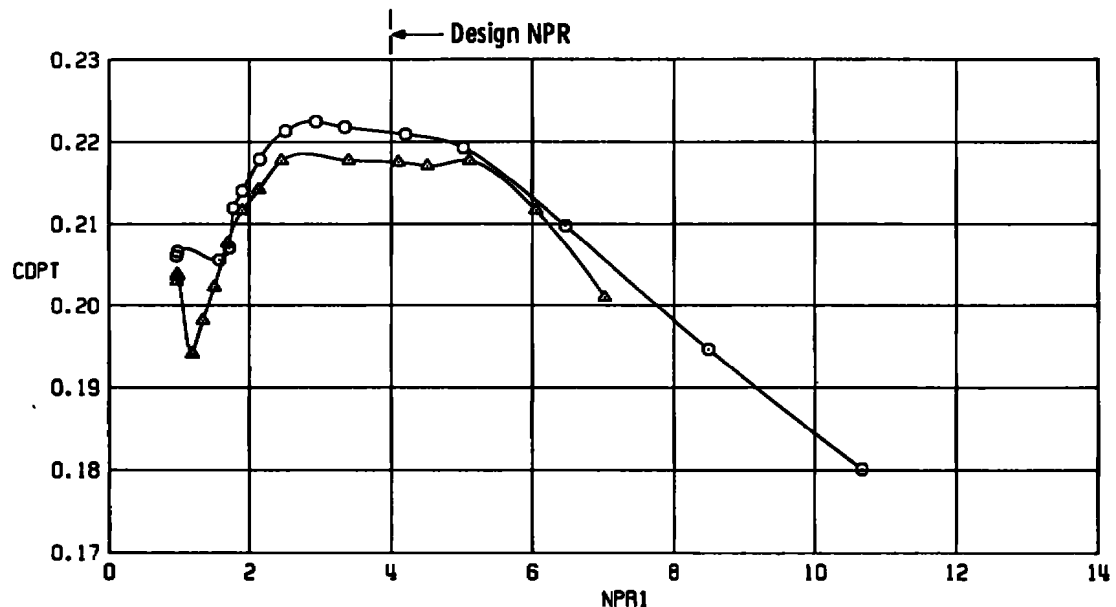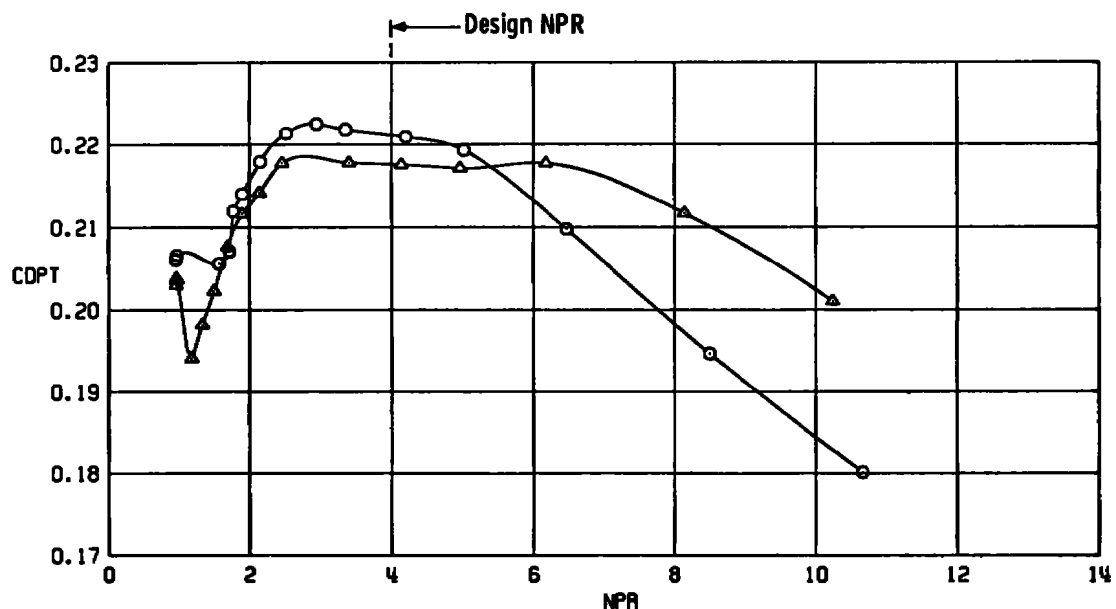
c. $M_\infty = 1.2$
Figure 33. Concluded.

88
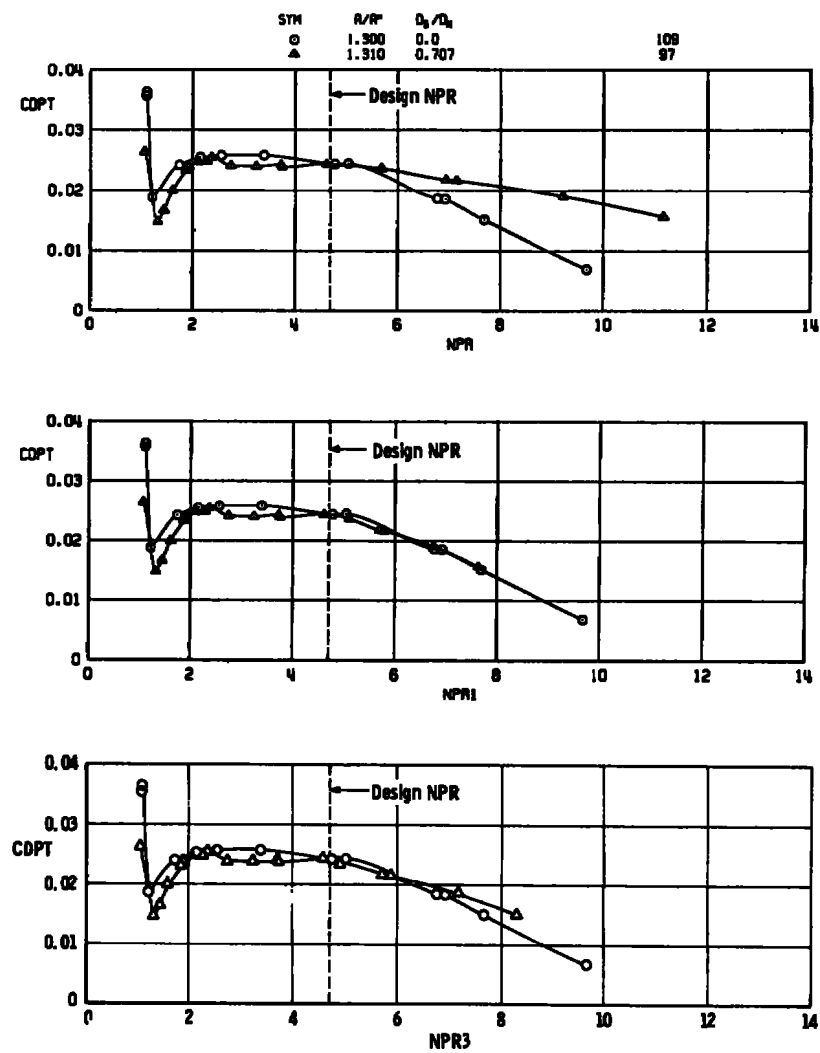
a. $M_\infty = 0.6$

Figure 34. Correlation of sting size effects on afterbody drag,
$A/A^* \approx 1.31$.

SYM	A/A*	Q_g/Q_M	
O	1.300	0.0	111
▲	1.310	0.707	98
◇	1.307	0.866	131
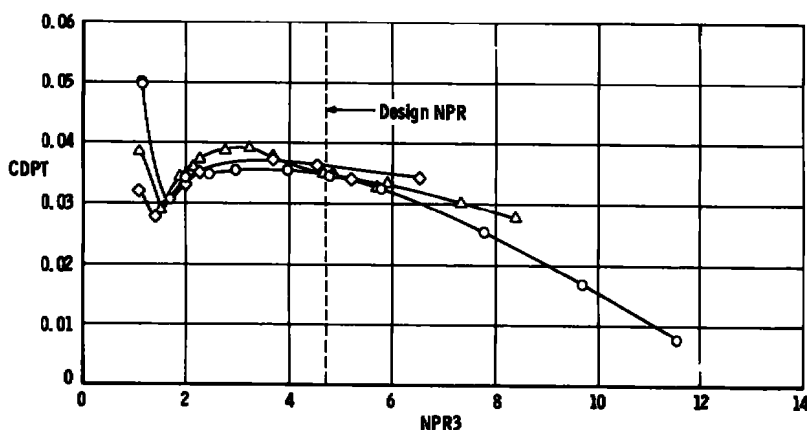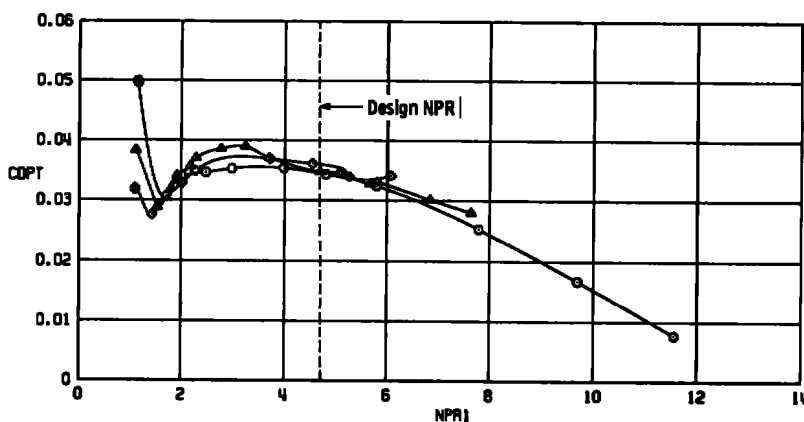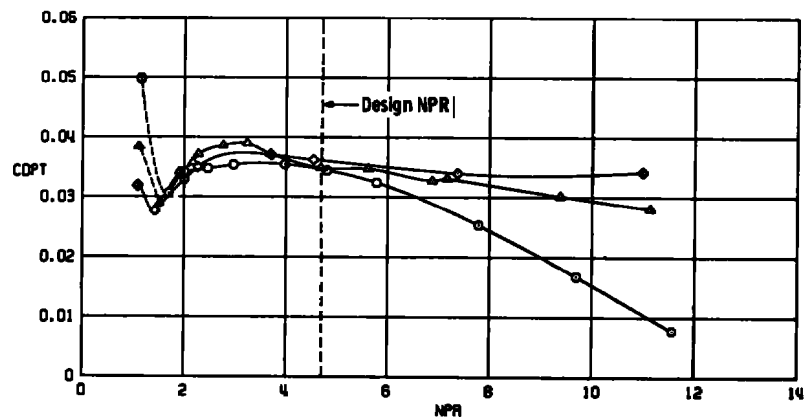
b. $M_\infty = 0.9$

Figure 34. Continued.

90
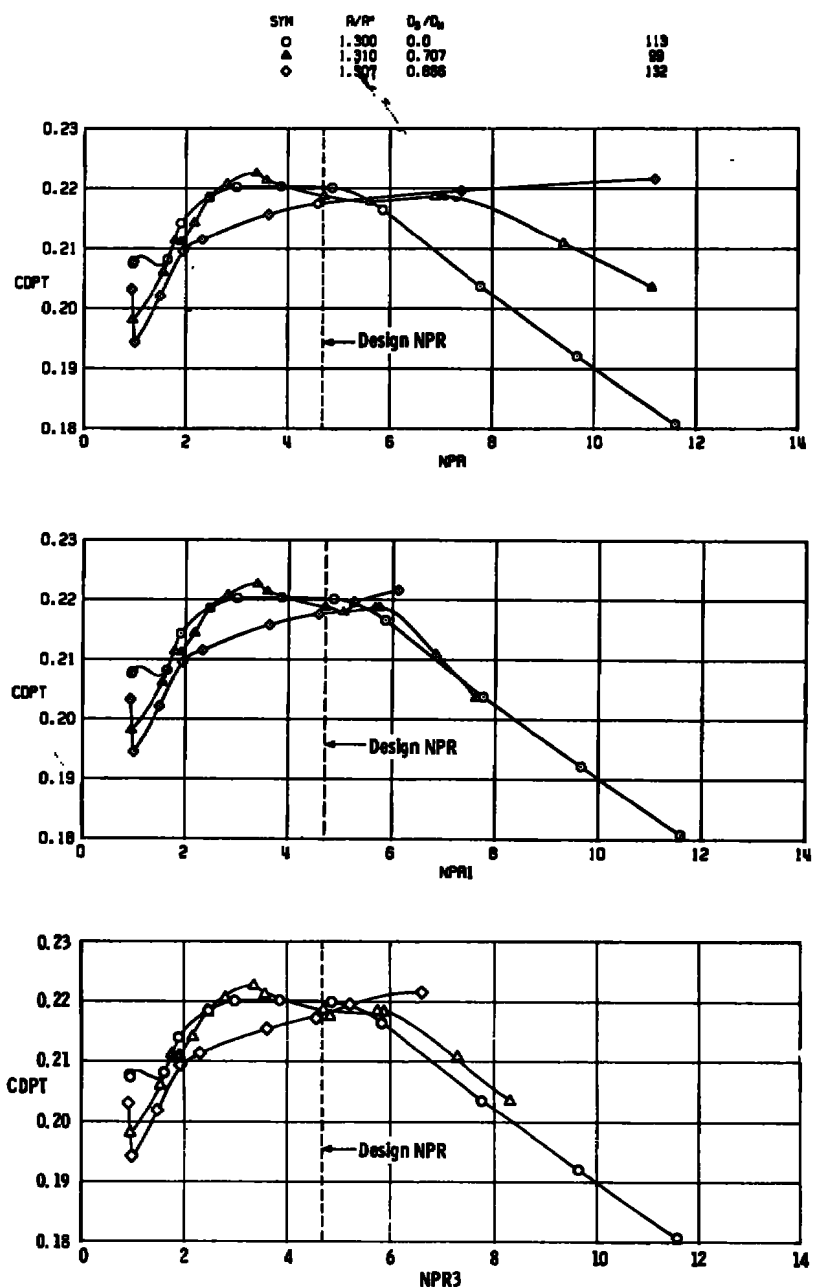
c. $M_\infty = 1.2$
Figure 34. Concluded.
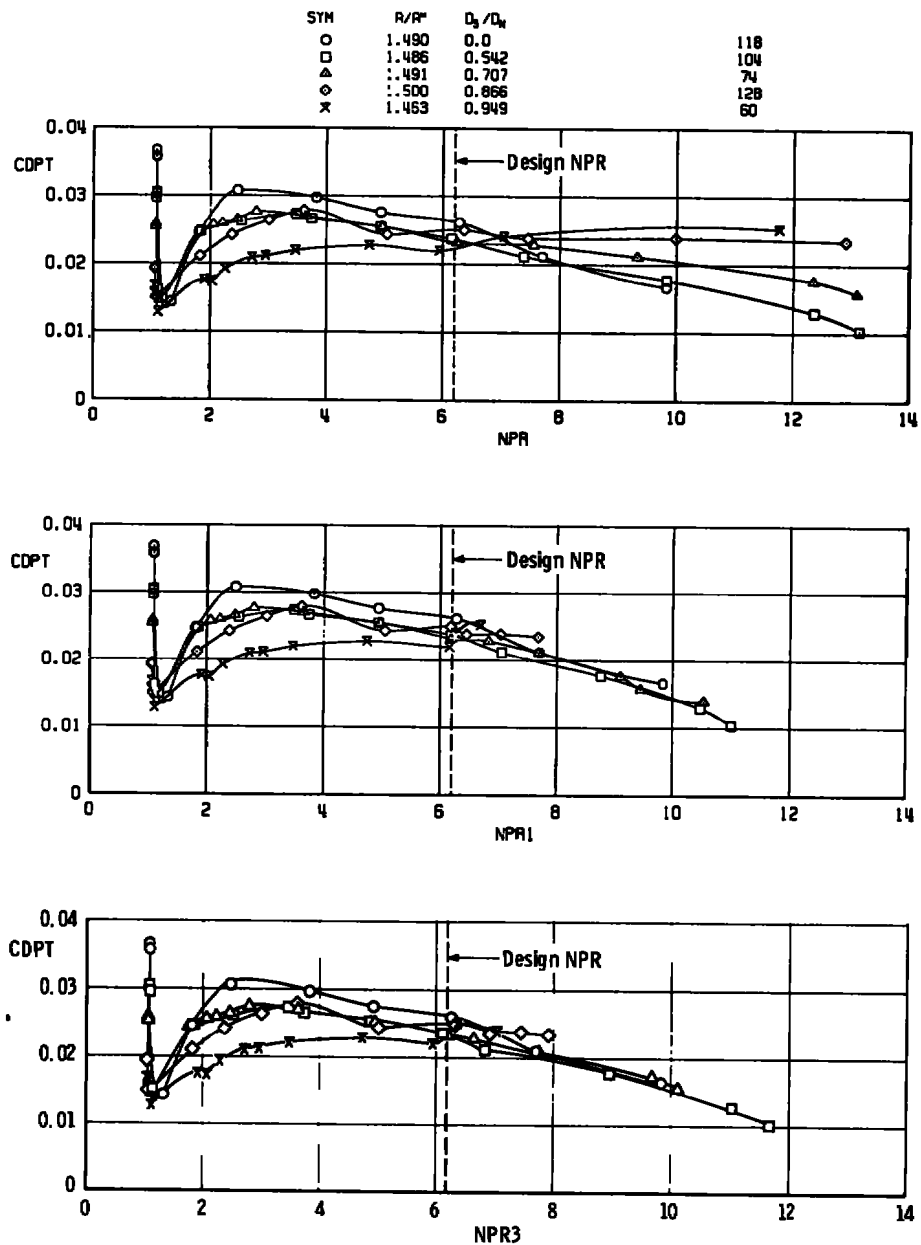
a. $M_\infty = 0.6$

Figure 35. Correlation of sting size effects on afterbody drag, $A/A^* \approx 1.49$.
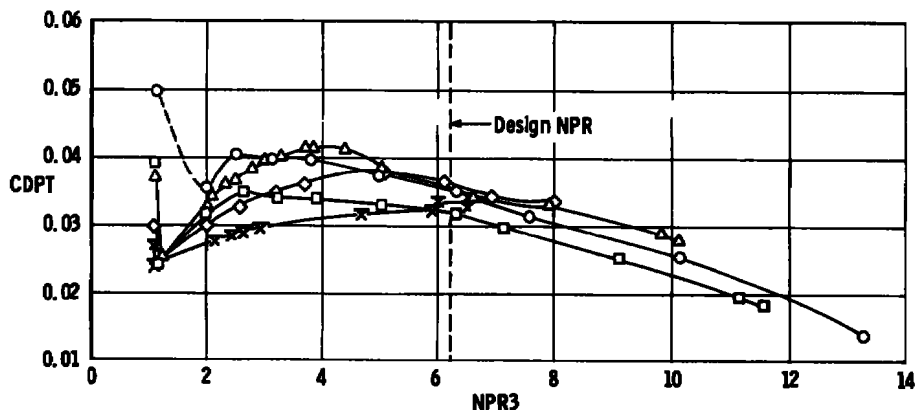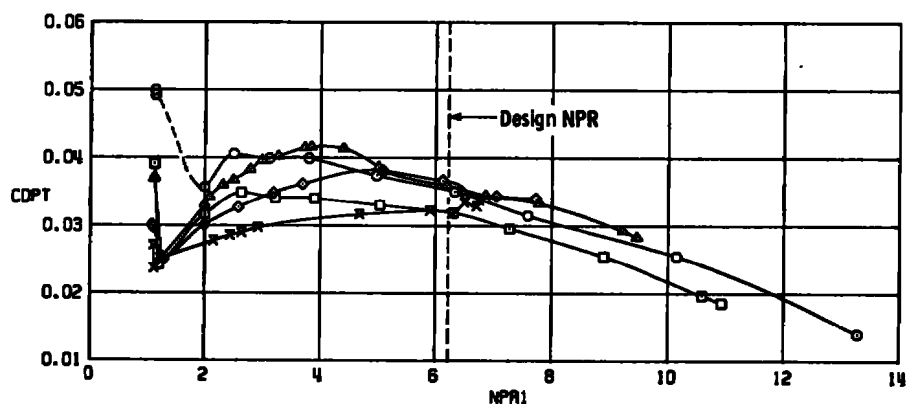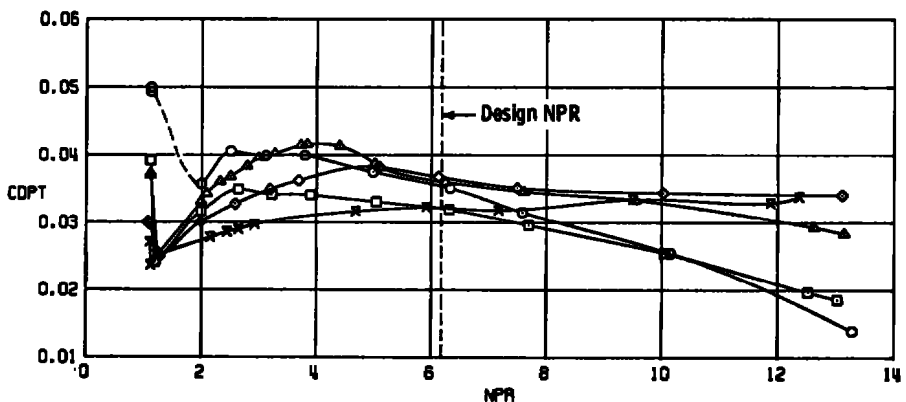
b. M∞ = 0.9
Figure 35. Continued.

SYM	A/A*	D_3/D_N	
○	1.490	0.0	122
□	1.486	0.542	106
△	1.491	0.707	78
◇	1.500	0.866	127
✕	1.463	0.949	64
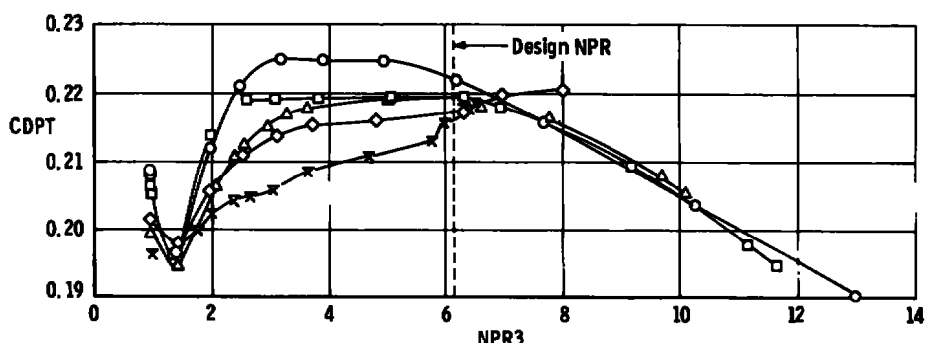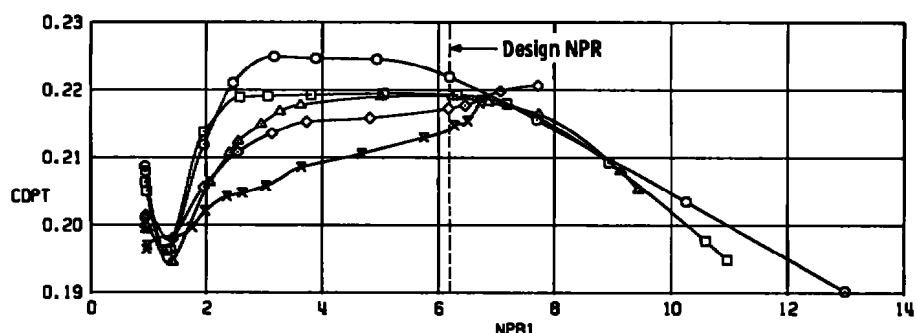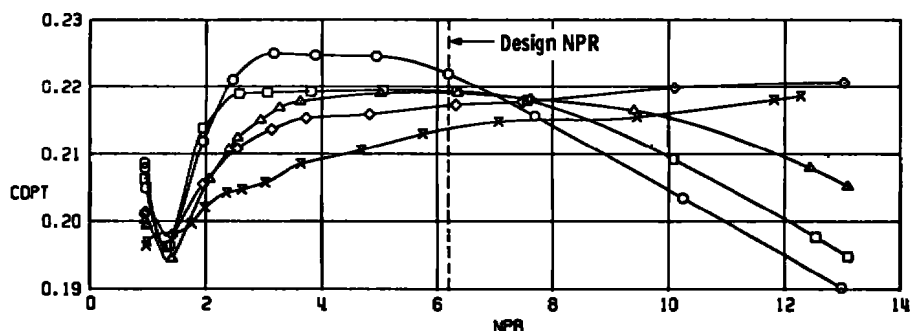
c. $M_\infty = 1.2$

Figure 35. Concluded.
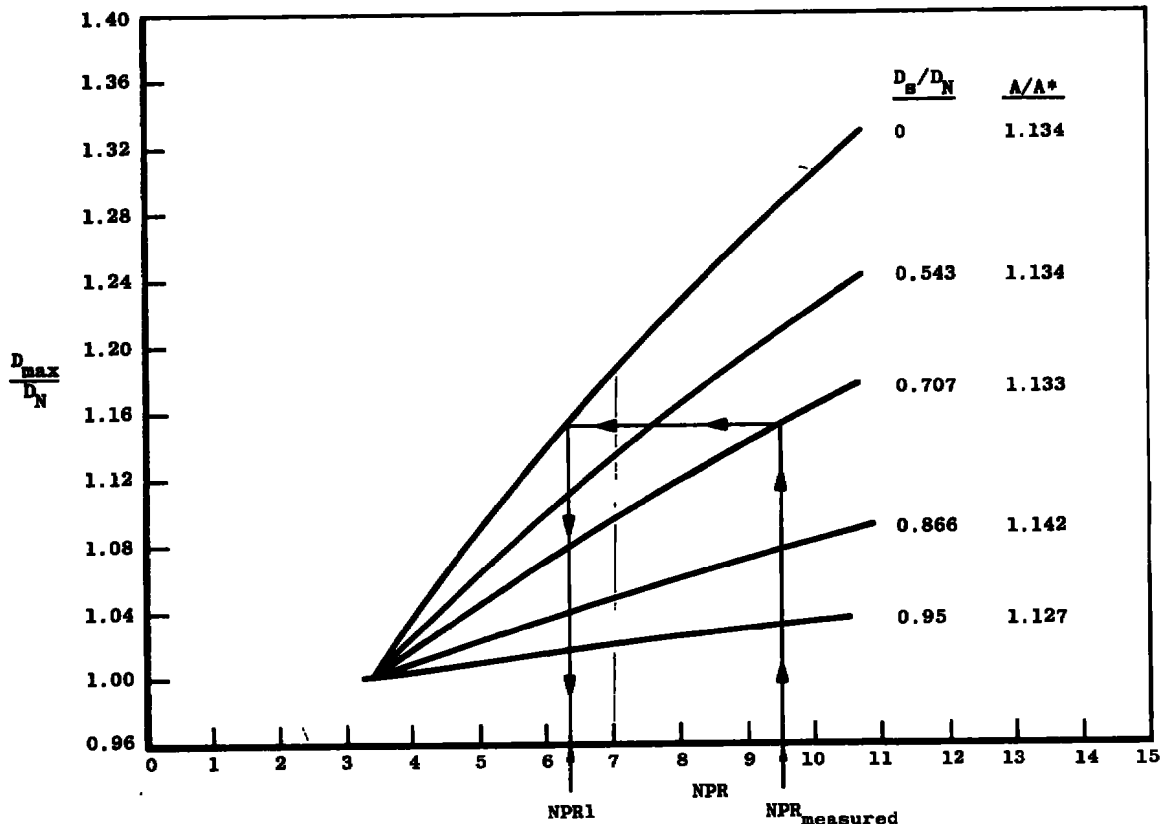
a. One-dimensional flow (NPR1)
Figure 36. Illustration of procedure for determining the
correlation pressure ratios.
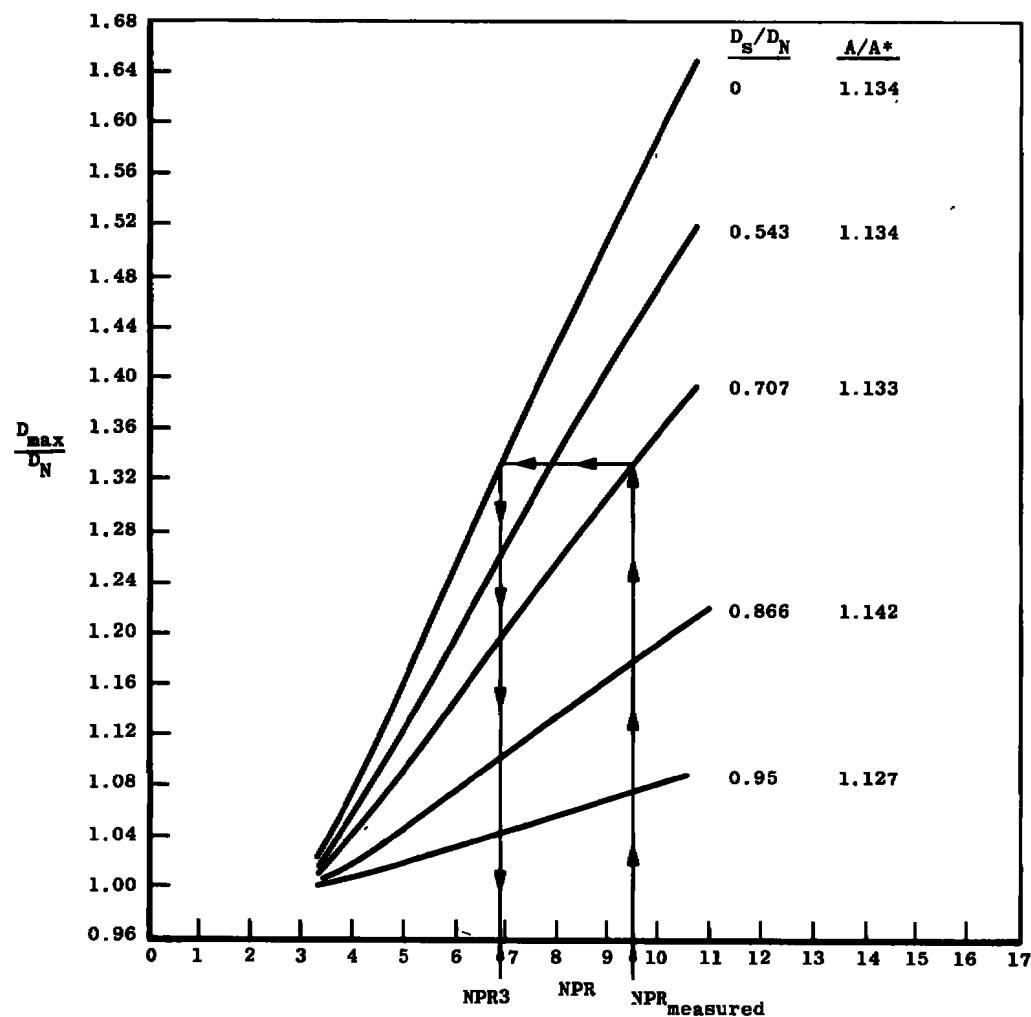
b. Method of characteristics (NPR3)
Figure 36. Concluded.

$$\Delta CDPT = (CDPT_{ann\ jet} - CDPT_{con\ jet})$$

| Sym	D_s/D_N
□	0.543
△	0.707
◇	0.866
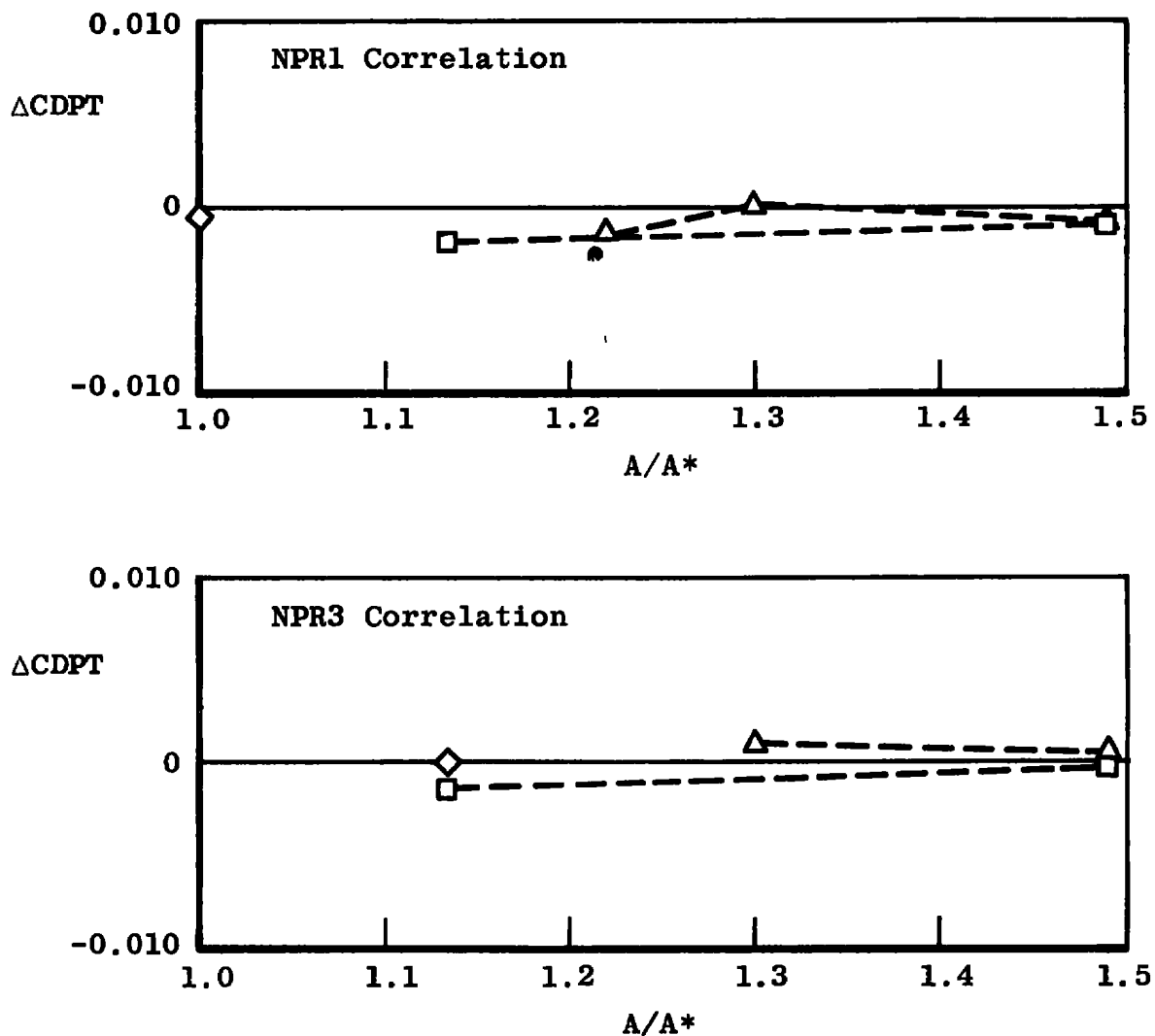
a. $M_\infty = 0.6$

Figure 37. Comparison of correlation methods at NSPR = 1.5.

$$\triangle CDPT = (CDPT_{ann\ jet} - CDPT_{con\ jet})$$

| Sym	D_S/D_N
□	0.543
△	0.707
◇	0.866
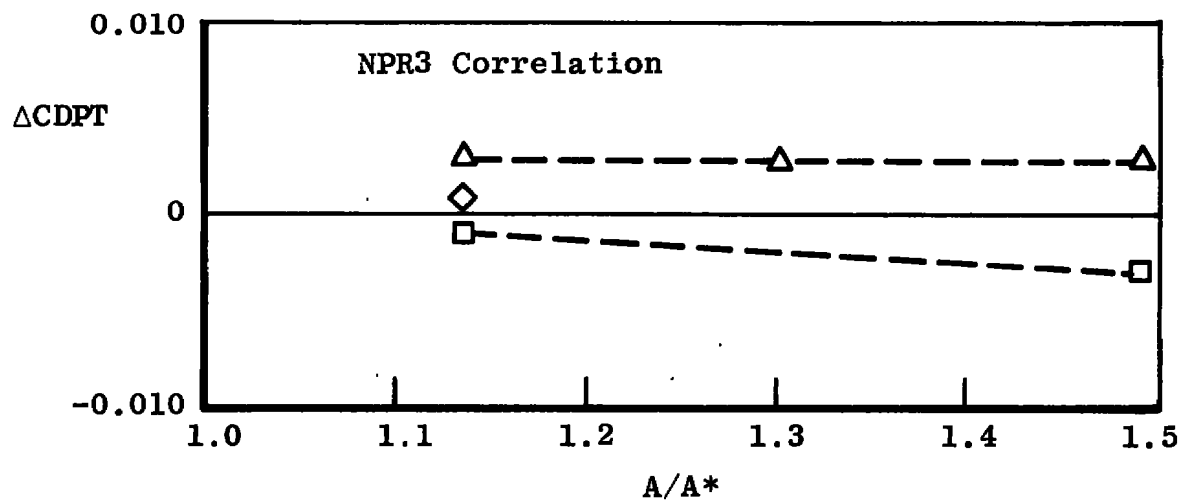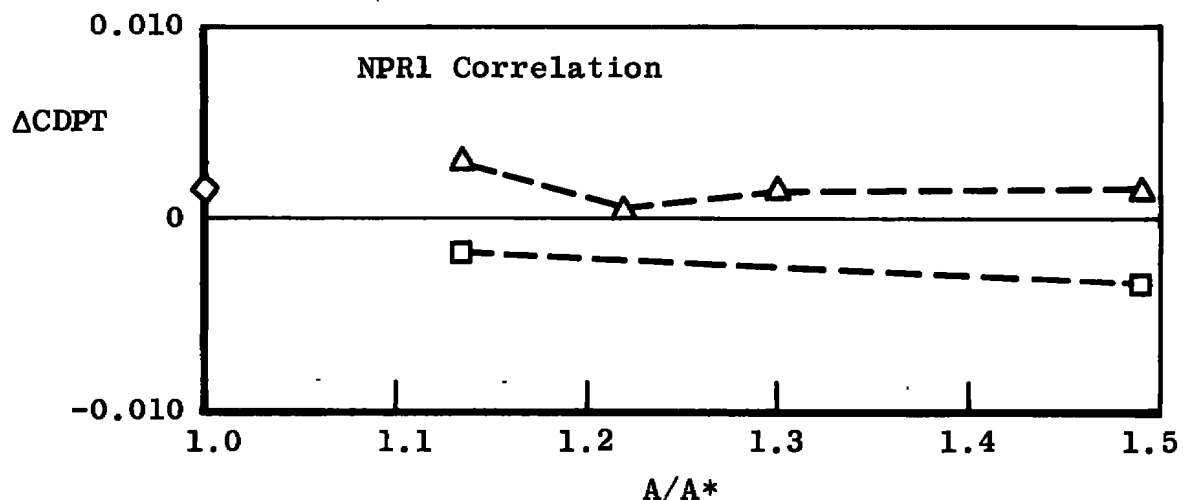
b. $M_\infty = 0.9$

Figure 37. Continued.

$$\Delta CDPT = (CDPT_{ann\ jet} - CDPT_{con\ jet})$$

Sym	D_s/D_N
□	0.543
△	0.707
◇	0.866
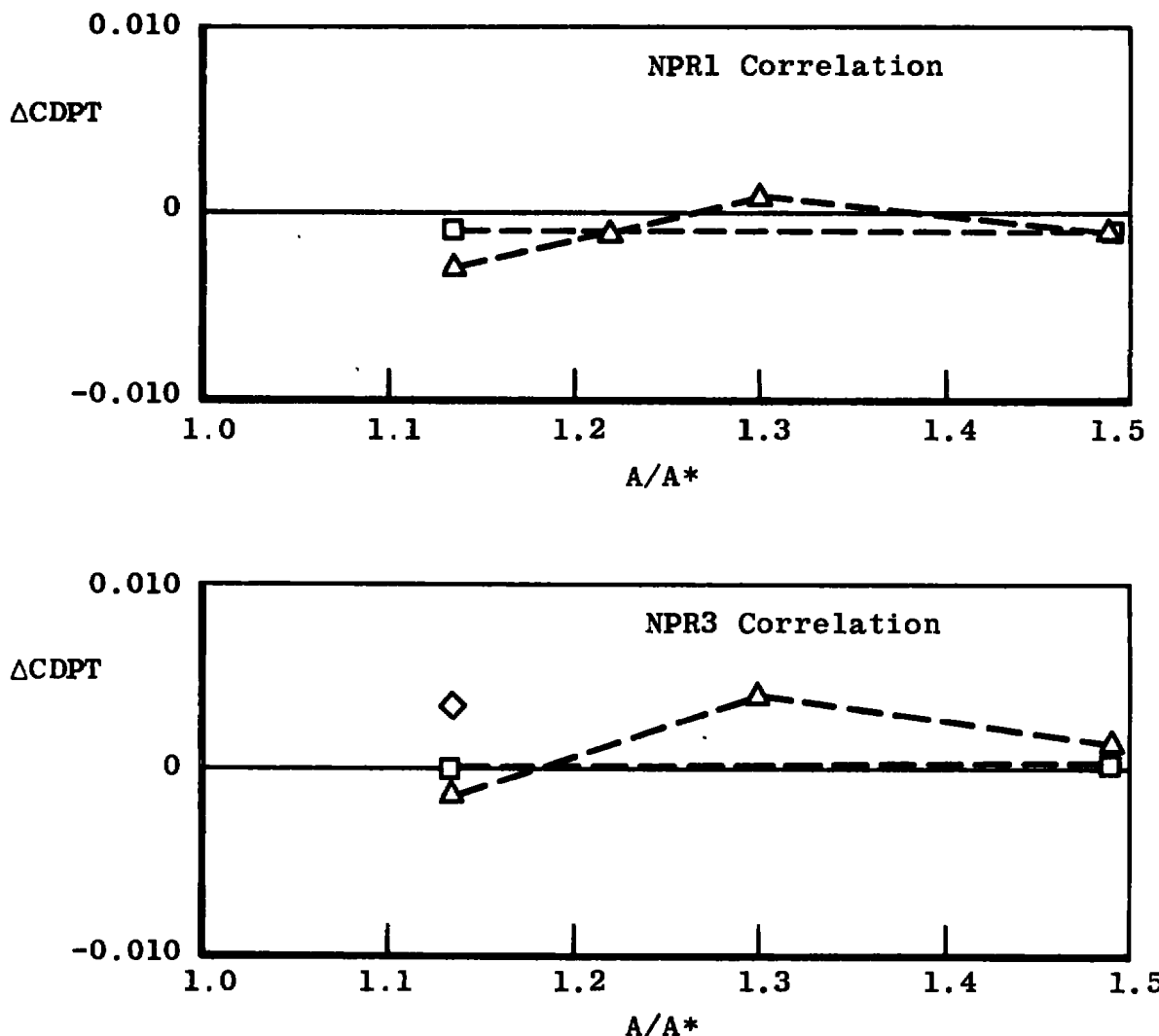
c. $M_\infty = 1.2$

Figure 37. Concluded.

$$\Delta CDPT = (CDPT_{ann\ jet} - CDPT_{con\ jet})$$

| Sym	D_s/D_N
□	0.543
△	0.707
◇	0.866
✗	0.950
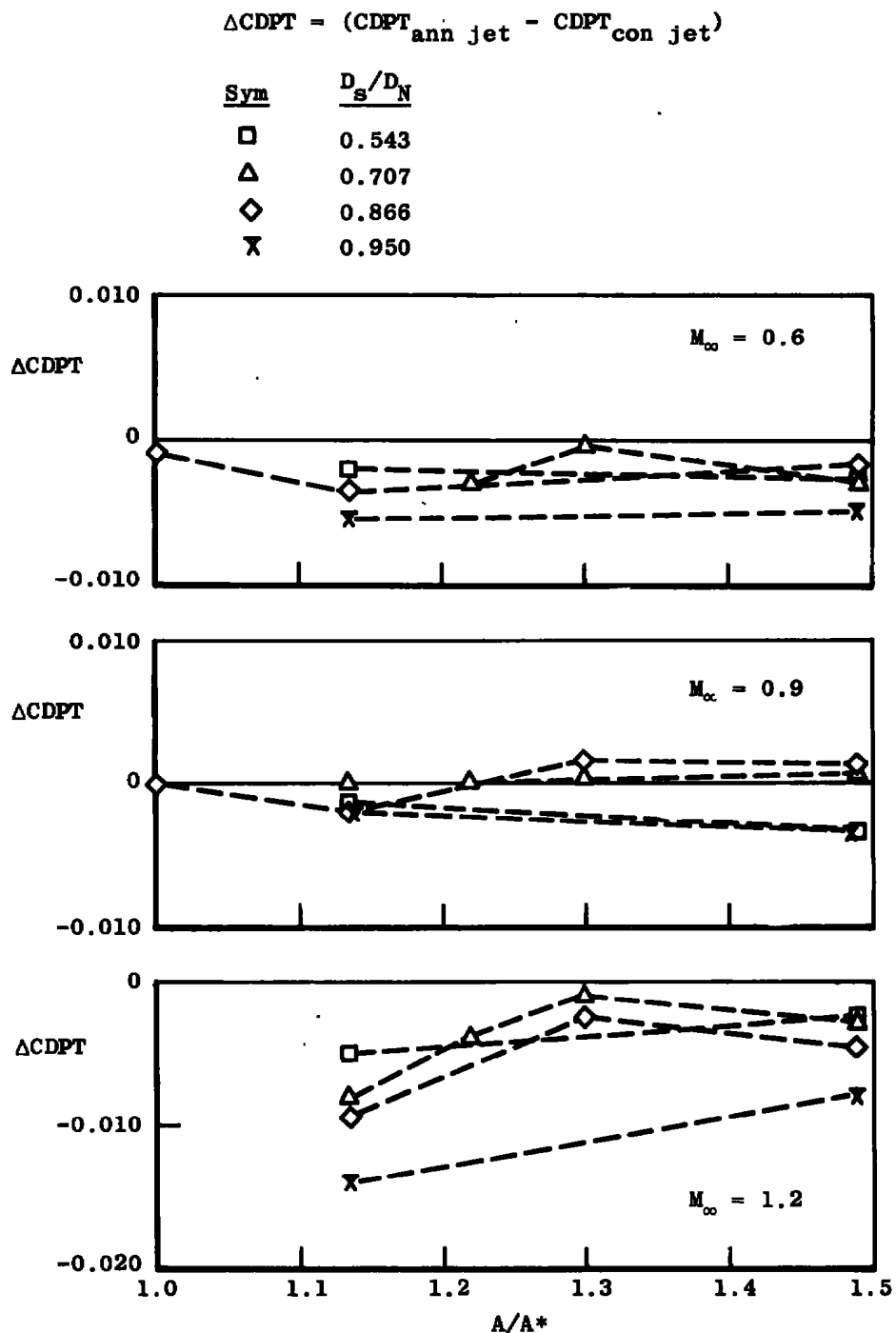
Figure 38. Comparison of drag coefficient increments between annular and conventional jet configurations at nozzle design pressure ratio (NSPR = 1.0).

| SYM	A/AF	Dₛ/Dₙ	
⊙	1.000	0.0	45
□	1.134	0.0	84
▲	1.221	0.0	92
◇	1.300	0.0	109
✕	1.490	0.0	118
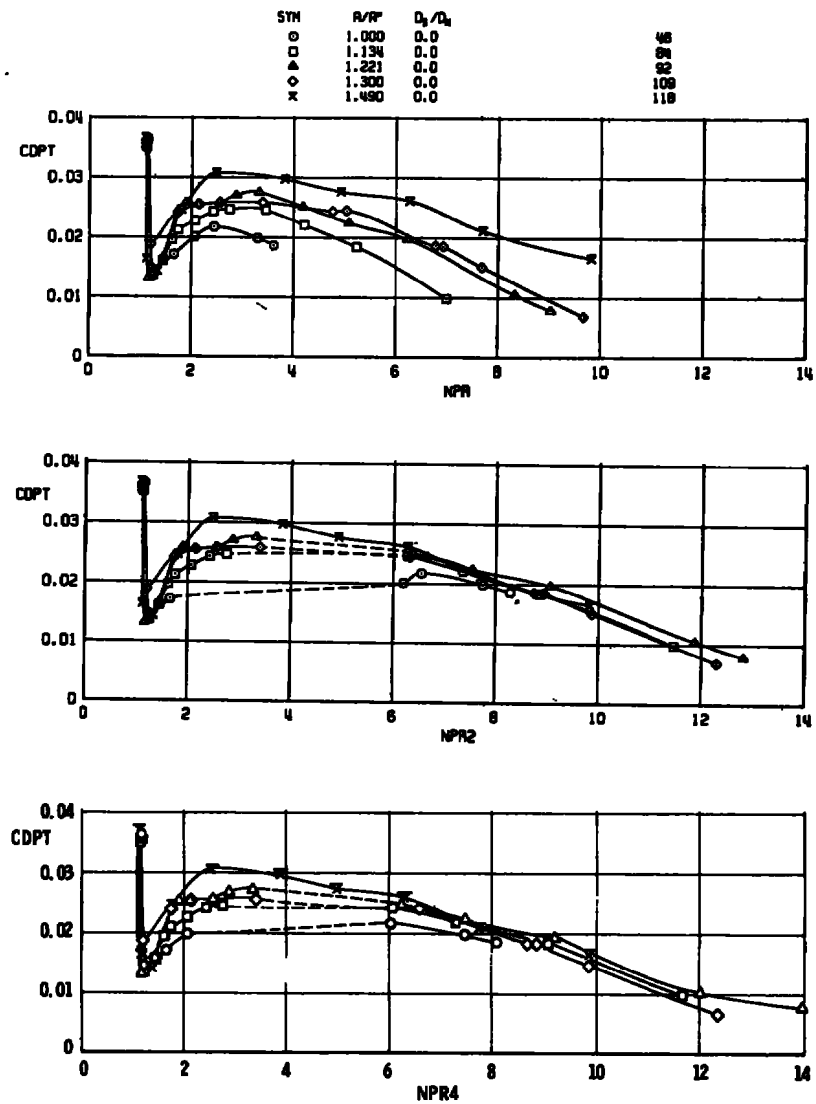
a. $M_\infty = 0.6$

Figure 39. Correlation of nozzle area ratio effects on afterbody drag, $D_s/D_N = 0$.
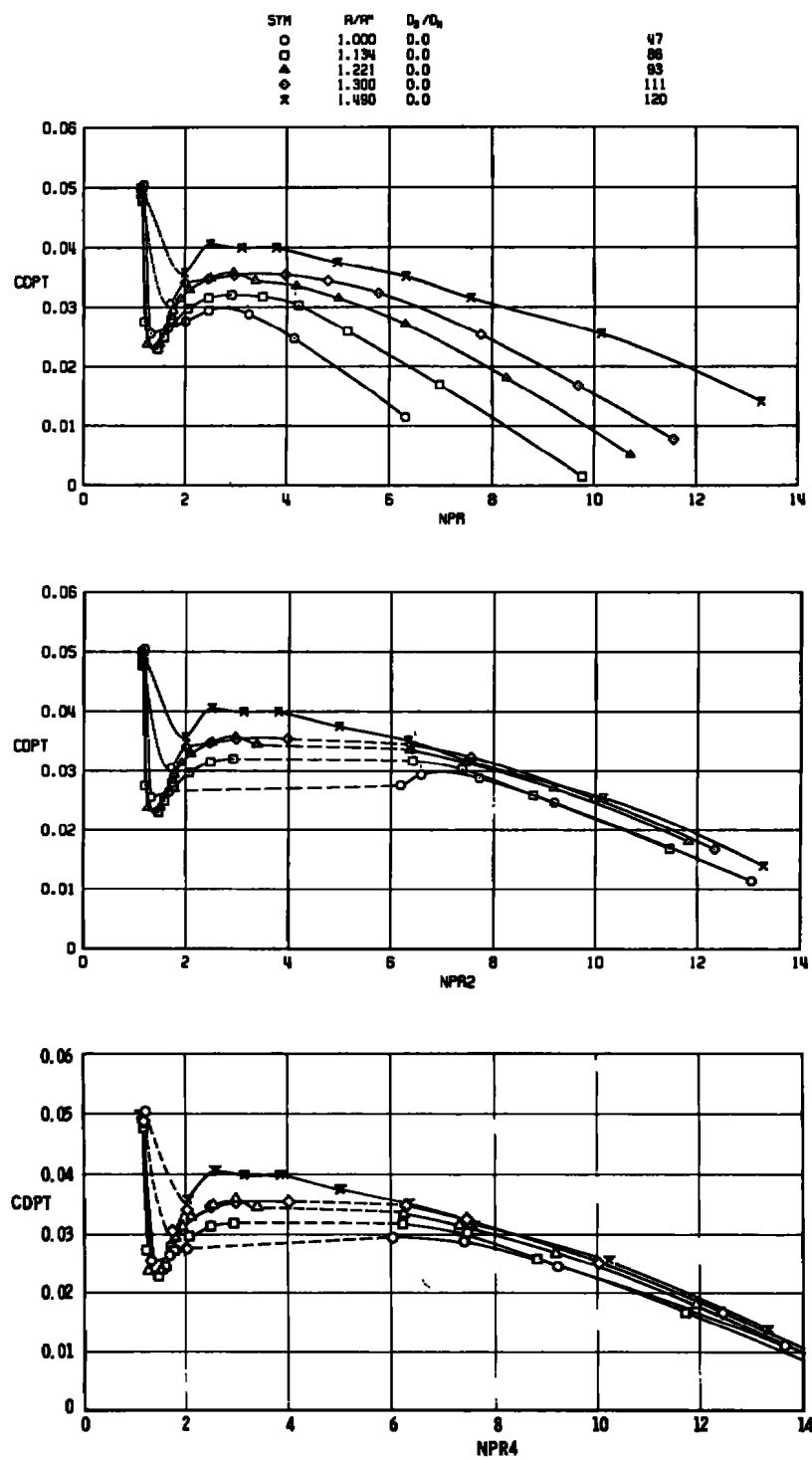
b. $M_\infty = 0.9$
Figure 39. Continued.
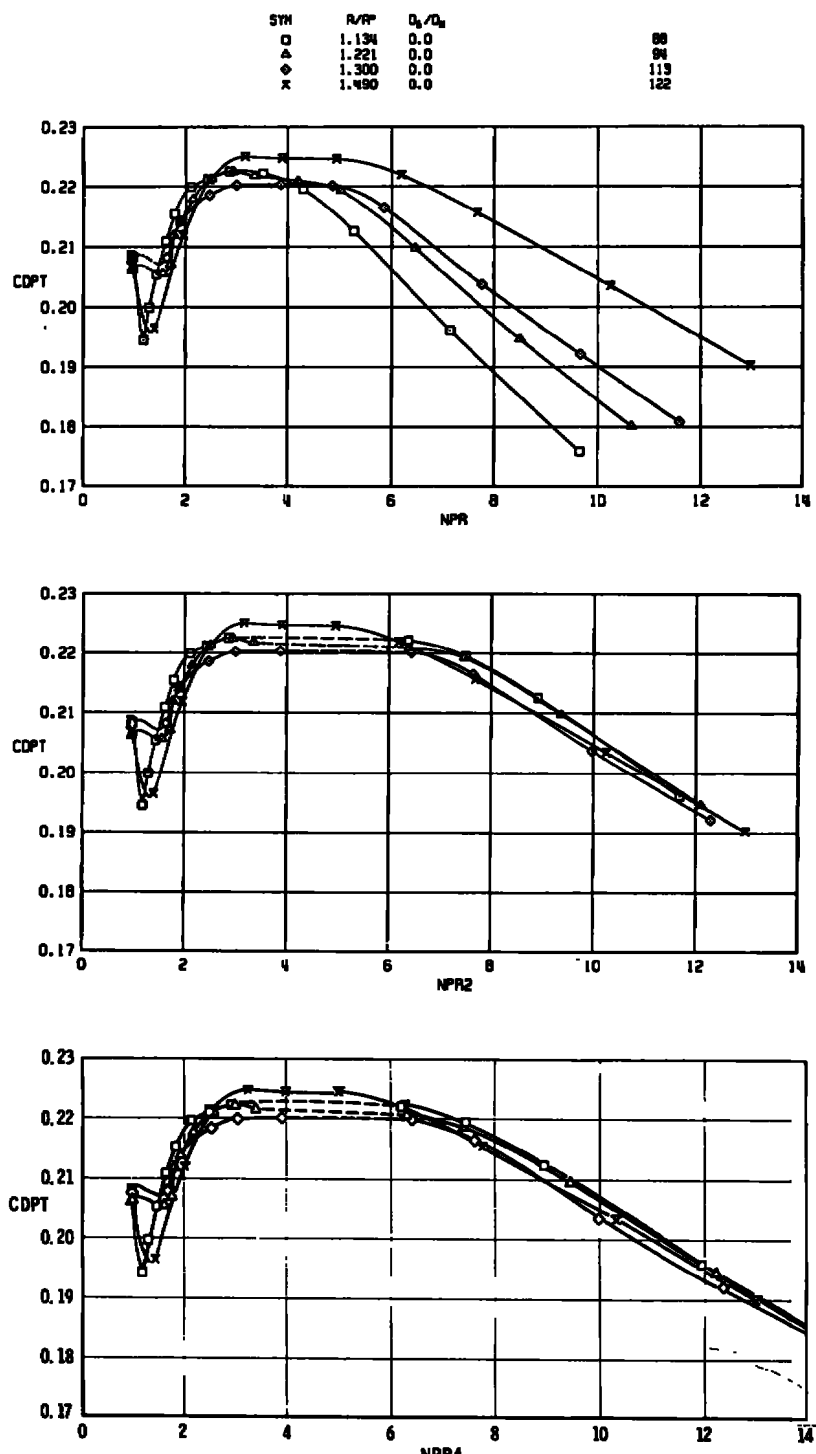
c. $M_\infty = 1.2$

Figure 39. Concluded.
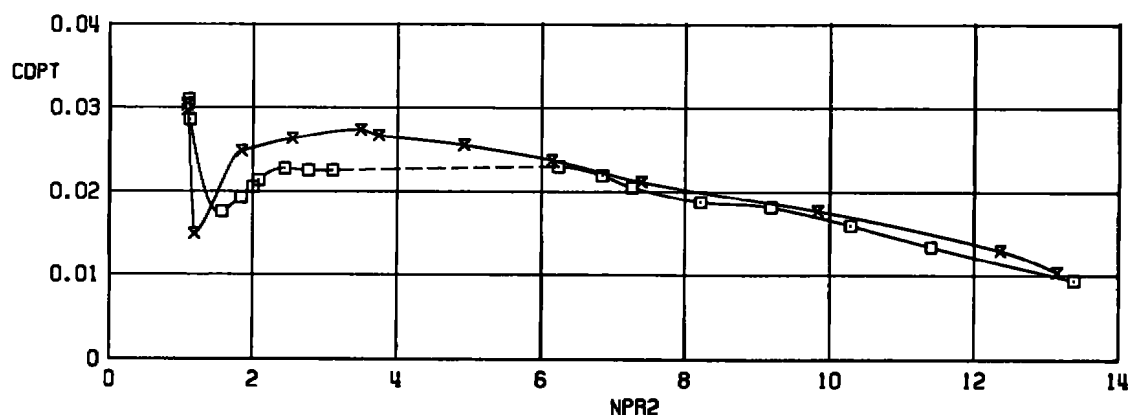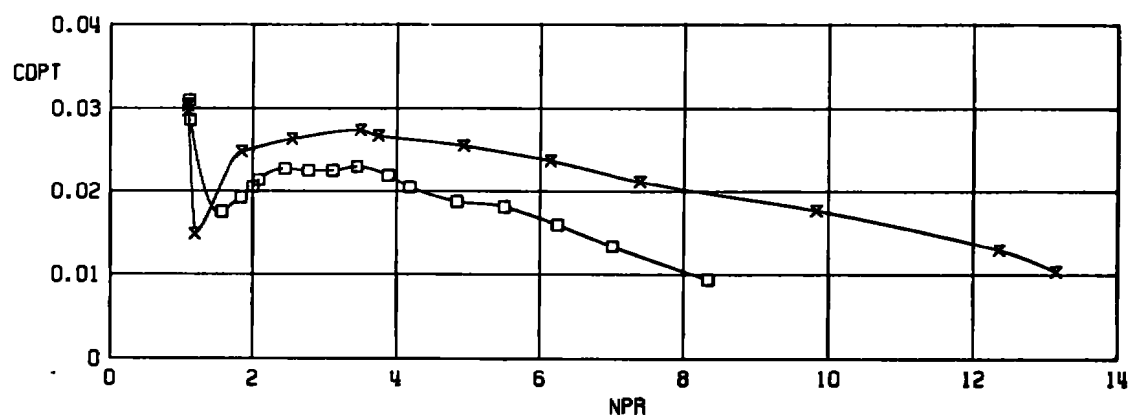
a. $M_\infty = 0.6$

Figure 40. Correlation of nozzle area ratio effects on afterbody drag, $D_s/D_N = 0.543$.

SYM	A/A*	D_S/D_N	
□	1.134	0.543	10
X	1.466	0.542	105
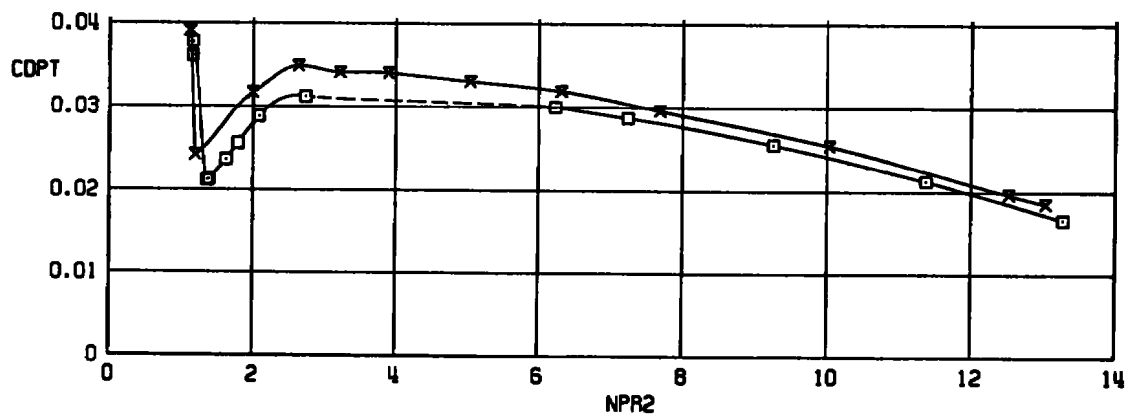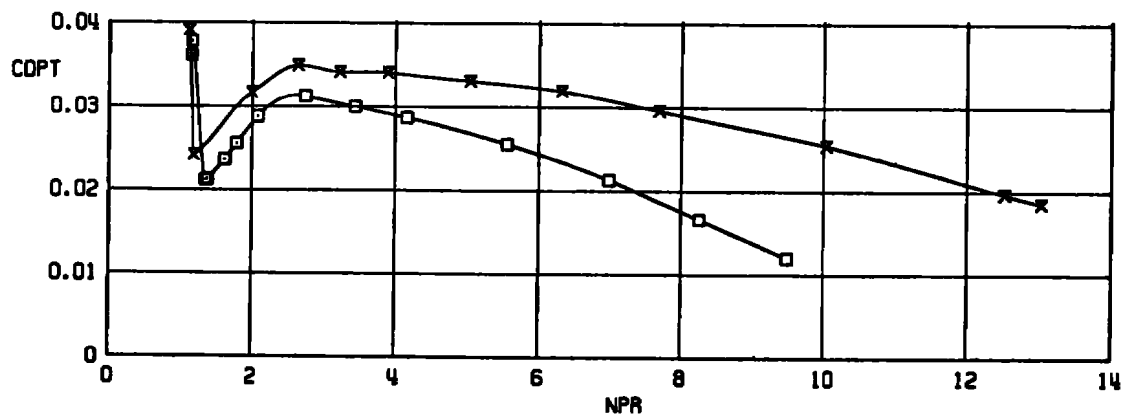
b. $M_\infty = 0.9$
Figure 40. Continued.

SYM	A/A^*	D_s/D_N	
□	1.134	0.543	11
x	1.486	0.542	106
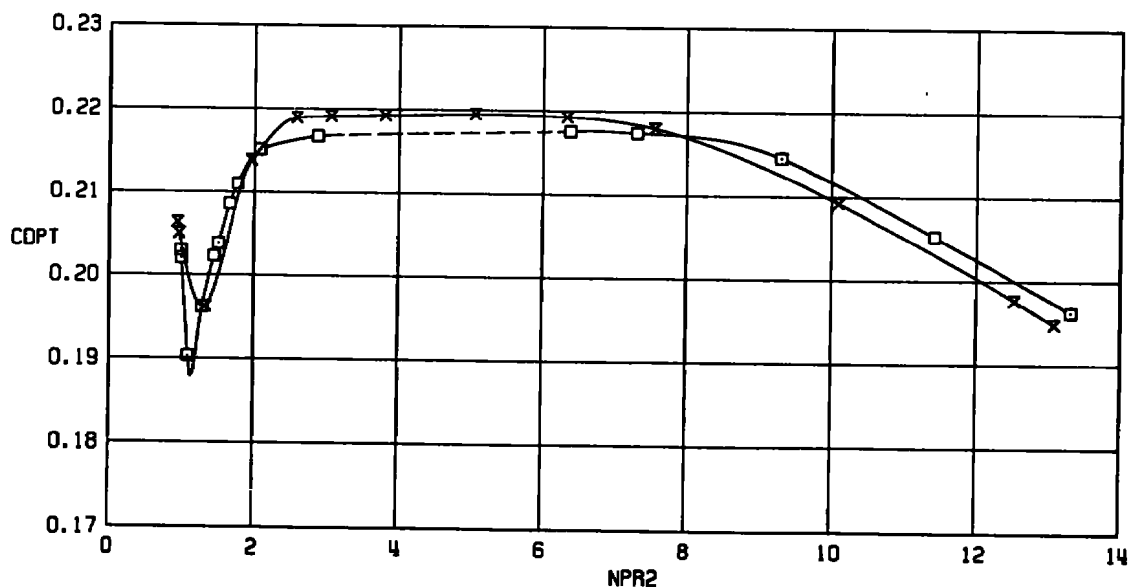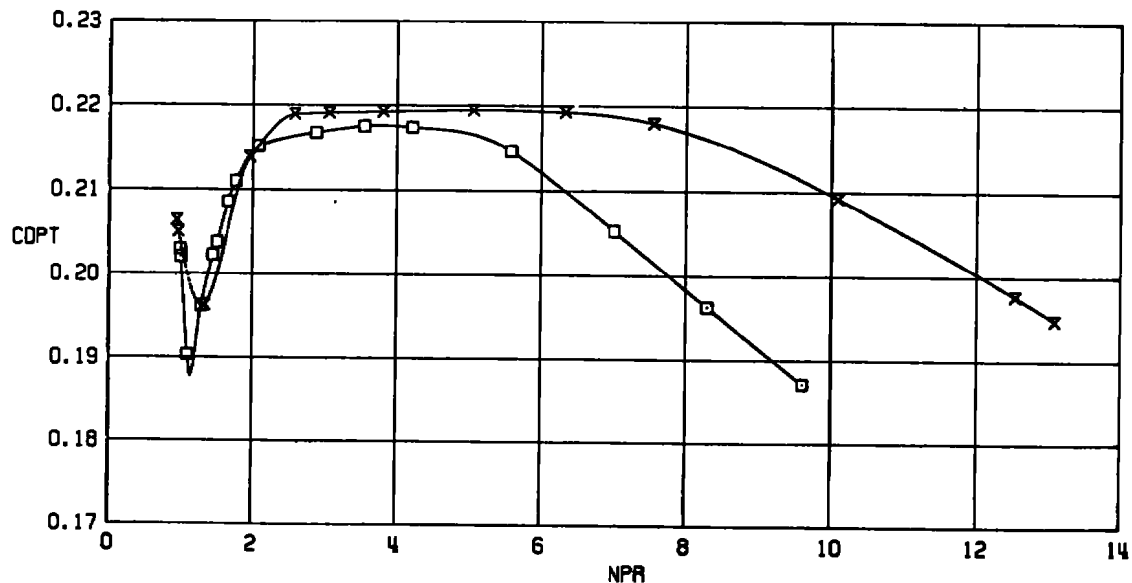
c. $M_\infty = 1.2$
Figure 40. Concluded.
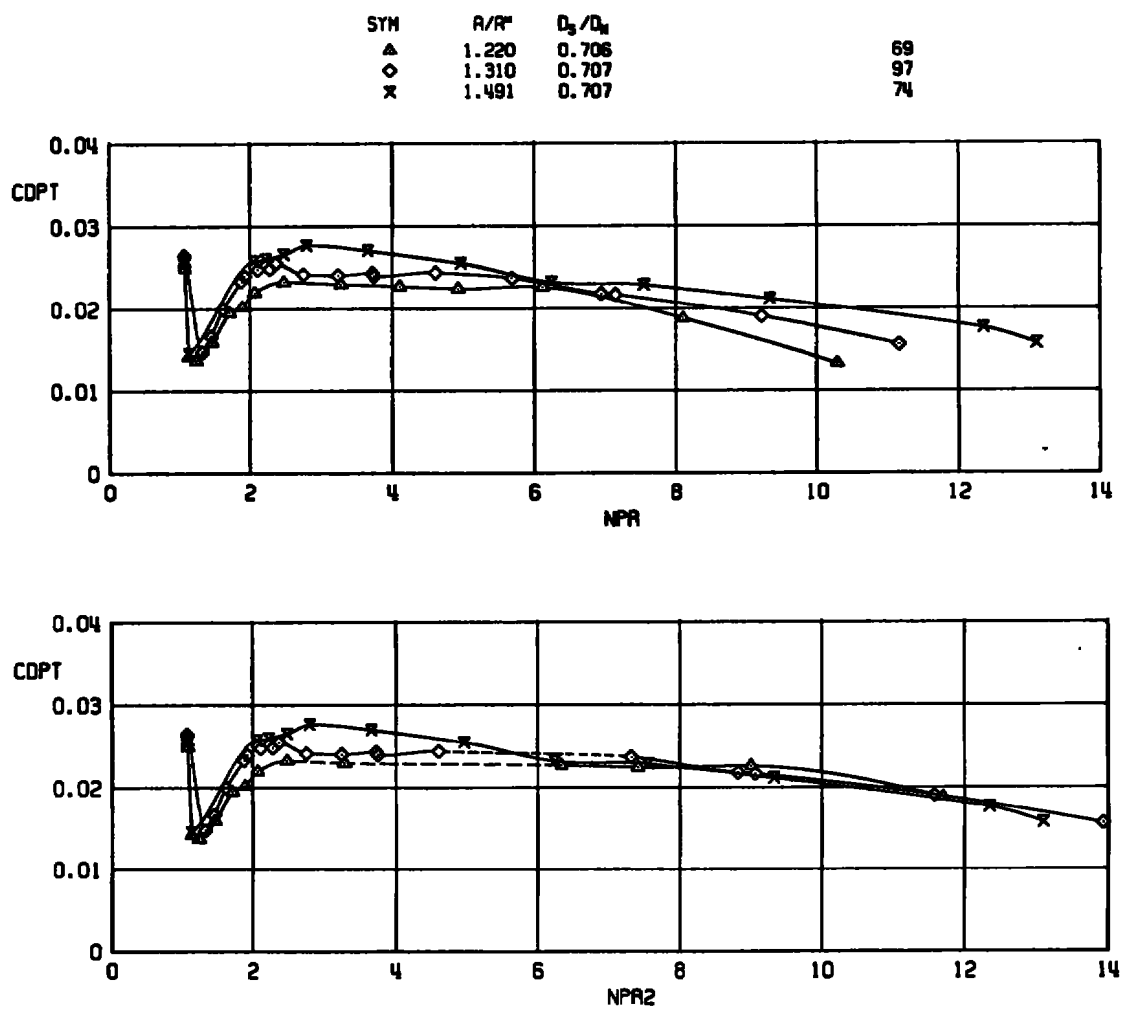
a. $M_\infty = 0.6$

Figure 41. Correlation of nozzle area ratio effects on afterbody
drag, $D_s/D_N = 0.707$.

| SYM	A/A*	D_S/D_M	
□	1.133	0.707	14
△	1.220	0.706	70
◇	1.310	0.707	98
✕	1.491	0.707	76
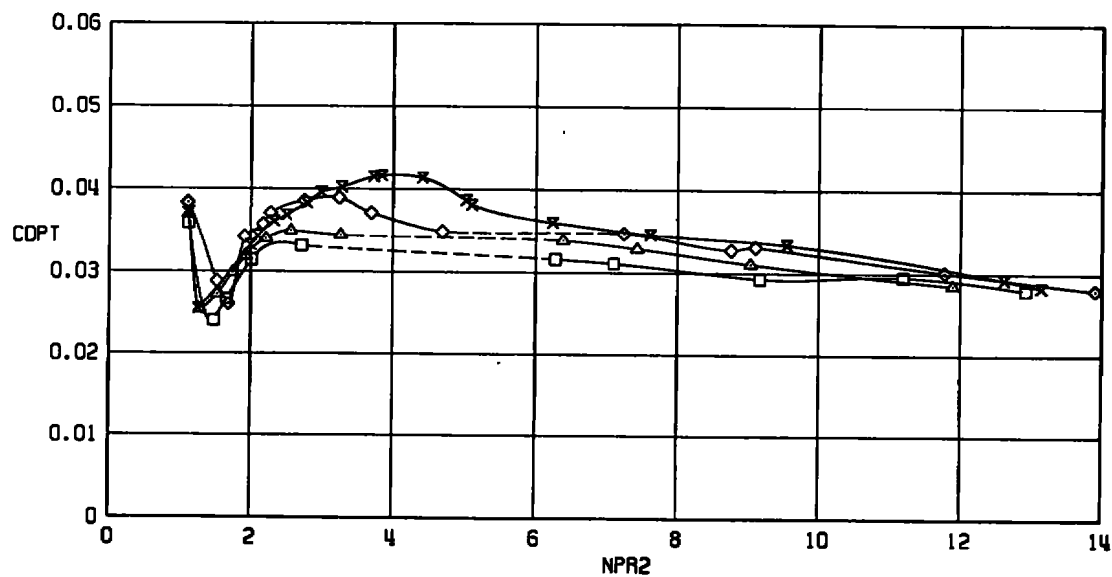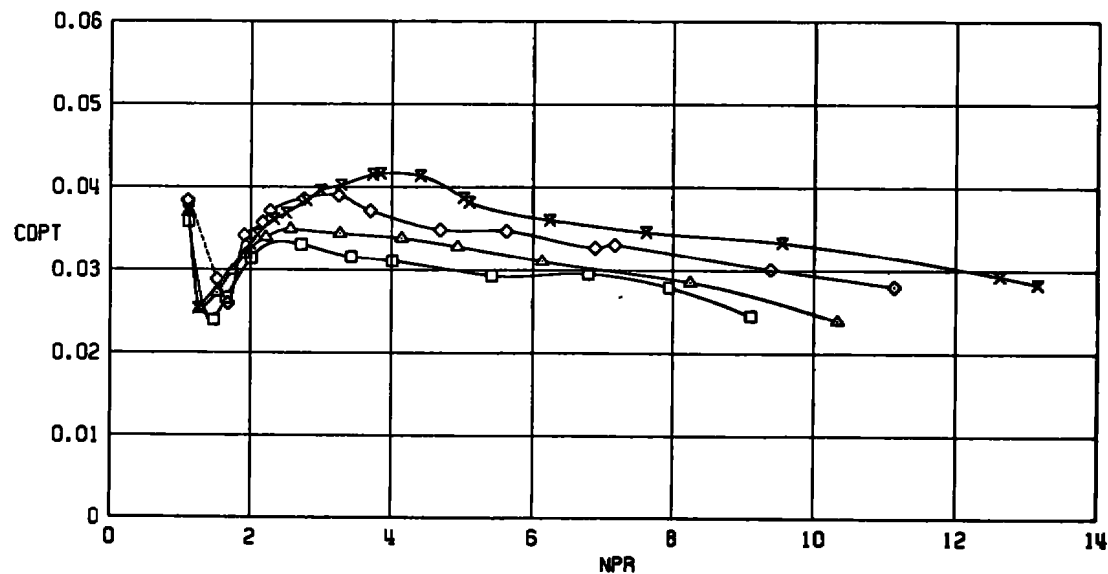
b. $M_\infty = 0.9$
Figure 41. Continued.

SYM	R/R"	D$_S$/D$_N$	
□	1.133	0.707	17
△	1.220	0.706	71
◇	1.310	0.707	99
✕	1.491	0.707	78
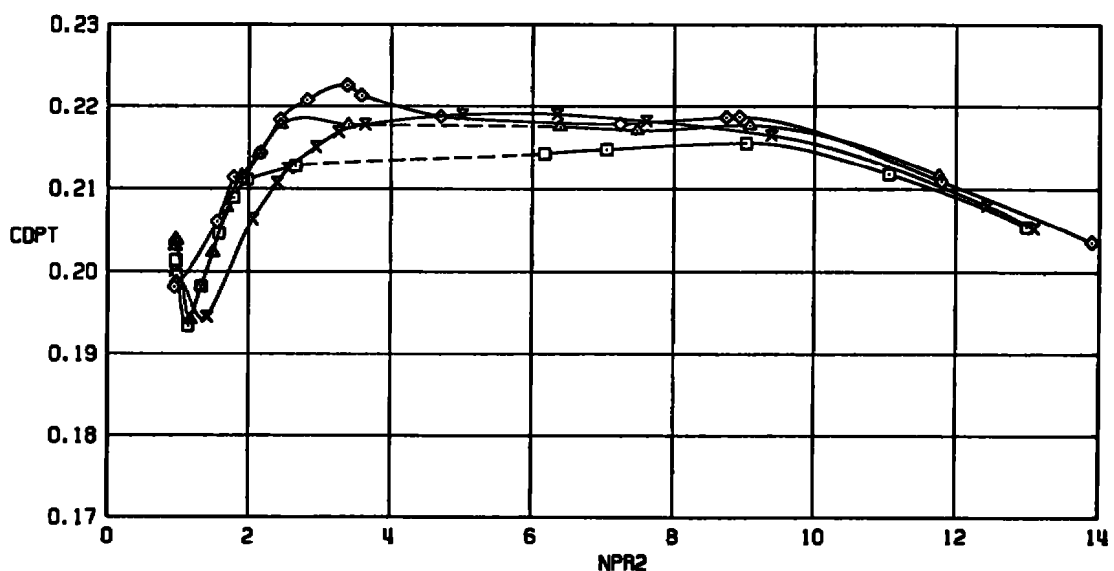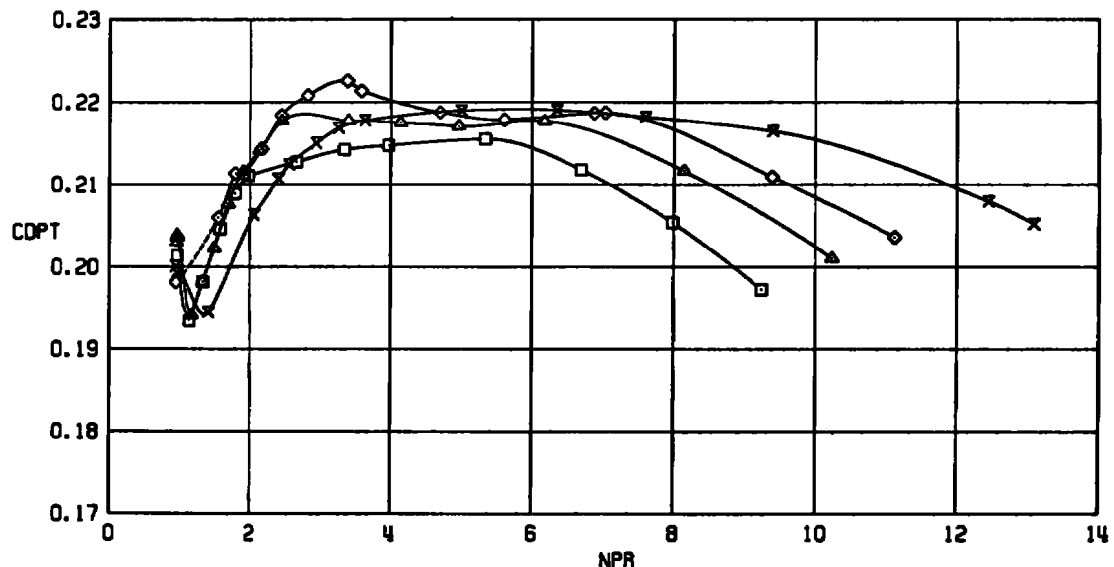
c. $M_\infty = 1.2$
Figure 41. Concluded.

SYM	A/A*	D_s/D_N	
o	1.000	0.866	41
□	1.142	0.866	35
x	1.500	0.866	128
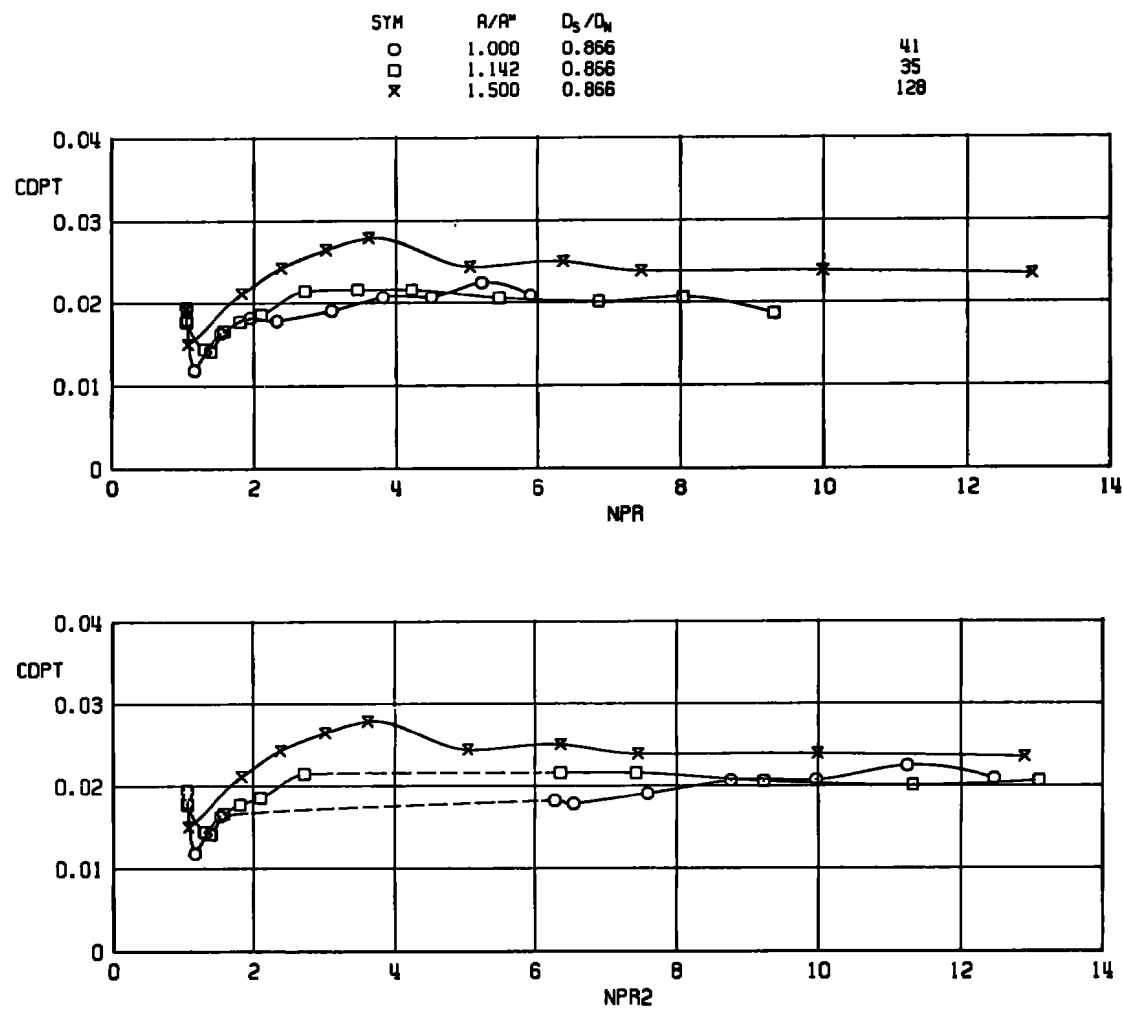
a. $M_\infty = 0.6$

Figure 42. Correlation of nozzle area ratio effects on afterbody
drag, D_s/D_N = 0.866.

110

SYM	A/A*	D$_S$/D$_N$	
O	1.000	0.866	42
□	1.142	0.866	36
◇	1.307	0.866	131
X	1.500	0.866	126
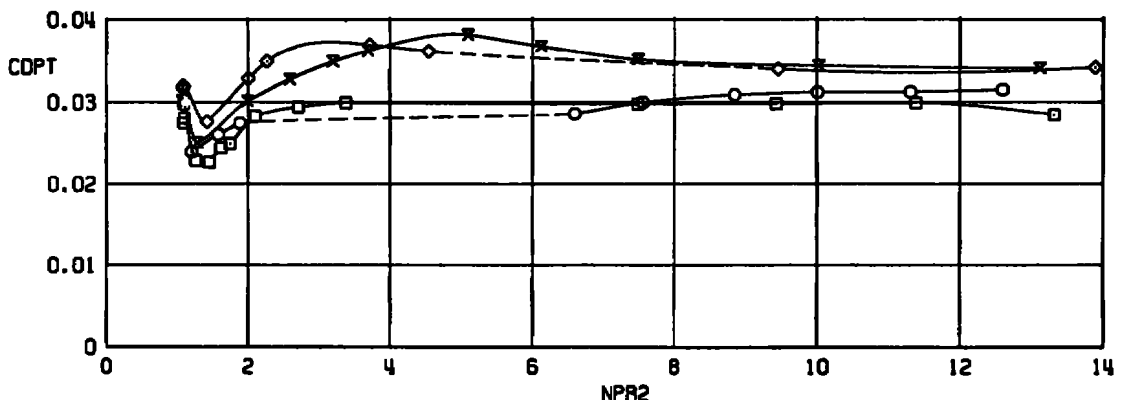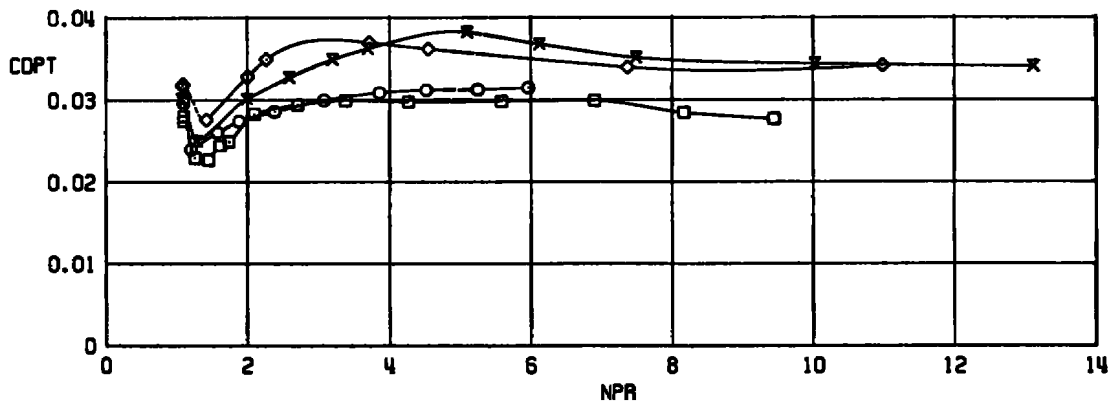
b. $M_\infty = 0.9$

Figure 42. Continued.

| SYM	A/A*	D_3/D_N	
O	1.000	0.866	43
□	1.142	0.866	38
◇	1.307	0.866	132
✕	1.500	0.866	127
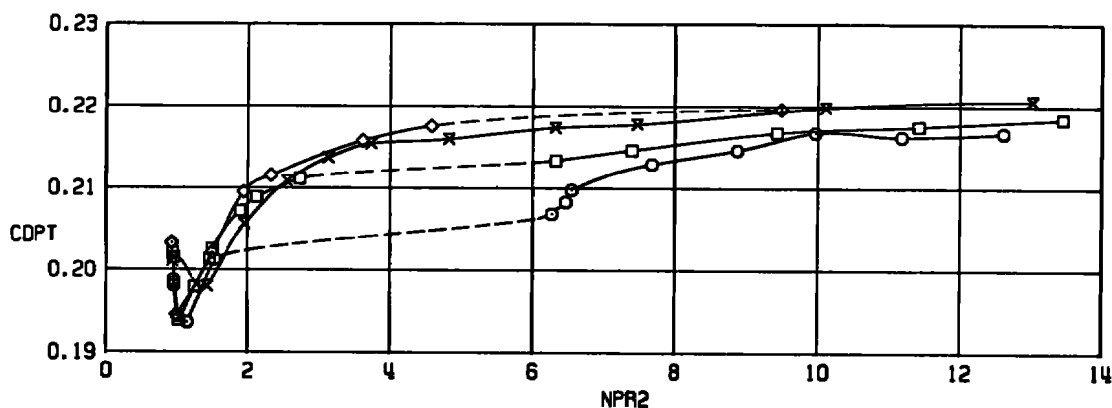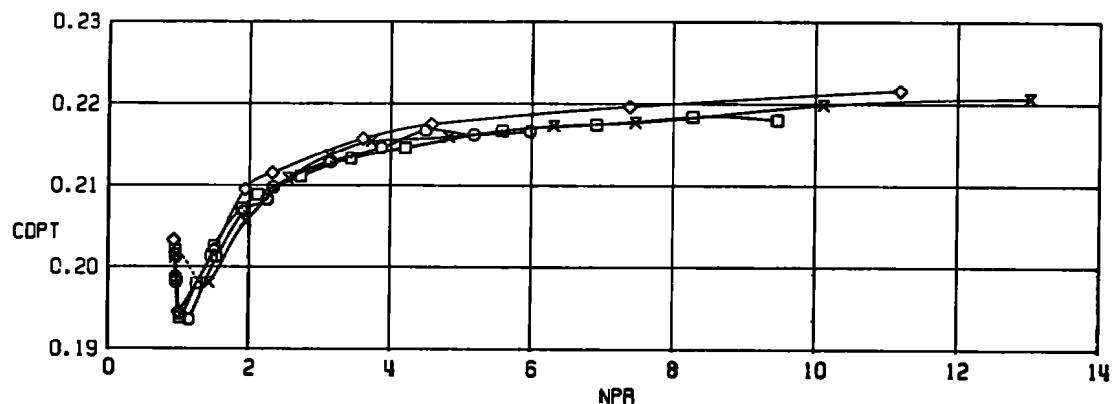
c. $M_\infty = 1.2$

Figure 42. Concluded.
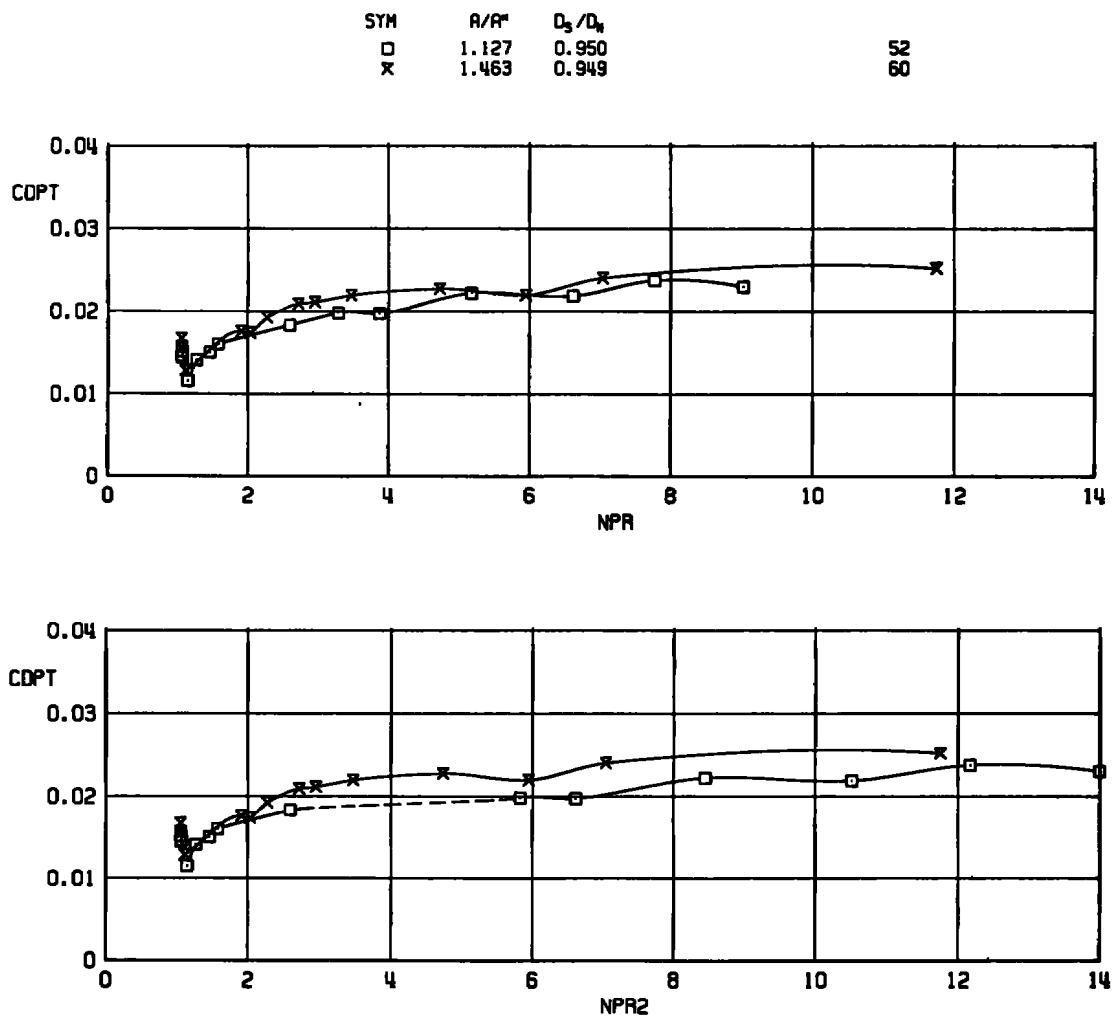
a. $M_\infty = 0.6$

Figure 43. Correlation of nozzle area ratio effects on afterbody drag, $D_s/D_N = 0.95$.

SYM	A/A*	D_S/D_N	
□	1.127	0.950	54
x	1.463	0.949	62
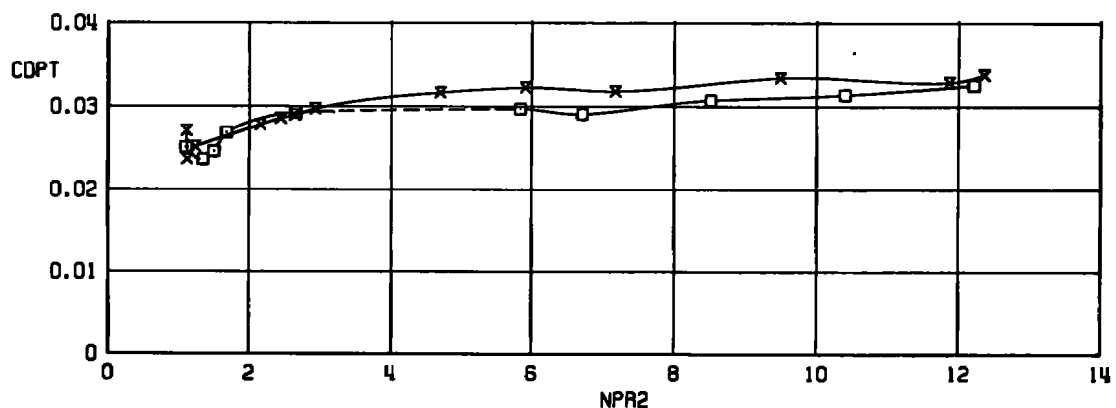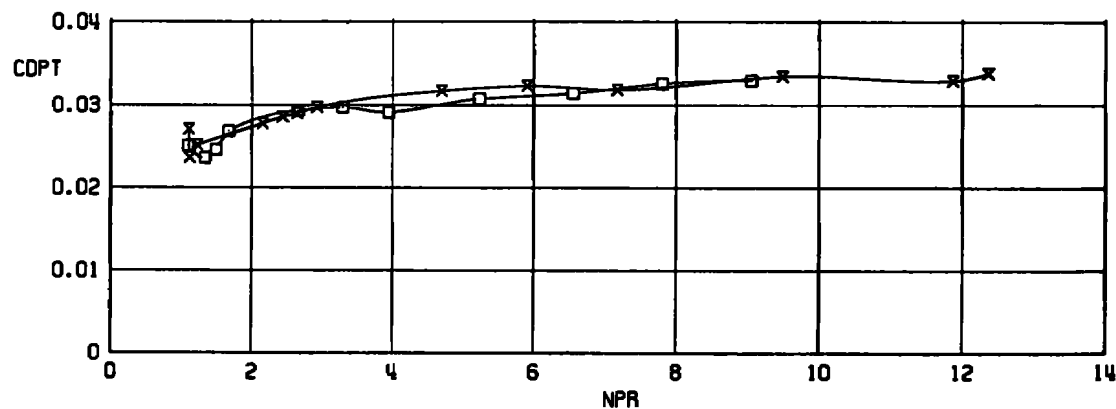
b. $M_\infty = 0.9$
Figure 43. Continued.

114
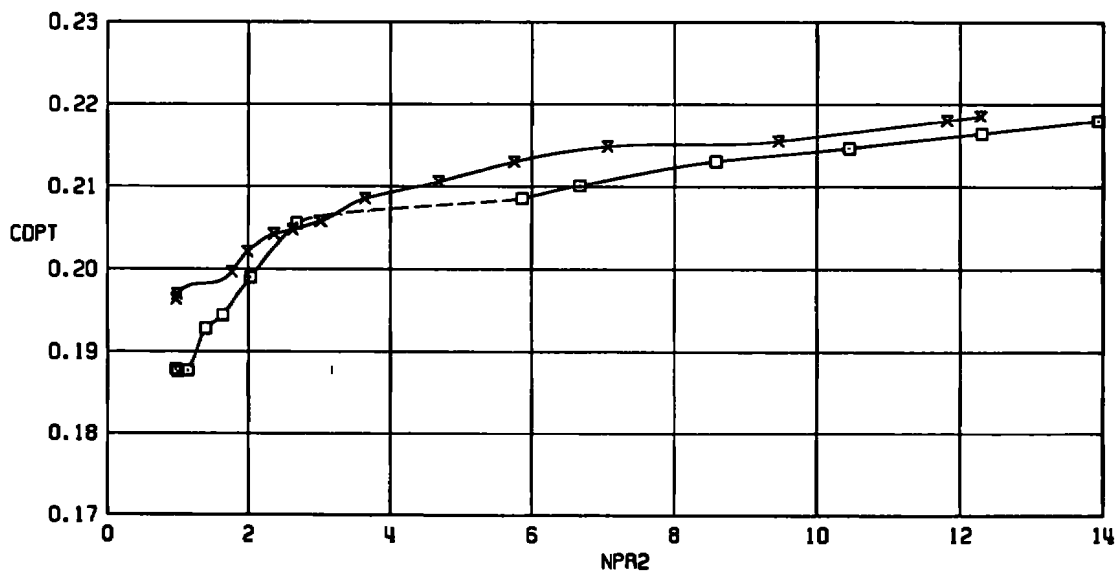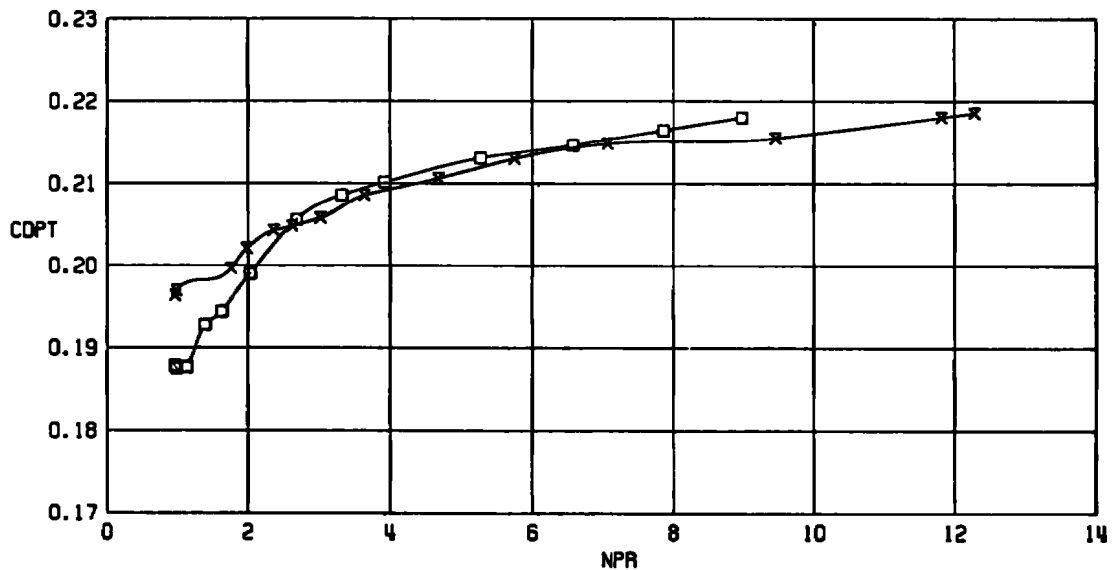
c. $M_\infty = 1.2$

Figure 43. Concluded.
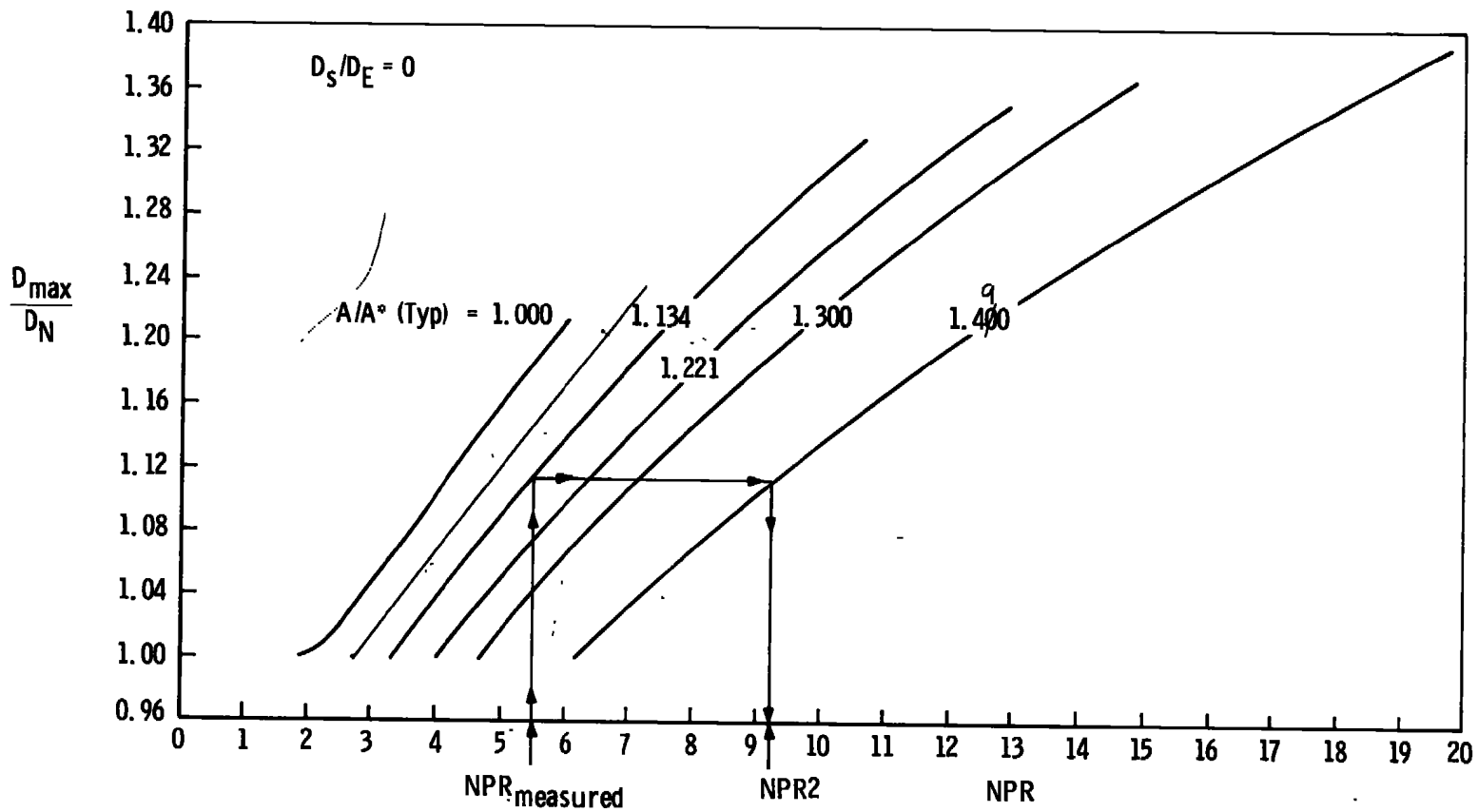
Figure 44. Illustration of procedure for determining the correlation pressure ratio NPR2.
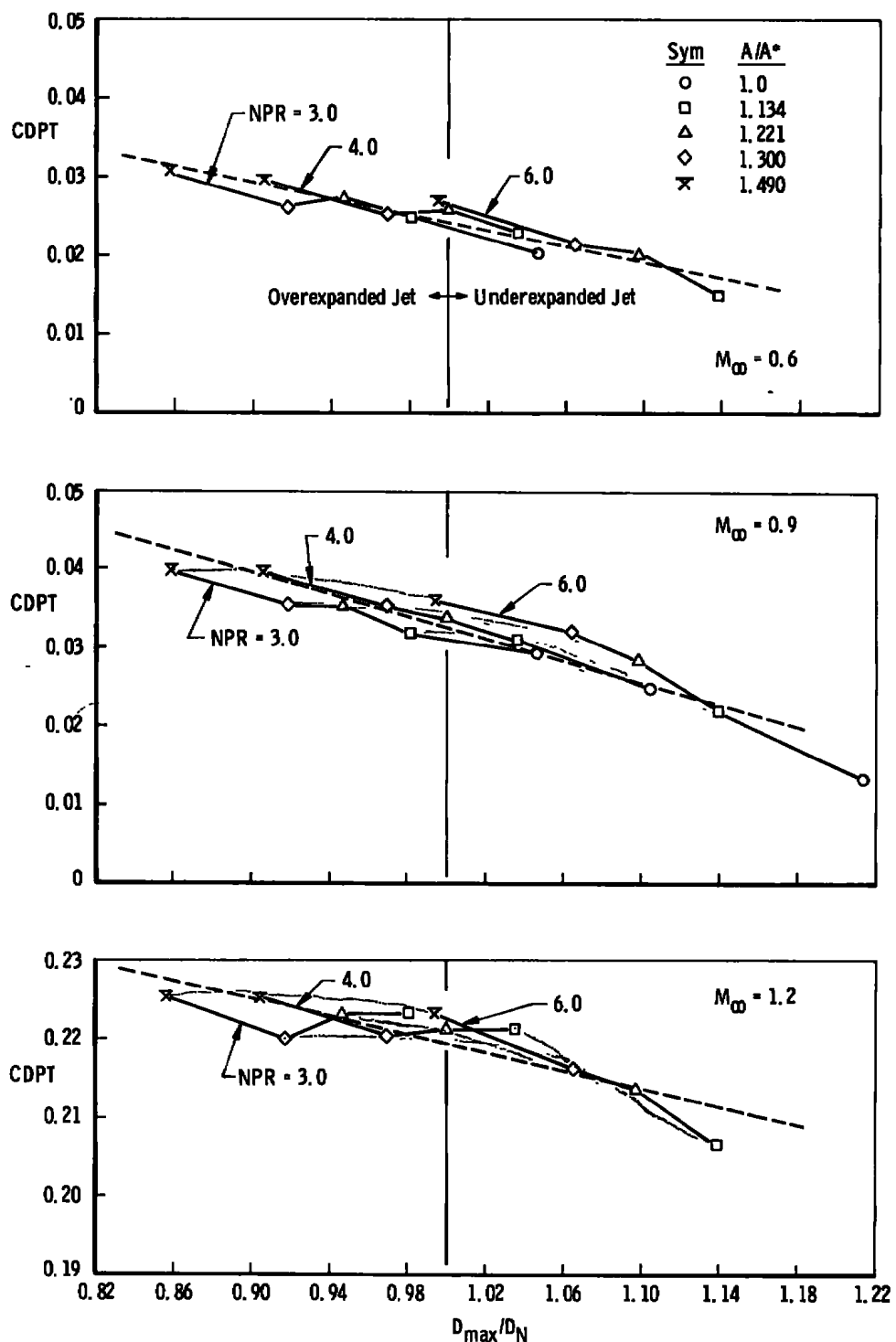
Figure 45. Variation of afterbody drag with exhaust plume maximum diameter, $D_s/D_N = 0$.

117
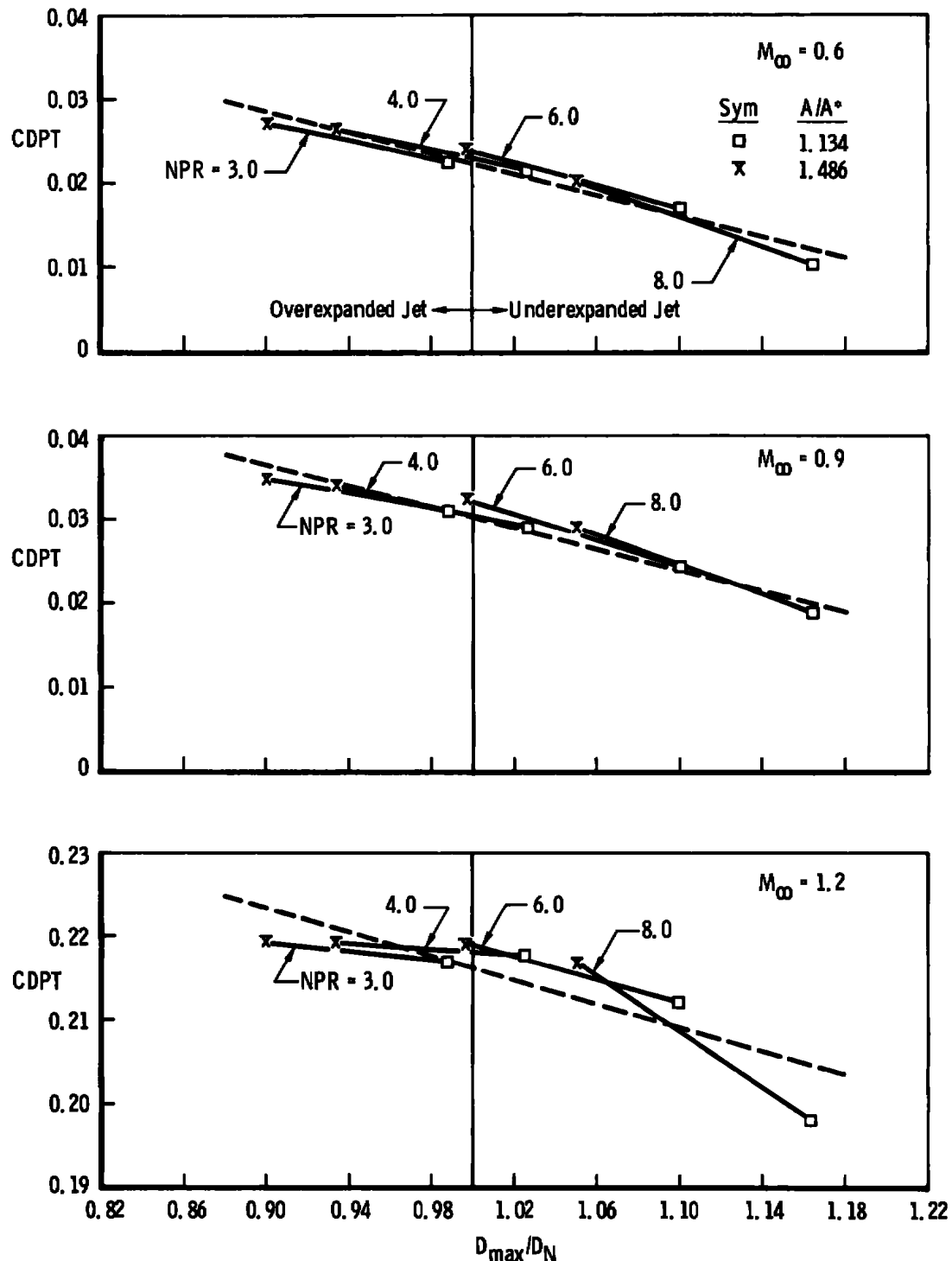
Figure 46. Variation of afterbody drag with exhaust plume maximum diameter, D_s/D_N = 0.543.
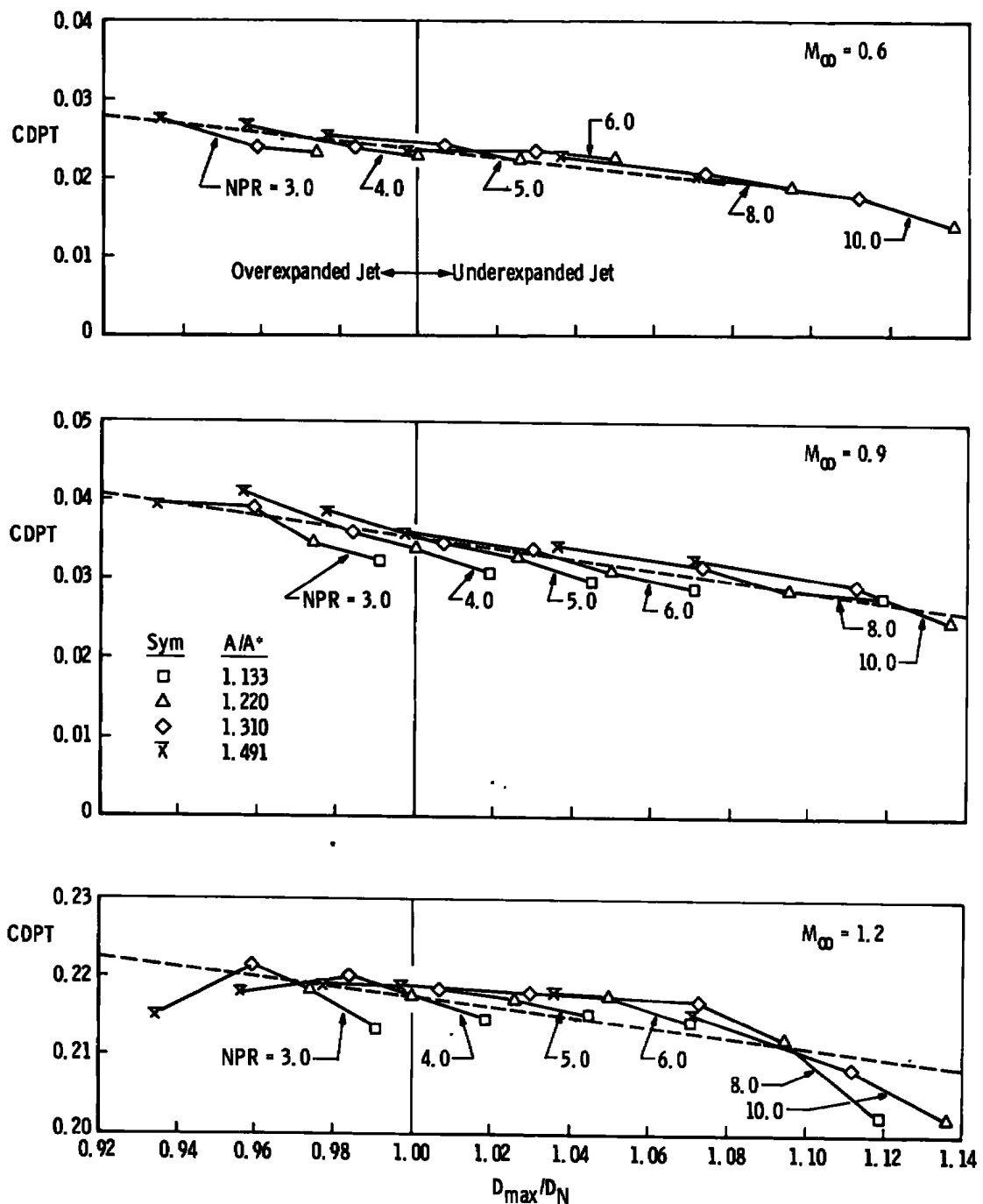
Figure 47. Variation of afterbody drag with exhaust plume
maximum diameter, D_s/D_N = 0.707.
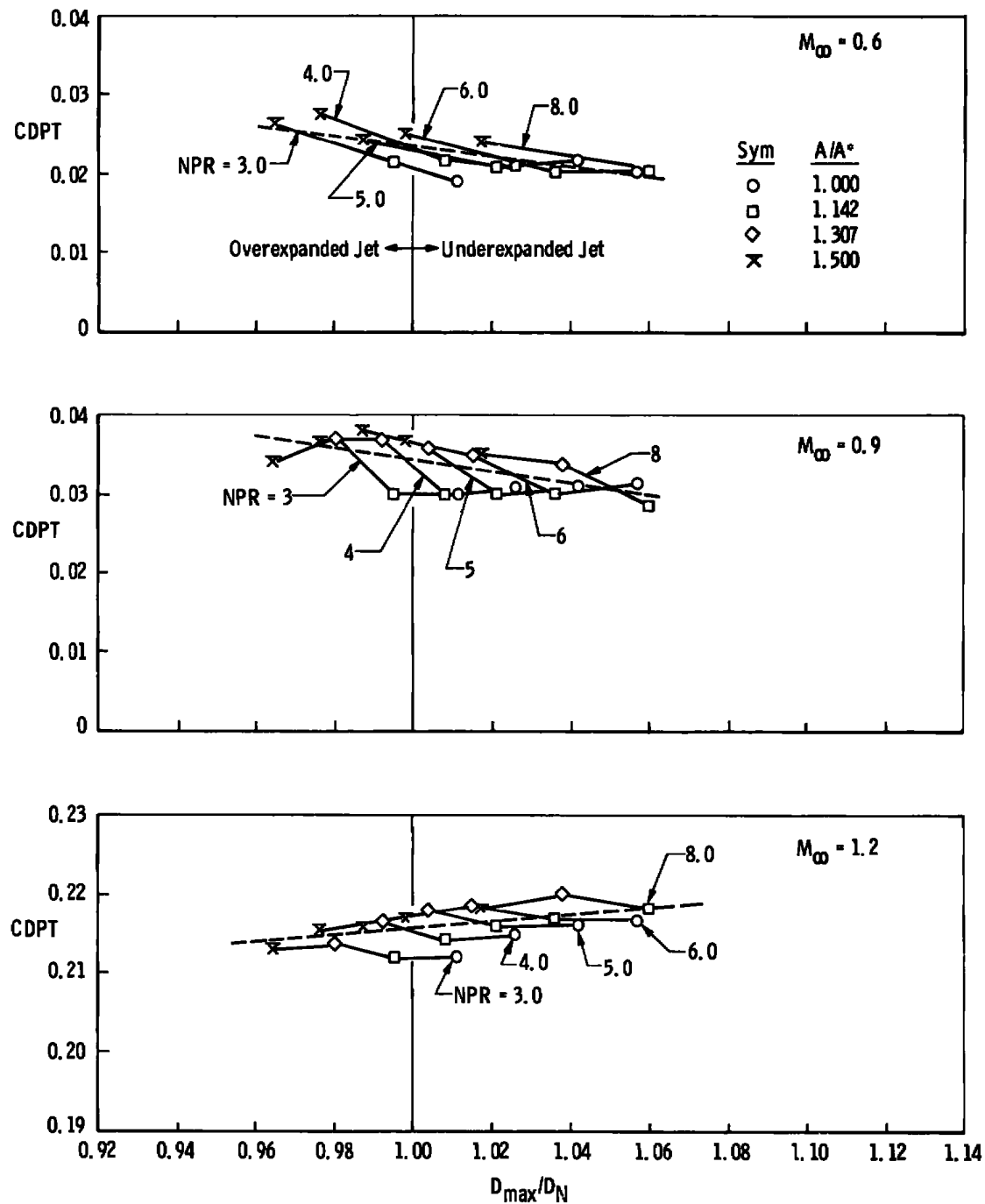
Figure 48. Variation of afterbody drag with exhaust plume
maximum diameter, D_s/D_N = 0.866.
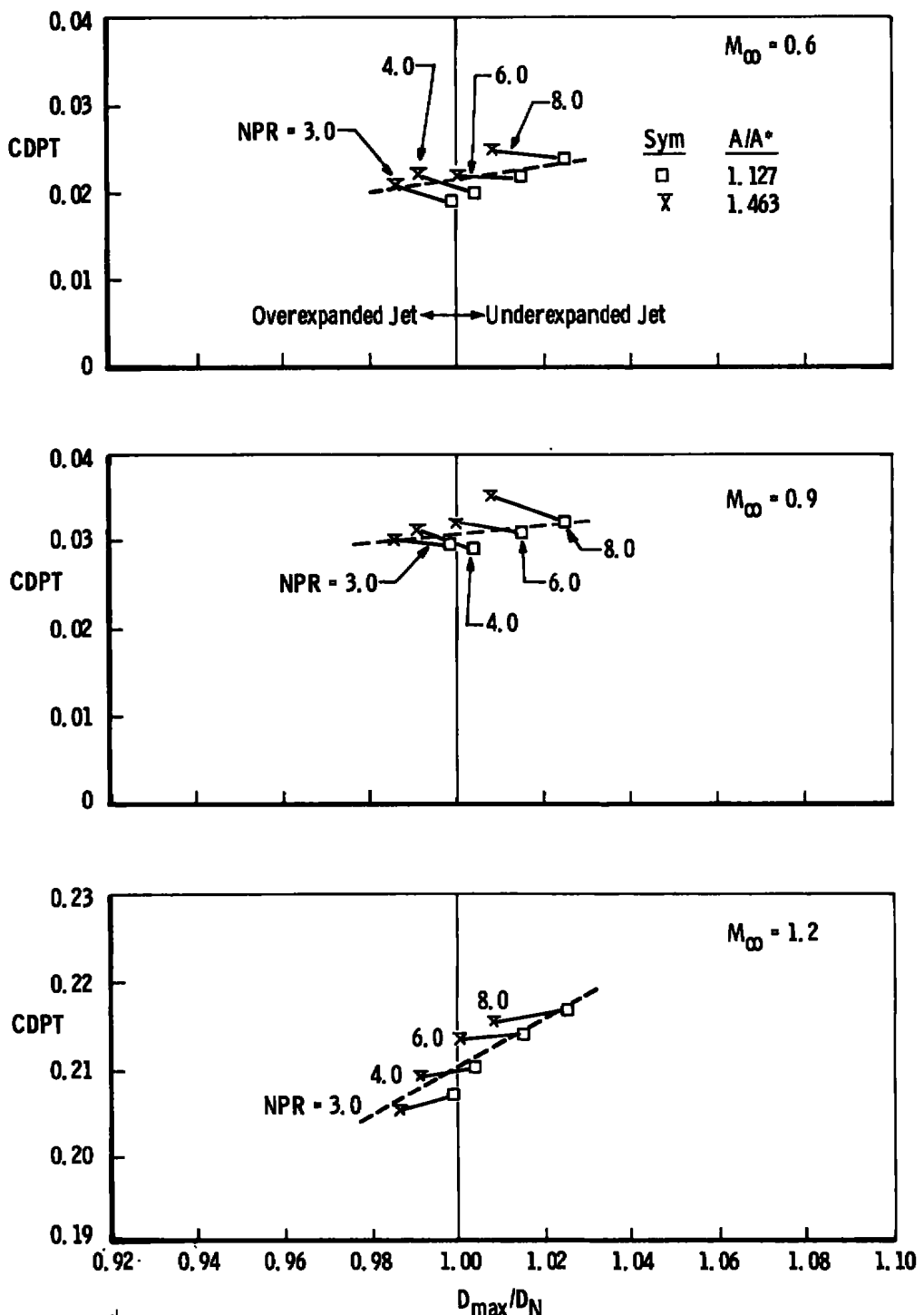
Figure 49. Variation of afterbody drag with exhaust plume
maximum diameter, D_s/D_N = 0.95.
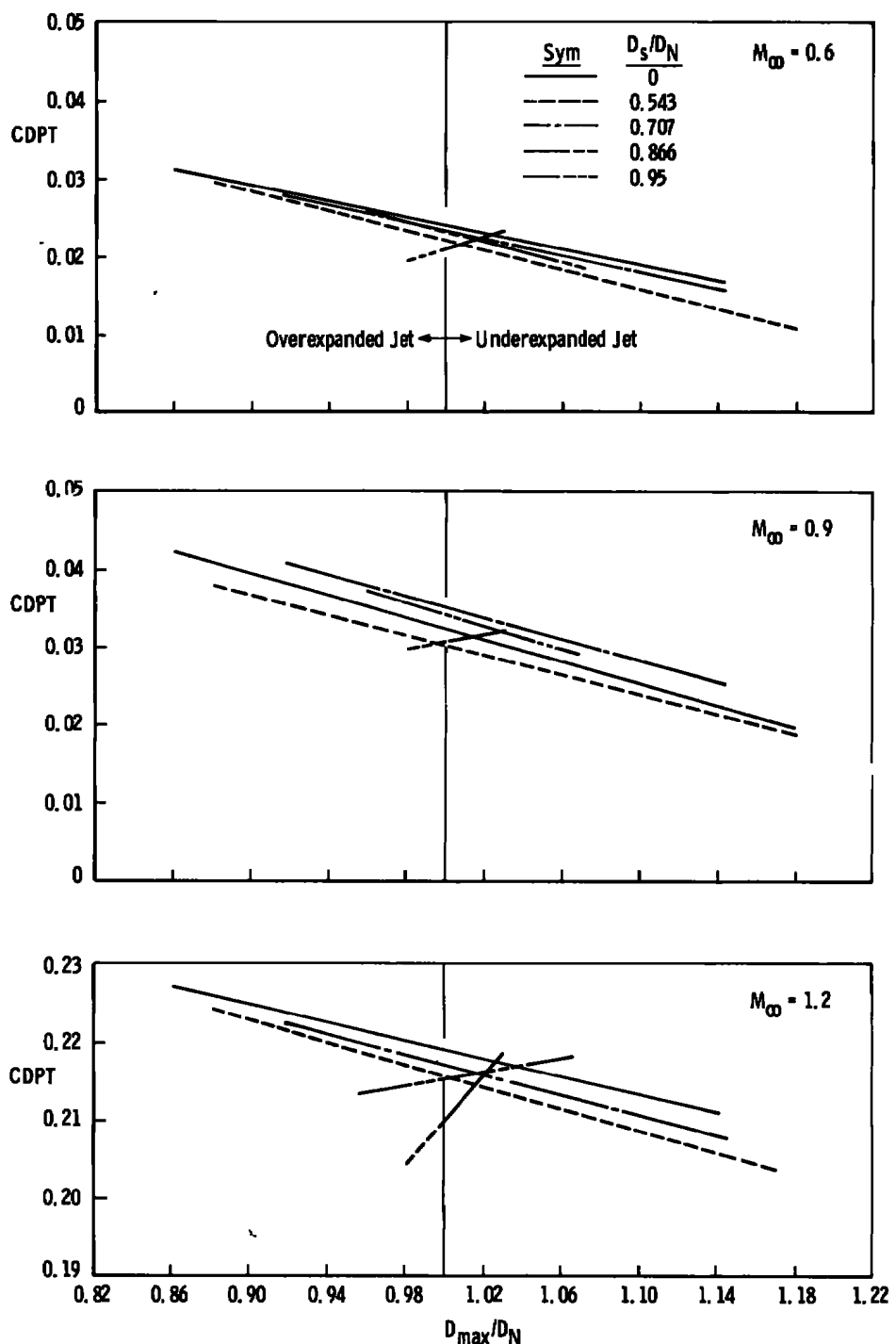
Figure 50. Comparison of the variation of afterbody drag with
plume maximum diameter for conventional and annular
jet configurations.

Table 1. External Pressure Orifice Locations
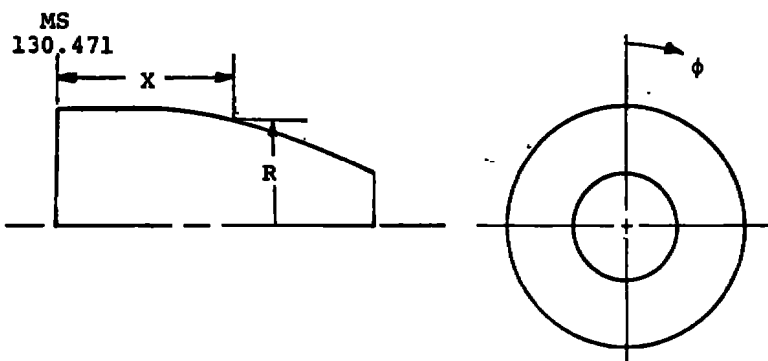
| φ = 0 deg			φ = 180 deg			φ = 270 deg		
Pressure No.	X	R	Pressure No.	X	R	Pressure No.	X	R
401	1.730	4.922						
402	2.725	4.925						
403	3.727	4.921						
404	4.725	4.920						
405	5.725	4.919						
406	6.725	4.884	442	6.727	4.888	464	6.727	4.886
407	7.503	4.795	443	7.503	4.800	465	7.508	4.797
408	8.156	4.693	444	8.154	4.699	466	8.157	4.696
409	8.707	4.591	445	8.707	4.598	467	8.709	4.594
410	9.302	4.470	446	9.302	4.478	468	9.304	4.473
411	9.850	4.352	447	9.850	4.361	469	9.850	4.355
412	10.294	4.245	448	10.294	4.253	470	10.294	4.248
413	10.764	4.117	449	10.761	4.127	471	10.764	4.121
414	11.154	4.004	450	11.155	4.015	472	11.157	4.008
415	11.565	3.882	451	11.562	3.892	473	11.565	3.886
416	11.958	3.756	452	11.956	3.767	474	11.959	3.760
417	12.385	3.615	453	12.384	3.628	475	12.387	3.620
418	12.787	3.477	454	12.787	3.490	476	12.790	3.482
419	13.155	3.345	455	13.152	3.358	477	13.157	3.350
420	13.657	3.160	456	13.652	3.172	478	13.657	3.163
421	13.960	3.042	457	13.960	3.057	479	13.961	3.047
422	14.581	2.795	458	14.579	2.815	480	14.584	2.802
423	15.069	2.584	459	15.069	2.604	481	15.072	2.593
424	15.560	2.364	460	15.560	2.386	482	15.565	2.374
425	16.120	2.144	461	16.117	2.165	483	16.118	2.152

APPENDIX A
AFTERBODY PRESSURE DISTRIBUTIONS

Plots of pressure coefficient data are presented for the top row of pressure orifices (ϕ = 0). The drag coefficients from integrating these data are included in the plot headings to illustrate the relationship between pressure coefficient changes and corresponding drag coefficient changes. Plots of pressure data are presented in the following order:

Figure

a. $M_\infty = 0.6$

Figure A-1. Effects of nozzle pressure ratio,
$D_s/D_N = 0$, $A/A^* = 1.134$.

SYM	A/A*	D_S/D_N	NPR	NSPR	CDPT	PN/PT
⊙	1.134	0.0	1.15	0.345	0.0477	86.04
▫	1.134	0.0	1.46	0.438	0.0230	86.07
△	1.134	0.0	3.53	1.059	0.0318	86.13
◇	1.134	0.0	5.19	1.554	0.0259	86.15
✗	1.134	0.0	6.98	2.092	0.0169	86.16

$\phi=0$ DEG

b. $\bar{M}_\infty = 0.9$
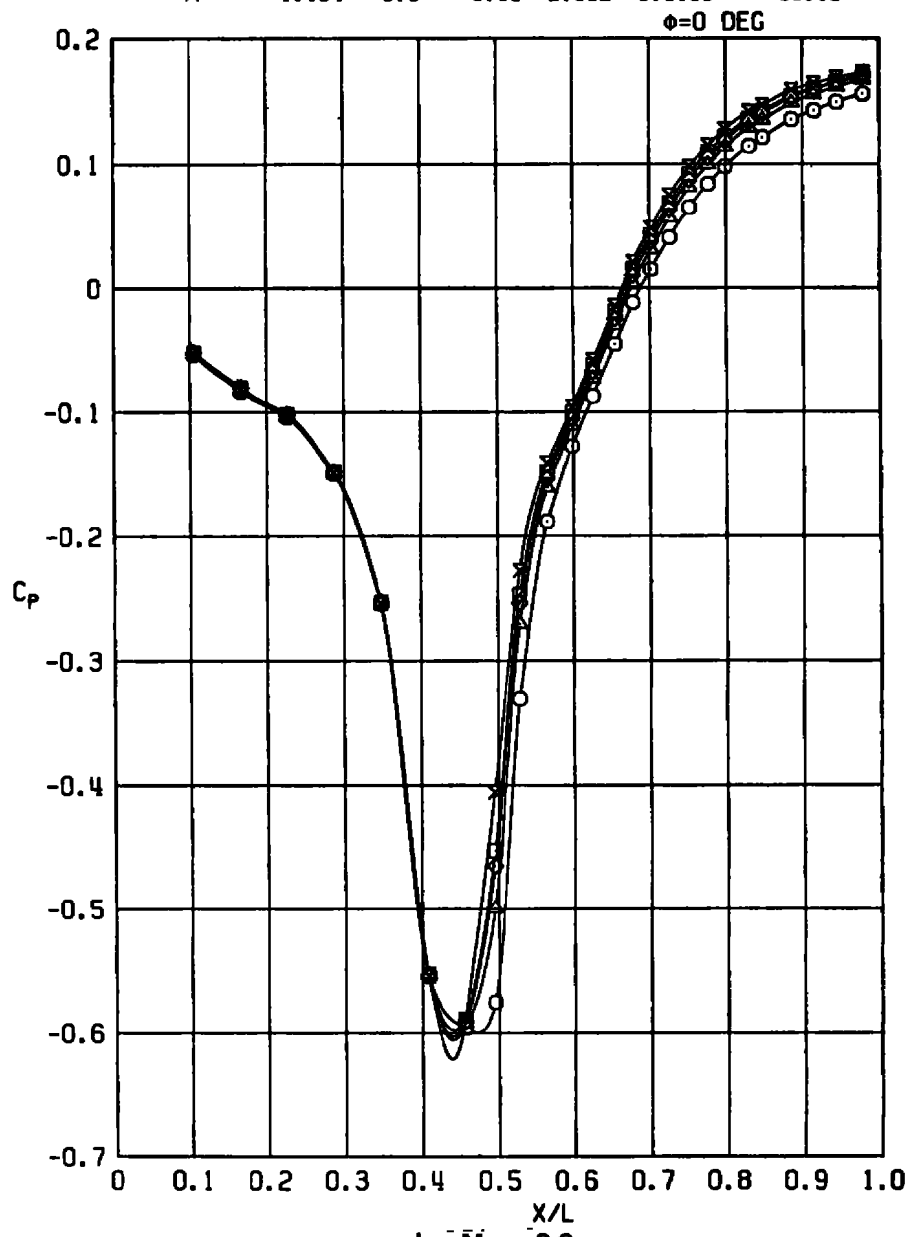
Figure A-1. Continued.

SYM	A/AP	Dв/DM	NPR	NSPR	COPT	PN/PT
⊙	1.134	0.0	0.98	0.293	0.2084	88.03
▣	1.134	0.0	1.18	0.352	0.1945	88.04
▲	1.134	0.0	3.51	1.052	0.2222	88.12
◇	1.134	0.0	5.28	1.583	0.2126	88.14
✕	1.134	0.0	7.14	2.141	0.1962	88.15
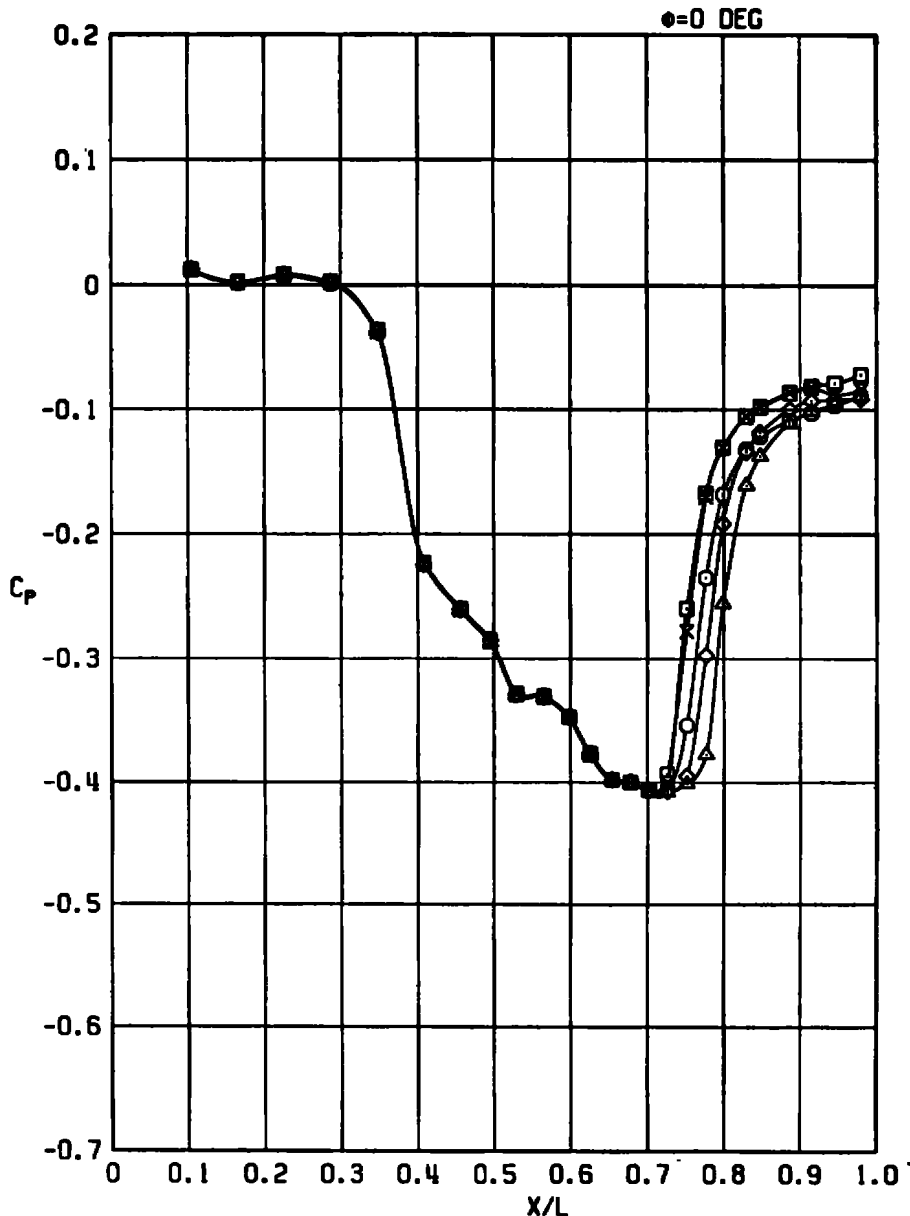
c. $M_\infty = 1.2$

Figure A-1. Concluded.

SYM	A/A*	D_s/D_N	NPR	NSPR	CDPT	PN/PT
⊙	1.490	0.0	1.08	0.175	0.0367	118.03
□	1.490	0.0	1.34	0.218	0.0144	118.05
△	1.490	0.0	6.27	1.018	0.0261	118.11
◇	1.490	0.0	9.83	1.595	0.0166	118.13
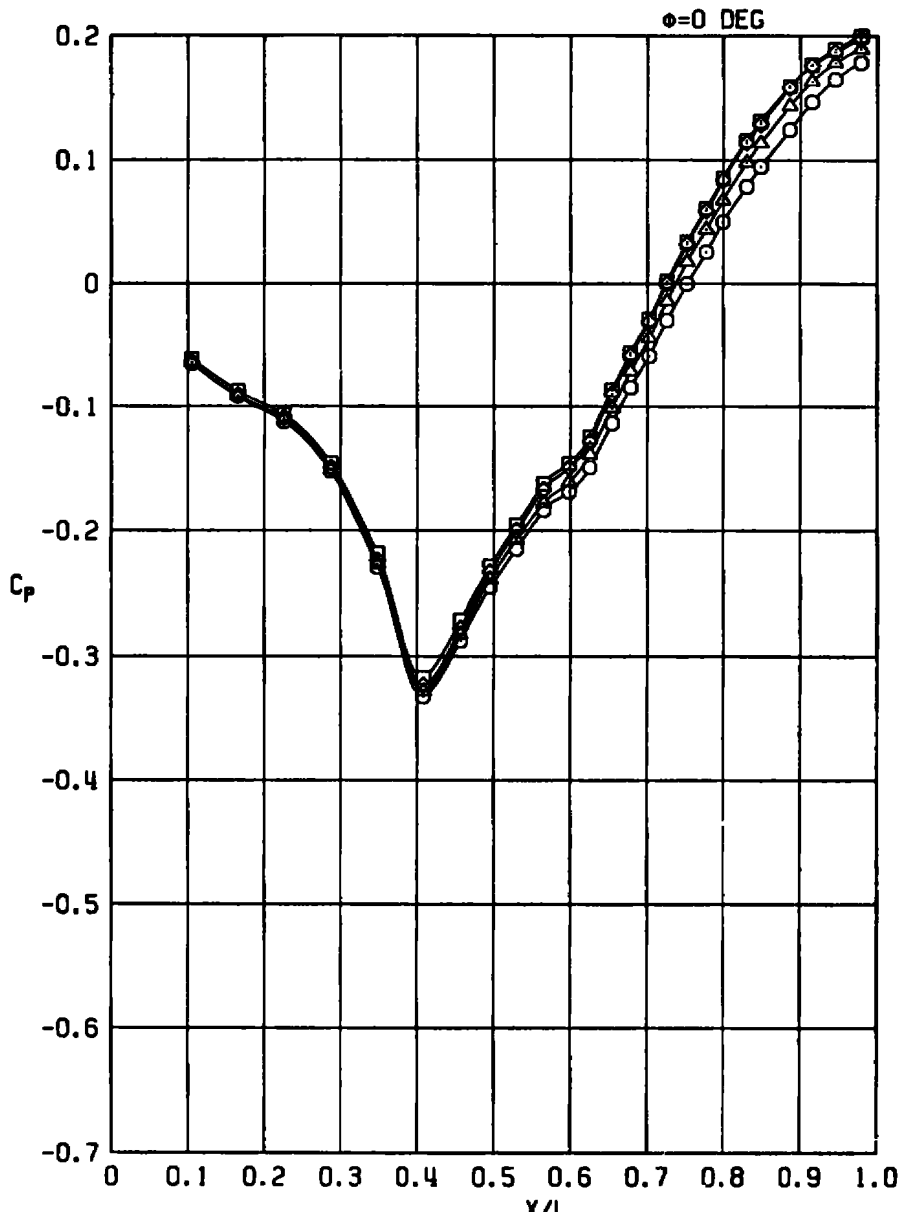
a. $M_\infty = 0.6$

Figure A-2. Effects of nozzle pressure ratio,
D_s/D_N = 0, A/A* = 1.490.

SYM	A/A*	D_S/D_N	NPR	NSPR	CDPT	PN/PT
⊙	1.490	0.0	1.13	0.183	0.0493	120.03
▣	1.490	0.0	2.00	0.324	0.0357	120.05
△	1.490	0.0	6.32	1.026	0.0351	120.10
◇	1.490	0.0	10.15	1.647	0.0255	120.12
✗	1.490	0.0	13.29	2.157	0.0140	120.13

Φ=0 DEG
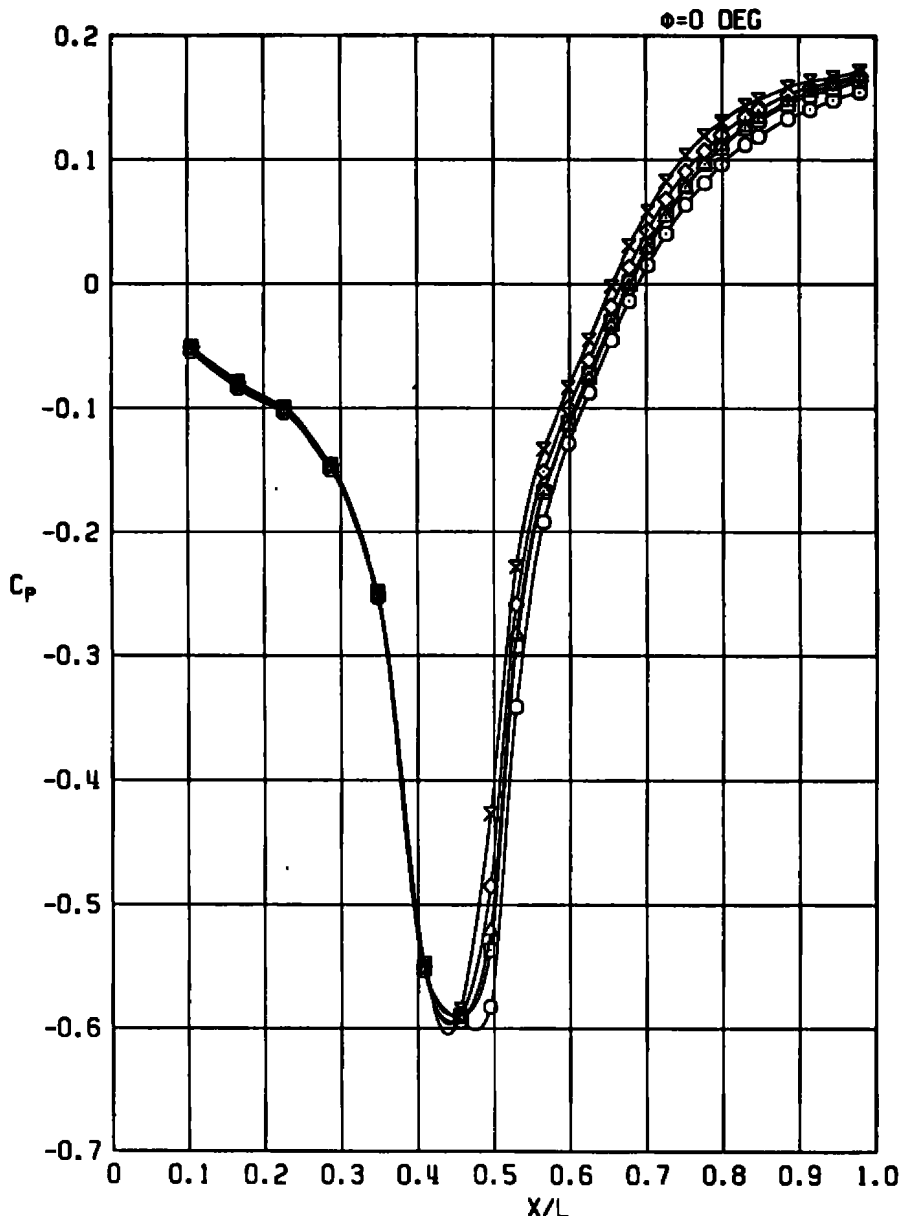
b. $M_\infty = 0.9$

Figure A-2. Continued.

SYM	A/A*	D_S/D_N	NPR	NSPR	COPT	PN/PT
⊙	1.490	0.0	0.95	0.154	0.2079	122.04
▫	1.490	0.0	1.39	0.226	0.1964	122.05
△	1.490	0.0	6.19	1.004	0.2219	122.11
◇	1.490	0.0	10.26	1.665	0.2035	122.13
✗	1.490	0.0	12.98	2.107	0.1902	122.14

Φ=0 DEG

c. M_∞ = 1.2
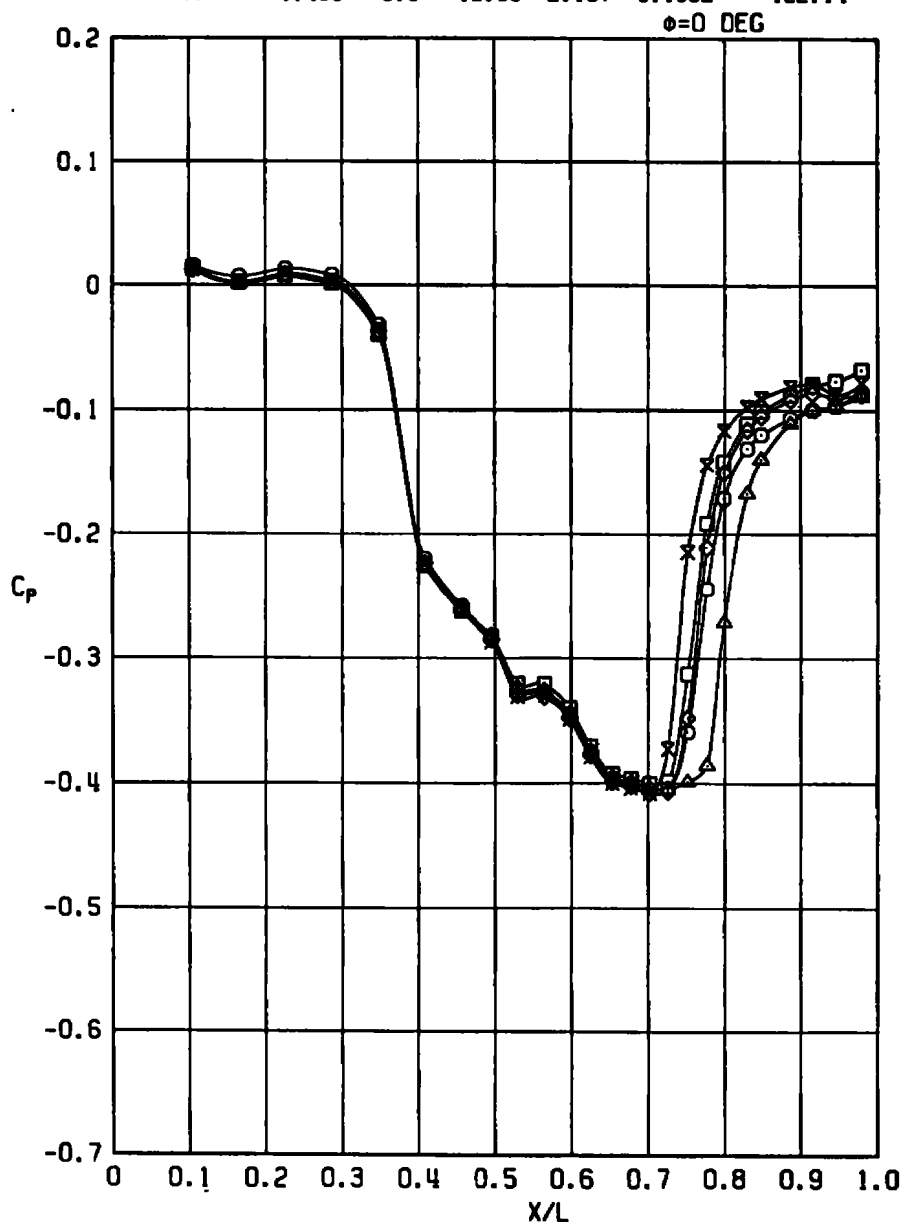
Figure A-2. Concluded.

132

SYM	A/A*	D_s/D_N	NPR	NSPR	CDPT	PN/PT
⊙	1.133	0.707	1.12	0.335	0.0358	14.01
▢	1.133	0.707	1.48	0.443	0.0240	14.02
△	1.133	0.707	3.42	1.028	0.0316	14.06
◇	1.133	0.707	5.42	1.628	0.0293	14.08
✗	1.133	0.707	6.79	2.038	0.0296	14.09

$\Phi = 0$ DEG

a. $M_\infty = 0.9$
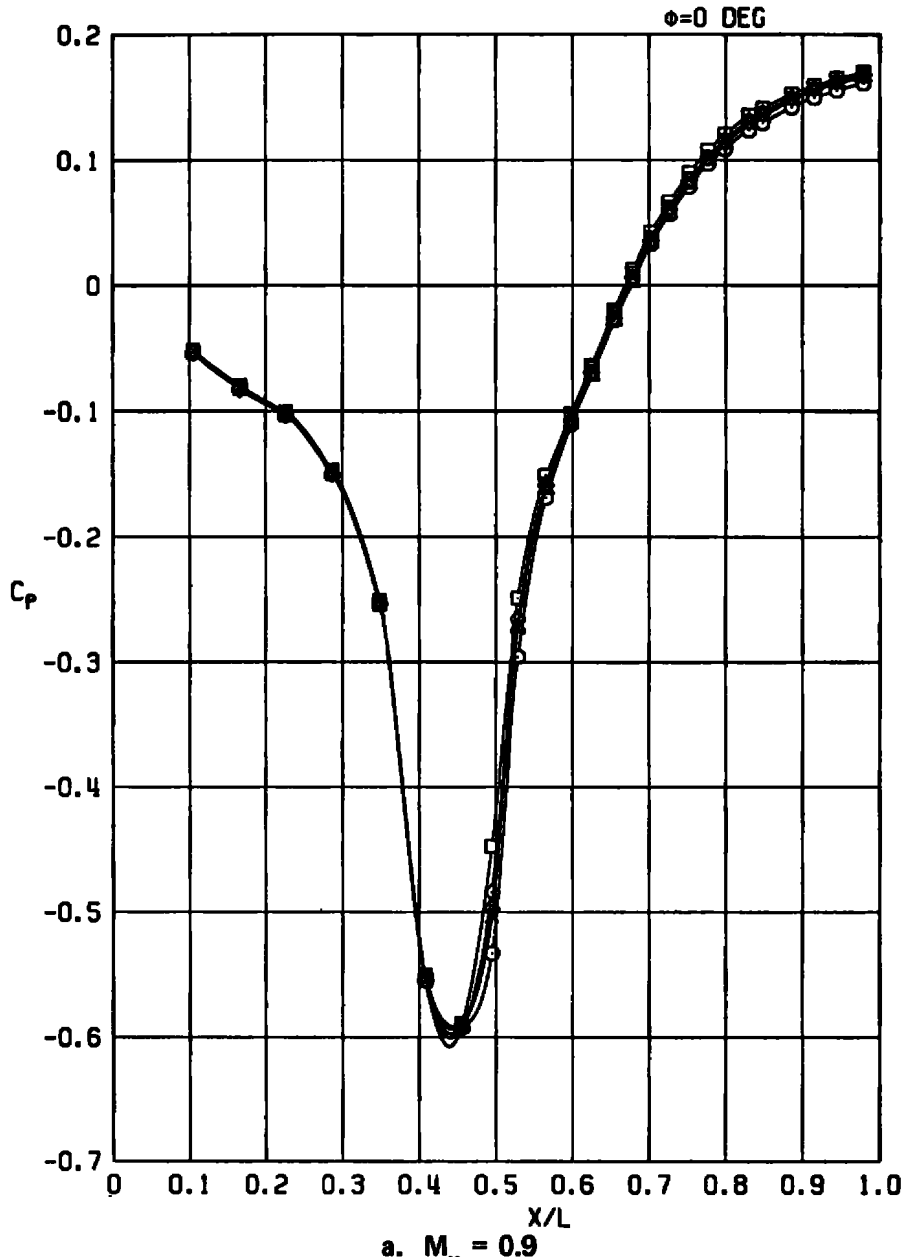
Figure A-3. Effects of nozzle pressure ratio,
D_s/D_N = 0.707, A/A* = 1.133.

SYM	A/A*	D_S/D_N	NPR	NSPR	CDPT	PN/PT
⊙	1.133	0.707	0.97	0.291	0.2014	17.01
⊡	1.133	0.707	1.14	0.343	0.1934	17.02
△	1.133	0.707	3.34	1.002	0.2143	17.08
◇	1.133	0.707	5.34	1.603	0.2156	17.10
✗	1.133	0.707	6.70	2.011	0.2118	17.11

Φ=0 DEG
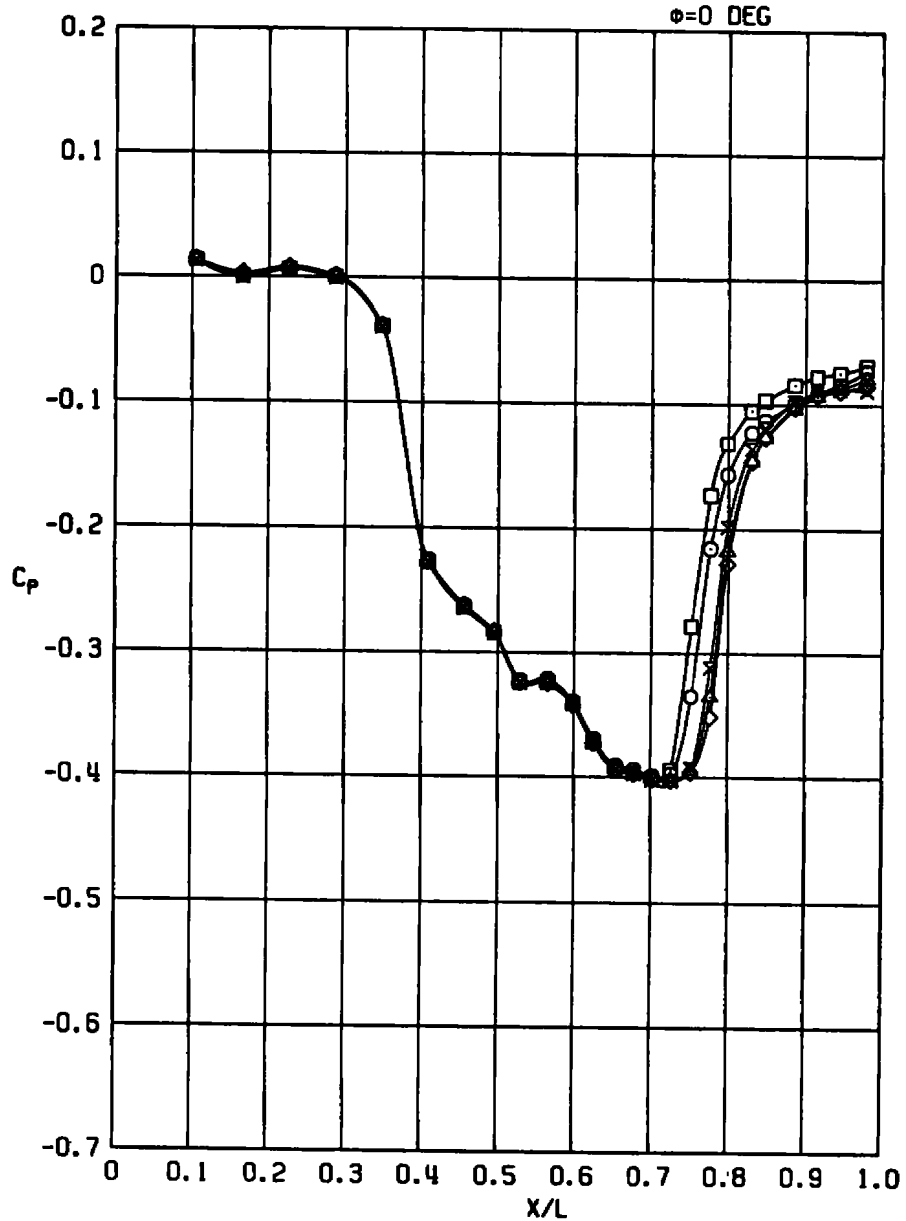
b. M_∞ = 1.2

Figure A-3. Concluded.

SYM	A/A*	D$_s$/D$_N$	NPR	NSPR	CDPT	PN/PT
☉	1.491	0.707	1.06	0.173	0.0254	74.03
▢	1.491	0.707	1.13	0.183	0.0146	74.04
△	1.491	0.707	6.24	1.011	0.0232	74.13
◇	1.491	0.707	9.33	1.512	0.0211	74.15
✗	1.491	0.707	12.35	2.001	0.0176	74.16
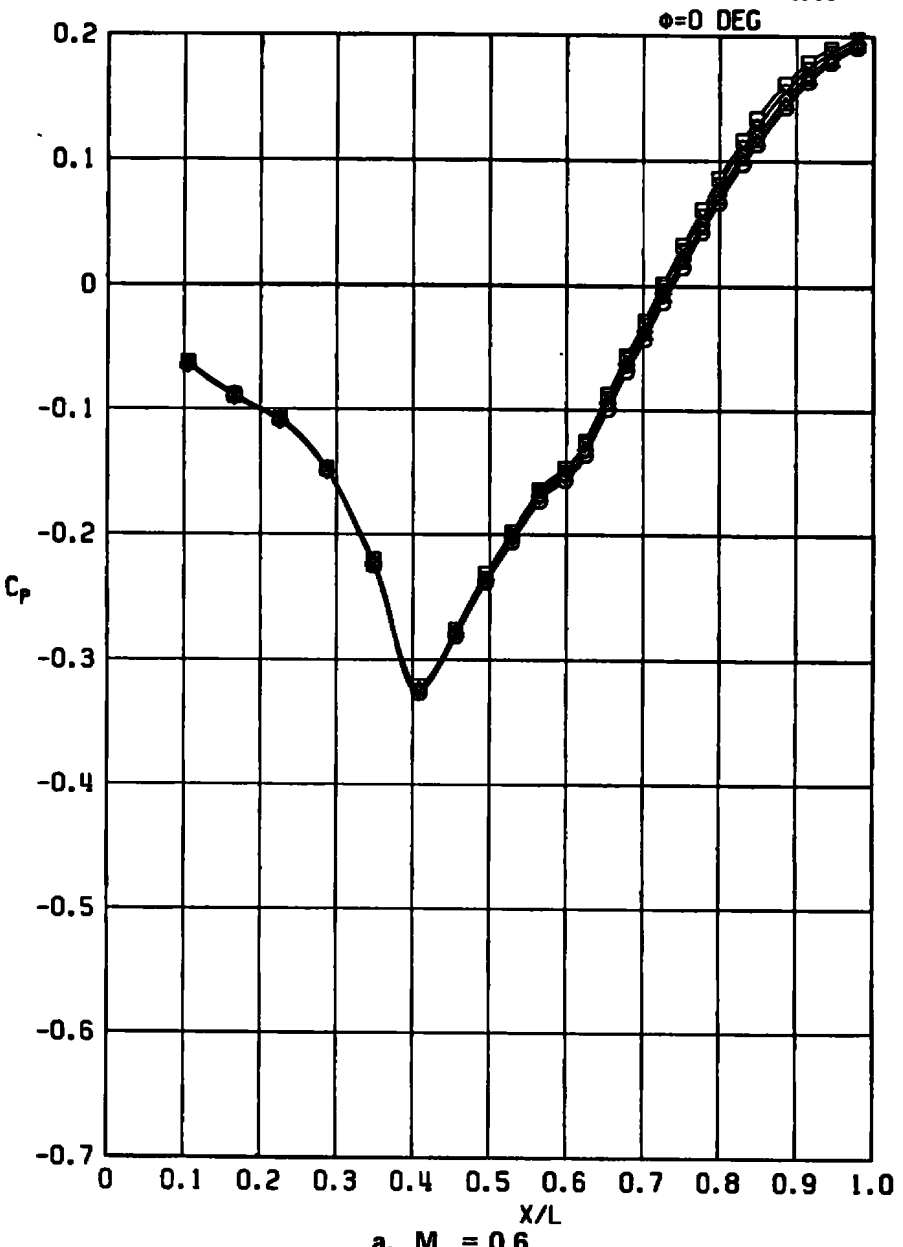
a. $M_\infty = 0.6$

Figure A-4. Effects of nozzle pressure ratio, D$_s$/D$_N$ = 0.707, A/A* = 1.491.

SYM	A/A*	D_S/D_N	NPR	NSPR	COPT	PN/PT
⊙	1.491	0.707	1.11	0.180	0.0370	76.04
⊡	1.491	0.707	1.26	0.204	0.0254	76.05
△	1.491	0.707	6.24	1.012	0.0360	76.14
◇	1.491	0.707	9.54	1.546	0.0334	76.16
✗	1.491	0.707	12.62	2.046	0.0293	76.17
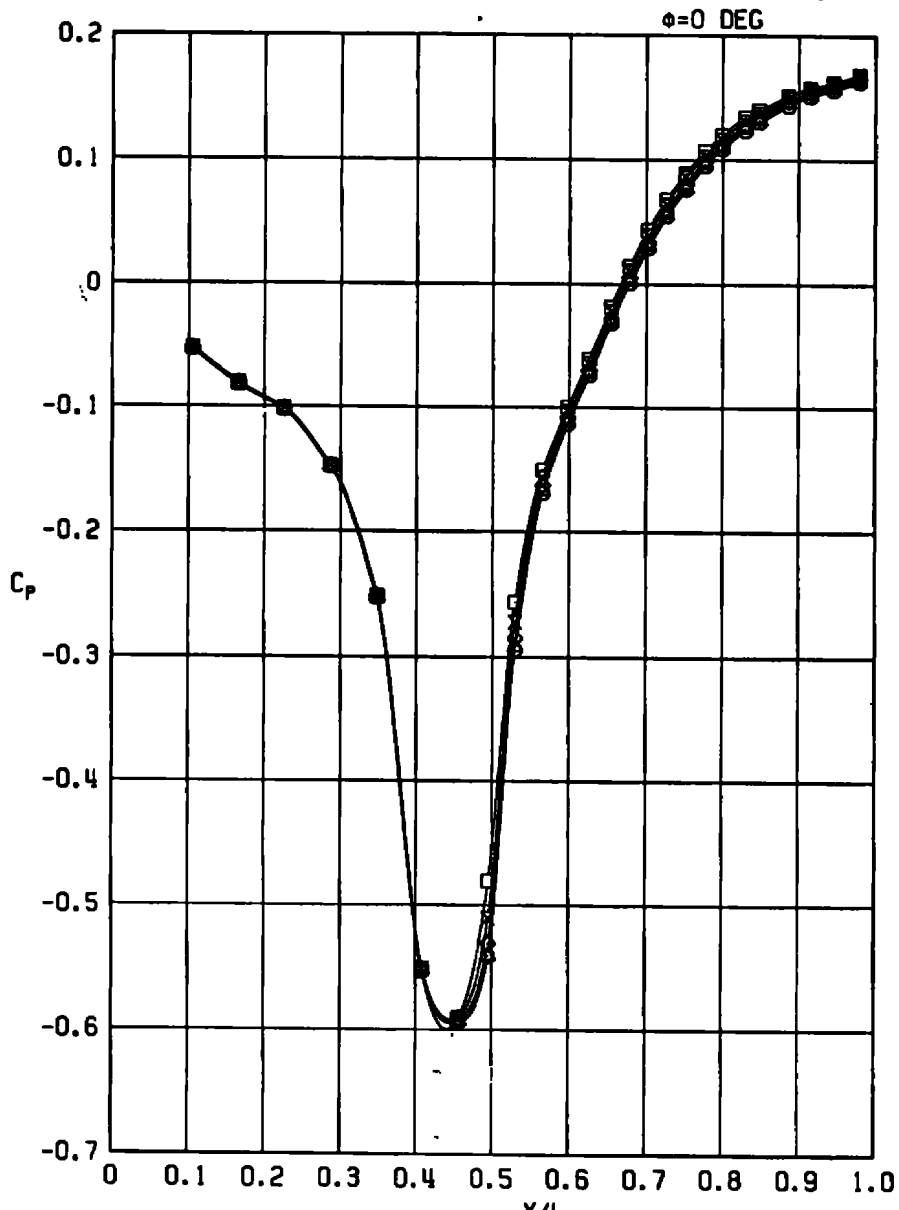
$\Phi = 0$ DEG

b. $M_\infty = 0.9$

Figure A-4. Continued.

SYM	A/A*	D$_3$/D$_N$	NPR	NSPR	COPT	PN/PT
⊙	1.491	0.707	0.97	0.156	0.1993	78.06
⊡	1.491	0.707	1.42	0.230	0.1945	78.08
△	1.491	0.707	6.35	1.029	0.2190	78.17
◇	1.491	0.707	9.40	1.524	0.2165	78.19
⊠	1.491	0.707	12.44	2.016	0.2080	78.20

c. $M_\infty = 1.2$
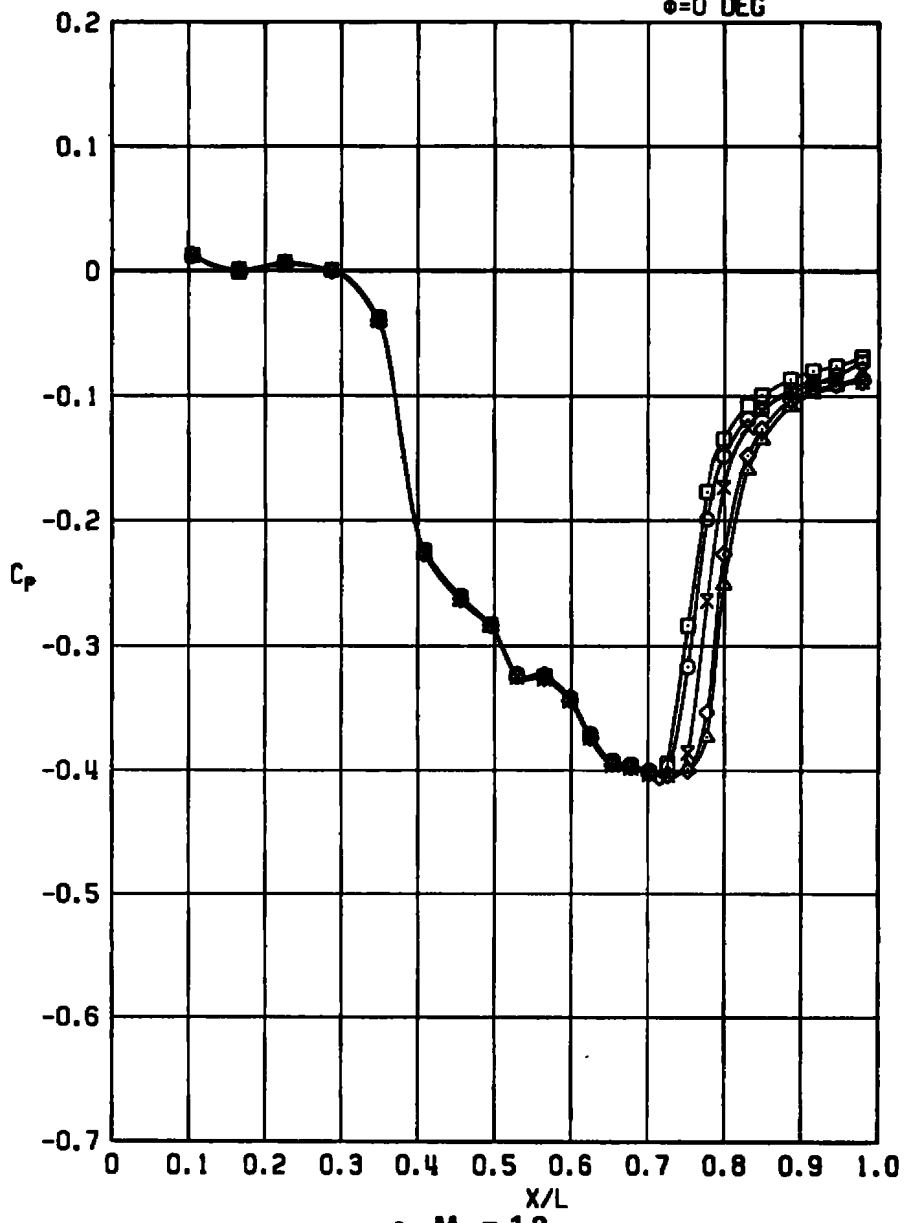
Figure A-4. Concluded.

SYM	A/A*	D_S/D_N	NPR	NSPR	CDPT	PN/PT
⊙	1.134	0.0	3.44	1.031	0.0246	84.11
□	1.134	0.543	3.44	1.032	0.0230	9.10
◇	1.142	0.866	3.46	1.019	0.0216	35.12
✕	1.127	0.950	3.29	1.003	0.0198	52.11

$\Phi = 0$ DEG

a. $M_\infty = 0.6$
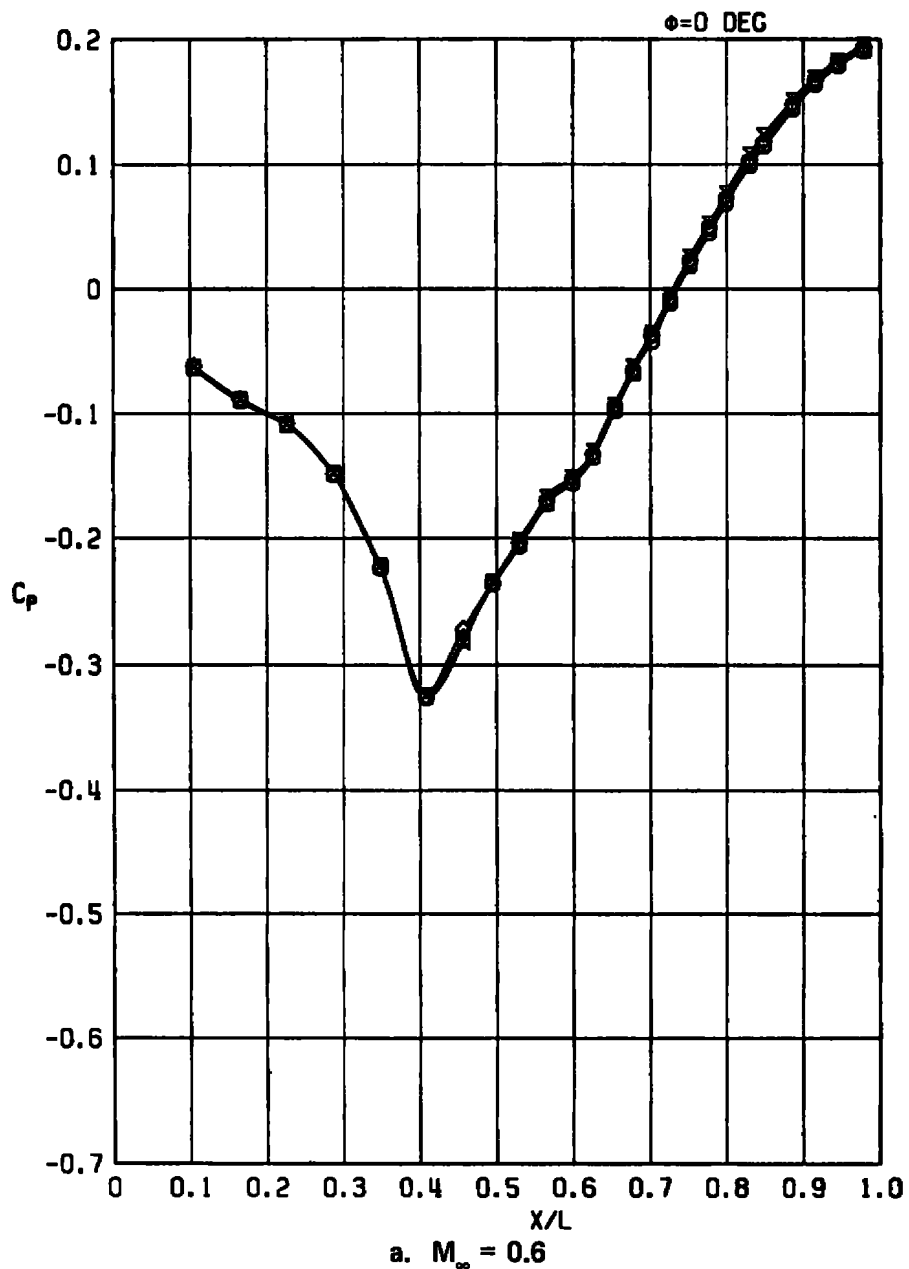
Figure A-5. Effects of sting to nozzle exit diameter ratio,
$A/A^* \approx 1.13$, NSPR ≈ 1.0.

SYM	A/A*	D_S/D_N	NPR	NSPR	CDPT	PN/PT
⊙	1.134	0.0	3.53	1.059	0.0318	86.13
⊡	1.134	0.543	3.44	1.029	0.0300	10.09
▲	1.133	0.707	3.42	1.028	0.0316	14.06
◇	1.142	0.866	3.37	0.992	0.0299	36.09
X	1.127	0.950	3.29	1.005	0.0297	54.13

$\Phi=0$ DEG
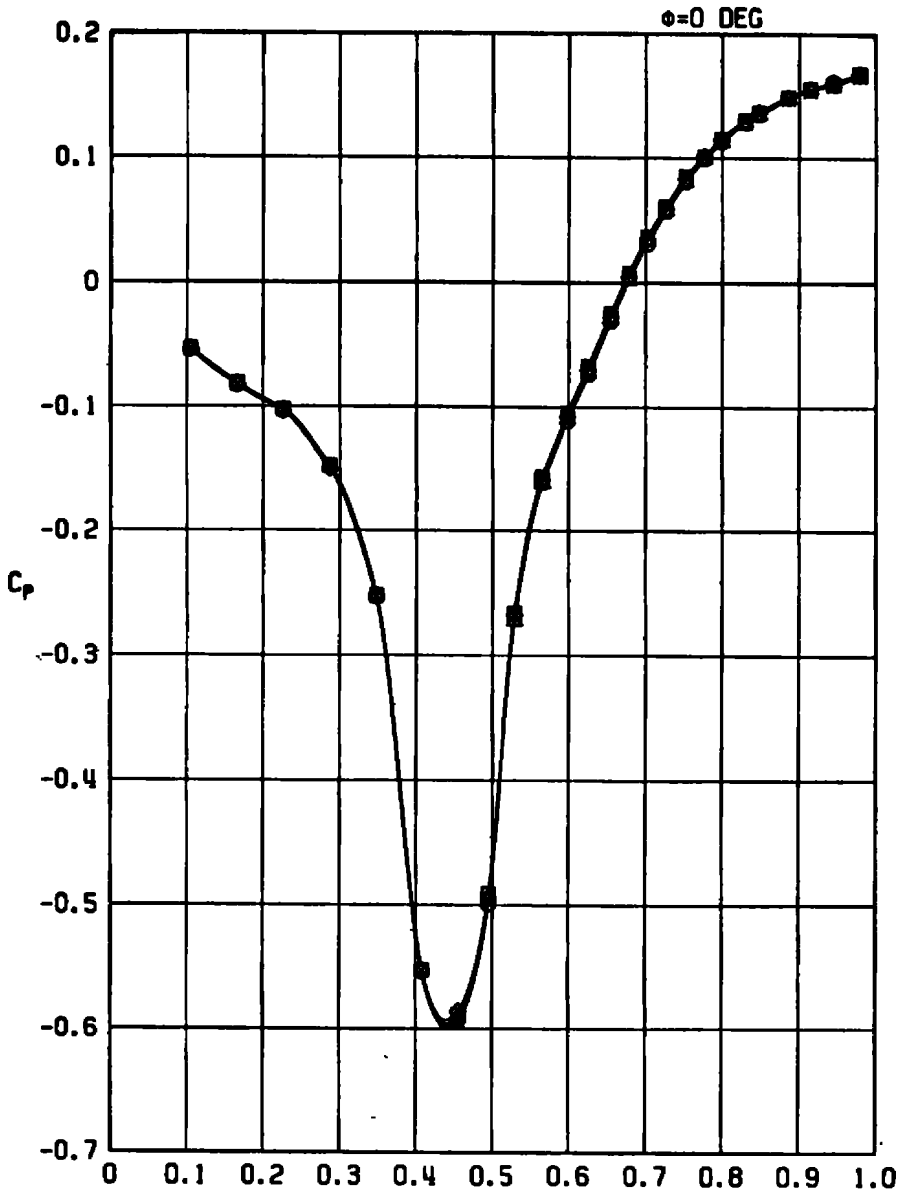
b. $M_\infty = 0.9$

Figure A-5. Continued.

SYM	A/A*	D_S/D_M	NPR	NSPR	CDPT	PN/PT
☉	1.134	0.0	3.51	1.052	0.2222	88.12
⊡	1.134	0.543	3.55	1.062	0.2176	11.11
△	1.133	0.707	3.34	1.002	0.2143	17.08
◇	1.142	0.866	3.44	1.012	0.2134	38.14
✕	1.127	0.950	3.32	1.012	0.2086	56.13

c. $M_\infty = 1.2$
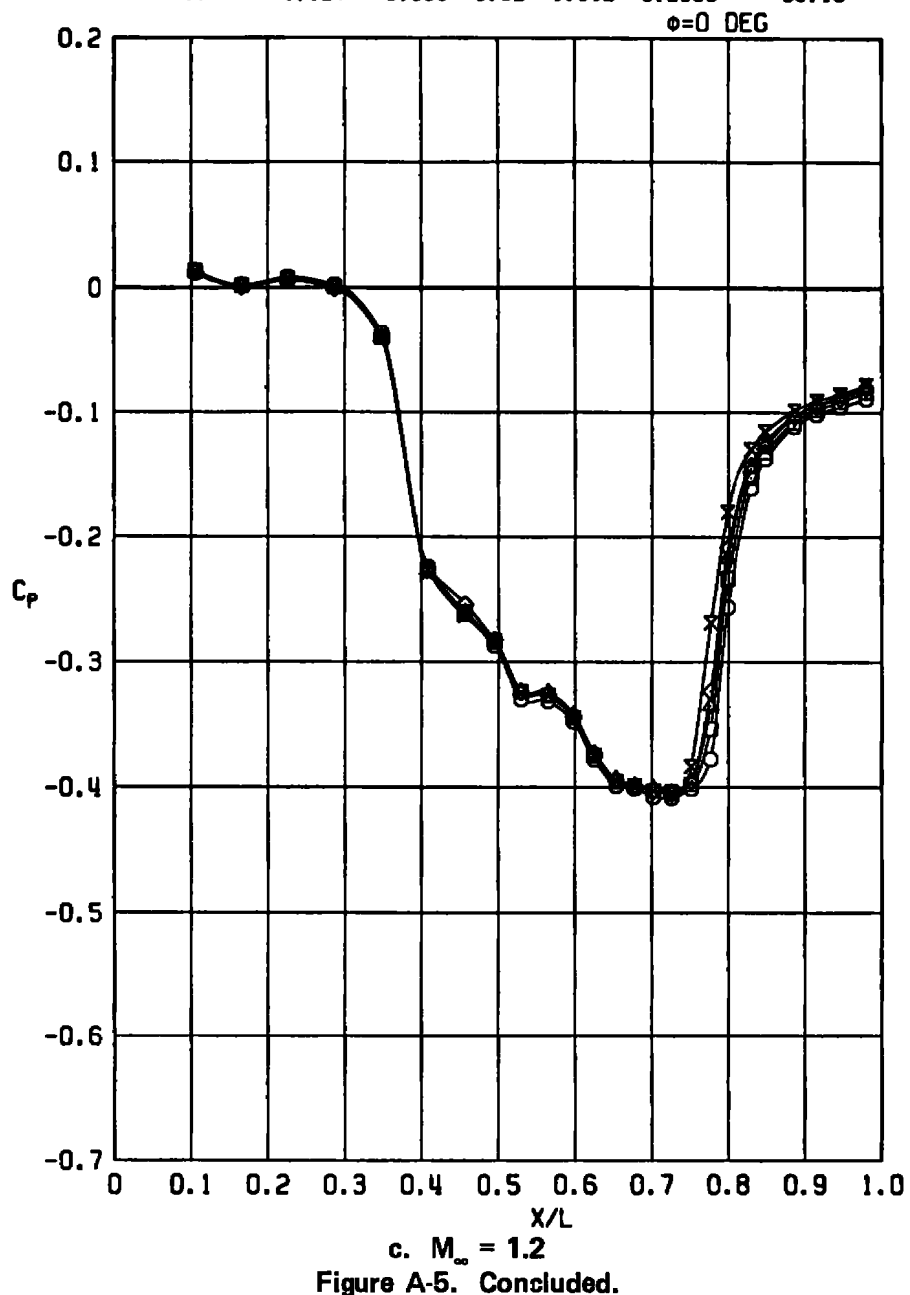
Figure A-5. Concluded.

SYM	A/A*	D_S/D_N	NPR	NSPR	CDPT	PN/PT
☉	1.134	0.0	7.00	2.097	0.0099	84.14
☐	1.134	0.543	7.00	2.098	0.0134	9.16
◇	1.142	0.866	6.85	2.016	0.0201	35.15
✗	1.127	0.950	6.62	2.020	0.0219	52.14
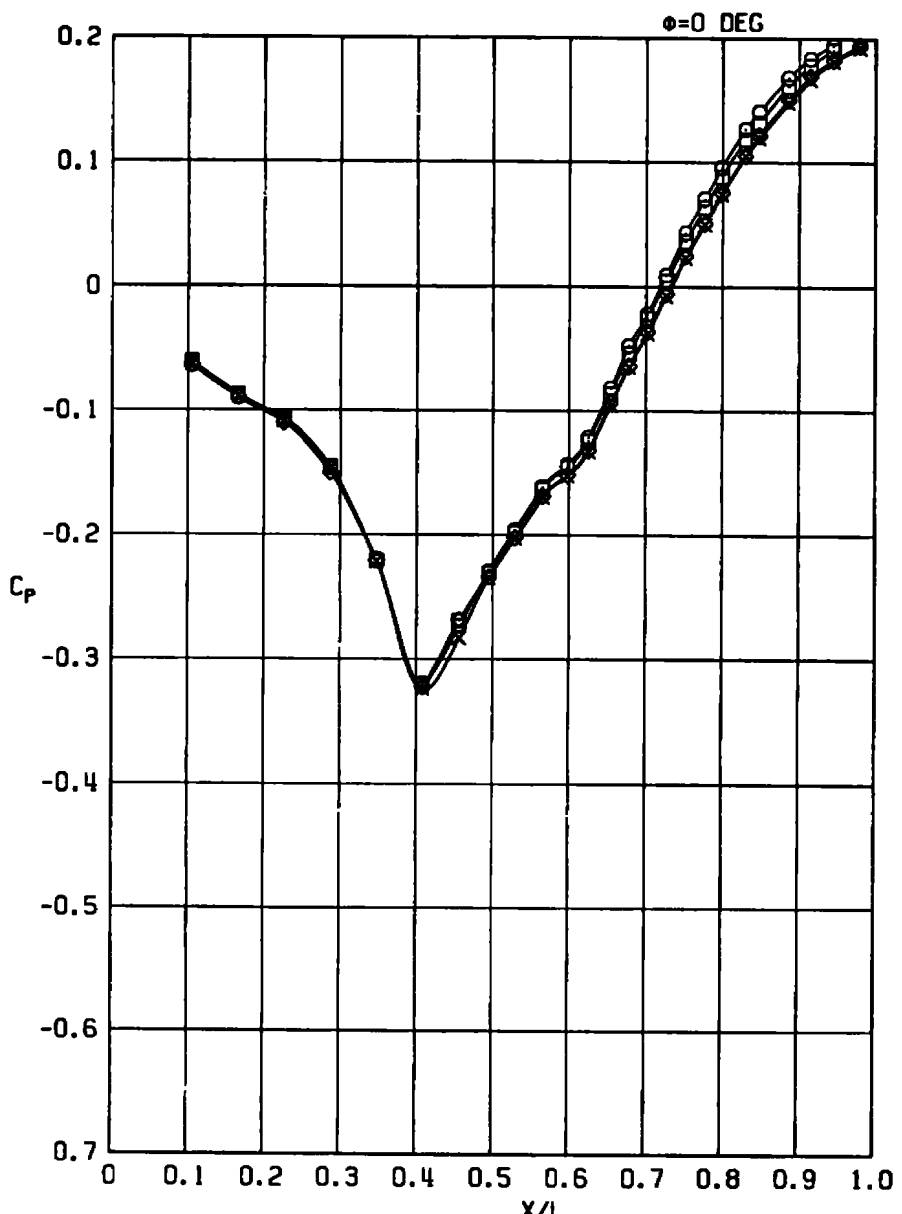
a. $M_\infty = 0.6$

Figure A-6. Effects of sting to nozzle exit diameter ratio,
$A/A^* \approx 1.13$, NSPR ≈ 2.0.

SYM	A/A^*	D_S/D_N	NPR	NSPR	CDPT	PN/PT
⊙	1.134	0.0	6.98	2.092	0.0169	86.16
▣	1.134	0.543	6.99	2.093	0.0213	10.12
△	1.133	0.707	6.79	2.038	0.0296	14.09
◇	1.142	0.866	6.89	2.028	0.0299	36.12
✗	1.127	0.950	6.55	1.997	0.0314	54.16

$\Phi = 0$ DEG
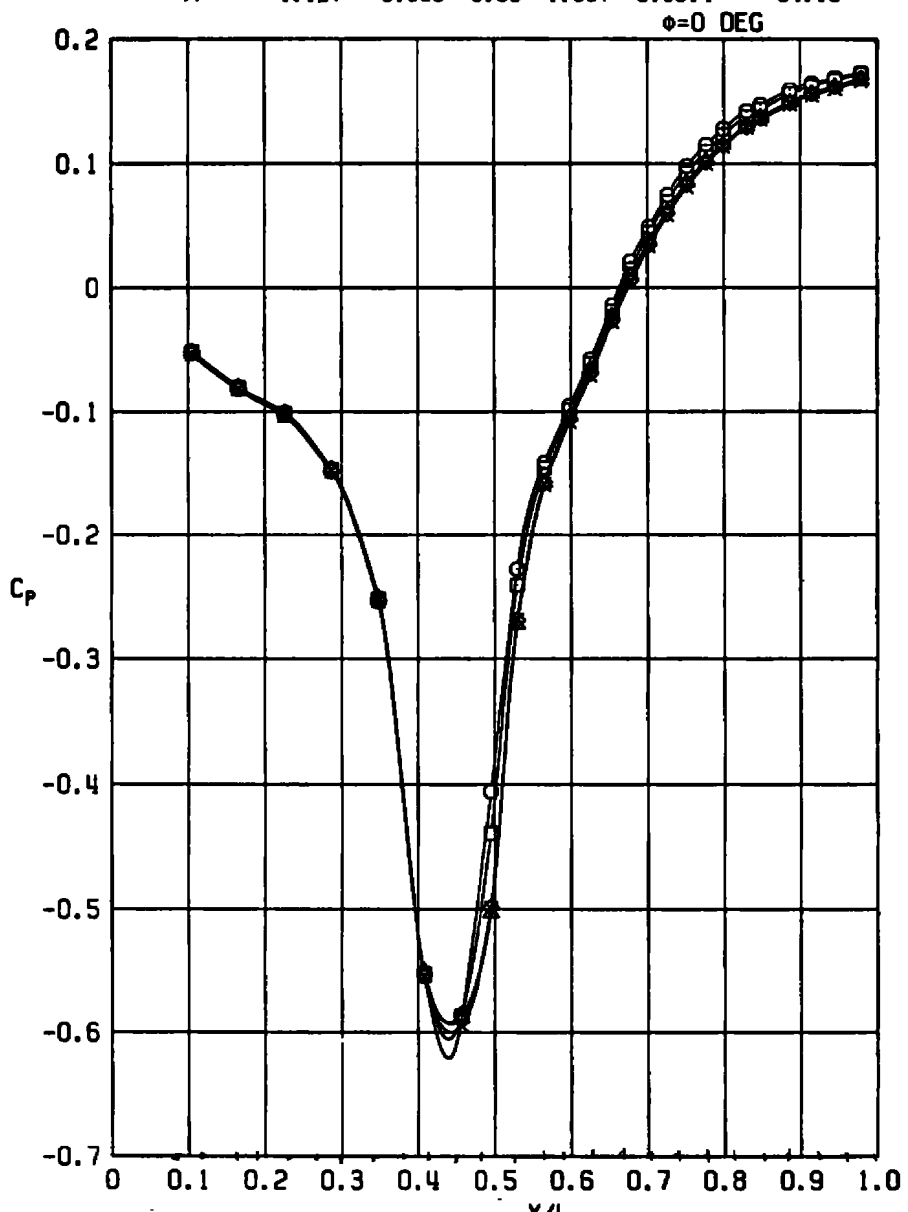
b. $M_\infty = 0.9$

Figure A-6. Continued.

SYM	A/A*	D_S/D_N	NPR	NSPR	COPT	PN/PT
⊙	1.134	0.0	7.14	2.141	0.1962	88.15
⊡	1.134	0.543	7.02	2.101	0.2053	11.14
△	1.133	0.707	6.70	2.011	0.2118	17.11
◇	1.142	0.866	6.92	2.035	0.2175	38.17
X	1.127	0.950	6.58	2.006	0.2146	56.16

c. $M_\infty = 1.2$

Figure A-6. Concluded.
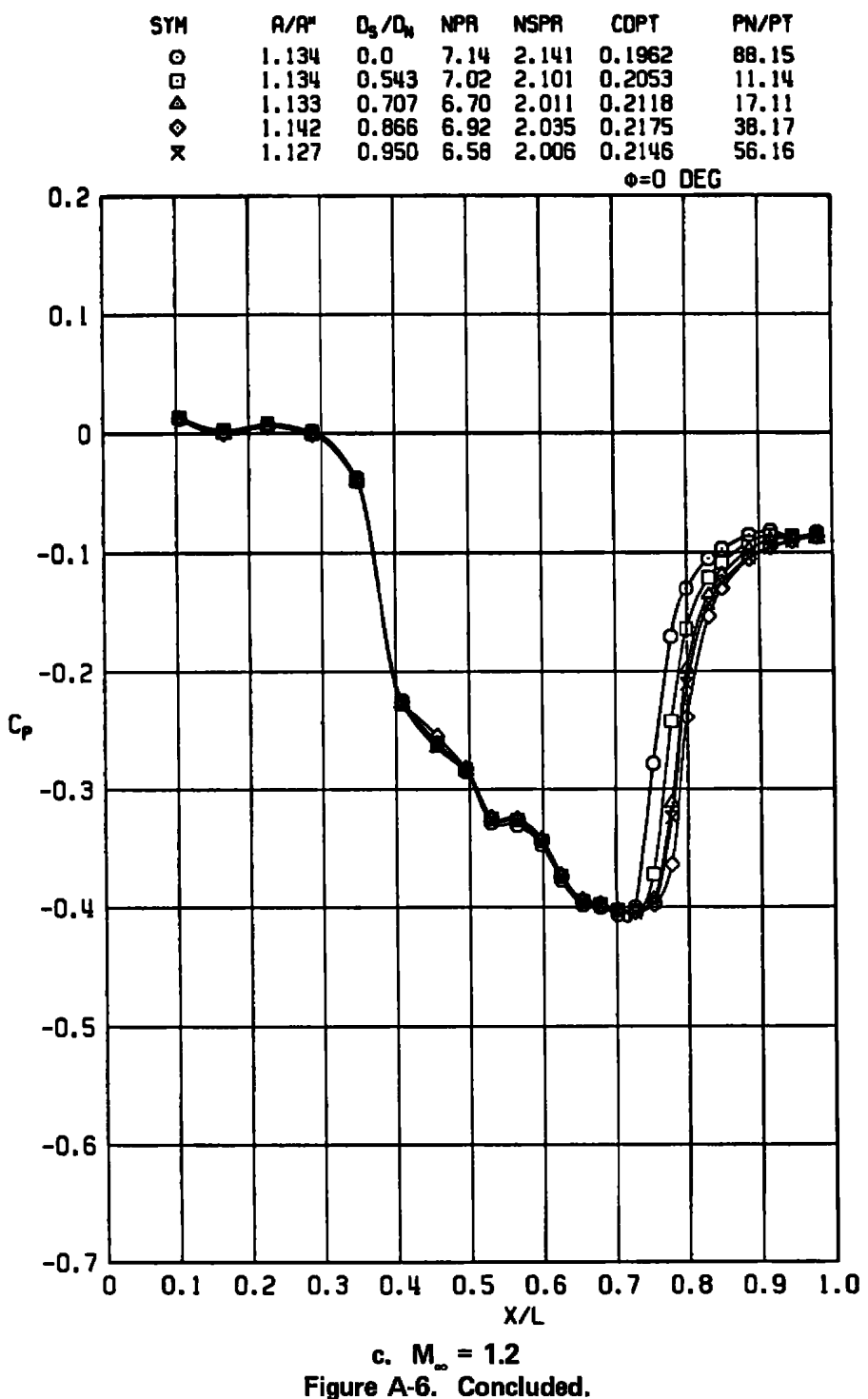
SYM	A/A*	D_S/D_N	NPR	NSPR	CDPT	PN/PT
⊙	1.490	0.0	6.27	1.018	0.0261	118.11
▢	1.486	0.542	6.15	1.003	0.0237	104.16
△	1.491	0.707	6.24	1.011	0.0232	74.13
◇	1.500	0.866	6.36	1.018	0.0250	128.11
✕	1.463	0.949	5.95	1.001	0.0220	60.13

Φ=0 DEG
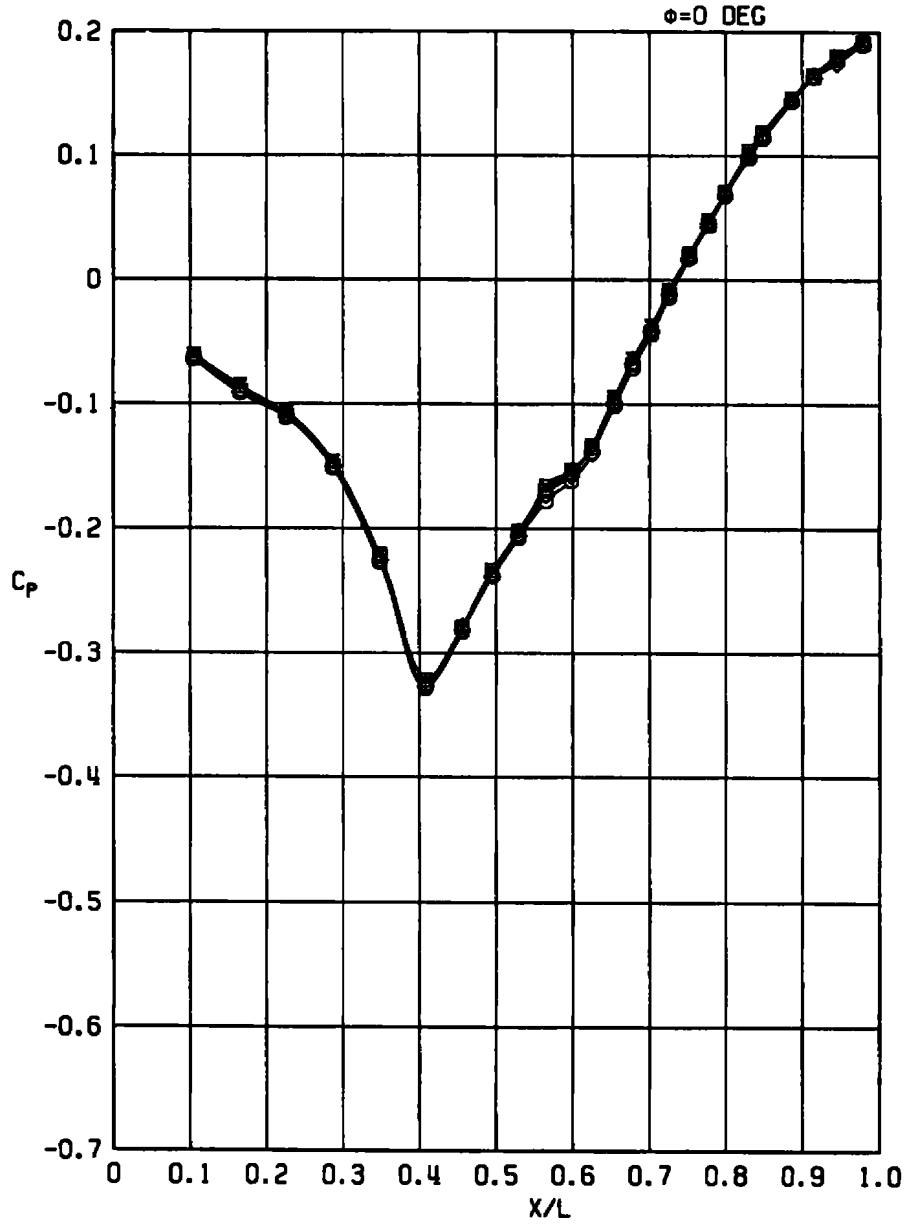
a. $M_\infty = 0.6$

Figure A-7. Effects of sting to nozzle exit diameter ratio,
A/A* ≈ 1.49, NSPR ≈ 1.0.

SYM	A/A*	D_S/D_N	NPR	NSPR	CDPT	PN/PT
⊙	1.490	0.0	6.32	1.026	0.0351	120.10
⊡	1.486	0.542	6.31	1.030	0.0319	105.12
△	1.491	0.707	6.24	1.012	0.0360	76.14
◇	1.500	0.866	6.12	0.980	0.0367	126.10
✕	1.463	0.949	5.91	0.994	0.0323	62.18

Φ=0 DEG
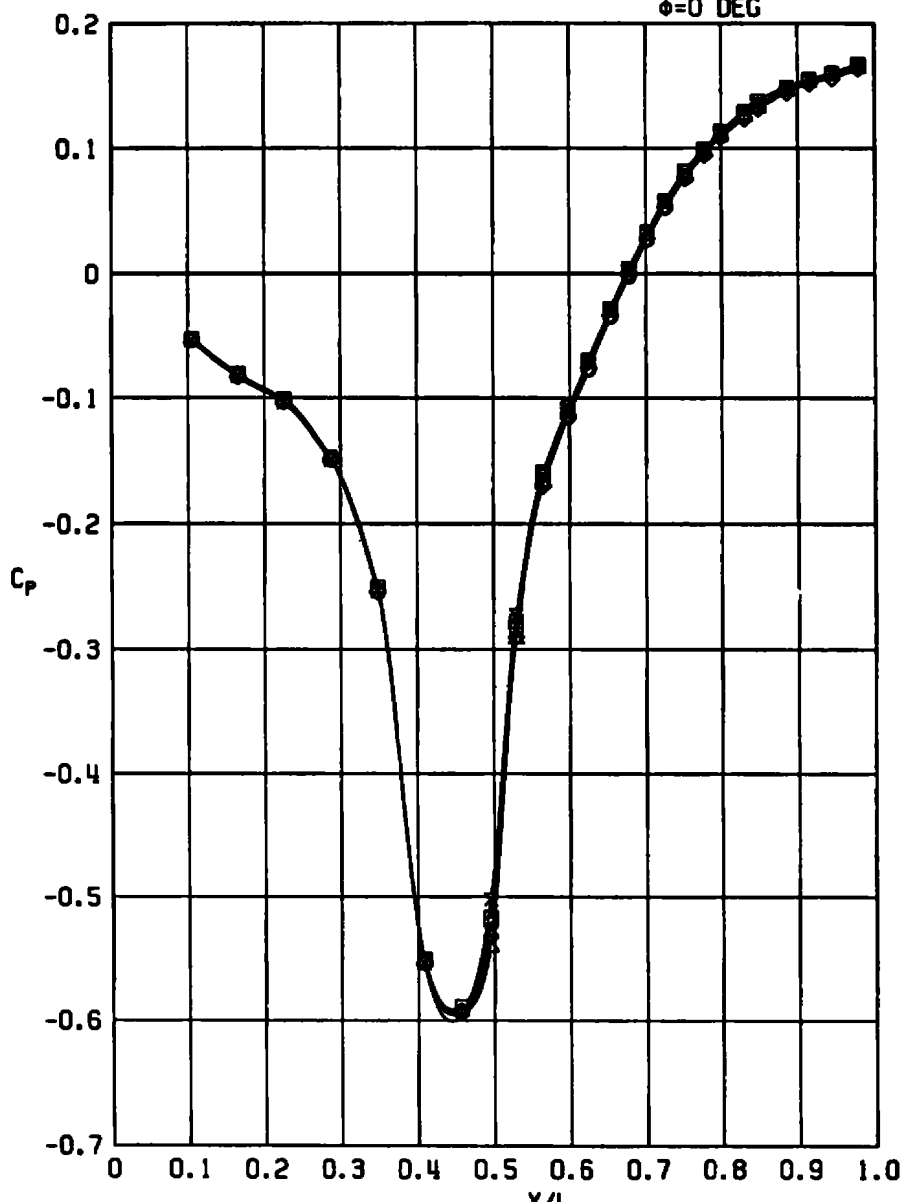
b. $M_\infty = 0.9$

Figure A-7. Continued.
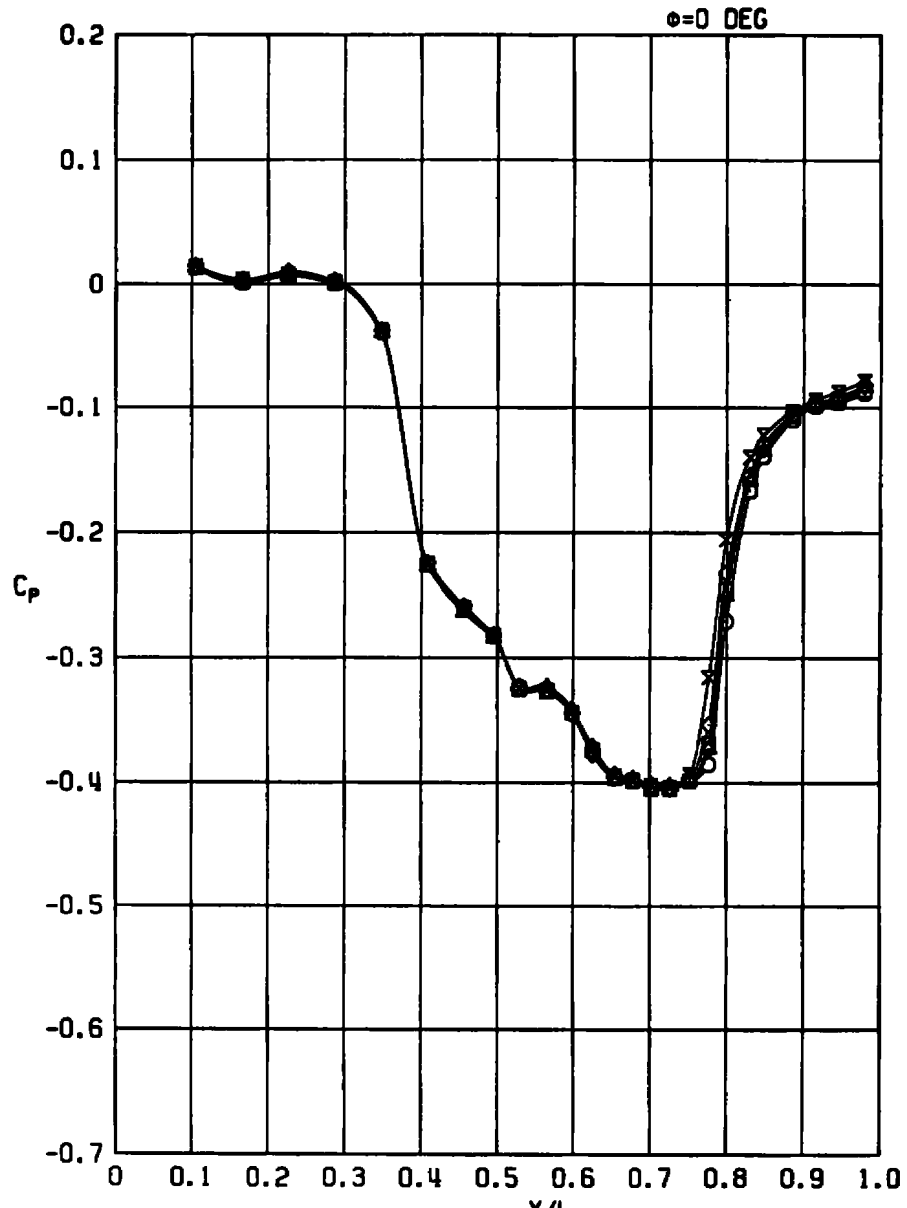
c. $M_\infty = 1.2$

Figure A-7. Concluded.

SYM	A/A*	D_S/D_N	NPR	NSPR	CDPT	PN/PT
□	1.486	0.542	12.37	2.019	0.0130	104.19
△	1.491	0.707	12.35	2.001	0.0176	74.16
◇	1.500	0.866	12.90	2.066	0.0235	128.14
✕	1.463	0.949	11.75	1.979	0.0252	60.16

Φ=0 DEG
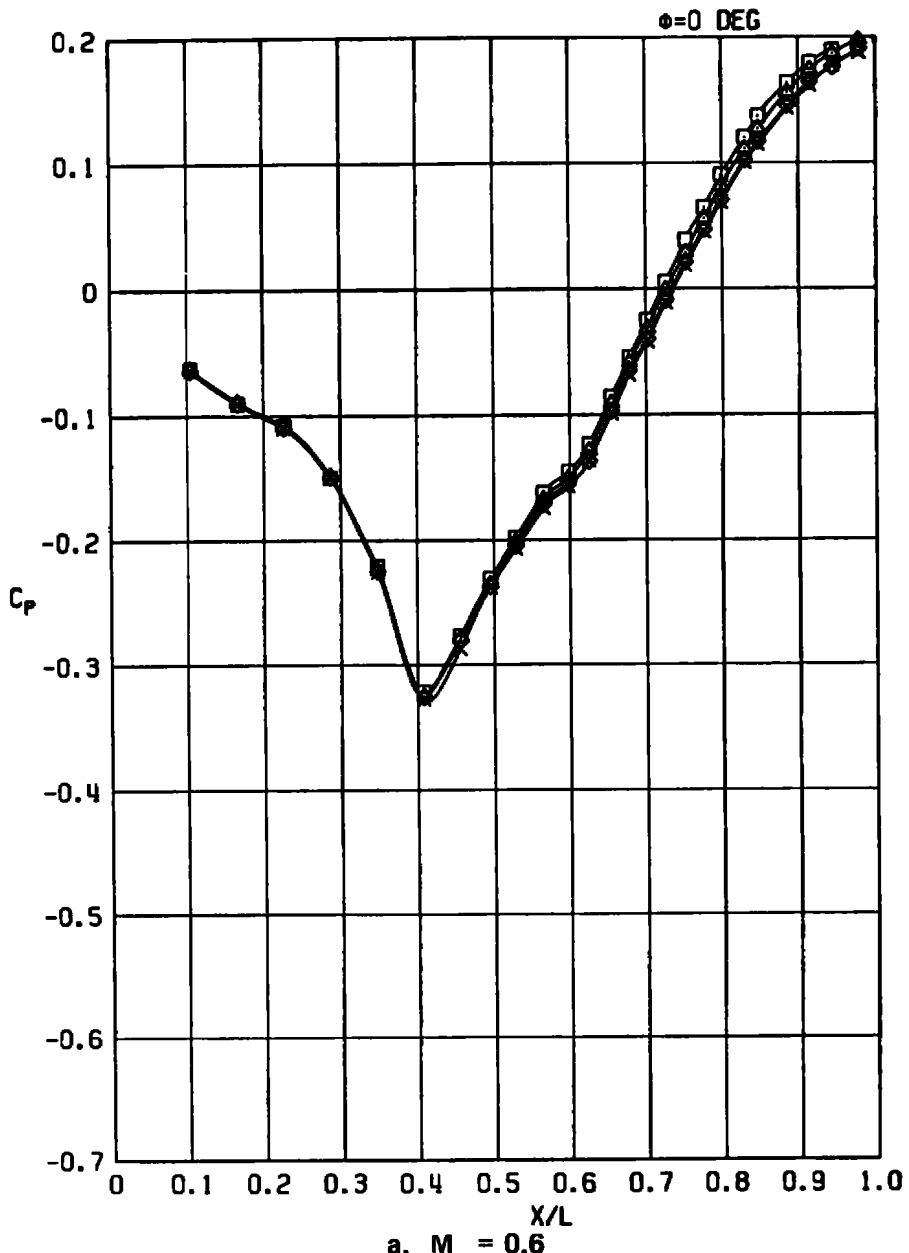
Figure A-8. Effects of sting to nozzle exit diameter ratio,
A/A* ≈ 1.49, NSPR ≈ 2.0.

a. $M_\infty = 0.6$

147

SYM	A/A*	D_S/D_N	NPR	NSPR	CDPT	PN/PT
⊙	1.490	0.0	13.29	2.157	0.0140	120.13
⊡	1.486	0.542	12.52	2.044	0.0197	105.15
△	1.491	0.707	12.62	2.046	0.0293	76.17
◇	1.500	0.866	13.12	2.101	0.0341	126.13
✕	1.463	0.949	11.87	1.998	0.0329	62.21

$\phi = 0$ DEG
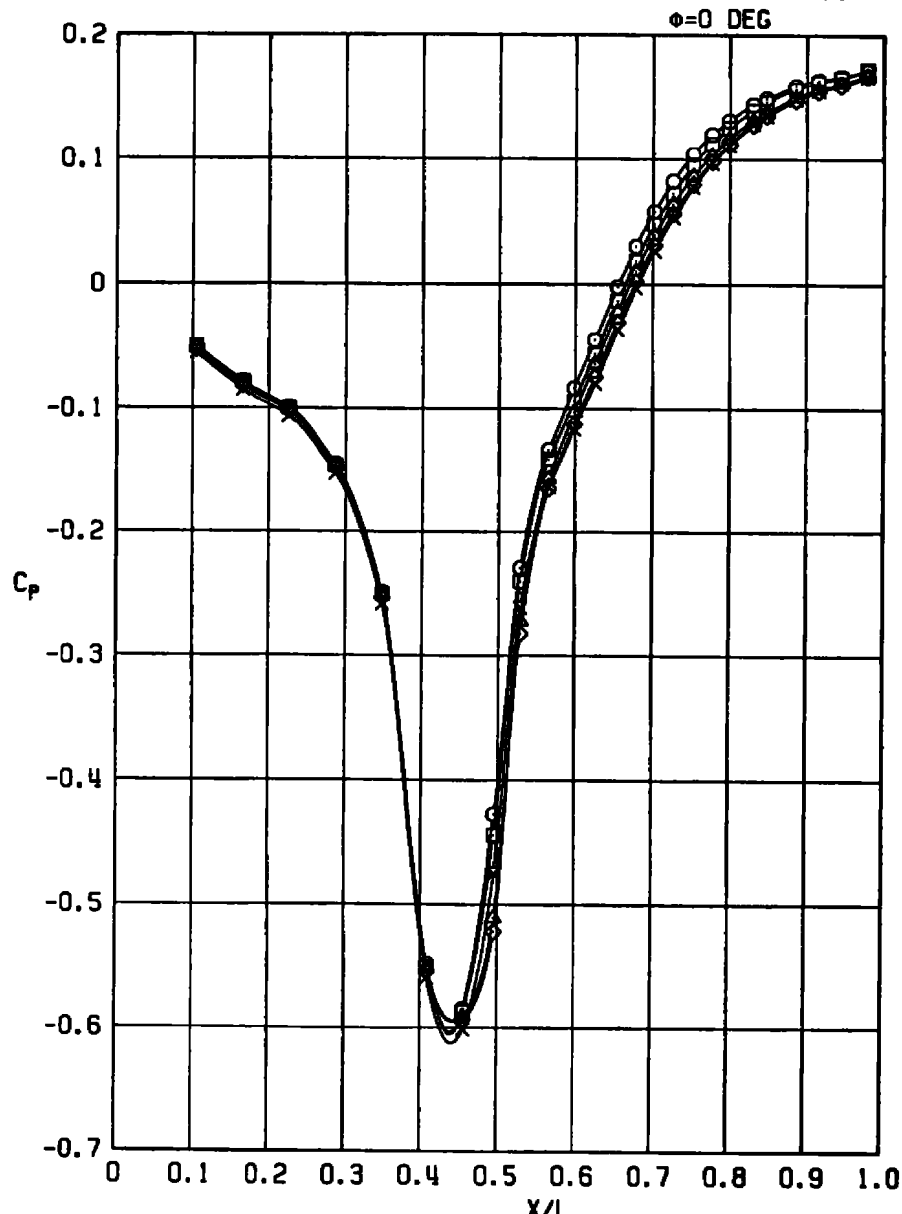
b. $M_\infty = 0.9$

Figure A-8. Continued.

SYM	A/A*	D$_S$/D$_M$	NPR	NSPR	CDPT	PN/PT
⊙	1.490	0.0	12.98	2.107	0.1902	122.14
□	1.486	0.542	12.54	2.047	0.1977	106.14
△	1.491	0.707	12.44	2.016	0.2080	78.20
◇	1.500	0.866	13.02	2.086	0.2207	127.13
✗	1.463	0.949	11.82	1.989	0.2180	64.15

c. $M_\infty = 1.2$

Figure A-8. Concluded.

a. $M_\infty = 0.6$

Figure A-9. Effects of nozzle area ratio, $D_s/D_N = 0$, NSPR $\approx$ 1.0.
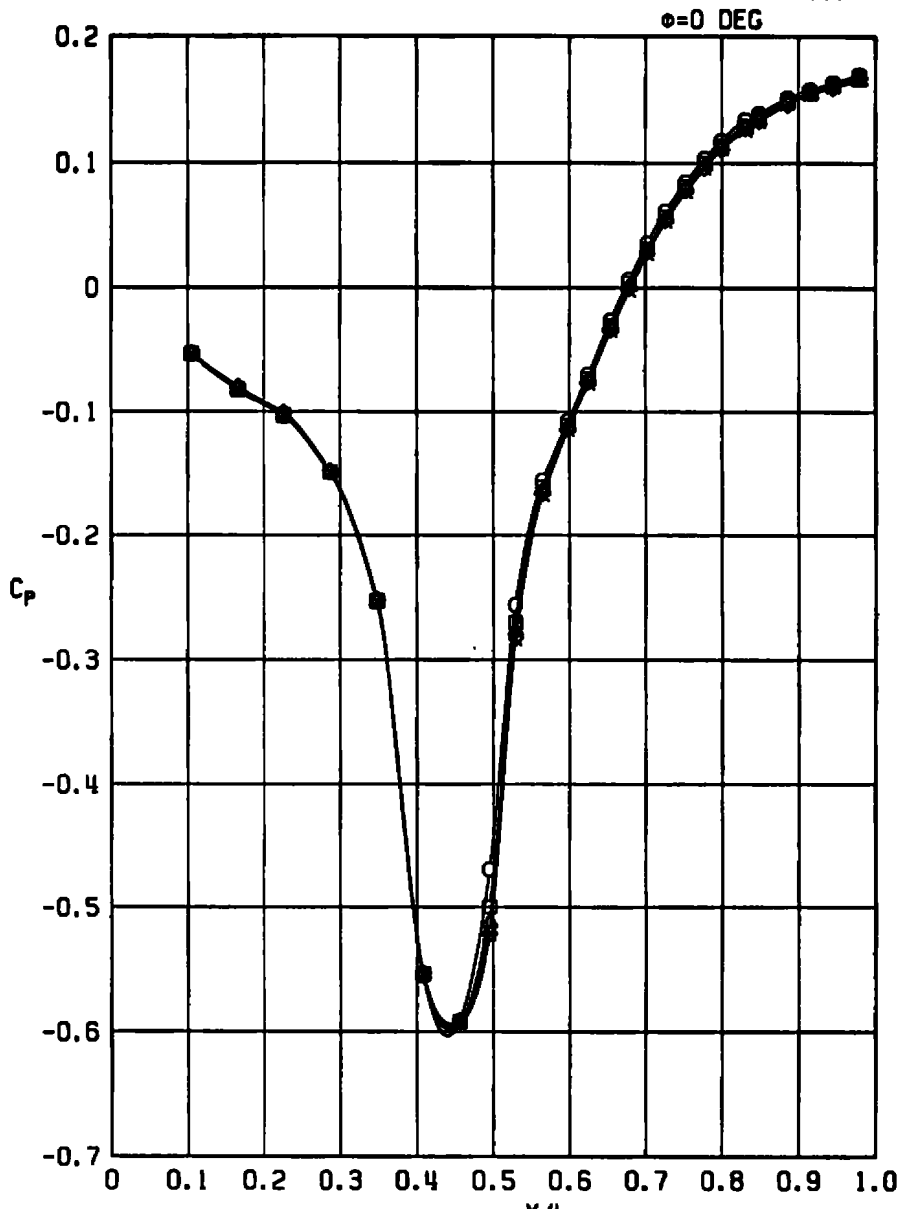
b. $M_\infty = 0.9$
Figure A-9. Continued.

STM	A/A*	D_S/D_N	NPR	NSPR	CDPT	PN/PT
□	1.134	0.0	3.51	1.052	0.2222	88.12
△	1.221	0.0	4.20	1.044	0.2209	94.12
◇	1.300	0.0	4.86	1.048	0.2201	113.10
✕	1.490	0.0	6.19	1.004	0.2219	122.11
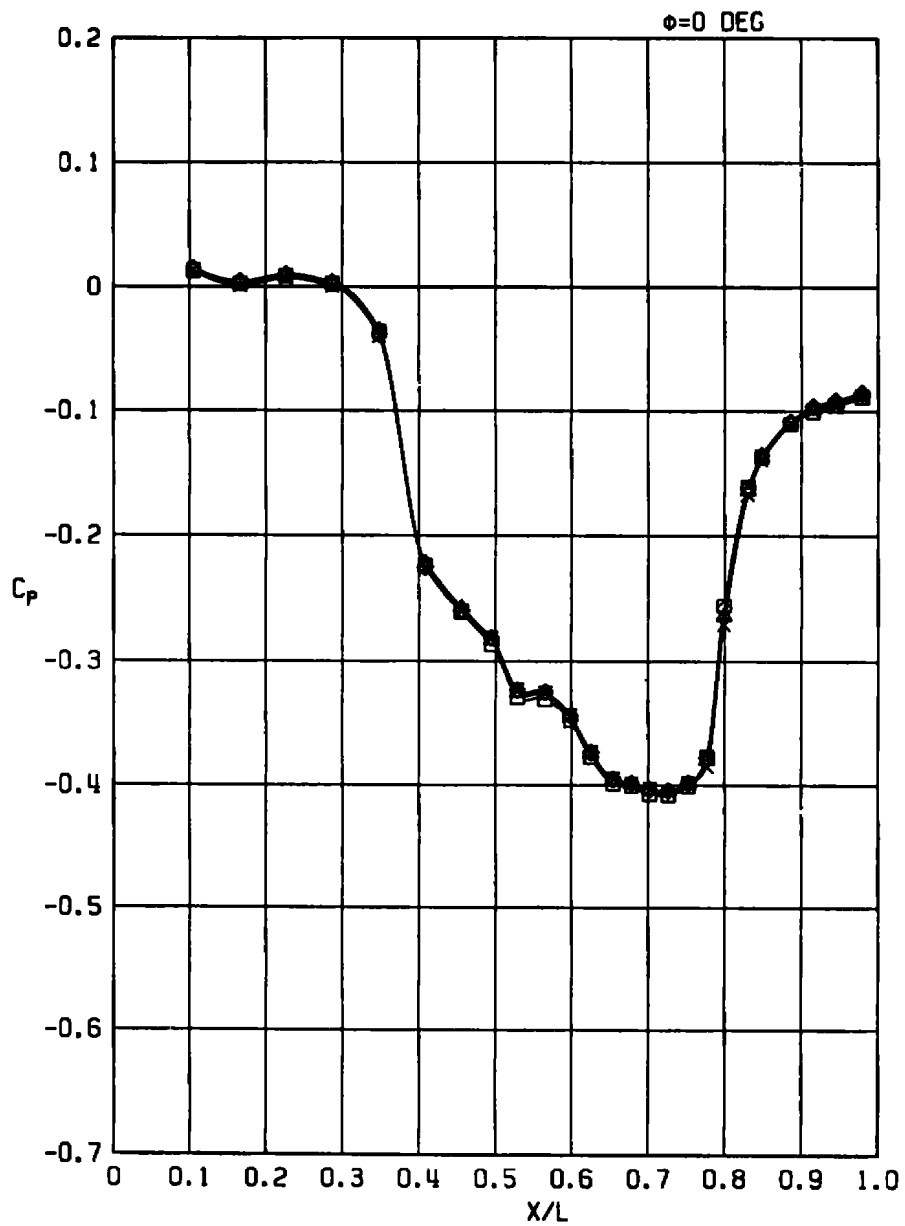
c. $M_\infty = 1.2$

Figure A-9. Concluded.

SYM	A/A*	D_S/D_N	NPR	NSPR	CDPT	PN/PT
⊙	1.000	0.0	3.61	1.899	0.0187	46.12
□	1.134	0.0	7.00	2.097	0.0099	84.14
△	1.221	0.0	8.33	2.071	0.0105	92.15
◇	1.300	0.0	9.67	2.085	0.0069	109.18
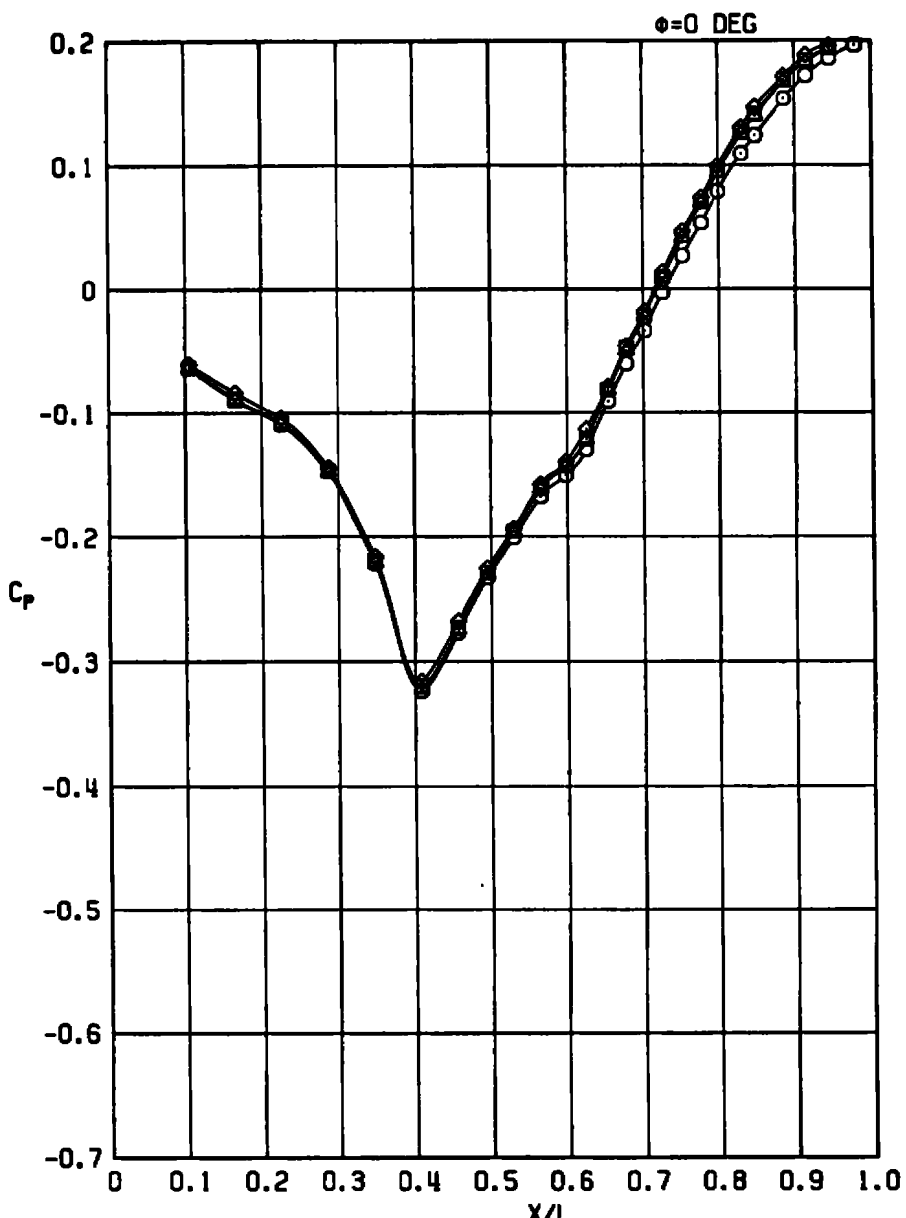
a. $M_\infty = 0.6$

Figure A-10. Effects of nozzle area ratio, $D_s/D_N = 0$, NSPR ≈ 2.0.

b. $M_\infty = 0.9$

Figure A-10. Continued.

154

c. $M_\infty = 1.2$

Figure 10. Concluded.

SYM	A/A*	D_s/D_N	NPR	NSPR	CDPT	PN/PT
△	1.220	0.706	4.10	1.022	0.0227	69.17
◇	1.310	0.707	4.61	0.977	0.0244	97.13
✕	1.491	0.707	6.24	1.011	0.0232	74.13
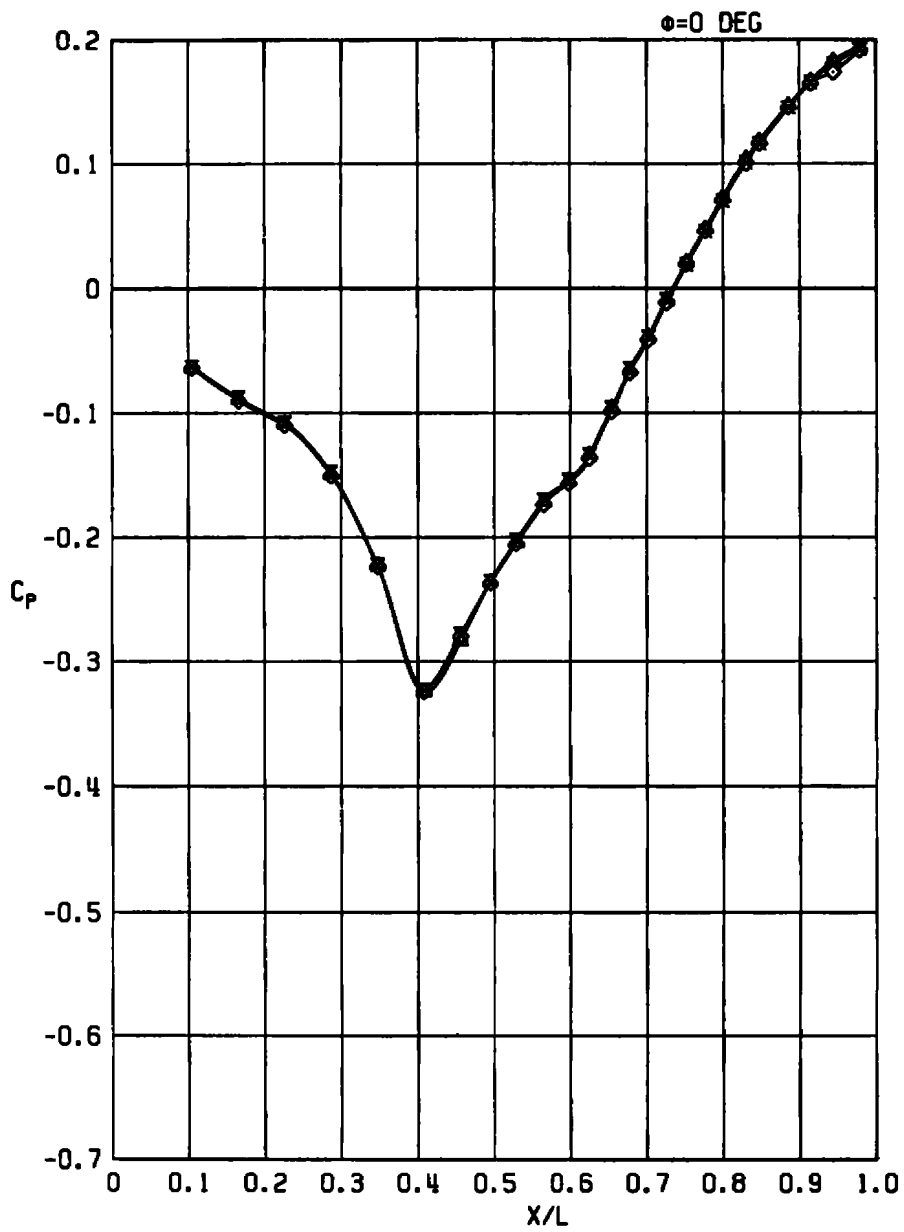
a. $M_\infty = 0.6$

Figure A-11. Effects of nozzle area ratio,
D_s/D_N = 0.707, NSPR ≈ 1.0.

SYM	A/A*	D_S/D_N	NPR	NSPR	CDPT	PN/PT
□	1.133	0.707	3.42	1.028	0.0316	14.06
△	1.220	0.706	4.14	1.032	0.0338	70.14
◇	1.310	0.707	4.69	0.995	0.0348	98.16
X	1.491	0.707	6.24	1.012	0.0360	76.14

b. $M_\infty = 0.9$

Figure A-11. Continued.

157
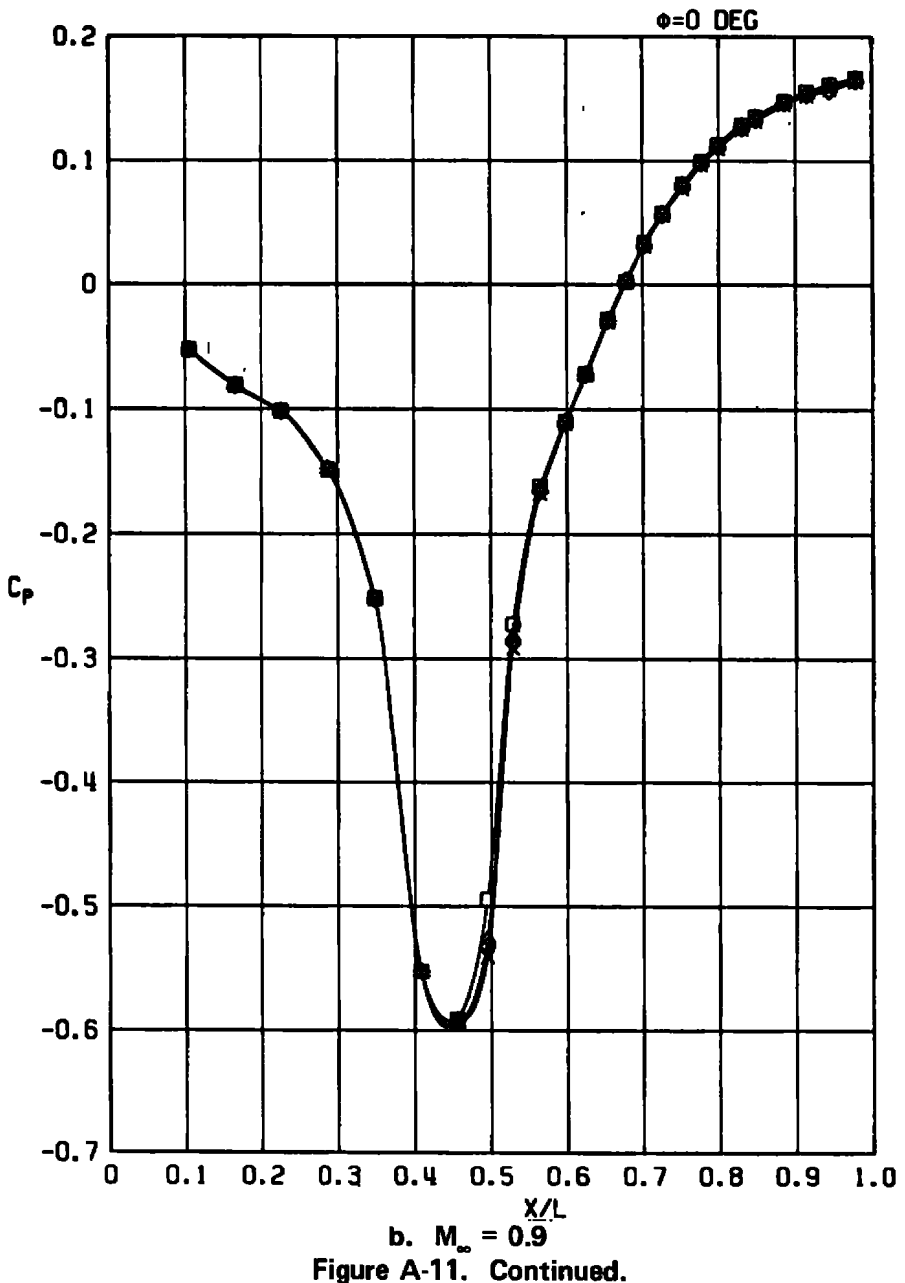
SYM	A/A*	D_S/D_N	NPR	NSPR	COPT	PN/PT
□	1.133	0.707	3.34	1.002	0.2143	17.08
△	1.220	0.706	4.14	1.031	0.2175	71.13
◇	1.310	0.707	4.70	0.997	0.2188	99.13
X	1.491	0.707	6.35	1.029	0.2190	78.17

$\phi=0$ DEG

c. $M_\infty = 1.2$
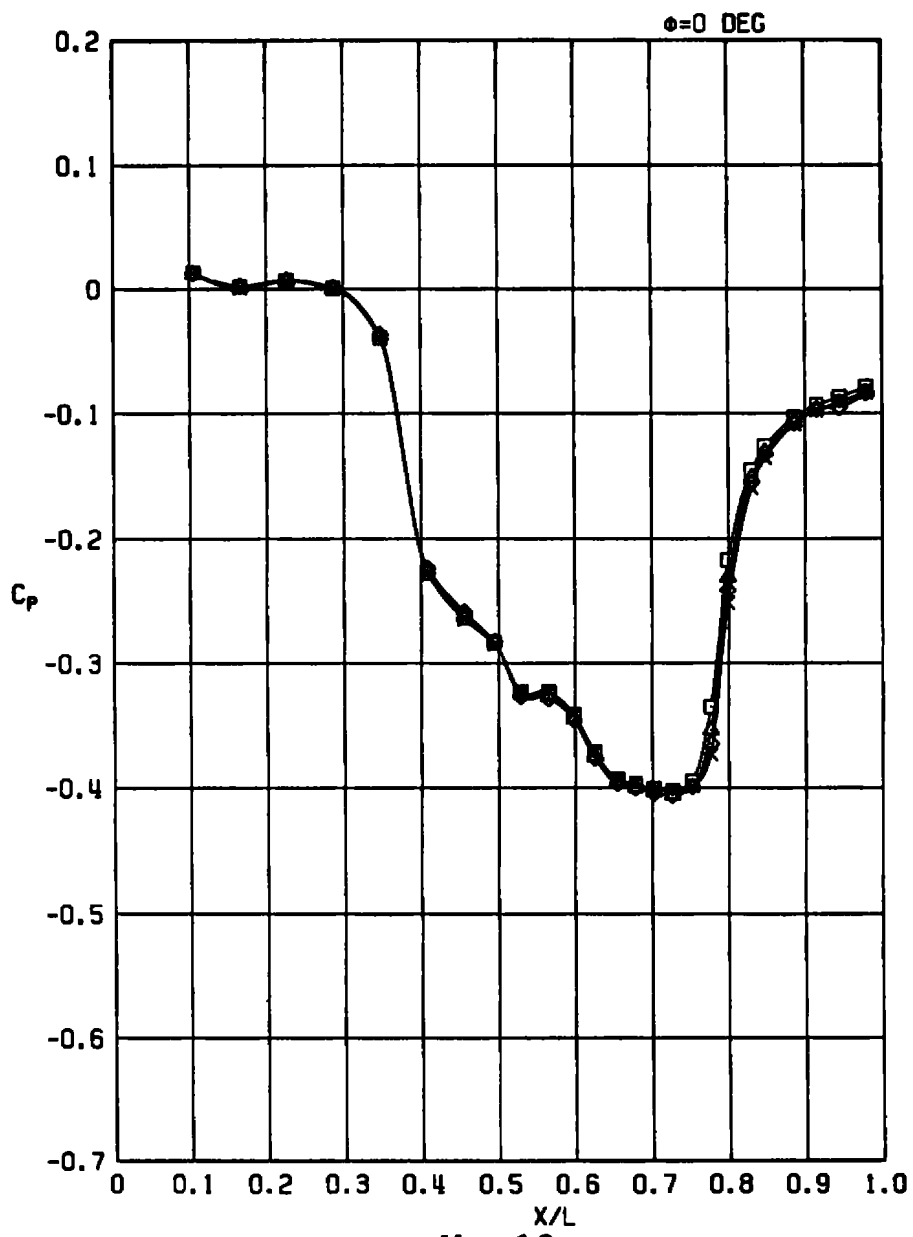
Figure A-11. Concluded.

SYM	A/A*	D$_s$/D$_N$	NPR	NSPR	COPT	PN/PT
△	1.220	0.706	8.11	2.019	0.0188	69.20
◇	1.310	0.707	9.22	1.954	0.0191	97.16
X	1.491	0.707	12.35	2.001	0.0176	74.16
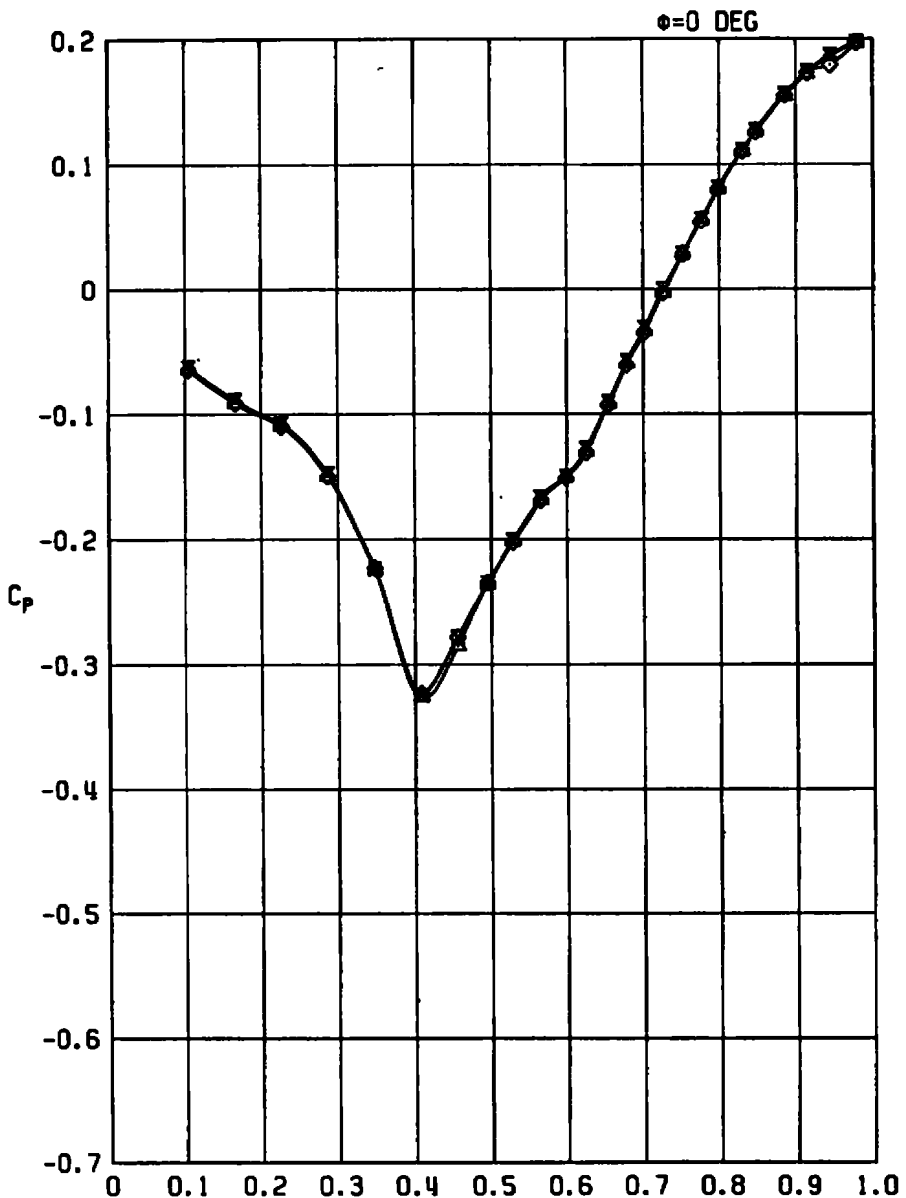
a. $M_\infty = 0.6$

Figure A-12. Effects of nozzle area ratio,
D_s/D_N = 0.707, NSPR ≈ 2.0.

SYM	A/A*	D_S/D_N	NPR	NSPR	COPT	PN/PT
□	1.133	0.707	6.79	2.038	0.0296	14.09
△	1.220	0.706	8.25	2.054	0.0286	70.17
◇	1.310	0.707	9.38	1.989	0.0301	98.19
✕	1.491	0.707	12.62	2.046	0.0293	76.17
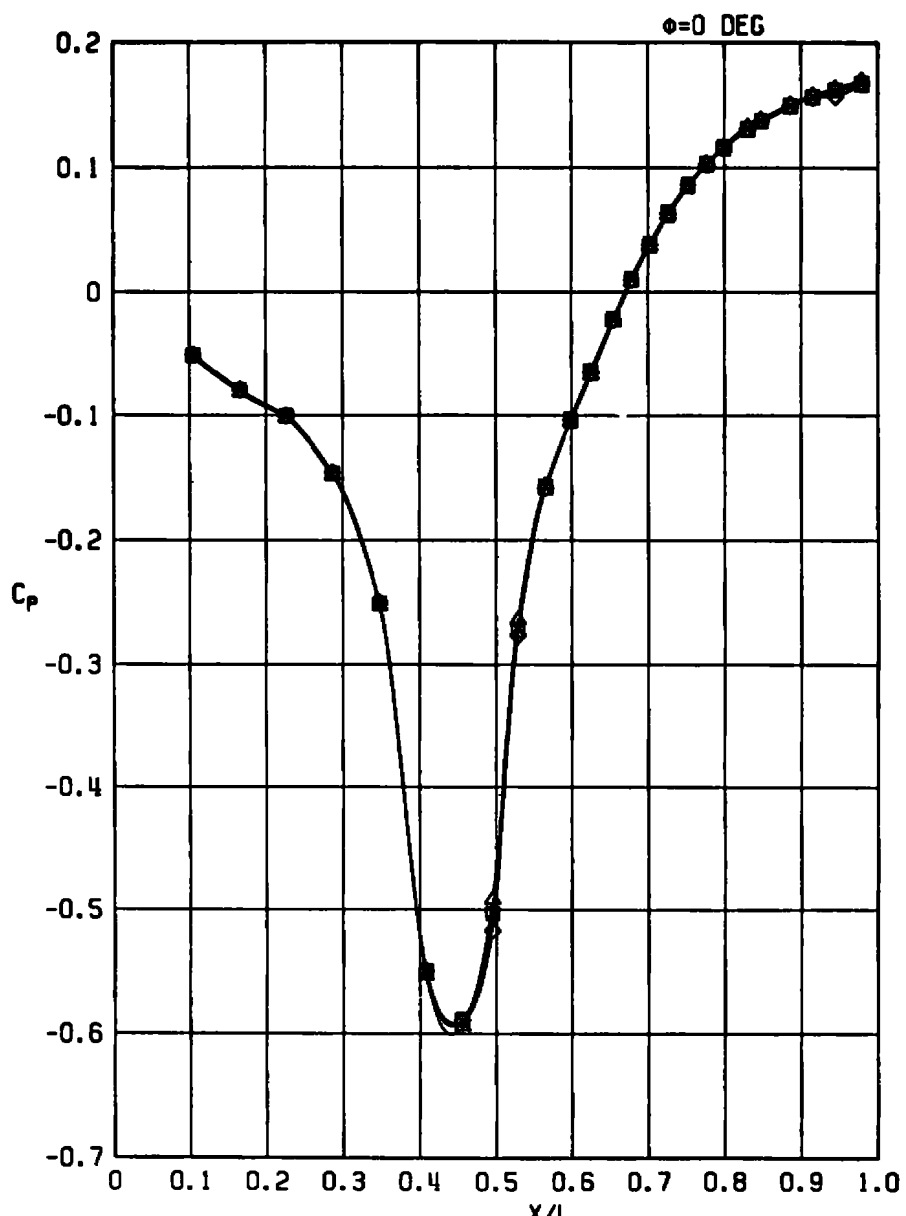
b. $M_\infty = 0.9$

Figure A-12. Continued.

SYM	A/A*	D_S/D_N	NPR	NSPR	CDPT	PN/PT
□	1.133	0.707	6.70	2.011	0.2118	17.11
△	1.220	0.706	8.14	2.029	0.2117	71.16
◇	1.310	0.707	9.39	1.991	0.2109	99.17
✕	1.491	0.707	12.44	2.016	0.2080	78.20
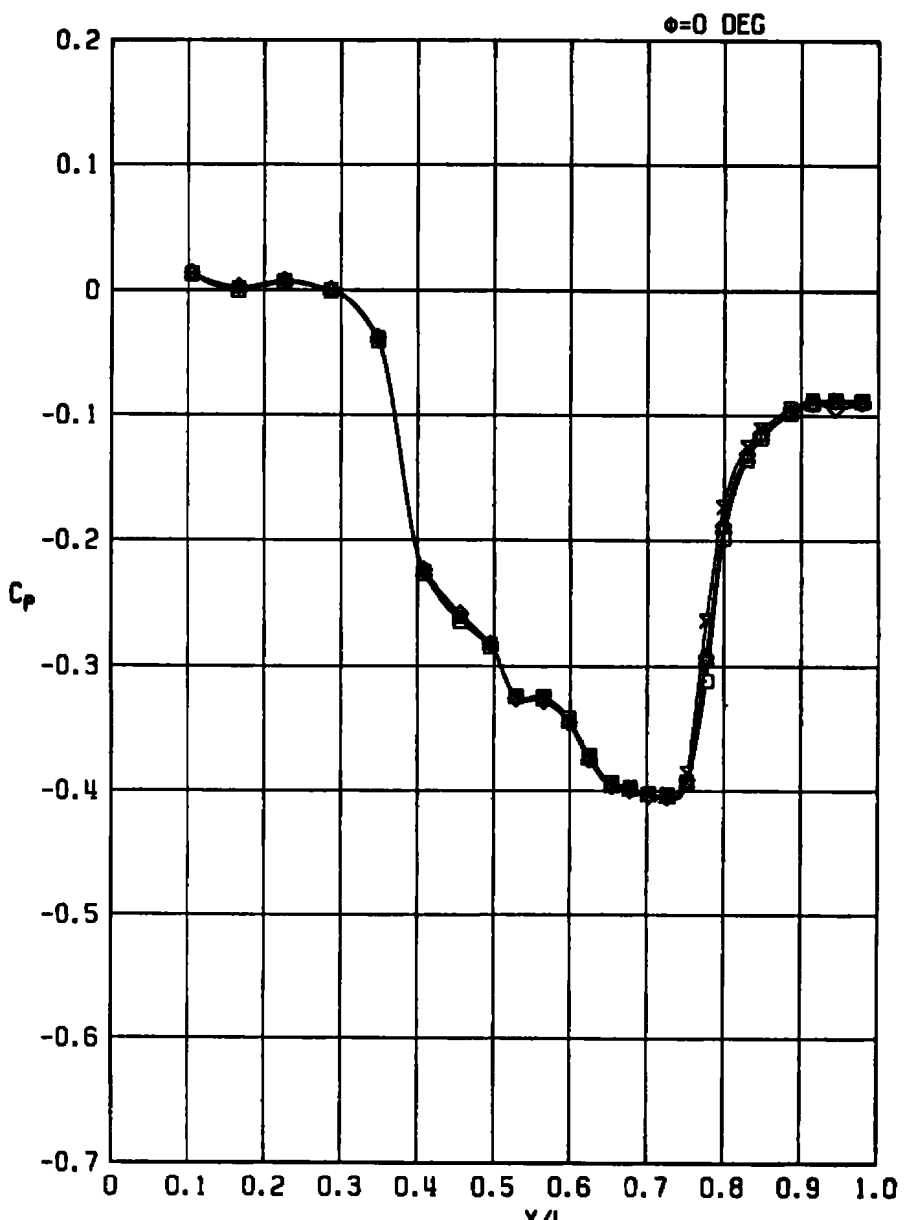
c. $M_\infty = 1.2$

Figure A-12. Concluded.

SYM	A/A*	D_s/D_N	NPR	NSPR	COPT	PN/PT	M_∞
⊙	1.134	0.0	3.44	1.031	0.0246	84.11	0.6
⊡	1.134	0.0	3.53	1.059	0.0318	86.13	0.9
△	1.134	0.0	3.51	1.052	0.2222	88.12	1.2
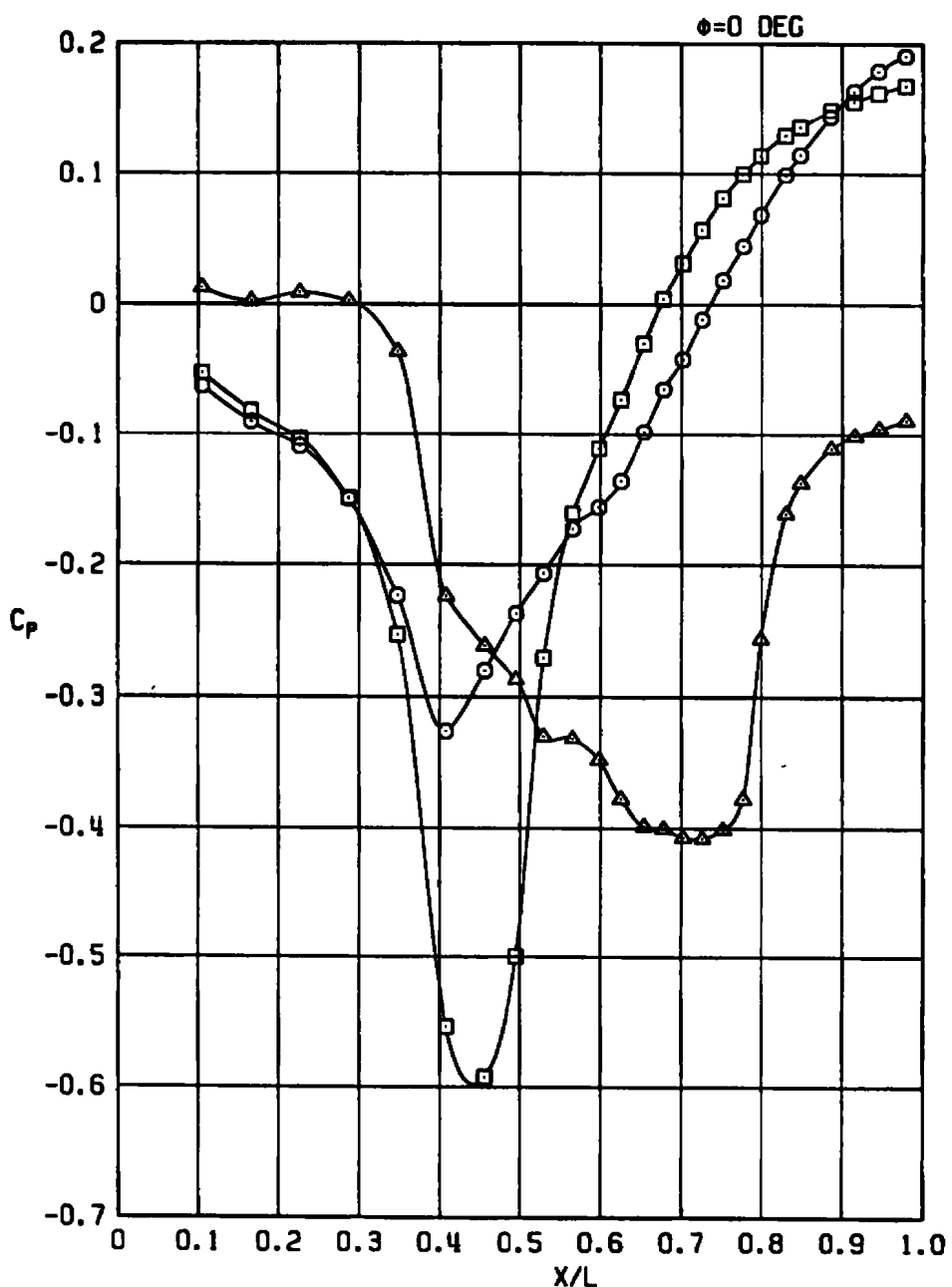
Figure A-13. Effects of Mach number, D_s/D_n = 0,
A/A* = 1.134, NSPR ≈ 1.0.

SYM	A/A*	D_S/D_N	NPR	NSPR	CDPT	PN/PT	M_∞
⊙	1.134	0.0	7.00	2.097	0.0099	84.14	0.6
▢	1.134	0.0	6.98	2.092	0.0169	86.16	0.9
△	1.134	0.0	7.14	2.141	0.1962	88.15	1.2

Φ=0 DEG

C_P

X/L
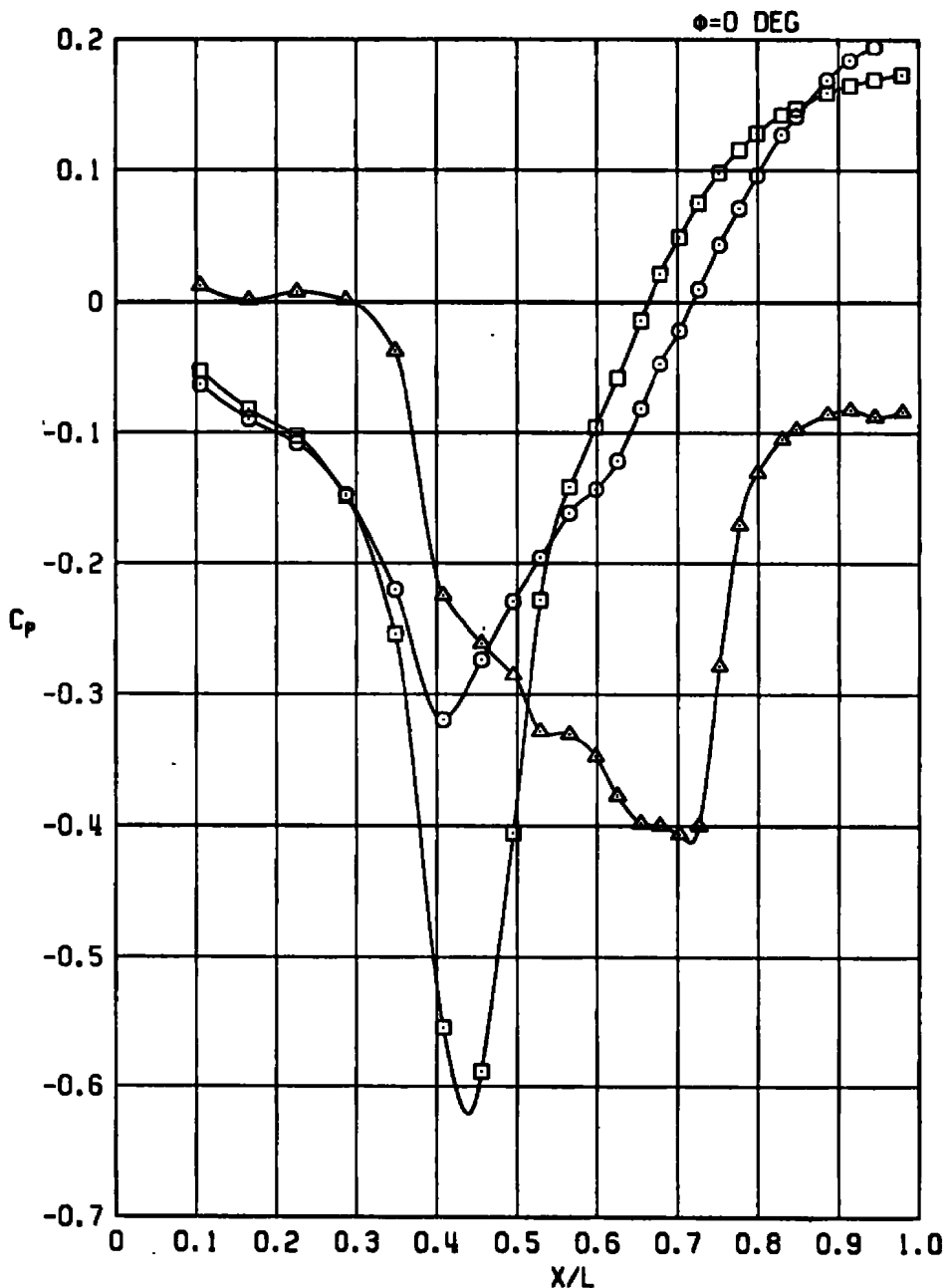
Figure A-14. Effects of Mach number, $D_s/D_N = 0$,
A/A*·= 1.134, NSPR ≈ 2.0.

SYM	A/A^*	D_s/D_N	NPR	NSPR	CDPT	PN/PT	M_∞
⊙	1.142	0.866	3.46	1.019	0.0216	35.12	0.6
⊡	1.142	0.866	3.37	0.992	0.0299	36.09	0.9
△	1.142	0.866	3.44	1.012	0.2134	38.14	1.2
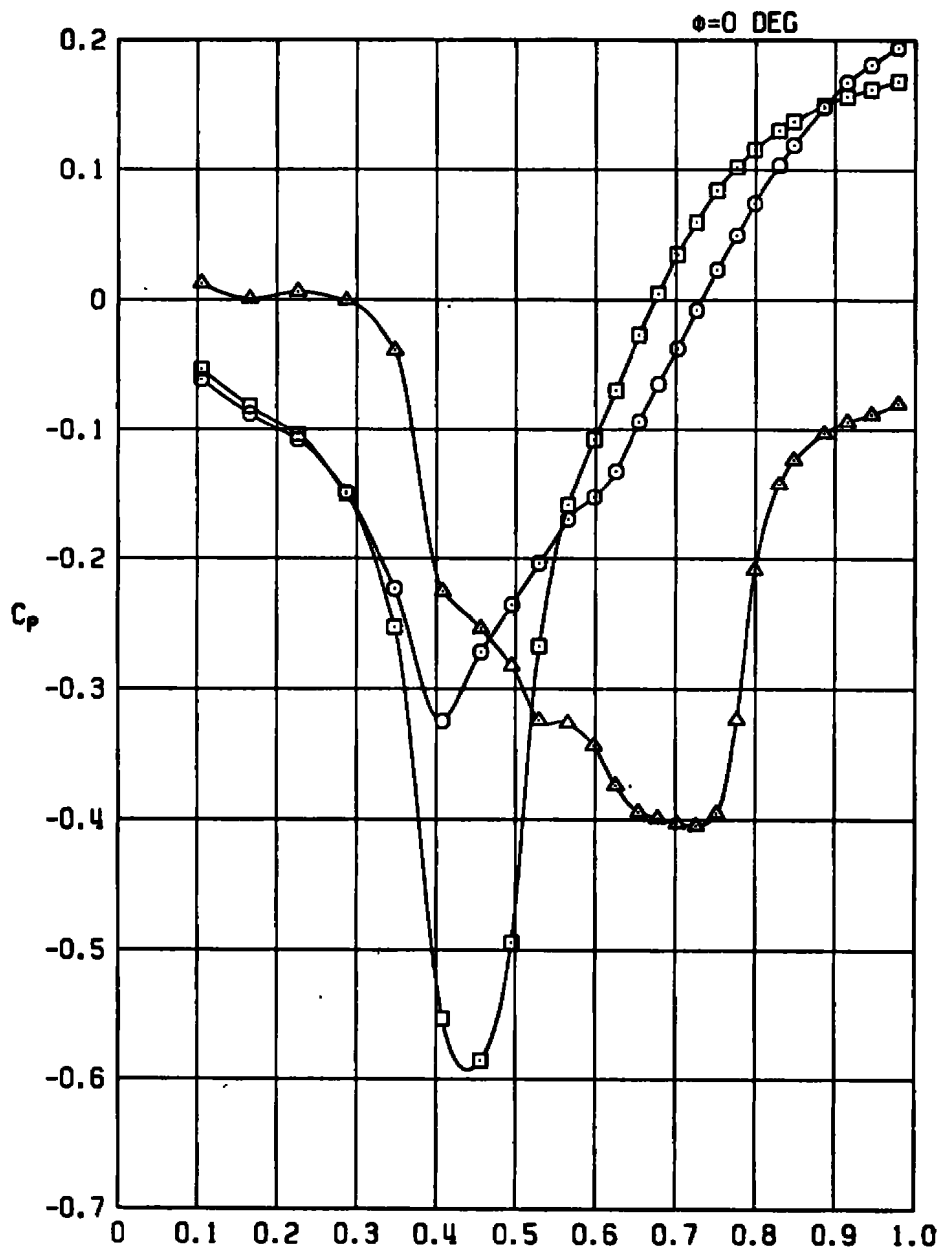
Figure A-15. Effects of Mach number, D_s/D_N = 0.866, A/A^* = 1.142, NSPR ≈ 1.0.

SYM	A/A*	D_s/D_N	NPR	NSPR	COPT	PN/PT	M_∞
⊙	1.142	0.866	6.85	2.016	0.0201	35.15	0.6
□	1.142	0.866	6.89	2.028	0.0299	36.12	0.9
△	1.142	0.866	6.92	2.035	0.2175	38.17	1.2

Φ=0 DEG
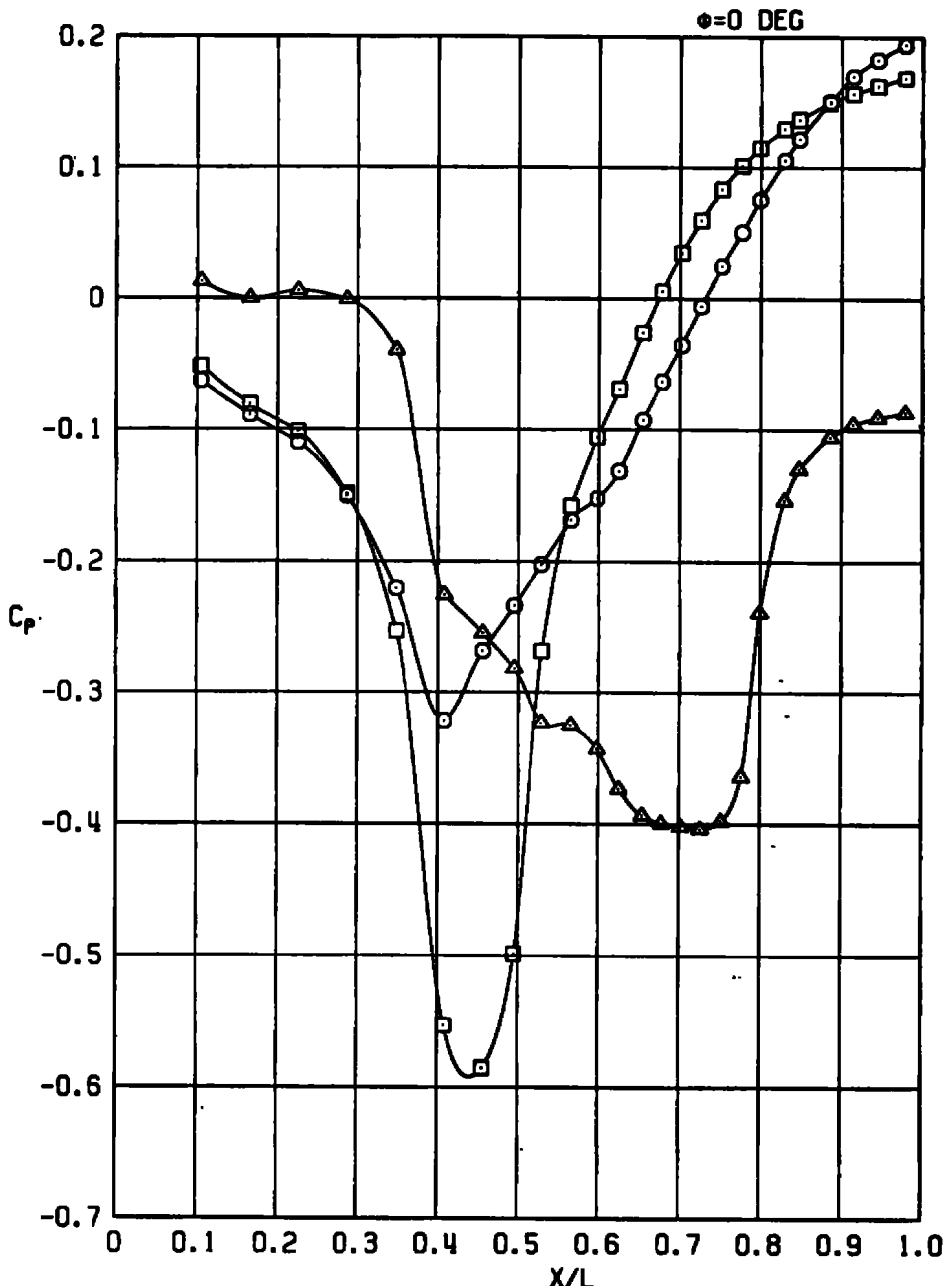
Figure A-16. Effects of Mach number, D_s/D_N = 0.866,
A/A* = 1.142, NSPR ≈ 2.0.

α, deg	SYM	A/A*	D_s/D_N	NPR	NSPR	CDPT	PN/PT
-2	⊙	1.490	0.0	6.34	1.029	0.0102	121.01
0	□	1.490	0.0	6.38	1.035	0.0343	121.02
2	△	1.490	0.0	6.39	1.038	0.0699	121.03
4	◇	1.490	0.0	6.42	1.043	0.1010	121.04

φ=0 DEG

a. $M_\infty = 0.9$
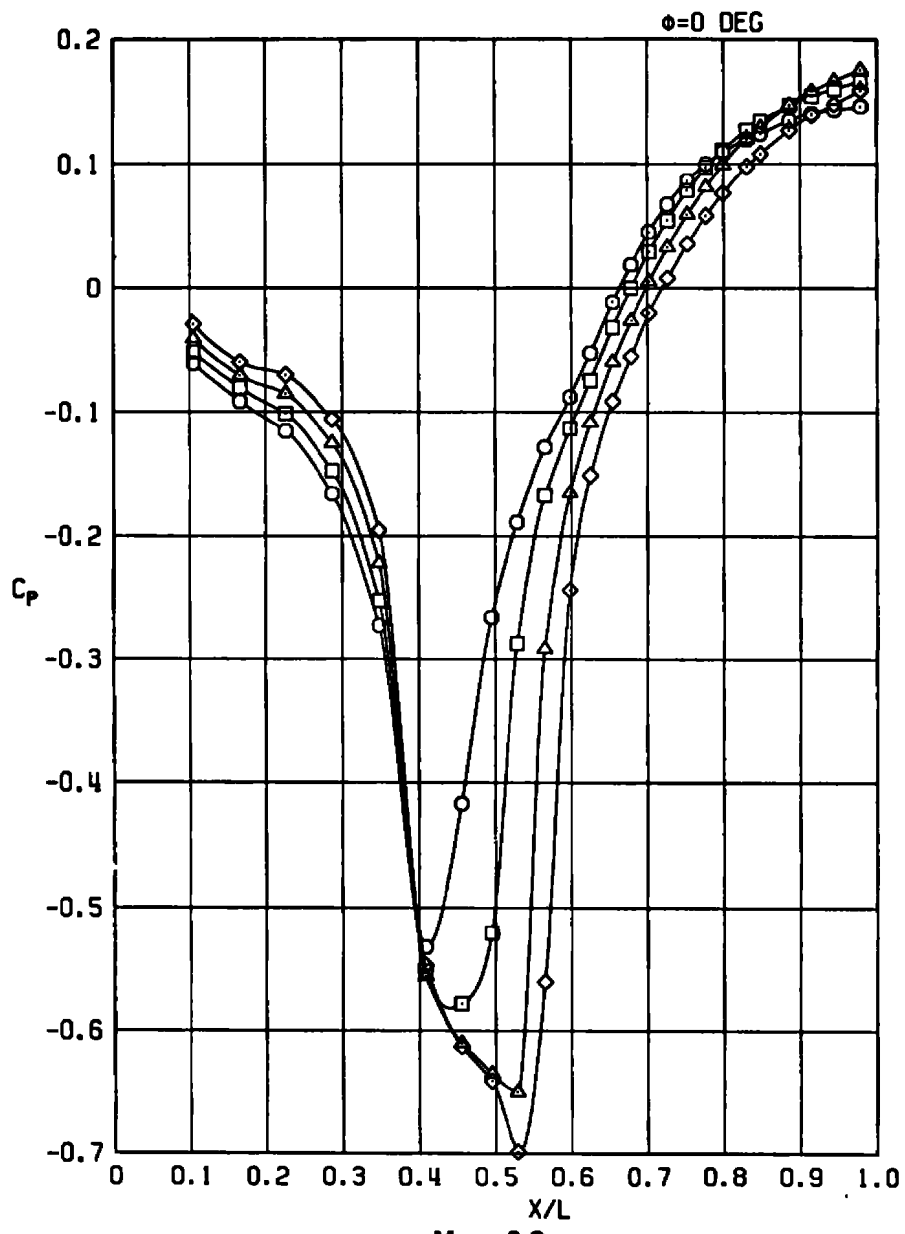
Figure A-17. Effects of angle of attack, $D_s/D_N = 0$, A/A* = 1.49, NSPR ≈ 1.0.

α, deg	SYM	A/A*	D_S/D_N	NPR	NSPR	COPT	PN/PT
-2	○	1.490	0.0	6.48	1.052	0.2150	123.01
0	⊡	1.490	0.0	6.53	1.060	0.2153	123.02
2	△	1.490	0.0	6.48	1.051	0.2235	123.03

b. $M_\infty = 1.2$
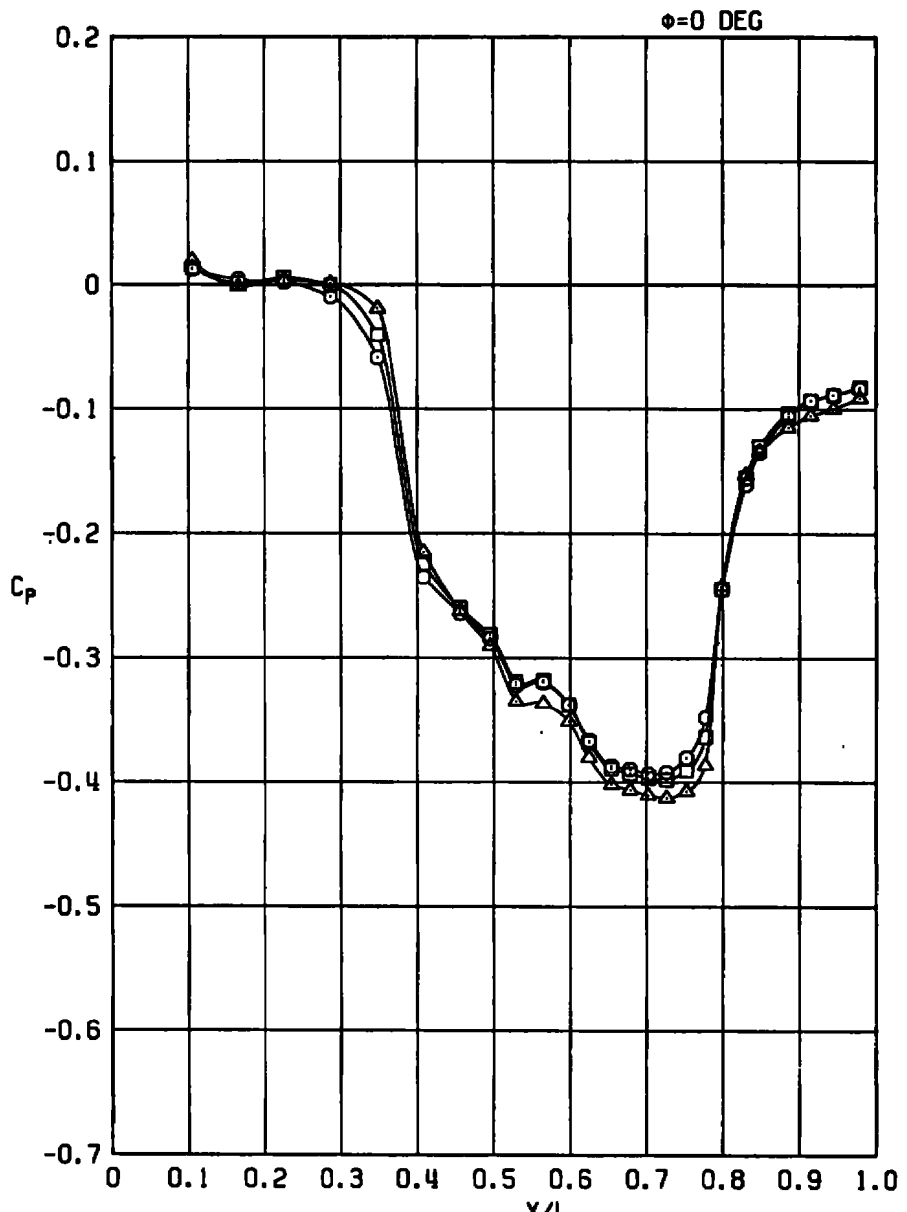
Figure A-17. Concluded.

α, deg	SYM	A/A*	D_S/D_N	NPR	NSPR	CDPT	PN/PT
-2	⊙	1.491	0.707	6.14	0.996	0.0108	75.01
0	▣	1.491	0.707	6.12	0.991	0.0241	75.02
2	△	1.491	0.707	6.10	0.989	0.0444	75.03
4	◇	1.491	0.707	6.09	0.987	0.0664	75.04

a. $M_\infty = 0.6$
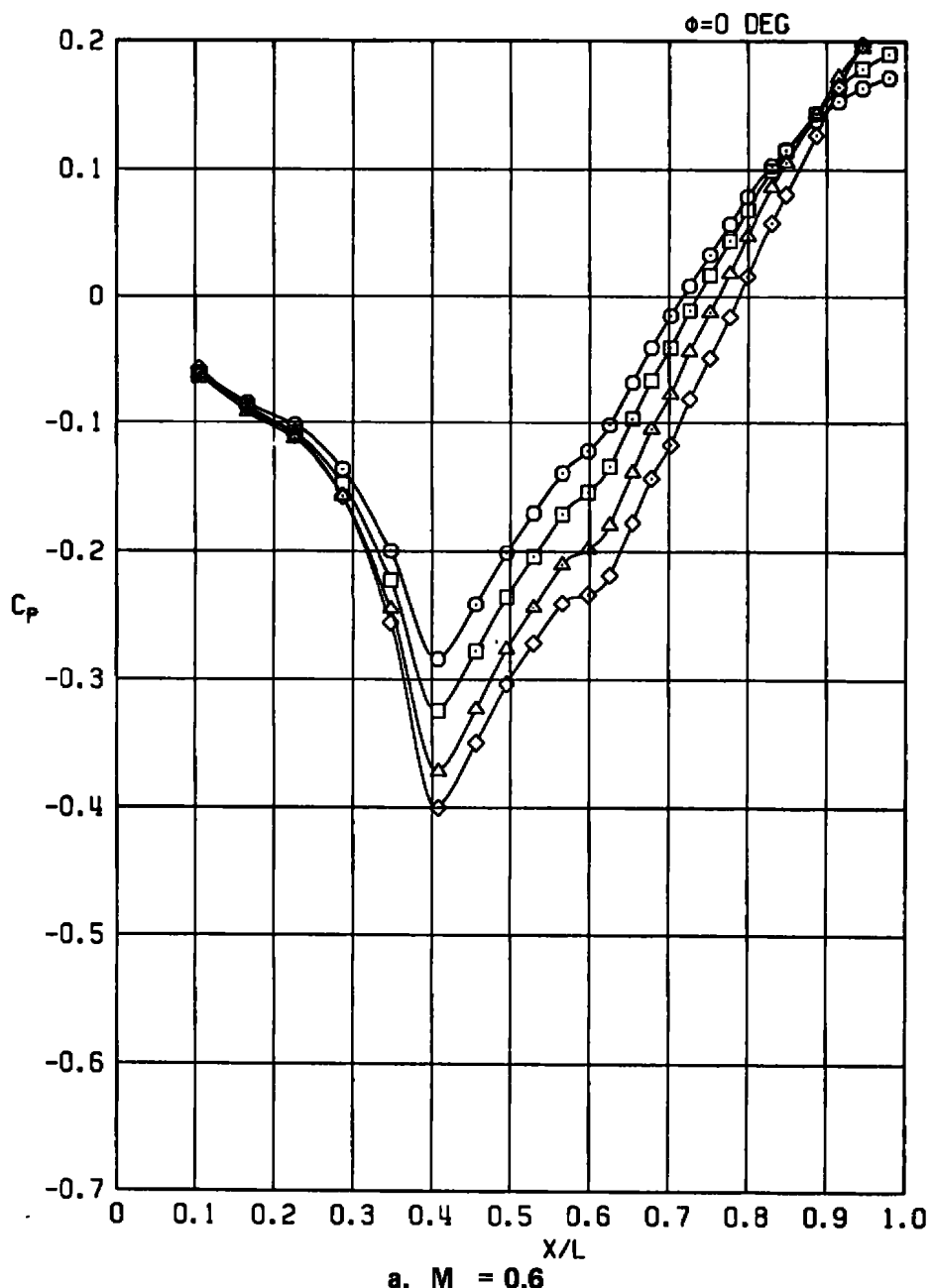
Figure A-18. Effects of angle of attack, D_s/D_N = 0.707,
A/A* = 1.491, NSPR ≈ 1.0.

α, deg	SYM	A/A^*	D_S/D_N	NPR	NSPR	CDPT	PN/PT
-2	⊙	1.491	0.707	6.27	1.017	0.0085	77.01
0	⊡	1.491	0.707	6.35	1.028	0.0336	77.02
2	△	1.491	0.707	6.33	1.026	0.0697	77.03
4	◇	1.491	0.707	6.34	1.027	0.1021	77.04
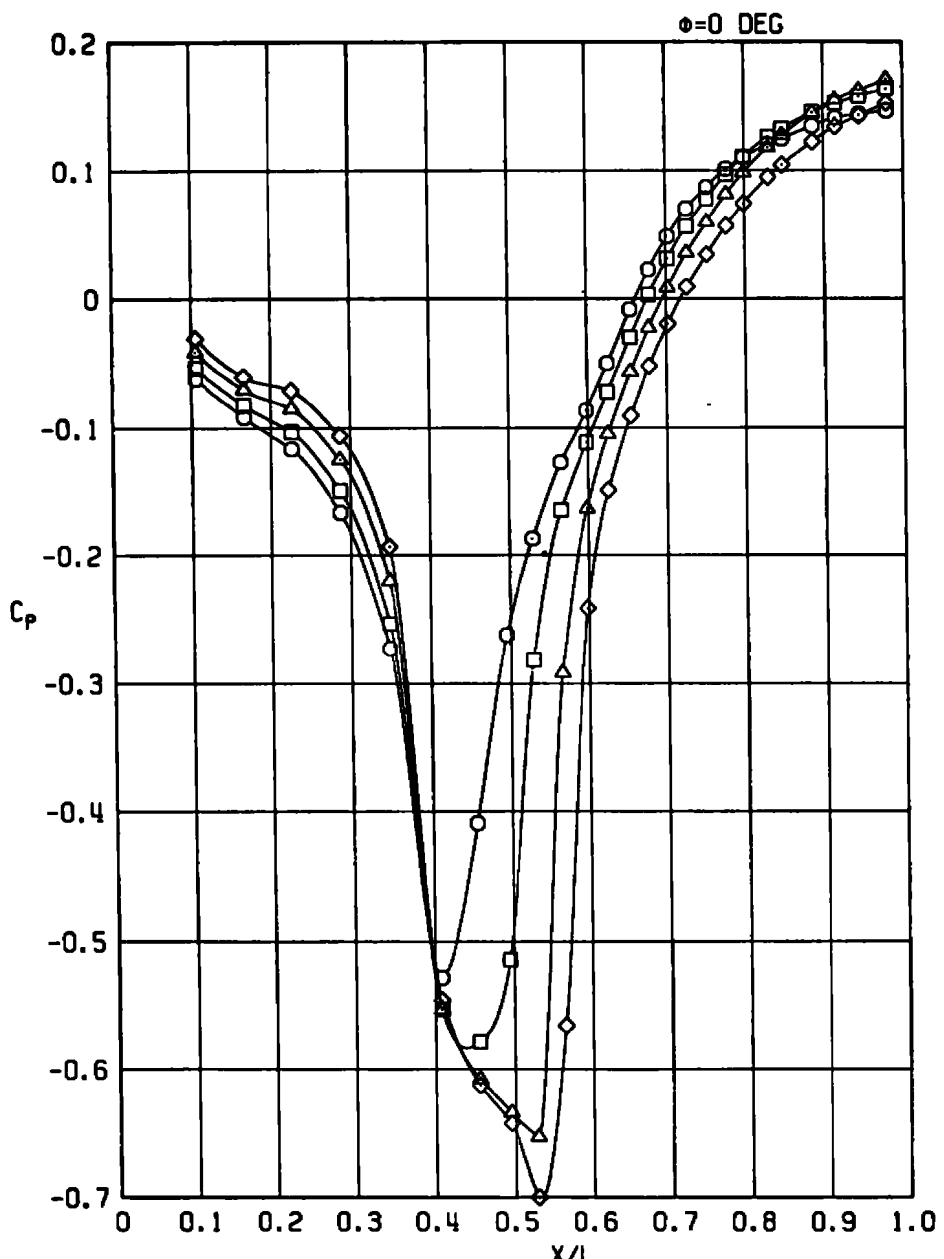
b. $M_\infty = 0.9$

Figure A-18. Continued.

α, deg	SYM	A/A*	D_S/D_N	NPR	NSPR	CDPT	PN/PT
-2	☉	1.491	0.707	6.26	1.015	0.2208	79.01
0	▣	1.491	0.707	6.29	1.019	0.2199	79.02
2	△	1.491	0.707	6.26	1.015	0.2253	79.03
4	◇	1.491	0.707	6.33	1.026	0.2304	79.04

Φ=0 DEG
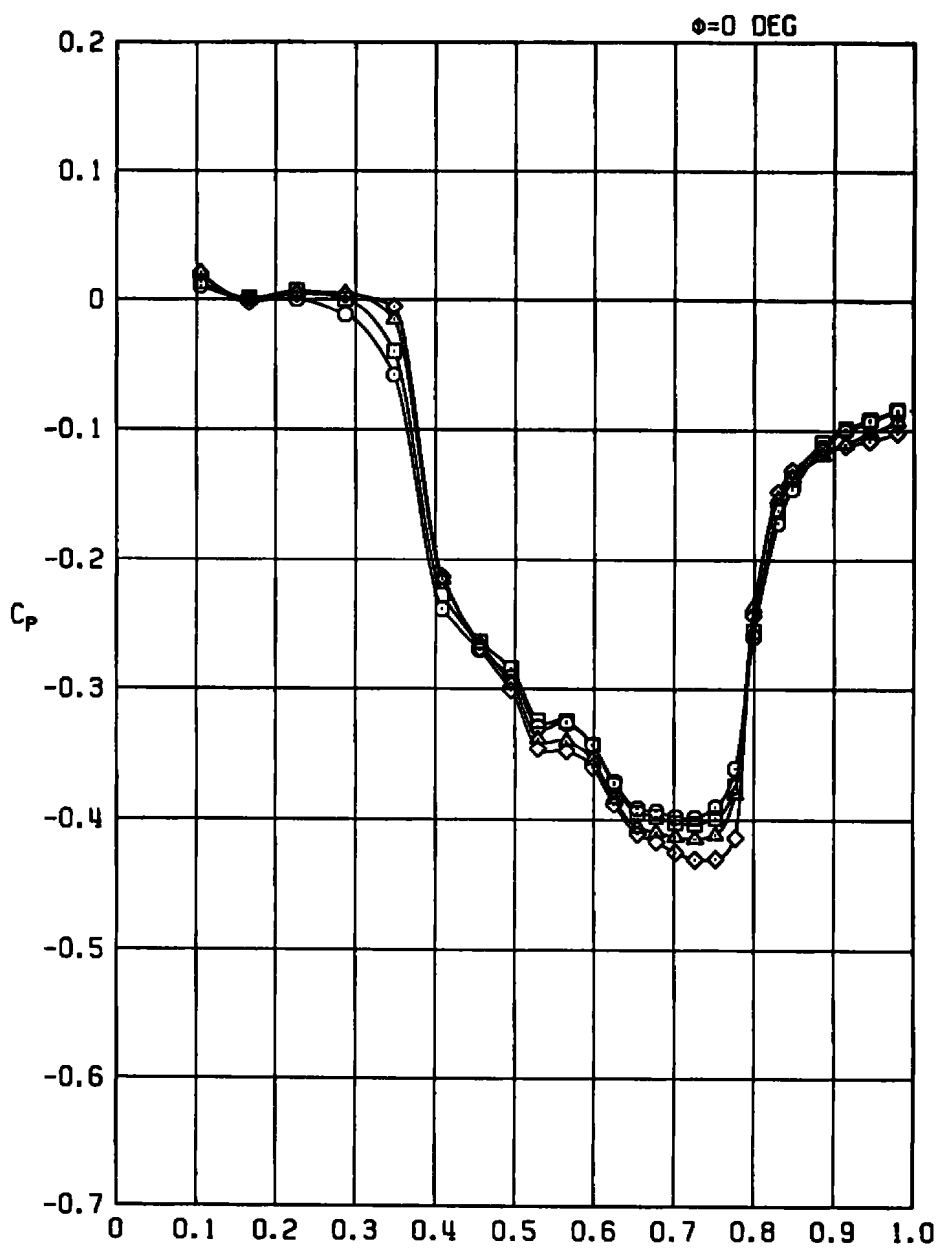
c. $M_\infty = 1.2$

Figure A-18. Concluded.

170

APPENDIX B
COMPARISON OF CONVENTIONAL JET CORRELATION PARAMETERS

These parameters follow some of the more conventional methods suggested in the literature for correlation of afterbody drag data. Data are shown in Figs. B-1 through B-3 at each Mach number as a function of NSPR, (NSPR)(A/A*), $\Delta\nu$, and $(\Delta\nu)(A/A^*)$. Of the four parameters presented here, the best correlation is achieved by $(\Delta\nu)(A/A^*)$. The degree of correlation achieved by this parameter is similar to that obtained by matching plume maximum diameter, as may be seen by comparing these data with the results in Fig. 26.
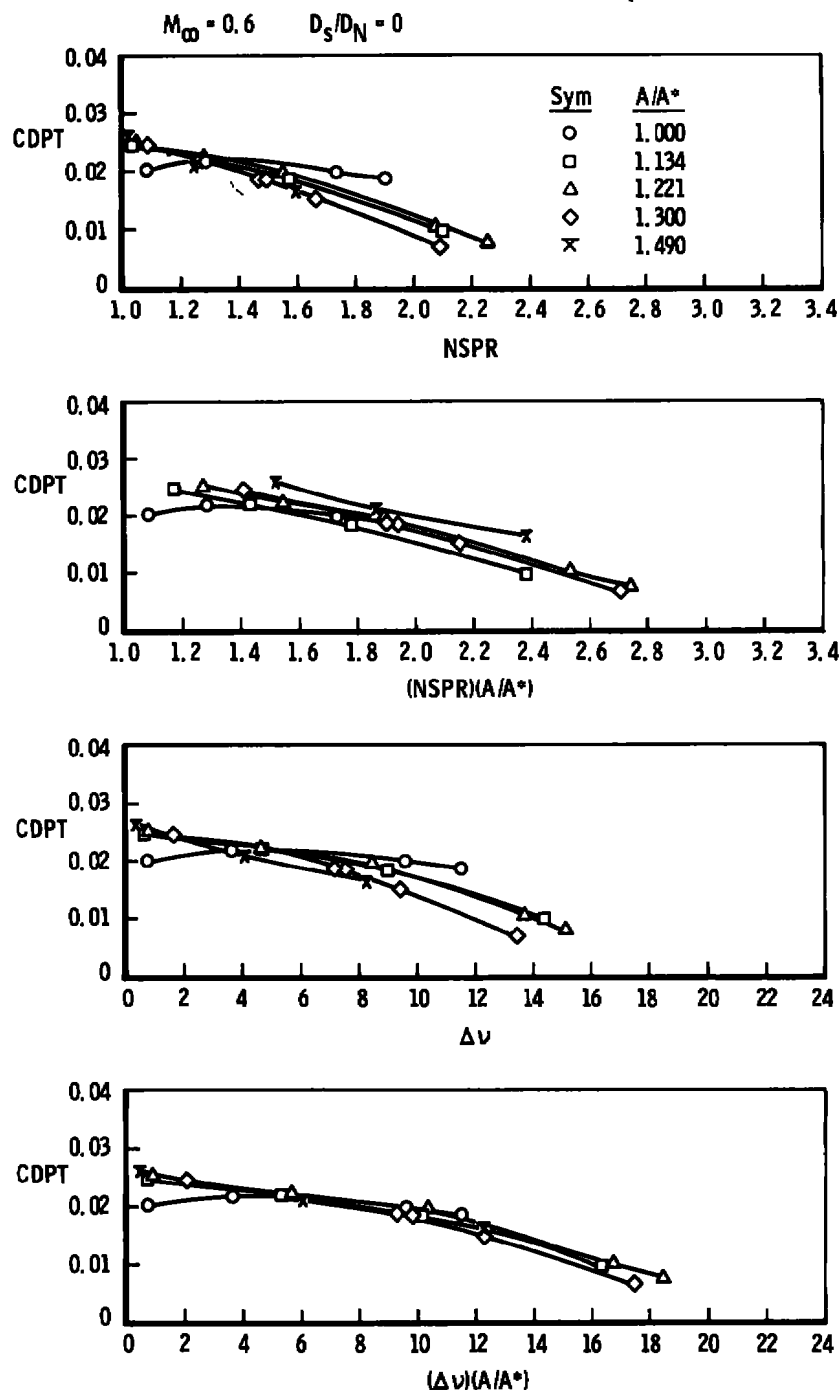
Figure B-1. Comparison of correlation parameters for conventional
jet data from various area ratio nozzles, $D_s/D_N = 0$,
$M_\infty = 0.6$.
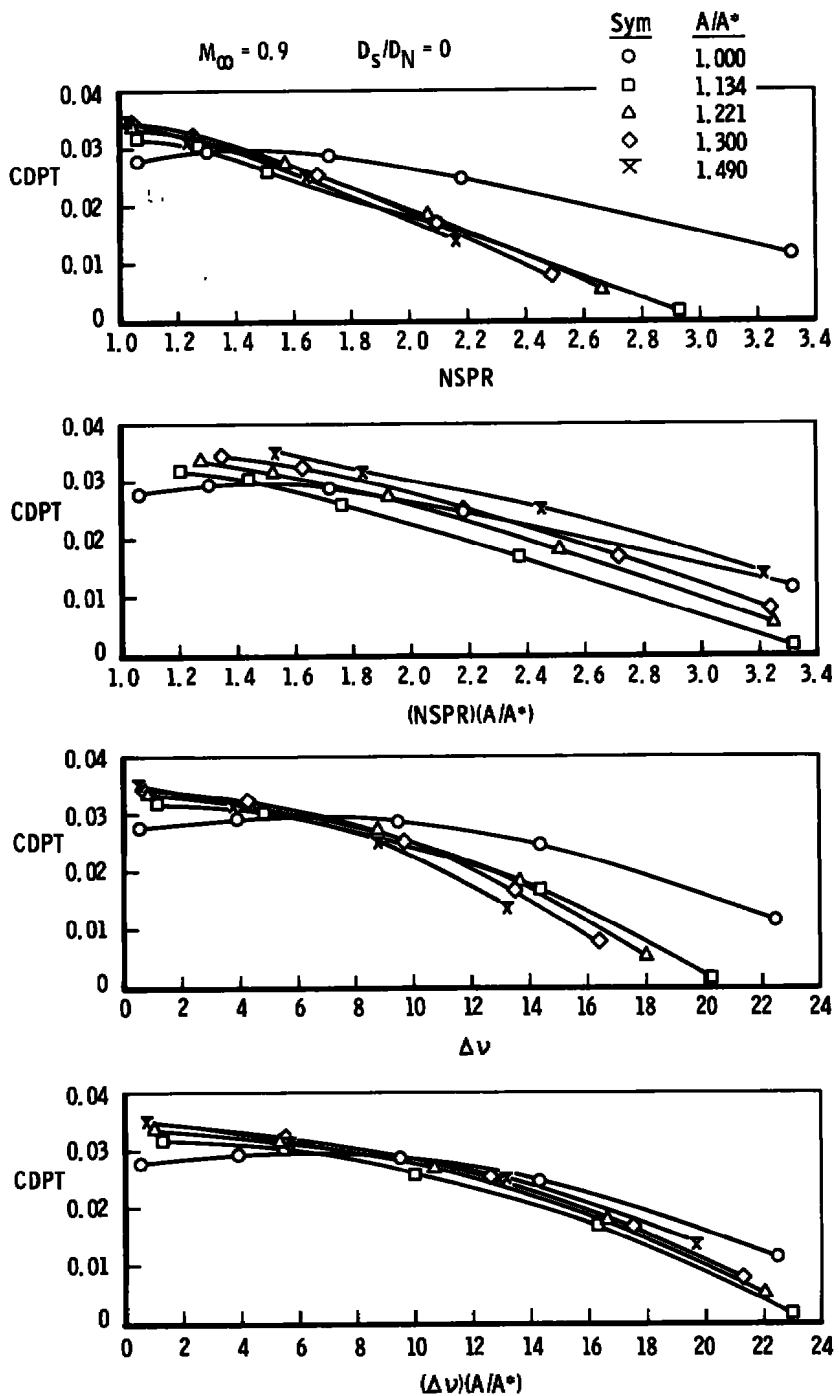
Figure B-2. Comparison of correlation parameters for conventional jet data from various area ratio nozzles, $D_s/D_N = 0$, $M_\infty = 0.9$.
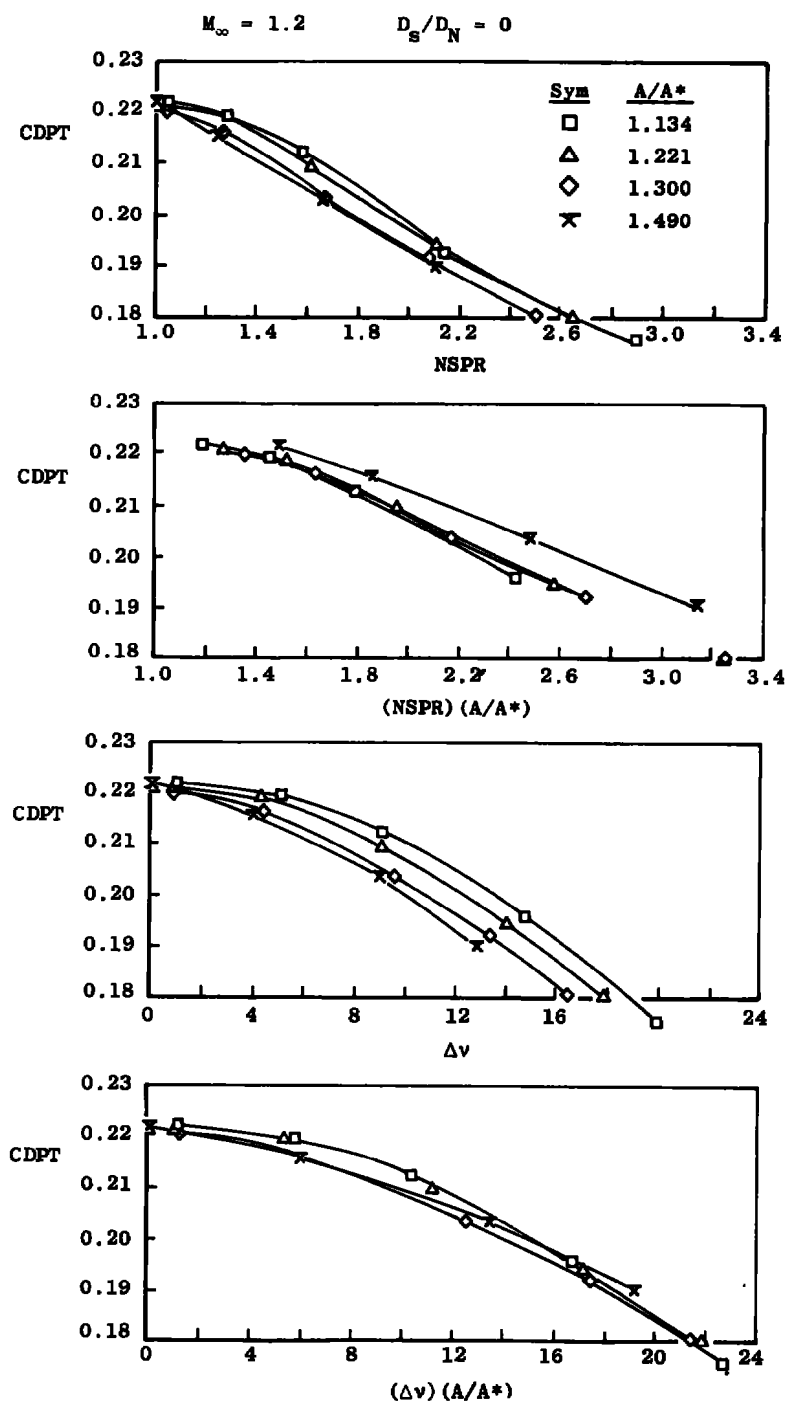
Figure B-3. Comparison of correlation parameters for conventional jet data from various area ratio nozzles, $N_s/D_N = 0$, $M_\infty = 1.2$.

NOMENCLATURE

A	Nozzle exit area, $[\pi/4\ (D_N^2 - D_s^2)]$, in.^{2}
A*	Nozzle throat area, $[\pi/4\ (D_T^2 - D_s^2)]$, in.^{2}
CDPT	Afterbody pressure drag coefficient in the body axis from integration of top row of pressures, nondimensionalized by model maximum cross-sectional area
C_p	Pressure coefficient, $(P_\ell - P_\infty)/q_\infty$
D_{max}	Plume maximum diameter, in.
D_N	Nozzle exit diameter, in.
D_s	Dummy sting diameter, in.
D_T	Nozzle throat diameter. in.
L	Length from face of dummy sting to sting pressure taps, in.
MOC	Method of characteristics
MS	Model station, in.
M_∞	Free-stream Mach number
NPR	Nozzle total pressure to free-stream static pressure ratio
NPR1	Correlation pressure ratio for correlating annular jet afterbody drag ($D_s/D_N >$ 0) data to conventional jet ($D_s/D_N = 0$) results using one-dimensional flow area relationships
NPR2	Correlation pressure ratio for correlating afterbody drag results from different area ratio nozzles using one-dimensional flow area relationships
NPR3	Correlation pressure ratio for correlating annular jet afterbody drag ($D_s/D_N >$ 0) data to conventional jet ($D_s/D_N = 0$) results using MOC
NPR4	Correlation pressure ratio for correlating afterbody drag results from different area ratio nozzles using MOC

NSPR   Nozzle exit static pressure to free-stream static pressure ratio

P_ℓ Local static pressure, psfa

$\overline{PN/PT}$ Part number/test point

p_∞ Free-stream static pressure, psfa

q_∞ Free-stream dynamic pressure, psf

R   Afterbody radius. in.

R_N Nozzle exit radius, in.

R_p Exhaust plume radius, in.

S   Length along instrumented sting from nozzle exit to last pressure tap, 14 in.

X' Longitudinal coordinate of afterbody contour relative to MS 130.471, in.

Y   Longitudinal distance along dummy stings relative to nozzle exit plane, in.

a Model angle of attack, positive nose down, deg

$\Delta\nu$ Incremental change in Prandtl-Meyer angle from conditions at the nozzle exit to free-stream conditions, deg

ϕ Angular location of afterbody pressure taps, deg